DIPL.-CHEM. BASTIAN M. NOLLER

DISSERTATION

JULIUS-MAXIMILIANS-UNIVERSITÄT WÜRZBURG
INSTITUT FÜR PHYSIKALISCHE CHEMIE

UNIVERSITÉ PARIS-SUD 11 &
LABORATOIRE FRANCIS PERRIN CEA SACLAY

Dipl.-Chem. Bastian M. Noller from Marbach am Neckar

Excited-State Dynamics of Organic Intermediates
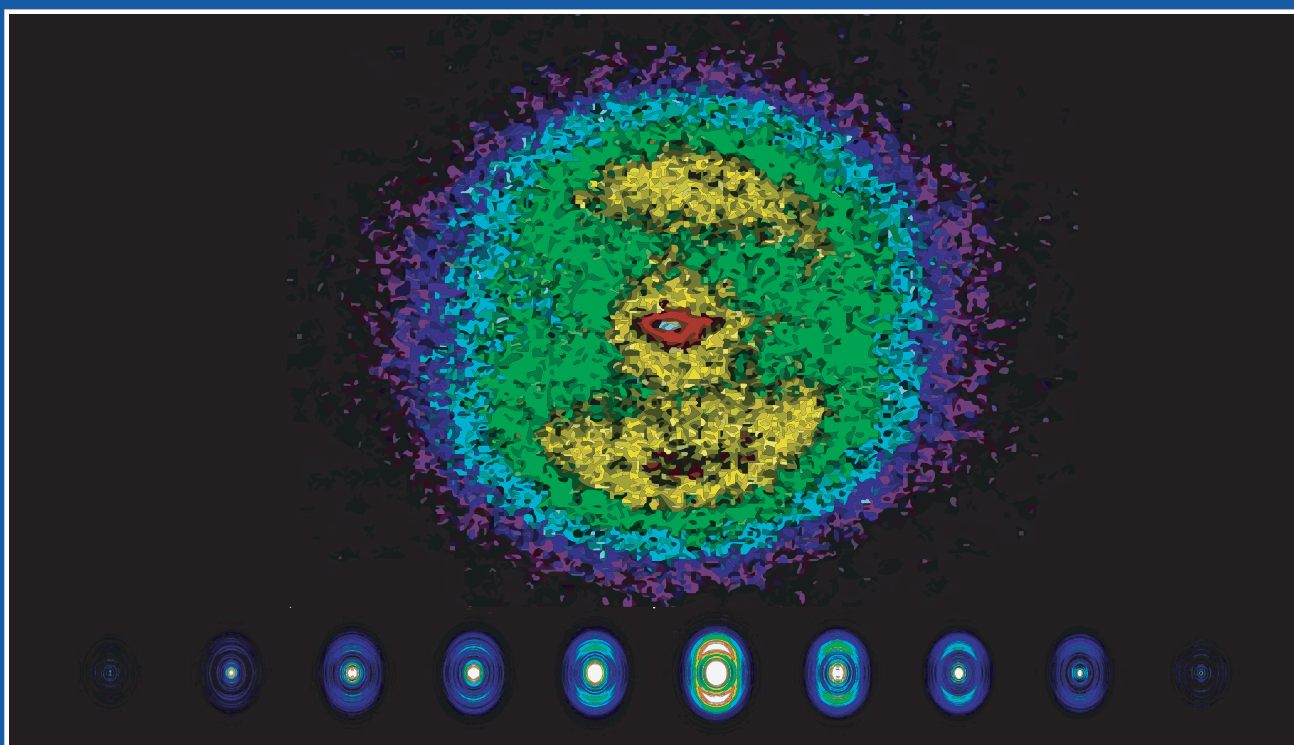
A thesis submitted for the degree of *Doctor of Natural Sciences*

Dissertation zur Erlangung des naturwissenschaftlichen Doktorgrades
der Julius-Maximilians-Universität Würzburg

Pour obtenir le grade de Docteur en Sciences
de l'Université Paris-Sud 11

SUPERVISORS:
PROF. DR. I. FISCHER (WÜRZBURG/GERMANY)
DR. J.-M. MESTDAGH (SACLAY/FRANCE)

PARIS/WÜRZBURG
MARCH 2009

No. d'ordre: 9420

THÈSE

présentée pour obtenir le grade de

DOCTEUR EN SCIENCES DE L'UNIVERSITÉ
PARIS-SUD 11

par

DIPL.-CHEM. BASTIAN M. NOLLER

Sujet:

Excited-State Dynamics of Organic Intermediates

Soutenue le lundi 11 mai 2009 devant la commission d'examen:

Prof. Dr. Mehran Mostafavi	Président
Prof. Dr. Christoph Meier	Rapporteur
Prof. Dr. Bernd Engels	Rapporteur
Prof. Dr. Tobias Brixner	Rapporteur
Prof. Dr. Ingo Fischer	Directeur de thèse
Dr. Jean-Michel Mestdagh	Directeur de thèse

Truly *to want something* means to do an experiment in order to find out what we can do.

—Friedrich Nietzsche

...dedicated to Alexandra

CONTENTS

ACRONYMS

AC   alternating current

AE   appearance energy

AS   active space

aq.   aqua

B3LYP   Becke (3 parameter) Lee, Yang and Parr

BASEX   basis set expansion

BMK   Boese, Martin for kinetics

BDE   bond dissociation energy

CAS   complete active space

CCD   charge-coupled device

CPC   chlorophenylcarbene

DC   direct current

DFT   density functional theory

DMB   2,3-dimethylbut-2-yl

DPI   dissociative photoionization

eq.   equilibrium

FC   Franck-Condon

FWHM   full width at half maximum

GUI   graphical user interface

HF   Hartree-Fock

HOMO   highest occupied molecular orbital

IC   internal conversion

IP   ionization potential

IR   infra red (light)

IRF   instrument response function

ISC   inter system crossing

LIF   laser induced fluorescence

LUMO   lowest unoccupied molecular orbital

MCP   micro channel plate

MP2   Møller-Plesset perturbation theory 2nd order

MRF   molecular response function

MS	mass spectrometry
MSP	micro sphere plate
NMR	nuclear magnetic resonance
PAD	photoelectron angular distribution
pBASEX	basis set expansion using polar coordinates
PEPICO	photoelectron/photoion coincidence
PES	photoelectron spectrum
PFI	pulsed field ionization
PI	photo ionization
q. c.	quantum chemical
QST	quadratic synchronous transit
REMPI	resonance enhanced multiphoton ionization
RRKM	Rice Ramsperger Kassel Marcus
SCF	self consistent field
SHG	second harmonic generation
SOMO	single occupied molecular orbital
SVB	split-valence basis set
TD-DFT	time-dependent density functional theory
TFPC	trifluoromethylphenylcarbene
TOF	time of flight
TPEPICO	threshold photoelectron/photoion coincidence
TPES	threshold photoelectron spectroscopy
TS	transition state
UV/Vis	ultraviolet/visible (light)
VMI	velocity map imaging
VSEPR	valence shell electron pair repulsion
VUV	vacuum ultraviolet (light)
ZEKE	zero kinetic energy
ZPE	zero point energy
ZPEC	zero point energy correction

INTRODUCTION

Almost all chemical reactions proceed over short-lived reactive molecular entities. Under normal conditions these transform on a time scale of only few molecular vibrations into the products. These highly reactive molecules, such as radicals, carbenes, carbocations and carbanions, are called intermediates. It is thus of considerable interest to characterize such species in order to acquire a full understanding of the dynamical processes involved during each step of a reaction. Several small hydrocarbon radicals and carbenes play key roles in combustion processes[2,3], interstellar space[4–7], polymerization[8,9] and hydrocarbon cracking[10]. Despite the relevance of hydrocarbon intermediates in high energy environments, only relatively little spectroscopic information on such systems is found in the literature due to the experimental challenge of producing such species under isolated conditions. For studies on free intermediates, side reactions as well as side product formation must be suppressed at the same time. However, since most of these molecules have very small barriers towards further reactions this is difficult to achieve (see fig. 1).

ⓘ Intermediate: A molecular entity with a lifetime appreciably longer than a molecular vibration that is formed from the reactants and reacts further to give the products of a chemical reaction[1].
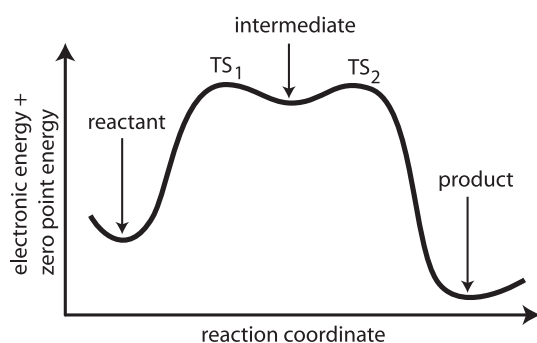
Figure 1: An intermediate has very low barriers toward further reactions and thus has only a short lifetime under normal conditions. Almost all chemical reactions proceed over reactive intermediates.

In this thesis spectroscopic properties and real-time excited-state dynamics of several important hydrocarbon intermediates have been studied in the gas phase by frequency- and time-resolved laser spectroscopy. Additionally, synchrotron radiation was applied in combination with TPEPICO spectroscopy. A variety of spectroscopic methods were applied in combination with intermediate sources. The goal was to cleanly produce isolated intermediates and elucidate there excited-state dynamics. Additionally, several of their spectroscopic characteristics such as absorption spectra, photodissociation dynamics, photoelectron spectra, ionization potentials and dissociative photoionization were studied. The investigations were focused on free carbenes as well as free radicals. However, the precursor molecules were studied as well, since these were used to generate the intermediates. This information is important for a clean intermediate formation, because know-

ing the behavior of the precursor is essential to understand possible effects on the spectra of the intermediates.

Experimental results were also compared to quantum chemical calculations to aid in the interpretation as well as to test the performance of theoretical approaches. Hydrocarbon radicals and carbenes are regarded as benchmark systems for computational methods due to their low-lying electronic states and open-shell electronic configuration. Thus the comparison with spectroscopic results on such species is important for evaluating and improving computational methods, especially those designed for predicting electronic structure of excited states[11].

Because of the very low barriers towards further reactions, intermediates are not stable under normal conditions. Hence over the last decades special methods were developed to prepare and preserve reactive intermediates for spectroscopic investigations. Common methods used for studying intermediates are: a.) matrix isolation[12], b.) studies in flames[13] and c.) molecular beam experiments[14,15].

In matrix isolation studies the intermediate is trapped and conserved inside an inert matrix at very low temperatures (e. g., argon at 10 K) and can be examined by various spectroscopic techniques such as IR or UV/Vis. Spectroscopy in flames can be done in special apparatus[16] while monitoring the concentration of reactive intermediates. Alternatively, spectroscopy can be performed through an optically accessible combustion chamber of an engine[17]. In this thesis specific isolated intermediates were prepared in a molecular beam by applying a technique called supersonic jet flash pyrolysis[18]. This method has the advantage that, while having the possibility of a mass selective detection of different species, the intermediates are formed under isolated conditions and "conserved" inside a cold molecular jet[19]. The beam is then crossed by a light source, e. g., lasers or synchrotron radiation (compare section 3.3). By synthetically designing precursor molecules, a clean beam of one specific intermediate can be generated. Hence such studies yield data that aids the interpretation of spectra recorded in interstellar space[20] and simplifies investigations of cracking and combustion processes. Such environments contain in general a complex mixture of several different intermediates. The more spectroscopic and dynamic properties of each isolated intermediate are known, the easier it is to identify it in such complex systems and to understand how it is involved and contributes to the overall mechanism. These are the basic requirements for a better understanding of combustion processes, for example. Here hydrocarbon radicals are known to play important roles in the formation of polycyclic aromatic hydrocarbons, which lead to soot[21]. Since increased densities of hydrocarbon intermediates are often present in high energy environments and have large influence on the overall reaction mechanism, this thesis also addresses the dynamics of the excited states of such species. Electronically excited states are formed if the electronic quantum state of a molecule (or atom) is increased in energy above the absolute minimum; thus electrons are excited into energetically higher-lying orbitals. Electronic excitation can take place by radiation[22], by particle collisions[23] or thermally at high temperatures[24].

Coupling molecular beam sources with modern laser spectroscopy has lead to many breakthroughs in the elucidation of the spectroscopic

properties of isolated reactive intermediates[25–28]. In this thesis several hydrocarbon intermediates have successfully been investigated by using this approach:

1. The photodissociation of propyl radicals (C_3H_7) was examined by photofragment Doppler spectroscopy applying nanosecond lasers. Hereby the rate constants of propene formation and the kinetic energy release of the H-atom photofragments was monitored as a function of the excitation wavelength. The results were compared to RRKM and DFT calculations.

2. The excited-state dynamics of propadienylidene was investigated in real time by femtosecond spectroscopy. The lifetime of the electronic $C\ ^1A_1$ state was determined after excitation at 250 nm.

3. The photodissociation of free propadienylidene (C_3H_2) carbenes was examined by photofragment Doppler spectroscopy using nanosecond lasers. The rate constant and the kinetic energy release of the H-atom photofragments were monitored after exciting the intermediate into an electronically excited state. The experimental rate constants were compared to RRKM calculations.

4. The primary photophysical processes of excited phenylcarbenes (Ph-C-R; R=CF$_3$, Cl) were elucidated by femtosecond time-resolved pump-probe spectroscopy. VMI of the ions has proven itself a very useful tool for generating a clean beam of intermediates. Additionally, VMI of the photoelectrons yields time-resolved photoelectron spectra, giving further insight into the dynamics of the excited states. The results were interpreted with the help of TDDFT calculations.

5. Synchrotron radiation was used to characterize the ionization potentials (IPs) of two phenylcarbenes (Ph-C-R; R=CF$_3$, Cl). The dissociative photoionization of the diazirine precursors, which were employed for producing the carbenes, was also studied as a function of the photon energy. Diazirines themselves are important photoaffinity labeling compounds[29]. The synchrotron experiments are essential for the interpretation of the femtosecond results.

6. The excited-state lifetime of the 2,3-dimethylbut-2-yl radical was investigated. These experiments give insights into the functional group dependence of excited-state deactivation by comparison to the closely related t-butyl radical[30].

This thesis is structured as follows: Chapter 2 describes the different experimental techniques, explains how they work and shows the capabilities for data retrieval they possess for the investigation of intermediates. Chapter 3 then introduces the experimental setups, which were used to characterize the intermediates and summarizes important general parameters for the reproducibility on these systems. Theoretical aspects of this thesis, which were used to interpret some of the experimental sections, are introduced briefly in chapter 4 and 5.

As the main part of this thesis, chapter 6 and following chapters present different experimental studies of specific reactive intermediates, put them into a context of current state of knowledge, describe

the results and draw conclusions[1]. These chapters also include specific experimental details. The results are organized by the different intermediates under investigation and by the applied experimental technique. In this thesis many different spectroscopic techniques were applied, and each method nicely amends the results of the other methods. Thus a variety of new information on the different intermediates was obtained.

At the end of this thesis, synthetic procedures are reviewed and a short summary of different developed scientific computer programs is given (chapter 14). These were programmed in order to solve different experimental and theoretical tasks[2].

The footnotes in this manuscript include supplementary information along the text. Additionally, this manuscript introduces margin notes, which show essential tables and figures that are important for the understanding of the presented experimental results. However, for further reading, nonessential margin notes are indicated with an "🛈" symbol. These include supporting information on topics presented in the main text and can be referred to if parts of the text need further clarification. Current related research fields are also briefly introduced herein.

---

[1] Additionally, the photodissociation of cyclopropenylidene (c-C_3H_2) was examined by photofragment Doppler spectroscopy and structured action spectra were acquired. The rate constants and the kinetic energy release of the H-atom photofragments were monitored at different excitation regions. Its IP as well as the corresponding cation was investigated using synchrotron light and PEPICO spectroscopy. The ultrafast excited-state dynamics of the benzyl radical discussed in my "master's thesis" were further examined using femtosecond spectroscopy. Since data analysis is still underway, these results are not yet included in this manuscript. [2] The software is available upon request: bastian.noller@phys-chemie.uni-wuerzburg.de

SPECTROSCOPIC TECHNIQUES

Several different spectroscopic methods were used for characterizing the intermediates and elucidating their dynamics. This chapter explains briefly how these methods work and which information can be gained by applying them.

2.1 REMPI SPECTROSCOPY

REMPI is the abbreviation for *resonant enhanced multiphoton ionization* and is a spectroscopic technique in which the ion yield is detected as a function of the irradiated wavelength[31]. The ion yield is strongly enhanced when the photon energy at the irradiated wavelength is equal (resonant) to an excited state of the molecule, and the ionization potential (IP) is reached by additional photons as illustrated in figure 2. In

ⓘ *REMPI schemes are denoted as: $[Np_e + Np_i^{\alpha}]$. Herein Np_e represents the number of photons used to excite the molecules (λ_1), Np_i stands for the number of photons used for ionization (λ_2). The exponent (α) is left blank if both steps use the same wavelength, otherwise it is replaced by a dash (').*
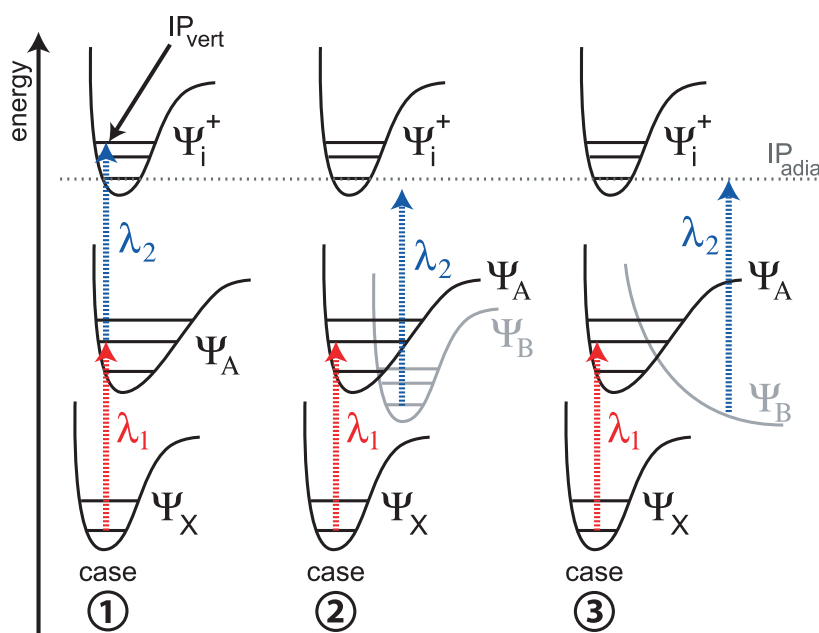
Figure 2: Three different REMPI schemes. The enhancement efficiency depends on the characteristics of the intermediate state.

this thesis nanosecond as well as femtosecond lasers were used, and it should be stressed that the time duration of the laser pulses has effects on the detection efficiency of intermediate states by REMPI[32]. The efficiency strongly depends on the lifetime of the intermediate state and is thus linked to the duration of the laser pulses. In the simplest case (fig. 2, case ①) the molecule is excited with a first photon λ_1 from the electronic and vibrational ground state Ψ_X into an excited state Ψ_A. In case ①, Ψ_A has a sufficiently long lifetime and to be ionized with a second photon λ_2. Different REMPI schemes can be employed. For example, two photons of longer wavelength can be used in the ionization step. If the excited state decays from Ψ_A to Ψ_B before the

ionization photon arrives, the ion signal is often weaker or completely gone[1]. Hence a state that shows a REMPI effect with femtosecond lasers does not necessarily result a strong signal when nanosecond lasers are applied. The deactivation of an excited state can, for example, take place by internal conversion (case ②) or by photodissociation (case ③) as illustrated in fig 2.

2.2 PHOTOFRAGMENT & DOPPLER SPECTROSCOPY

To examine the unimolecular dissociation of molecules after electronic excitation, photofragment Doppler spectroscopy of H-atom fragments was performed (fig. 3). The apparatus used in the experiments is presented in chapter 3.3.1 (fig. 18). The sensitivity of the method is based on the high oscillator strength of the 1 $^2S \rightarrow$ 2 ^2P transition of hydrogen (Lyman-α line).

After the molecule has been excited into an electronic excited state Ψ_A (fig. 3, left) by the first laser, the deposited energy can redistribute over the internal degrees of freedom of the molecule. If the photon energy ($E_p = h\nu$) of laser 1 is larger than the activation energy needed to break a C–H bond, a dissociation can take place. The C–H bond can break either directly in the excited state if Ψ_A is a dissociative state or alternatively after the molecule has relaxed by internal conversion back to the hot ground state (Ψ_X). A dissociation from Ψ_X is more common in the case of hydrocarbon radicals. The hydrogen photofragments
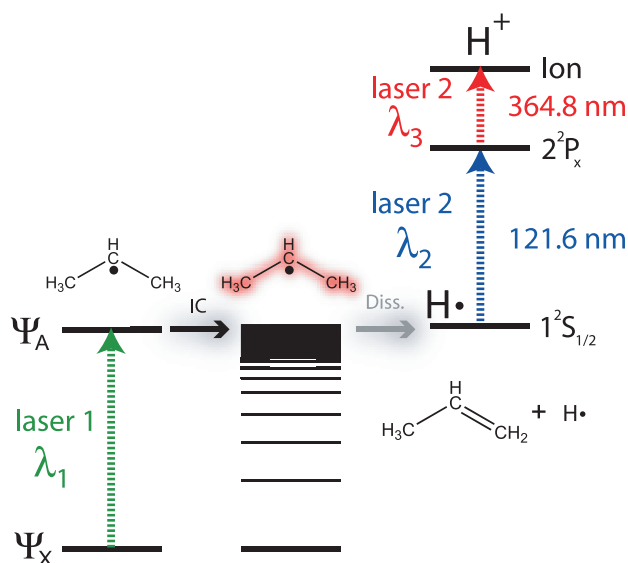
Figure 3: Excitation and detection scheme used to elucidate the dynamics of the hydrogen photofragments after excitation into Ψ_A

(H·) are then ionized by laser 2 in a subsequent $[1 + 1']$ REMPI process (compare section 2.1). As described in section 3.3.1 a VUV wavelength of around 121.6 nm is generated by frequency tripling of the 364.8-nm output of a tunable dye laser. The 121.6-nm laser light induces the

---

[1] Note that the energy of the molecule is conserved in gas phase experiments. Thermal energy, which is distributed over the molecule after deactivation, does not effectively contribute to the ionization probability.

Lyman-α transition in hydrogen, and the excited hydrogen atoms are ionized using the residual 364.8 nm (fig. 3, right-hand side).

This detection scheme enables several different types of excitation-detection experiments, which can be exploited to elucidate the photodissociation dynamics of reactive intermediates:

1. *Delay scans:* By recording the hydrogen ion intensity as a function of the delay time between the pulses of laser 1 and those of laser 2, the reaction rate of the dissociation process can be measured by analyzing how fast the H signal rises in an excitation-detection experiment. Thus information can be gathered on how fast the intermediates dissociate after a specific amount of energy has been deposited into the molecule (see equation 6.3 on page 44 presented together with an example in chapter 6.4).

2. *Doppler profiles:* The time delay between both lasers is held fixed, while the wavelength of laser 2 is scanned (see fig. 3). Since the molecular beam is crossed perpendicular by the laser beams, all species inside the molecular beam have a negligible velocity in direction of the laser beam. Thus the absorption bands of the examined species in the molecular beam show negligible Doppler broadening. However, if a C–H bond is cleaved, the photofragments (H·) carry away a considerable amount of kinetic energy because of momentum conservation. This leads to a Doppler broadening of the Lyman-α transition. The FWHM (full width at half maximum) of the transition is thus dependent on the amount of excess energy deposited into the fragment. By scanning laser 2 and recording the Doppler profile, information on the speed distribution of the hydrogen fragments can be gained, which allows conclusions on the dissociation mechanism (see, e.g., chapter 6). For cases in which the molecules dissociate statistically and the photofragments show an isotropic distribution, the expectation value[2] for the kinetic energy of the photofragments can be calculated from the FWHM of the Doppler profiles according to equation 2.1. Herein, c is the speed of light, $\tilde{\nu}_0$ is the wavenumber of Lyman-α transition in rest and m_H resembles the mass of fragment[36]. A detailed discussion on how to extract information of Doppler profiles is given in chapter 6.3.

$$\langle E_t \rangle = \left(\frac{\text{FWHM} \cdot c}{\tilde{\nu}_0} \right)^2 \cdot \frac{3\, m_H}{16 \ln 2} \tag{2.1}$$

3. *Action spectra:* The intensity of the fragment signal is monitored as a function of the wavelength of the excitation laser (laser 1). When a transition has a high oscillator strength, many molecules are excited inside the beam and hence the amount of photofragments increases. Thus by integrating the photofragment signal as a function of the wavelength used to excite the intermediates, their absorption spectra can be measured[3].

ⓘ Doppler broadening: *According to* $f_{lab} = f_0 \left(1 - \frac{\vec{v}_z}{c} \right)$, *an atom moving with a velocity component* $\vec{v}_z$ *in the direction of the light source absorbs at a frequency* f_{lab} *instead of* f_0 *when it is not moving* (c = *speed of light*)[35]. *The atom registers a higher frequency than is produced by the laboratory laser system* (f_{lab}). *Hence to hit the resonance of the atom* f_{lab} *must be chosen smaller than* f_0.

---

[2] To calculate the most probable value E_{mp} for the energy rather than $\langle E_t \rangle$, the factor $(3/16)$ has to be replaced by $(1/8)$ in equation 2.1[35]. The equation is derived by assuming a *Maxwell* speed distribution for gas particles.   [3] Action spectra can be used to identify the origin of photofragments by comparing the known absorption spectrum of molecules with their action spectrum. Nevertheless, it should be mentioned that this method is also very sensitive and can be used if other absorption methods are not applicable, i.e., if the IP of a molecule is difficult to reach by REMPI or intermediates states are short lived.
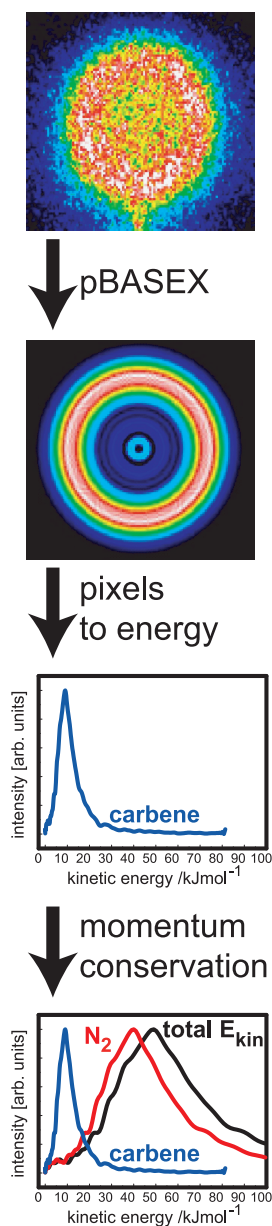
Velocity map imaging (VMI) is a relatively new technique developed in the late 1990s by the *Parker* group for measuring the kinetic energy distributions of charged particles[37] after they have been ionized by lasers. The method has several advantages over TOF mass spectrometry[4] and conventional photoelectron spectroscopy. In this thesis VMI was used to optimize parameters for an efficient intermediate generation by the pyrolysis source (see chapter 9.3.1) and to elucidate the excited-state dynamics of the reactive species. The detector of a VMI spectrometer is designed not only to detect the ion intensities mass selectively but also to register the position where the particles collide with the detector. Fast particles with a velocity component perpendicular to the direction of extraction will hit the detector on a larger radius than particles with a small velocity. The method is very sensitive[5] and can be used to detect both *ions and photoelectrons with the same experimental setup*, depending on the polarization of the extraction voltages. Velocity map imaging of the electrons has similarities to conventional photoelectron spectroscopy. By measuring the intensity of the electrons as a function of the radius on the detector, one can later on reconstruct the photoelectron spectrum. In conventional photoelectron spectroscopy the information is usually restricted to the intensity as a function of kinetic energy[6]. In VMI the angular distribution is directly measurable[38]. The angular distribution of photoelectrons as a function of the irradiated laser polarization is, e.g., dependent on the symmetry of the ionized electronic state of the molecule. Since the photoelectron angular distributions (PADs) reflect the electronic symmetry, VMI can in principle be used for probing and differentiating electronically induced processes, e.g., nonradiative transitions[7] such as IC and ISC[39].

When a molecule absorbs photons of sufficient energy, an electron can leave the molecular framework. The kinetic energy of these photoelectrons is given by equation 2.2.

$$Ekin_e = E_{phot} - \left(IP_0 + E_{rv}^+ + E_{el}^+\right) \tag{2.2}$$

The higher the ionization potential (IP_0) and the more energy remains in the cation in form of rovibrational (E_{rv}^+) and electronic energy[8] (E_{el}^+), the smaller the kinetic energy of the emitted photoelectron ($Ekin_e$) will be. In cases of multiphoton ionization processes (compare section 2.1) the irradiated photon energy (E_{phot}) equals the sum of the energy of all participating photons.

Figure 5 gives a schematic overview of a VMI spectrometer. In this example pump-probe spectroscopy is applied, which produces photoparticles (electrons or ions). Depending on the polarization of the extractor and repeller voltages, electrons as well as ions can be accelerated onto the MCP at the end of a flight tube. An electron cascade

pBASEX

pixels to energy

intensity [arb. units]

carbene

0 10 20 30 40 50 60 70 80 90 100
kinetic energy /kJmol^{-1}

momentum conservation

intensity [arb. units]

N_2 total E$_{kin}$

carbene

0 10 20 30 40 50 60 70 80 90 100
kinetic energy /kJmol^{-1}

Figure 4: VMI can be used to study the dissociative photo-ionization of diazirines.

---

4 However, VMI has a considerably inferior mass resolution as compared to TOF mass spectrometry.   5 detection efficiency $\approx 60\%$ 6 Conventional PES can, however, be recorded from different detection angles and/or employing different laser polarization to extract angular dependence.   7 Nevertheless, experimental results with clear interpretations are till now restricted to small molecular structures.   8 When irradiating a molecule with a photon energy considerably higher than the adiabatic IP an electronic state of the cation can be populated. Thus E_{el}^+ denotes the energy of the excited-state in the cation. If the ground electronic state of the cation is populated then $E_{el}^+ = 0$.
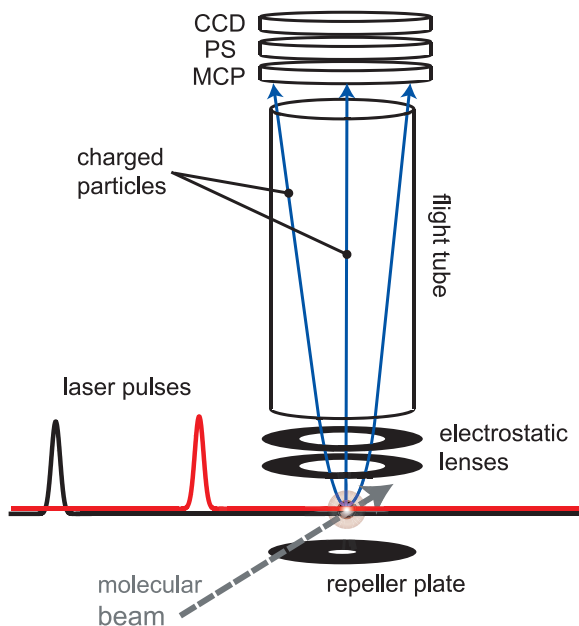
Figure 5: Schematic overview of a VMI spectrometer. Charged particles are registered on a position-sensitive detector.

is induced when a charged particle hits the surface of the MCP and a following phosphoresce screen (PS) emits photons at this position, which can easily be seen with the bare eye. These raw images (fig. 4, top) of the charged particles are then monitored as a function of the delay time between pump and probe pulse by a CCD camera for further analysis.

The raw images are generated by accelerating and projecting a three dimensional (3D) distribution of charged particles, with different kinetic energy, onto a flat surface. Thus in many cases information is lost, since the photoparticles originally spread out in three dimensions according to their kinetic energy on so called *Newton* spheres as illustrated in fig. 7. Each sphere represents particles with the same kinetic energy. Only the intensity of the most outer part of the raw image is directly proportional to the amount of particles with highest kinetic energy. The particles towards the center of the raw image correspond to several different kinetic energies. However, due to the cylindrical symmetry of the problem, *the central slice* of the original energy distribution can be reconstructed by computer assisted inversion methods (see, e. g., fig. 4); this corresponds to the central slice of the Newton spheres, which yields information on the angular distribution of the particles.

2.3.1 *Inversion Methods*

There are several different inversion methods based on the inversed *Abel* integral[38]. The central slice of the *Newton* sphere and the measured image are directly convertible by forward and backward *Abel* transformation. However, direct analytic methods have some drawbacks. They are very sensitive to noise in the recorded raw spectra (es-

ⓘ *Note that the complete original 3D* Newton *sphere is not recovered by* Abel *transformation; only its central slice parallel to the detector is reconstructed.*

9
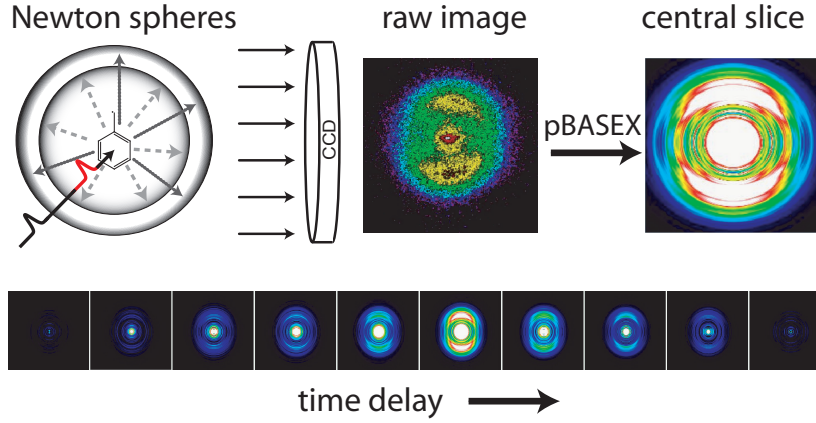
Figure 7: Overview of the VMI process and the reconstruction of the original center slice of the Newton sphere by the pBASEX method. The bottom shows the images evolving in time.
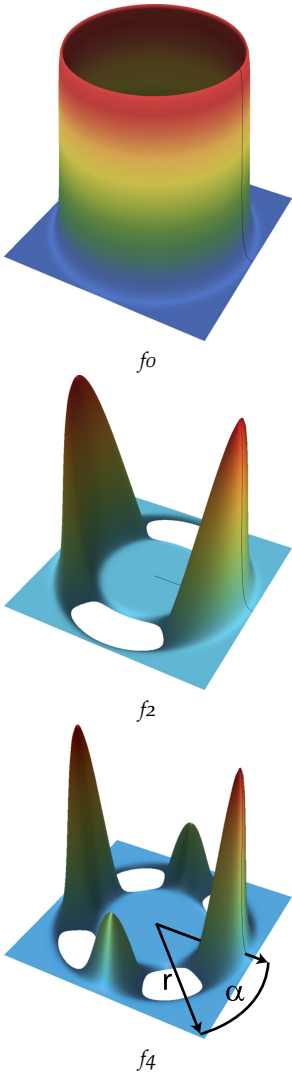
Figure 6: Examples of $f_{(\alpha,r)}$ functions in pBASEX

pecially towards the center) and thus incorporate unwanted artifacts in the reproduced energy distributions[38]. More modern methods exist such as a "basis set expansion using polar coordinates" (pBASEX) which was used throughout this thesis[37,40]. The pBASEX reconstruction, developed by *G. Garcia et al.*, is a forward convolution method[37]. Compared to other methods it has relatively small computational cost, is insensitive to noise in raw images and has a very good resolution in terms of energy and angular dependency[38]. It requires, however, more memory and the basic shape of the spectra has to be imposed by the experimentalist before applying the method to the spectrum[9]. Additionally, the method distinguishes between different polarized structures in the images; for most other inversion methods contributions of different polarization to central slice have to be analyzed and distinguished in additional steps. In the pBASEX method the raw images are described by a basis set[37]. The basis set functions $p_{(\alpha,r)}$ are functions that were calculated by forward *Abel*-transforming "trial" functions $f_{(\alpha,r)}$. The trial functions $f_{(\alpha,r)}$ are formed by taking Gaussian profiles for describing the radial dependence and multiplying them by *Legendre* polynomials of different order for describing the angular dependence. Examples are given in fig. 6. The linear combination of all $p_{(\alpha,r)}$ is fitted to the experimental spectrum in the form of equation 2.3. Capital P_i denote the sum of several $p_{(\alpha,r)}$ functions (one for every radius). The coefficients b_i depend on the examined system[41]. For example, photoelectron spectra can be described using only P0 and P2 when using linear polarized light, randomly orientated nonchiral molecules and a one-photon ionization; for all other P_i the coefficients are zero[41,42].

$$I_{(\alpha,r)} = P0(\cos\alpha) + \sum_{i=1}^{n} b_i P_i(\cos\alpha) \tag{2.3}$$

Since a linear combination of all $f_{(\alpha,r)}$ (absolute values) directly yields the central slice of the original 3D *Newton* sphere (fig. 7, upper right), knowing the best-fit coefficients of the basis set, the original center

---

[9] However, many different forms can be systematically tested (P0, P2...Pn) and those parts neglected that have small coefficients.

slice is defined as well. The spectrum can afterwards be divided into different "P_i" parts (P_0, P_2, P_4, etc.). The P_0 part e. g., denotes the intensity of the image that was properly described by a *Legendre* polynomial of zeroth order (circle, unpolarized part) with no nodes. P_0+P_2 parts, on the other hand, have one node and correspond to polarized parts of the image (fig. 6). The sum over all b_2 coefficients is proportional[37] to the so called anisotropy parameter β in photoionization experiments for single-photon processes in which the target forms two fragments[41] (e. g., one ion and one electron).

2.4 FEMTOSECOND TIME-RESOLVED PUMP-PROBE SPECTROSCOPY

Femtosecond pump-probe spectroscopy evolved from laser induced coherence studies in solids and gases[44] and is based on the work of *R. M. Hochstrasser* and *A. H. Zewail*[45,46]. In principle, the method works in a similar manner as was described in section 2.2. However, two (or more) femtosecond laser pulses are used to follow molecular dynamics (femtochemisty). The first laser initiates a process in the molecule (pump) and a second delayed pulse (probe) produces a detectable species[10] that can be followed as a function of the delay time between the two pulses (fig. 8).

A big challenge for following molecular processes on a femtosecond time scale is to produce very short laser pulses of only a few femtoseconds (fs, 1×10^{-15} s) and to precisely control the delay time between them. In contrast to nanosecond time-resolved experiments the delay of the laser pulses can no longer be controlled by electronic delay generators in the femtosecond (and picosecond) regime. Thus usually variable delay stages are employed which delay one of the laser pulses by increasing the path length compared to the first pulse as depicted in fig. 8 and 19 (1 mm $\widehat{=}$ 3335.7 fs in vacuum and 3336.6 fs in air).
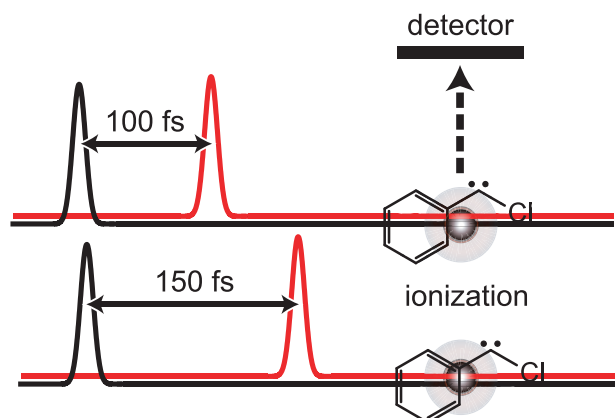
Figure 8: In fs pump-probe spectroscopy the first laser pulse triggers the process and a second laser pulse produces a detectable species (e. g., ions).

Several detection possibilities can be applied. In the gas phase, e. g., time-of-flight mass spectrometry (TOF), photoelectron spectroscopy,

---

[10] In this context detectable species denote, e. g., fluorescent electronic states (LIF), electrons (e^--VMI) or ions (TOF-MS), depending on the chosen detection method.
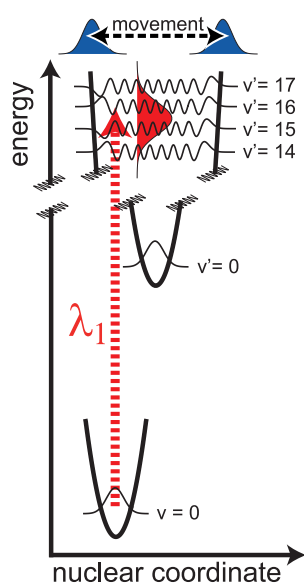
ZEKE spectroscopy, photoion imaging (I$^+$-VMI), photoelectron imaging (e$^-$-VMI) and laser induced fluorescence (LIF) are popular methods used for detection.

Due to the time-energy uncertainty principle, the femtosecond laser pulses must possess a relatively large spectral width (approx. 10 nm = FWHM at a wavelength of 800 nm for a 100 fs pulse) when compared to nanosecond laser pulses. Femtosecond pulses are formed by superposing several different wavelengths. Hence when irradiating a molecule, the pump pulse also produces a superposition of several molecular states within its bandwidth. Usually a number of vibrational states are excited simultaneously and form a so called *wave packet* via a linear combination of the incorporated vibrational wave functions (fig. 9). Wave packets propagate in time[44] and move along potential energy surfaces similar to classical motions, as is illustrated in fig. 10. Depending on the position and shape of the wave packet on the potential energy surface, it can be further excited to detectable states by the second laser pulse or not. Thus by following the intensity of the detectable species as a function of the delay time between the two pulses, the dynamics of the primary induced wave packet can be followed, which correlates to molecular motion such as, for example, bond breaking.

By probing the propagation of the wave packet on the excited state potential energy surface, depending on the system and the detection method, different dynamical properties of a molecular system can be elucidated. Some important cases are listed in the following:

- Molecular reactions in the excited state, i.e., bond cleavage and transition state formation[46]. This was demonstrated in the *Zewail* group by following the dissociation of excited I–CN using LIF as detection method.

- Photoinduced electron transfer reactions[47], which are linked to molecular geometry changes.

- Non radiative deactivation mechanisms of excited states, e.g., by internal conversion or through conical intersections[44,48]. For the studied reactive intermediates these seemed to be the favorable deactivation mechanisms after optical excitation.

In the following measurements of this thesis the femtosecond experiments were performed in the gas phase by applying TOF mass spectrometry and velocity map imaging (chapter 2.3). In both cases charged particles are detected. Thus the probe pulse projects the wave packet, produced from the pump pulse, into an ionic state (fig. 10) — ions and electrons are produced.

The intensity of free ions and electrons reaching the detector are directly dependent on the ionization probability of the wave packed produced by the pump pulse[11]. Depending on the current geometry and electronic state of the molecule at the time the probe pulse arrives (λ_2), the ionization probability differs due to, e.g., variations of the Franck-Condon factors for the ionization of the excited state. Hence molecular motion can be followed in real time by monitoring the ion or electron intensity as a function of the delay time between pump and probe. Some deactivation mechanisms of the primary populated

Figure 9: A broad band laser pulse induces wave packets in excited states of molecules by superposing several wave functions.

---

[11] Refer to chapter 5 for a description on how time-dependent spectra were analyzed.
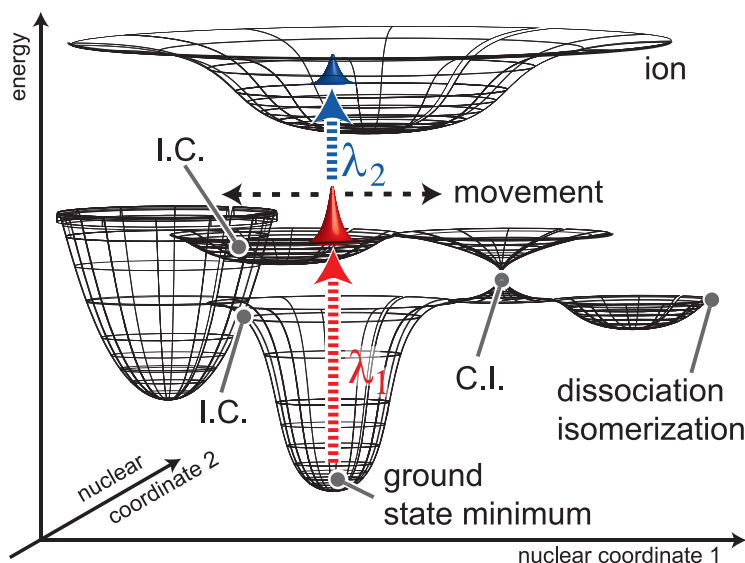
Figure 10: Illustration of different deactivation mechanisms of the primarily induced excited state wave packet. Depending on the current geometry and electronic state of the molecule at the time the probe pulse arrives (λ_2), the ionization probability differs. Thus molecular motion can be followed in real time by monitoring the ion or electron intensity as a function of the delay time between pump and probe.

excited state, which lead to changing ionization probabilities, are summarized in fig. 10. A strong change in Franck-Condon factors and ionization probability is especially found when the molecule relaxes over: Conical intersections (CI), internal conversion (IC) and bond breakage. But other relaxation mechanisms are possible, e. g., dephasing of the wave packet in the excited state has been reported in the literature[49].

In the initial femtosecond time-resolved pump-probe experiments only small molecular model systems were studied and their LIF or ion yield signals were comparatively straightforward to interpret, since fewer degrees of freedom were excited in these molecules[46]. Nowadays the trend clearly goes to elucidating dynamical processes in large polyatomic molecules with many more degrees of freedom[50]. The acquired spectra have become considerably more difficult to interpret and more assumptions have to be made to find a consistent dynamical model with the observed time-dependent ion signals.

A deeper insight into excited-state molecular dynamics can be gathered using time-resolved photoelectron spectroscopy (TRPES)[50]. In this work photoelectron spectra were recorded by velocity map imaging of the electron distributions as described in chapter 2.3. In contrast to observing the ion yield alone, photoelectron spectroscopy is a state selective technique. Depending on the molecular system and the electronic state it is in, the ionization potential differs (see, e. g., fig. 79 on page 93), which is reflected in different kinetic energy of the photoelectrons (equation 2.2). For example, electronic energy is converted into thermal energy if a excited state deactivates by IC. Thermal energy does often not efficiently contribute to the ionization probability. Hence the signal declines and the rate of IC can be measured. Since a

new lower-lying electronic state is now populated, the kinetic energy of the photoelectrons changes and in an ideal case induces a new band in the photoelectron spectrum[50] as long as the lower state is still ionizable by the probe pulse. Thus the time dependence of this band correlates to the population transfer into the lower state. Photoelectron signals are observable as long as energy is not fully transferred into vibrational energy and dispersed over the molecule. Another important aspect with regard to ionization probability is the correlation of excited states with ionic states[51]. When ionizing a molecule the probe pulse projects the current state into a final ionic state. In a one-photon ionization the electronic structure of the final state correlates to the *same* electron configuration as the ionized state after removing one electron[51]. A strong enhancement of the photoelectron intensity is observable when the given electronic state correlates to the ionic ground state after removing the energetically highest electron.

2.5 SYNCHROTRON LIGHT SOURCES & REACTIVE INTERMEDIATES
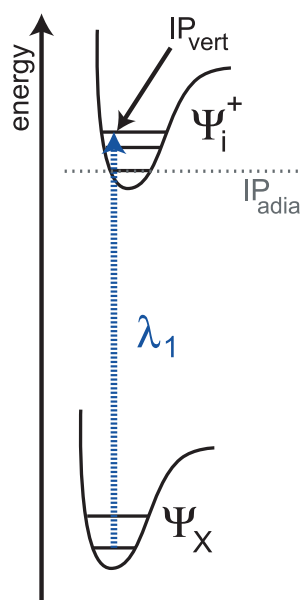
Due to the experimental challenge of producing a clean source of reactive intermediates, only relatively few ionization potentials (IP) of reactive intermediates are precisely known. Photoionization of intermediates inside a molecular beam is a convenient method for determining their IPs (fig. 11). Since intermediates can only be generated in low concentrations and the IPs are not well known, such direct ionization measurements can only efficiently be performed if the light source used for ionization is quickly tunable over a wide energy range, has high energy resolution and high photon flux. VUV generation using four-wave mixing techniques of nanosecond lasers possesses a tuning range of only about 0.1–0.2 eV for a given set of experimental parameters[52]. Thus such techniques are only efficiently applicable if the IPs are roughly known. Fortunately synchrotron radiation possesses broad tunability and fulfills all requirements for studying photoionization, dissociative photoionization and ionic state structures of reactive intermediates[53]. Appearance energies and IPs can be determined by following the ion (and electron) yields of specific mass channels as a function of the radiation wavelength. When the IP is reached, the ion yield usually increases strongly. The appearance energies of fragments are measurable by following the mass channels of molecules, produced by dissociative photoionization, as a function of the photon energy. Thus the dissociation pathways and dissociation energies of the corresponding carbocations can be determined.

Knowing the IP of molecular species considerably helps to identify them in complex mixtures and can thus be used to verify, e. g., atmospheric compositions or combustion products. An illustrative example is given fig. 12. In this experiment n-propylnitrite was pyrolysed and the ion yield of $m/z = 30$ was monitored as a function of the irradiated VUV wavelength[12]. As visible the ion yield curve shows two steps. The first step in the spectrum is found at 9.25 ± 0.1 eV and the second one at 10.6 ± 0.2 eV. Both values reflect the known IPs of formaldehyde (OCH_2, 10.88 eV) and nitric oxide (NO, 9.264 eV), respec-

Figure 11: Synchrotron radiation delivers tunable VUV radiation. Direct photoionization is thus possible.

---

[12] This spectrum was recorded together with *C. Alcaraz et al.* — note that the energy resolution of this scan is very low. The figure is shown to demonstrate the principle.
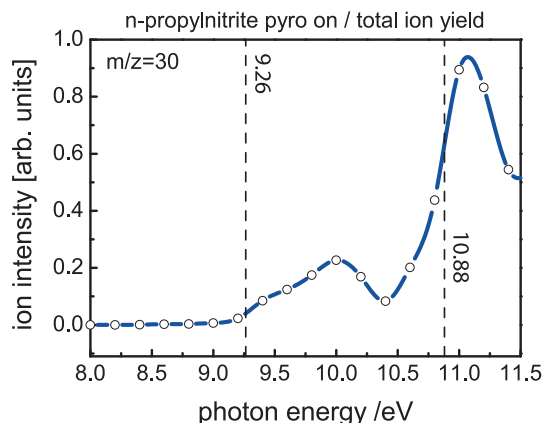
Figure 12: Nitric oxide and formaldehyde (both $m/z = 30$) are detected simultaneously by PEPICO spectroscopy with *n*-propylnitrite as precursor. The dashed lines mark the values of the adiabatic IPs of NO and H_2CO taken from the literature[54,55].

tively[54,55]. Hence conclusions can be drawn on the thermal decomposition of *n*-propylnitrite, since ethyl with $m/z = 29$ is detected as well (scheme 1).
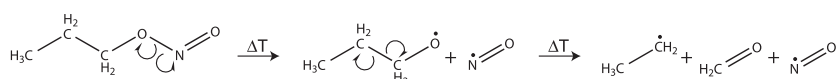
Scheme 1: Thermal decomposition of *n*-propylnitrite

2.5.1 *TPEPICO Spectroscopy*

VMI (chapter 2.3) was also applied in the synchrotron studies[56]. In comparison with lasers, synchrotron radiation has considerably less photon flux. Thus only very few ions are produced in the interaction region at the same time. This enables to correlate single electrons with certain ions. Additionally, only a low density of intermediates can be produced, which makes the experiments challenging on the one hand; on the other hand, the very small ion current can be used to count single coincidences of electrons and ions. This has many advantages as will be discussed below. In contrast to the laser experiments the photon source is nearly continuous. Hence many counting cycles can be performed per time unit, and counting rates of coincidences are in the region of hundreds or thousands of coincidences per minute. In coincidence spectroscopy each ion can be assigned to one specific electron[13], since the experiment is triggered by the detection of a single electron (fig. 13). Once a photoelectron is produced, it is extracted by a continuous field towards the VMI detector, where it is detected. This photoelectron signal triggers the detection window of the much heavier photoion, which is detected immediately afterwards and the

---

[13] after subtraction of so called "false coincidences" in which more than one ion was produced in the detection time window.
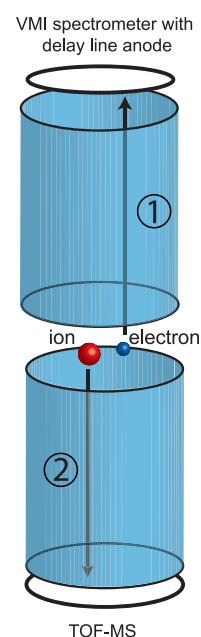
Figure 13: Each electron triggers ion detection in PEPICO spectroscopy.

15

time of flight of the ion is registered. The electron can thus be assigned to a specific ion mass.

This method is named PEPICO spectroscopy[56]. PEPICO spectroscopy enables to correlate each mass channel in the TOF-MS with an entire photoelectron spectrum, which is especially useful when side products are generated in the pyrolysis source[14].

A further feature when using a VMI spectrometer for detection of the photoelectrons is that a high detection efficiency is achieved for the photoelectrons. Photoelectrons with high kinetic energy and photoelectrons with low kinetic energy are detected. These can be distinguished via VMI, since slow electrons hit the detector preferentially close to the center (fig. 14, top trace). The total ion signal of a specific mass can be broken down and only those counts taken into account that correspond to photoelectrons below a certain kinetic energy threshold (threshold PEPICO, TPEPICO). Hence one degree of freedom is pinned down in a similar manner as is discussed for ZEKE spectroscopy in appendix A.2, and the internal energy deposited onto the corresponding ion is determined. This leads to a higher spectroscopic resolution, since much less quantum states (vibrational and rotational) of the ion contribute to the signal. The procedure is illustrated in figure 14 on the example of cyclopropenylidene (c-C_3H_3).
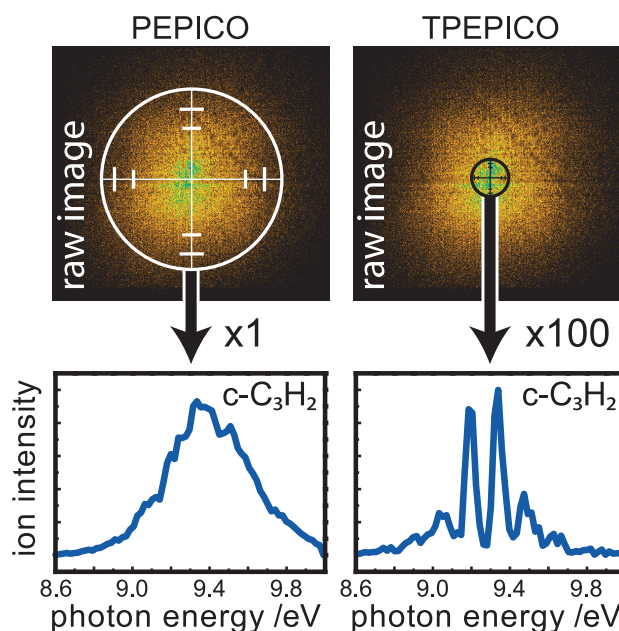
Figure 14: In PEPICO all ions of one specific mass are registered as a function of the photon energy. TPEPICO discriminates all ions corresponding to electrons above a certain threshold energy. Hence the resolution increases.

---

[14] Due to the continuous mode of the pyrolysis, more side products are usually produced as compared to the pulsed mode applied in the presented laser experiments.

EXPERIMENTAL SETUP

3.1 CARBENE AND RADICAL SOURCES

3.1.1 *Water Cooled Pyrolysis Source*

The intermediates in this thesis were generated by supersonic jet flash pyrolysis. The pyrolysis source of *Chen et al.*[18] is described elsewhere in more detail[58,59]. In brief an electrically heatable silicon carbide (SiC) tube is mounted to the exit of a General Valve (*Parker Hannifin*, series 9) operated at the repetition rate of the laser system. SiC is
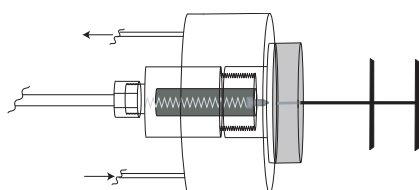
Figure 15: The pyrolysis source: To prevent overheating and too early degeneration of the precursors a water cooling system was attached to the solenoid valve.

chemically very inert and can be heated simply by applying an electrical current, since it is a semiconducting material. An improvement was achieved by augmenting the solenoid valve with an active water cooling system[60], allowing operation temperatures of the valve below 50°C. This modification assured a very stable operation of the valve over the entire temperature range of the SiC tube (300–2000°C). Thus precursors with strong inter-atomic bonds could be cleaved using high temperatures and without effecting the operation of the pulsed valve. On the other hand, it was also assured that precursors did not decompose before reaching the end of heated SiC tube, resulting in superior signal intensities. This is of fundamental importance for thermally very unstable precursor molecules such as diazirines that would decompose inside the valve before reaching the SiC tube, leading to many side products. The construction also implemented the possibility to adjust the General Valve from the outside of the apparatus, following the idea of *C. Jouvet* and the *C. Alcaraz* group at *CLUPS* in Orsay/France, who use a similar construction in order to adjust noble gas beams for VUV generation (see fig. 16). While the faceplate of the General Valve is held fixed by the water cooling head, the entire body of the valve can be rotated by turning the connected pipe (rod) from the outside of the apparatus. Thus the space between the faceplate and the General Valve itself can be optimized. Readjusting this very important parameter helps to optimize the pulse width and intensity of the molecular beam pulse, which is important to achieve the best possible conversion efficiency and cooling of the intermediates. This can now be performed without breaking the vacuum and while simultaneously monitoring the signals on the oscilloscope, two factors that save a lot

of time and assure better signal quality. The idea of augmenting the pyrolysis source by a water cooling system has made many new experiments possible that were not performable before (see chapters 9 and 11).
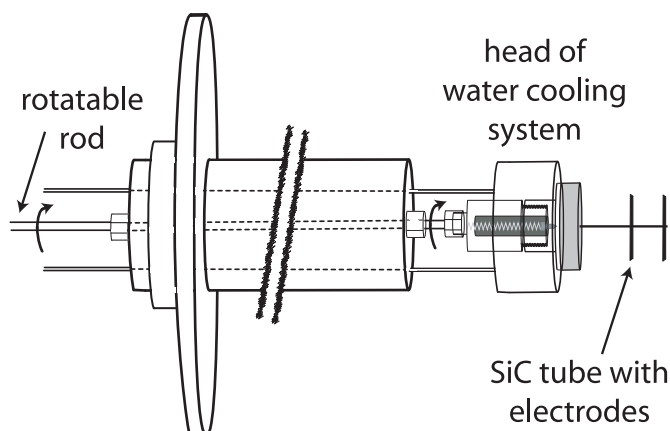
Figure 16: The General Valve can be adjusted from the outside of the apparatus.

3.2 SEEDING PYROPHORUS COMPOUNDS INTO A MOLECULAR BEAM

Some of the available precursors for generating intermediates decompose easily on metal surfaces, since they are often very reactive by their own. To prevent direct contact of the precursor with the steel walls of the sample containers, glass inlays were designed (fig. 17). Pure glass sample containers without steel mantle were too fragile, difficult to seal and caused safety issues at the applied backing pressures (1–4 bar). In order to be able to handle pyrophorus substances without the need of an expensive glove box, a sample container was designed to directly inject precursors into an inert gas atmosphere (fig. 17a). A standard septum was tightened into the top of the sample container by an aluminum lid. The injection was then preformed through a hole at the top of the lid, which could be sealed off by a Teflon-coated screw. With this setup sample injections are possible during the measurement without breaking the inert gas stream. The construction also works at high backing pressures (≤ 5 bar). The container depicted in fig. 17b is equipped with a glass window at the bottom. This gives two enhancements: a) It is a comfortable way to check if there enough precursor left during measurements. b) When handling explosive compounds, it is essential to take safety precautions. At very high pressures (> 50 bar) the glass in the bottom of the container will break first, releasing the pressure. Both stainless steel containers were designed to be easy to refill and were sealed by o-ring KF 40 flanges when working at room temperature. For experiments in which the precursor was directly condensed into the container, the KF 40 flange was sealed using special low temperature aluminum gaskets. Alternatively, the bottom part was replaced by a special sealed glass tube with KF 40 flange connector (*Aachner Quarz-Glas Technologie Nr. 025040*).
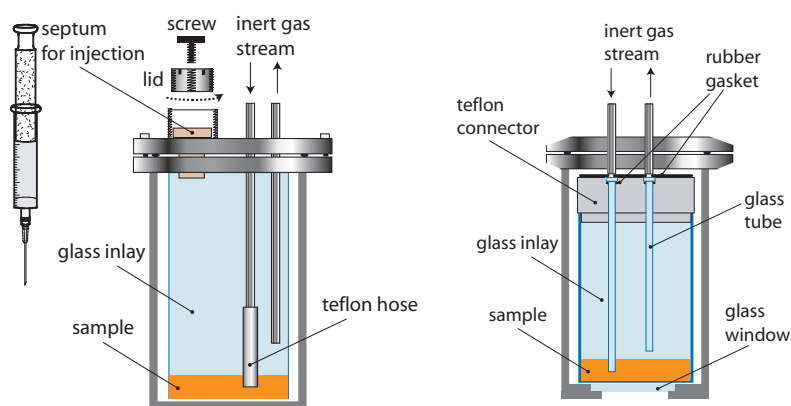
(a) Glassware for seeding pyrophorus precursors

(b) Glassware for seeding precursors

Figure 17: Many precursors for intermediates are already very reactive by themselves. Glass inlays prevent decomposition on the stainless steel walls of the sample container.

3.3.1 *Laser System & Molecular Beam Apparatus*

After passing the SiC tube of the intermediate source, the fragments were expanded into a differentially pumped standard molecular beam apparatus (1×10^{-4} mbar source chamber, 2×10^{-6} mbar ionization chamber) equipped with a 0.5 m time-of-flight mass spectrometer[61]. An electron detector (see appendix A.1) was attached on the opposite side of the mass spectrometer. The apparatus is schematically shown in fig. 18. The molecular beam passes a skimmer before entering the main ionization chamber, where it is crossed by one or two laser beams. 118 nm.

For one-color experiments such as REMPI and for excitation of the molecules, the frequency doubled output of a *Sirah Cobra CSTR-G-24* dye laser, which was pumped by a *Continuum SLI-10* Nd:YAG laser, was applied (alternatively a *Quanta-Ray DCR* Nd:YAG laser was used for pumping the dye laser). Both dye lasers produced tunable horizontally polarized light between 218 (SHG) and 900 nm (fundamental). BBO and KDP crystals were used for second harmonic generation (SHG). For generating fundamental wavelengths between 400 and 560 nm the dye laser was pumped at 355 nm and for wavelengths between 561 and 900 nm the dye lasers were pumped at 532 nm. For recording two-color REMPI spectra, Doppler profiles and time-delay scans a second dye laser setup was used for ionization. It consisted of a *Sirah Precision Scan PRSC-LG-18* dye laser pumped by the output of a *Spectra-Physics Lab-170* Nd:YAG laser. The laser spot size of the excitation laser was around 0.35 cm in diameter and was used unfocused. In photofragment spectroscopic investigations the H atoms were ionized in a [1+2′] multiphoton ionization step. For this purpose the output of the second dye laser (around 13 mJ at 365 nm) was focused by a 100-mm lens into a cell filled with 100 mbar of krypton to produce
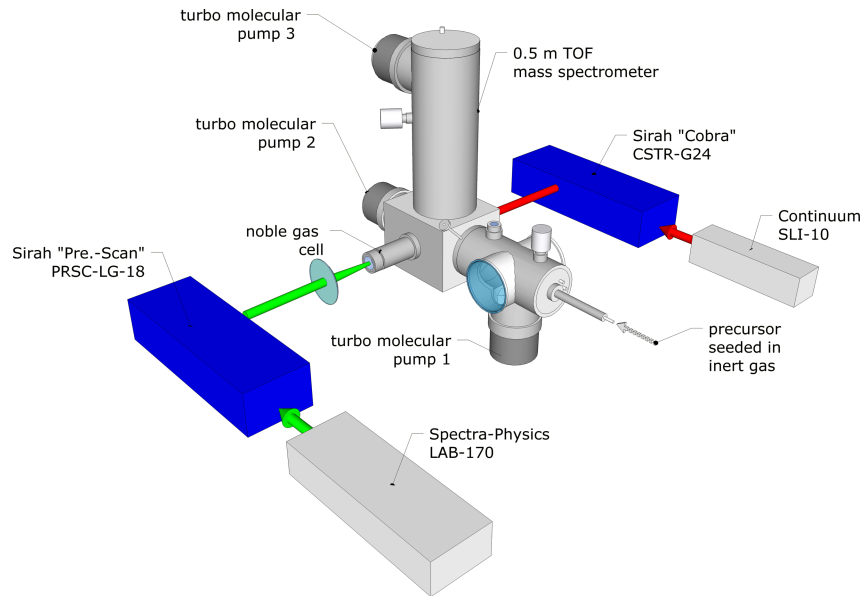
Figure 18: Nanosecond laser system and molecular beam apparatus of the University of Würzburg

VUV radiation of around 121.6 nm (Lyman-α transition). Alternatively the cell was filled with xenon (18 mbar) and 13 mJ of 355 nm radiation were focused into the cell to generate 118 nm via frequency tripling. The horizontally polarized VUV light was then refocused into the ionization region by a 100-mm MgF_2 lens mounted at the exit of the cell.

While absorption of Lyman-α radiation excites H atoms to the $^2P_{1/2}$ and $^2P_{3/2}$ states, the residual fundamental (365 nm) ionizes the excited atoms. The bandwidth of the VUV pulse is estimated to be around 0.2 cm^{-1}. The H$^+$ ions are subsequently detected by the *Wiley-McLaren* time-of-flight mass spectrometer[61]. A single stage micro sphere plate (MSP) detector (*El-Mul Technologies*) was used as electron multiplier. This detector was later on replaced by a micro channel plate (MCP) chevron detector Fields of 300 Vcm^{-1} and 1000 Vcm^{-1} were employed in the two acceleration regions of the *Wiley-McLaren* setup. The signals were recorded over a digital storage oscilloscope and then transferred to a computer. The laser systems as well as the pulsed valve were synchronized by digital delay generators (*Stanford Research DG535*) within better than 2 ns. The recorded mass spectra were digitized by a *LeCroy Waverunner LT343* 500 MHz oscilloscope and transferred to a computer. Data acquisition was controlled by LabView programs.

3.4.1 *Laser System*

A 20 Hz femtosecond Ti:Sa oscillator/amplifier chain was used for the experiments. An overview on the most important components is given in fig. 19.
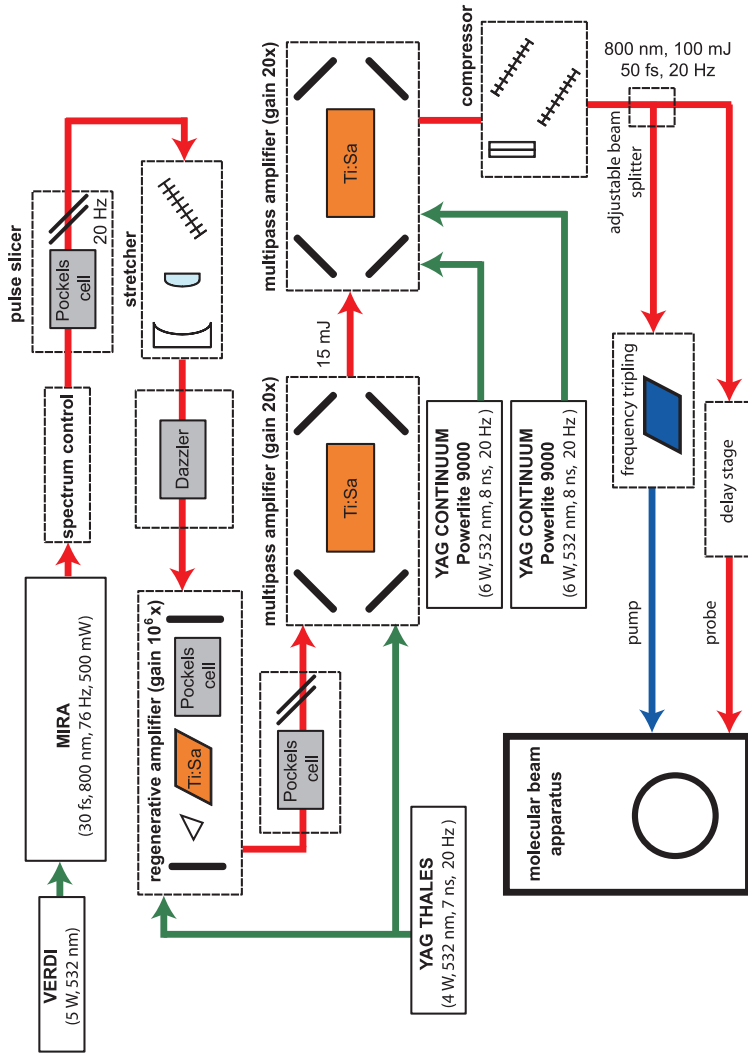
Figure 19: LUCA femtosecond laser system at the CEA in Saclay/France. The system was shared in several parallel experiments.

A *Mira* oscillator was pumped by the output of an *Verdi* continuous wave laser, producing laser pulses of around 30 fs FWHM and ≈ 7 nJ/pulse energy (0.5 W/76 MHz). This output was stretched and consecutively amplified over three stages (1×regenerative amplifier, 2×multipass amplifier) before it was recompressed (fig. 19). After splitting the beam, one beam was frequency tripled (≈ 265 nm) and the residual fundamental was sent into a delay line. The delay stage was actuated by a computer-controlled stepper motor.

Usually the third harmonic of the Ti:Sa laser (≈ 265 nm, 2 µJ) was used as pump pulse and the fundamental of the Ti:Sa (≈ 795 nm,

480 µJ) was applied as probe pulse in a multiphoton ionization process[1]. Both laser beams were horizontally polarized. The time intervals between two data points were not chosen constant in a given time scan and adjusted to the slope of the decay signal. Around zero time delay data points were taken typically every 8 fs, whereas at early and late delay times longer intervals were chosen. The beams were overlapped in a small angle and focused into the interaction region by a 70-cm lens for the 265 nm and a 50-cm lens for the 795 nm. The 795-nm beam was focused 5 cm away from the interaction region; the focus of the 265-nm beam was 14 cm away. For pump-probe contrast optimization the probe and the pump beam were attenuated until the one-color background signal was minimized. The laser cross correlation of pump and probe was typically around 100 fs.

3.4.2 Molecular Beam Apparatus

For the femtosecond experiments a similar standard molecular beam apparatus was used as presented in chapter 3.3.1. In contrast to the nanosecond laser setup the lasers were sent into the machine from the same side. The pressure in the source chamber was 2.0×10^{-5} mbar. After passing a 1-mm skimmer, the molecular beam reached the detection chamber (2.0×10^{-7} mbar), which was equipped with a time-of-flight mass spectrometer (TOF-MS) and a velocity map imaging (VMI) detector used for mapping ion or electron kinetic energy distributions. Both detectors were mounted perpendicular to the molecular beam on opposite sides of the main chamber. The intermediates were produced by the source described in section 3.1.1. The General Valve was operated at 20 Hz.

3.4.3 Velocity Map Imaging Spectrometer

The photoions or photoelectrons in the intersection area were collected by an assembly of three-electrode electrostatic lenses. These could be adjusted by a stepper motor from the outside of the apparatus to optimize the deflection of the particles in the axis of detection. After passing a field-free TOF tube, the particles hit the position-sensitive detector, which consisted of a MCP, a phosphor screen and a CCD camera[63] as depicted in fig. 5. The voltages were set to: Repeller 4000 V, phosphor screen 4763 V, extractor 2871 V and MCP 1144 V. After a selectable time delay a high-voltage (546 V) pulse of 300 ns duration was applied to the front of the MCP to open a detection gate (200 ns for electrons). The time gate enabled a mass selective detection for photoions by TOF discrimination and reduces considerably the noise in the photoelectron studies. The raw images were digitalized off the phosphor screen by a CCD camera (*PCO Sensicam*, 640 × 480 pixel), accumulated over several hundred laser shots and transferred to a computer. The images were then analyzed using the pBASEX algorithm[37], which was implemented in a *LabView* program[40]. For a description on how velocity map imaging works in detail refer to chapter 2.3.

An alternative imaging technique called slice imaging has been developed in 2001. It applies very short HV pulses on the MCP after sufficiently spreading the ion distribution in the TOF region. Hence no inversion method such as pBASEX (chapter 2.3.1) is needed, since only the central region of the ion packet is selectively detected[62].

---

[1] The output of a Ti:Sa laser has a rel. broad spectrum with a central wavelength of 800 nm. However, in the performed experiments of this thesis the output of the laser setup was determined by a spectrometer to be slightly detuned and centered at 795 nm.

The synchrotron experiments were carried out at the *Desirs* beamline of the *Soleil* storage ring (France), using the *Saphirs* setup[64]. The synchrotron was operated in multibunch mode (3/4 filling). The *Ophelie-2* undulator provides tunable radiation in the energy range between 5 and 40 eV. After passing an argon gas filter (0.23 mbar for attenuation of 100) to block higher harmonics[65], the wavelength was selected by an normal incidence monochromator (focal length 6.65 m). The monochromator was equipped with a 200 gr/mm grating, which enables a photon energy resolution of 5 meV at 9 eV when using an exit slit of 100 µm. An illustrative scheme of the beamline is given in figure 20. The beamline provided a photon flux of approx. 1×10^{12} photons/s in the utilized energy range (7–10 eV).
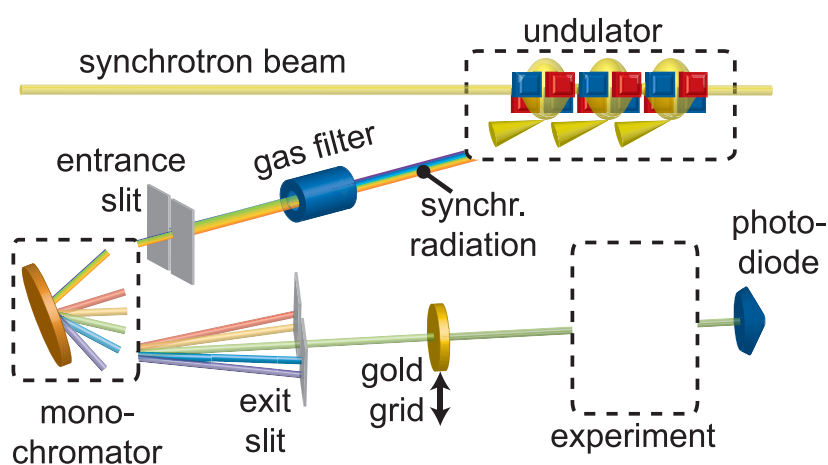
Figure 20: Scheme of the beam line setup (*Desirs*) at the *Soleil* storage ring in France.

The measurements were performed in a standard molecular beam apparatus (*Saphirs*) equipped with a velocity map imaging spectrometer and TOF-MS suited for (threshold) photoelectron-photoion coincidence (PEPICO) detection[66]. Because of the relatively low photon flux of synchrotron radiation and the quasi-continuous repetition rate, single event counting could be used. Electrons were extracted in static fields[2] and detected on an imaging detector with a fast delay-line anode[57]. Recorded raw spectra were normalized to the photon flux, which was measured with a calibrated gold grid or a photodiode[3]. Conventional photoelectron spectra were extracted from raw images which were collected at a fixed photon energy by using the pBASEX reconstruction algorithm (see chapter 2.3.1). Supplementing ion images were recorded by reversing the polarity of the extraction voltages of the VMI spectrometer. For generating the intermediates, the source presented in section 3.1.1 was used in continuous mode. The diameter of the orifice faceplate was 50–100 µm. Two electrodes were fixed 2 mm apart. The precursors were seeded in 0.5 bar (absolute) of Ar and the pyrolysis temperature was adjusted for optimal precursor conversion.

ⓘ *The pulsed mode of the pyrolysis has several advantages over the continuous mode: The cooling is more efficient, the pulse width can be adjusted for maximum conversion, higher backing pressures are applicable, the pulse delay is can be optimized and side products can be discriminated by irradiating specific parts of the pulse.*

---

[2] The fields were freely adjustable. However, at the cost of signal the voltages can be reduced to enable a better threshold electron discrimination. In the carbene experiments below several different settings were tested: 95 + 333 Vcm^{-1} or 190 + 666 Vcm^{-1}. [3] The response function of the gold grid was also accounted for.

COMPUTATIONAL TOOLS FOR EXPERIMENTALISTS

This short chapter is by no means intended to give a precise explanation on how the many different computational methods work in detail. This thesis consists mainly of experimental results that are at some points augmented by different computational methods. Due to the many different *ab initio* and DFT methods as well as the amount of basis sets available to the experimentalist nowadays, choosing a good method for a certain problem can be difficult. The main objective of this thesis was the spectroscopic characterization of organic intermediates. This chapter thus intends to give a brief overview on *some* of the different computational methods and how they perform in predicting, e. g., unimolecular dissociation barriers, finding transition states (TS) and predicting absorption spectra for reactive intermediates. Since many of the examined species were open shell molecules the sensitivity of each method towards spin contamination plays a crucial role.

This computational abstract consists mainly of experience gained on performing calculations on reactive organic intermediates during the evaluation of this thesis[1]. Which methods and functionals yield relatively trustworthy vibrational frequencies, have little spin contamination and are cost effective when calculating a TS structure for a hydrogen abstraction of a radical?

4.1 RESTRICTED AND UNRESTRICTED CALCULATIONS

For molecules with a singlet ground state, a Hartree-Fock (HF) self consistent field calculation can be performed, assuming that all electron spins are paired ($\langle S^2 \rangle = 0$). Hence the calculation can be done with one set of spatial orbitals and does not show any spin contamination. These calculations are called restricted (e. g., RHF, RMP2). For radicals with one *un*paired electron ($\langle S^2 \rangle = 0.75$), two complete sets of spatial orbitals with different orbital coefficients (one for the α and one for the β orbitals) can be taken to solve to self consistent field. The calculation is then called *un*restricted (e. g., UHF, UMP2, UB3LYP etc.). A disadvantage of this procedure is that the ground state wave function is no longer an eigenfunction of the total spin. This is due to the fact that in unrestricted calculations higher spin states mix into the ground state wave function, resulting in a systematic error for the prediction of molecular properties such as geometries[67]. A third possibility is to perform restricted open shell calculations, which cost more computational time and are not efficiently implemented yet in most computational packages. This method cancels spin contaminations of the wave function.

An attempt to give a qualitative overview on some important computational methods is given in table 1.

ⓘ *The expectation value for the total spin of a calculation $\langle S^2 \rangle$ should differ by less than $\approx 10\%$ from $\frac{n}{2}(\frac{n}{2} + 1)$ where $n =$ number of unpaired electrons*[67].

---

[1] I understand myself as an experimentalist and my experience in performing quantum chemical calculations is restricted to calculations performed in the last 2¹/₂ years as a support for my measurements. At this point I would like to thank the group of *Prof. B. Engels* for a crash course on quantum chemical calculations.

Table 1: Qualitative overview of some important quantum chemical methods and how they perform (✔=yes, ✘=no).

Method	Type	Var.	Si.Con.	Bar.	E.S.	Scaling	Sp.Con.	Eq.P.
HF	ab initio	✔	✔	-	✘	N^3	-	-
MP2	ab initio	✘	✔	o	✘	N^5	-	++
B3LYP	Hyb-DFT	✘	(✔)	o	(✘)^2	N^3	+	++
BMK	Hyb-DFT	✘	(✔)	+	(✘)^2	N^3	+	+
CASSCF	ab initio	✔	✔	+	✔	$e^{N_{as}}$	+++	(+)
CASPT2	ab initio	✘	✔	++	✔	$N^2 e^{N_{as}}$	+++	(++)
CCSD	ab initio	✘	✔	+	(✘)^2	N^6	o	+
CCSD(T)	ab initio	✘	✔	++	(✘)^2	N^7	o	++
CCSDT	ab initio	✘	✔	++	(✘)^2	N^8	o	++
CIS	ab initio	✔	✘	-	✔	$s * N^3$	-	-
CISD	ab initio	✔	✘	o	✔	N^6	o	+
FullCI	ab initio	✔	✔	+++	✔	$\approx e^N$	+++	+++

bad (-), approximative (o), good (+), very good (++), perfect (+++)

In this table the legend is the following:

Var. = variational ⇒ A method is variational if the result improves towards (and is never below) the correct energy when improving the basis set.; *Si.Con. = size consistent* ⇒ If a method is not size consistent, calculating A——B (two molecular entities far apart) will give a different energy as when calculating A and B separately and adding up the energies. *Bar. = barrier heights* ⇒ Methods that give a good prediction rank higher.; *E.S. = excited states* ⇒ Method that implements the calculation of electronic excited states; *Scaling* ⇒ Helps to predict the cost of a calculation. It shows the dependency on the number of basis set functions. *Sp.Con. = spin contamination* ⇒ Shows how sensitive a method is towards spin contamination in unrestricted calculations. The less sensitive, the better the ranking. *Eq.P. = equilibrium properties* ⇒ Shows how good a method performs in predicting equilibrium properties of a molecule in the ground state (excluding high multi reference cases)[68].

4.2 CALCULATING GROUND STATE EQUILIBRIUM PROPERTIES

As a rule of thumb, the ground state properties of hydrocarbon intermediates (not all presented explicitly in this thesis) with 1–4 carbon atoms could be treated in a reasonable amount of time with quantum chemical (q. c.) methods scaling up to $\leq N^7$, while for systems with 5–8 carbons methods with $\leq N^6$ were more appropriate[3]. Even larger systems were treatable by methods scaling with $\leq N^5$ (compare fig. 21). For the ground state equilibrium geometry, good results on molecular bond lengths, vibrational frequencies and rotational constants etc. of hydrocarbon intermediates can usually already be gained at a rel. low level of theory[4]. At MP2 level of theory the obtained

---

[2] DFT functionals can calculate excited states with TDDFT and CC methods using EOM-CC   [3] Calculations were performed on an AMD64 Opteron 2 Ghz, 8 Gb RAM system. N denotes the number of basis functions used in the calculation   [4] Example keyword input in *Gaussian 03*: #B3LYP/6-311^{++}G** Int=UltraFine opt=(tight,GDIIS) freq

vibrational frequencies are sufficiently precise for simple RRKM calculations (compare section 4.6). B3LYP and MP2 calculations with low spin contamination usually gave good predictions for eq. properties also in unrestricted calculations. DFT methods, such as B3LYP, are more robust towards spin contamination. The frequencies can be further improved using empirical factors afterwards[69]. For very small systems CCSD(T) gives very reliable results[68,70] at reasonable cost. The methods that employ an active space (CASSCF and CASPT2) can give very good results if the orbitals and the number of electrons is chosen well[5].

4.3 TRANSITION STATES AND DISSOCIATION ENERGIES

4.3.1 *Methods and Transition States*

Finding a transition state (TS) along a reaction coordinate is considerably more challenging than calculating equilibrium properties, since excited states contribute stronger to the ground state when bonds are lengthened beyond the equilibrium geometry (non-dynamic or structural correlation). Thus a higher level of theory has to be employed, incorporating a more precise correlation in *ab initio* methods. When calculating dissociation barriers of hydrocarbon radicals, MP2 usually overestimated the barriers; the popular B3LYP hybrid-DFT functional underestimated them (by roughly $12\,\mathrm{kJmol^{-1}}$). This is also known from other studies[71,72]. Recently new third generation DFT functionals have been developed to overcome this drawback in DFT[73]. A functional for predicting good barrier heights, transition states and atomization energies is the BMK functional[74] as has been demonstrated on a large set of molecules[75]. The BMK functional was developed and trained explicitly to model reaction mechanisms[6].

A multi-configurational approach should be chosen to predict transition states and dissociation energies when using *ab initio* methods. Unfortunately these methods usually have a high scaling factor. Hence even though CCSD(T) gives very good values for small hydrocarbon intermediates[70], it was too expensive for larger systems, e. g., chlorophenylcarbene presented in chapter 9. Even for small systems pure CCSD(T) calculations for geometry optimizations *and* TS searching are usually too time consuming. An approach is thus to use, e. g., B3LYP for optimizing the reactant, product and TS geometries as well as to determine the zero point energy (ZPE) and then using CCSD(T) in a consecutive calculation without reoptimizing the geometry to determine the electronic energy[76]. This procedure also works remarkably well for predicting adiabatic ionization potentials.

ⓘ *When calculating bond dissociations, restricted calculations give wrong results (e. g., RHF, RMP2). Unrestricted calculations allow homogeneous bond cleavage, whereas restricted calculations converge to a HF wave function with 50% ionic character and E_{diss} is predicted much too high (heterogeneous dissociation). Alternatively, multi reference methods can be employed.*

---

5 However, for a simple geometry optimization at the ground state equilibrium the CAS methods are not economical.   6 New functionals with even better performance than BMK have been developed by the *Truhlar* group (e. g., M06-2x). Unfortunately these are not yet implemented properly in *Gaussian 03* (Rev. D01)

4.3.2 *How to Find Precise Transition States*

There are several implementations to find a transition state (TS). They can be used, for example, in a BMK/6-311^{++}G** calculation[7]:

- *relaxed potential energy surface scan:* This approach is very robust but also time consuming. One coordinate is successively changed (e. g., a C–H bond length) while all other coordinates are reoptimized at every new point. The TS is approximately found at the maximum of the resulting potential energy surface.

- *guess the transition state and optimize to saddle point (TS option):* Some computational packages support this option, but it usually failed for several calculated intermediates. A good guess can be taken from a relaxed potential energy surface scan.

- *the QST2 method[77]:* The TS is found "automatically" by a synchronous transit-guided quasi-Newton method. The input requires an optimized geometry for the reactant and for the product. The TS is guessed by a linear extrapolation between the two geometries and then optimized. This method only worked in some cases for C–H hydrogen dissociation.

- *the QST3 method[77]:* This method always worked with every intermediate (compare, e. g., chapter 9). The method is similar to the QST2 but the computational program is provided with *three* geometries: the reactant, the TS guess and the product. In this thesis the TS guess was always taken from a relaxed potential energy surface scan. This procedure is more time consuming to operate but worked very reliable.

4.4 EXCITED-STATE CALCULATIONS

Generally all CI methods are able to calculate *electronic* excited-state energies (e. g., CIS, CISD) because they describe each state by a linear combination of excited determinants. Nevertheless, since CIS only takes single excitations into account, this method only gives an approximation on the location of the states. Another drawback is that truncated CI calculations[8] tend to spin contamination when calculating open shell systems[78] and are not size consistent. Hence a good approach is to use CASSCF (eventually followed by a CASPT2 calculation) for calculating excited states of radicals. These methods do a full CI calculation in an chosen active space (AS) and even the unrestricted case does not show any spin contamination[79]. The user has to define which occupied and virtual orbitals are of considerable importance for the excitation and how many electrons are involved. The result is thus directly dependent on the choice of the AS. The CASPT2 method "expands" the active space towards a full CI calculation by perturbation theory (and can partially correct for a poor AS).

Since hydrocarbon intermediates (e. g., *t*-butyl) have low-lying excited Rydberg states it is important to include diffuse functions in the basis set (compare section 4.5 and A.5). To get a good first estimate

---

[7] Example keywords for a QST3 calculation using *Gaussian 03*: #BMK/6-311^{++}G** Int=UltraFine opt=(QST3,tight) freq   [8] *Truncated CI calculations:* All CI calculations except full CI.

on the location of the excited states, a very cost effective method is to perform time-dependent DFT calculations (TDDFT)[9]. These calculations can also serve as a template for determining a good active space for following CASSCF calculations. TDDFT calculations can be performed with any functional, since the energies are not strongly dependent on them. However, of several tested functionals the B3P86 functional seems to predict values closest to the experimental ones[81]. The method is good for low-lying states but usually starts to continually overestimate the excitation energies towards higher excitations as can be seen in chapter 10.3.4 in the case of propadienylidene.

For calculating excited state potential energy surfaces of intermediates, the ground state geometries can be taken from a relaxed potential energy surface scan (acquired, e. g., by a BMK calculation) along one (or two) coordinates. These geometries are then used in a consecutive excited-state calculation (e. g., CASSCF). Special programs developed during this thesis to efficiently perform this task are presented in chapter 14. Using TDDFT for predicting excited potential energy surfaces yields qualitatively good results. However, they are not as reliable as predicted by CASPT2 but are considerably cheaper and usually more precise than those acquired by CIS[82].

ⓘ *TDDFT describes the interaction of E.M. fields with matter. It is based on the direct correspondence between an external time-dependent potential and the electron density evolving from an initial state[80].*

4.5 SELECTING SENSEFUL BASIS SETS

Many different basis sets are available, and some have been developed for specific applications. The computational cost strongly depends on them as can be seen in figure 21. Hence selecting a proper basis set plays an important role when calculating molecular properties.

ⓘ *6-311G** is a triple-zeta split-valence basis set (SVB). Three basis functions are used to describe the valence orbitals. 6 Gaussian functions are summed up to describe the core orbitals. The 3, 1 and 1 indicate that the valence orbitals are described by a linear combination of three basis functions. The first one is a linear combination of 3 primitive Gaussian functions, the other two consist of only 1 primitive Gaussian function. The stars denote that functions for describing polarizations are added for all atoms other than H (d-type, first star) and p-type polarization functions for each H atom (second star)[83].*

Figure 21: Dependence of cost on method and number of basis functions

The basis sets used in this thesis are for general use: *Dunning's correlation consistent basis sets*[84] (cc-pVDZ < cc-pVTZ < cc-pVQZ) and Gaussian type orbitals (GTOs) introduced by *J. A. Pople et al.*[85] (3-21G < 6-31G < 6-311G < 6-311G** < 6-311^{++}G** < 6-311^{++}G(3df,2pd)).

---

[9] Example keywords for a TDDFT calculation using *Gaussian 03*: #TD=(NStates=5) B3P86/6-311++g** FormCheck=all

Methods which employ a lot of correlation (e. g., CCSDT, CASSCF) should not be used with small basis sets. On the other hand, using huge basis sets with methods that incorporate only little correlation is not senseful as well (e. g., MP2, B3LYP). The advantage of the Dunning basis sets is that they reduce the basis set truncation error in a systematic way when going from pVDZ to pVTZ to pVQZ to pV5Z and so on[10]. Hence these basis sets are powerful in combination with variational methods. On the other hand, calculations using the *Pople* basis sets usually converge faster, and the basis sets are more flexible[86]. Some Basis sets perform especially well with DFT methods (i. e., B3LYP, BMK) such as TZ2P and TZ3P, but basis sets of the *Pople* type also give good results[87].

4.6 RRKM THEORY FOR PREDICTING UNIMOLECULAR REACTION RATES

In the present work, reactive intermediates were electronically excited by a precise amount of energy. As the different femtosecond and nanosecond results will present in the forthcoming chapters of this thesis, most hydrocarbon intermediates quickly deactivate by internal conversion (IC) to the *hot* ground state. Here the intermediates possess enough internal energy for unimolecular C–H-bond dissociations, which could be followed using nanosecond pulsed lasers (compare section 2.2). The measured reaction rates were afterwards compared to those predicted by RRKM theory as a function of the internal energy deposited into the intermediates. Since the experiments were performed in a vibrationally cold molecular beam, the internal energy of the excited molecule is nearly equal to the photon energy of the excitation laser[11].

Rice, Ramsperger, Kassel and Marcus (RRKM) theory was developed for prediction of unimolecular reaction rates of energy rich molecules in the gas phase as function of pressure ($\propto [M]$), temperature, activation energy and molecular properties[88]. It evolved from Lindemann-Hinshelwood and RRK theory[89]. RRK and RRKM theory take into account that the more degrees of freedom there are in an energy rich molecule, the easier the excess energy inside the molecule can be delocalized over the different vibrational and rotational states, which slows down the reaction[90]. The assumed mechanism used to derive RRKM theory is shown in equation 4.1[88,91] and augments the RRK mechanism by the postulation of a transition state (TS).

$$ \text{R} \; + \; \text{M}^* \; \underset{k_{-1}}{\overset{k_1}{\rightleftharpoons}} \; \text{R}^* \; + \; \text{M} \; \underset{\text{-M}}{\overset{k_a}{\longrightarrow}} \; \text{R}^\ddagger \; \rightarrow \; \text{Products} \qquad (4.1) $$
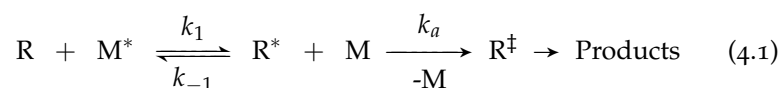
The TS ($\text{R}^\ddagger$) is localized at the saddle point at the maximum energy of the reaction path (compare fig. 1, page 1). In the original version of RRKM theory the reactant R is activated, e. g., by a collision with a diluent M^* and possesses enough internal energy for reaction (R^*).

---

[10] Diffuse functions can be added to the basis sets of Dunning by adding the prefix aug-VXZ. The X denotes double, triple, quadruple, quintuple-zeta... basis sets respectively. The Pople basis sets are augmented by diffuse functions by adding a (+).

[11] This assumption excludes the zero point energy of the molecule E_{zp} and the low thermal energy still present in the molecular beam E_{mb} ($T\text{vib}_{mb} \approx 100\,\text{K}$). But since $E_{zp} + E_{mb} << h \cdot \nu$ this is a good approximation.

The activated molecule R^* then passes a transition state $R^{\ddagger}$ to form the products. Taking further assumptions:

- all accessible states of a molecule are occupied and unoccupied with the same probability (microcanonical ensemble)

- a steady-state approximation is possible to $R^{\ddagger}$

- in contrast to RRK theory the zero point energy, the vibrational *and* rotational states and the external degrees of freedom are taken into account (quantum statistical treatment).

Marcus could derive expressions[89] for k_a ($R^* \rightarrow$ Prod.) as well as for k_{uni} ($R \rightarrow$ Prod.) shown in equation 4.2 and 4.3, respectively[12].

$$ka_{(E_0+E^{\ddagger})} = \frac{s\,q_r^{\ddagger}}{hq_r\rho_{(E_0+E^{\ddagger})}} \sum_{E_{vr}^{\ddagger}=0}^{E_{vr}^{\ddagger}=E^{\ddagger}} P_{(E_{vr}^{\ddagger})} = s\cdot\frac{q_r^{\ddagger}}{q_r}\cdot\frac{W_{(E_{vr}^{\ddagger})}}{h\rho_{(E_0+E^{\ddagger})}} \qquad (4.2)$$

$$k_{\mathrm{uni}} = \frac{s\,q_r^{\ddagger}}{hq_rq_{(R)}}\mathrm{e}^{\frac{-E_0}{kT}}\int_{E^{\ddagger}=0}^{E^{\ddagger}=\infty}\frac{\sum_{E_{vr}^{\ddagger}=0}^{E_{vr}^{\ddagger}=E^{\ddagger}}P_{(E_{vr}^{\ddagger})}}{1+ka_{(E_0+E^{\ddagger})}/k_{-1}[M]}\mathrm{e}^{\frac{-E^{\ddagger}}{kT}}\,\mathrm{d}E^{\ddagger} \qquad (4.3)$$

In this work, the molecules were not activated by collisions but by optical excitation. The mechanism can thus be described by equation 4.4.

$$\mathrm{R\text{–}H} \xrightarrow{h\nu+\mathrm{IC}} [\mathrm{R\text{–}H}]^* \xrightarrow{k_H} [\mathrm{R\text{—}H}]^{\ddagger} \rightarrow \mathrm{R\cdot} + \mathrm{H\cdot} \qquad (4.4)$$
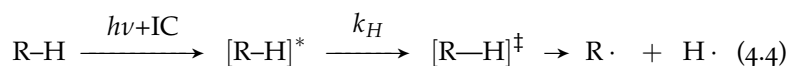
However, such photo induced reactions can also be treated by RRKM theory[92]. With the experimental setup described in chapter 2.2 the microcanonical rate constant k_H for the loss of hydrogen (compare equation 4.2) is directly accessible and reflects k_a in equation 4.2. The molecules are thermally activated after internal conversion of an excited state took place to the hot ground state. The total energy deposited into the molecule ($E_{\mathrm{total}} = h\nu = E_0 + E^{\ddagger}$) can be adjusted by varying the wavelength of the excitation laser. According to the equation the probability that the bond will break depends on:

1. The total internal energy ($E_{\mathrm{total}} = h\nu = E_0 + E^{\ddagger}$)

2. The number and characteristics of the vibrational and rotational modes of the reactant $\Rightarrow q_r$, $\rho_{(h\nu)}$

3. The number and characteristics of the vibrational and rotational modes of the transition state $\Rightarrow q_r^{\ddagger}$, $W_{(E_{vr}^{\ddagger})}$

4. The dissociation barrier (E_0)

5. The number of degenerate possibilities for the reaction to proceed (s).

---

s = statistical factor

$q_r^{\ddagger}$ = rotational partition function (PF) of TS

$q_{(R)}$ = molecular PF of R

q_r = rotational (PF) of R

h = Planck's constant

k = Boltzmann constant

T = absolute temperature

E_0 = reaction barrier ($R \rightarrow R^{\ddagger}$)

$E^{\ddagger} = E_{total} - E_0$ = excess energy over reaction barrier

$E_{vr}^{\ddagger} = E^{\ddagger} - E_{kin}$ sum of vibr. and rot. non-fixed energy in the TS

$P_{(E_{vr}^{\ddagger})}$ = amount of rotational and vibrational quantum states of the TS with energy equal to $E_{vr}^{\ddagger}$

$[M]$ = concentration of M ($\propto$ pressure)

$\rho_{(E_0+E^{\ddagger})}$ = density of states of R^* at $E_0 + E^{\ddagger}$

$W_{(E_{vr}^{\ddagger})}$ = Sum of rotational and vibrational states up to $E^{\ddagger}$ of TS

ⓘ *A molecular partition function q is defined as: $q = \sum_0^{\infty} g_i \exp\frac{-E_i}{kT}$. It is a measure for the average number of states accessible by a molecule at a given temperature.*

---

12 Versions of equation 4.3 and 4.2 exist in which an enhanced treatment of adiabatic rotations is included.

Hence to calculate the rate for an unimolecular dissociation process one needs to know how much internal energy is deposited into one of the molecules, the rotational constants of the reactant and TS, the vibrational frequencies of the reactant and TS, the moments of inertia of reactant and TS and the reaction path degeneracy. An example on how to evaluate the reaction path degeneracy is given in chapter 6.5. All other molecular properties can be taken, e.g., from standard quantum chemical calculations (as explained in section 4.2)[13].

By comparison of the RRKM rates for k_H with the experimental results, information on the photophysics can be gained, i.e., whether the deposited energy is statistically redistributed over the internal modes of the intermediate after IC.

---

[13] A graphical user interface for generating a *Fortran* input from Gaussian output files is given in chapter 14. This *Fortran* input file is then directly sent to a program (QCPE 291) which calculates the rate constants.

CONVOLUTION IN FEMTOSECOND SPECTROSCOPY

5.1 THE CONVOLUTION OF SIGNALS

The time-resolved spectra of the femtosecond experiments were interpreted by comparing the measured data to several different analytical models. These models consisted of a convolution of an instrument response function (IRF) with a function describing the kinetics of the relaxation process called molecular response function (MRF). A convolution is defined as the time-integral over the product of two functions $A_{(t)}$ and $B_{(t)}$ (see equation 5.1)[93]. The function $B_{(t)}$ is hereby shifted in time compared to function $A_{(t)}$.

$$A_{(t)} * B_{(t)} = \int_{-\infty}^{\infty} A_{(u)} \cdot B_{(t-u)} \, \mathrm{d}u \tag{5.1}$$

The convolution of two functions occurs in many physical problems such as chromatography[94], electrical signal transmission and time-resolved spectroscopic experiments[95]. The true MRF signal $A_{(t)}$ is hereby smeared out by an IRF $B_{(t)}$. This phenomenon occurs if the true MRF being measured has fast dynamics, which lie in the temporal region of response of the measuring method itself. The MRF signal is then a convolution of the instrument response function and the molecular response function. Thus it is the goal of any pump-probe experiment to extract the MRF, since it reflects the entire dynamical information of the molecular system accessible by the experiment. There are two ways of calculating a convoluted function: 1.) the numerical method and 2.) the analytical method. A numerical method is relatively easy to program[96]. A major drawback of this method is that the convolution itself is then dependent on the number of points used for describing each of the two functions. A second problem occurs when describing data points that are not equally spaced, since a correct numerical convolution is only possible if the ordinate values are equidistant. Thus an analytical function is advantageous, since it will be more precise, faster to fit to the data and independent of the recorded data points. Both methods were implemented in a *Labview* program as can be seen in chapter 14.8 (fig. 108, page 141).

In this study the ion and electron yields were monitored as a function of the delay time between the pump and the probe laser pulse. Thus models describing the measured ion (or electron) signal as a function of time are discussed in the following (see figure 22). In pump-probe spectroscopy the time resolution of the experiment is limited by the pulse width of the *two* lasers. The instrument response function IRF (also sometimes referred to as laser system response function) is given by the convolution of the pump and probe laser pulse $P_{\mathrm{pu}}(t)$ and $P_{\mathrm{pr}}(t)$[95].[1] The broader each of the laser pulses is, the broader

---

[1] $P_{\mathrm{pu}}(t)$ and $P_{\mathrm{pr}}(t)$ are usually assumed to have a Gaussian shape. Sometimes the IRF is also described as a cross-correlation of the two laser pulses. Since Gaussian functions are even, performing a cross-correlation or convolution of the two Gaussian functions give the same result.

also the IRF will be. The IRF can be directly measured if the excited molecule shows no time response and the MRF can be described by the *Dirac*-delta function. This would be the case if a molecule is excited non-resonantly in the pump step. The convolution of two Gaussian profiles delivers a new Gaussian profile; hence the IRF can be described as a Gaussian function given in equation 5.5. *In pump-probe experiments the pure molecular response signal as a function of time has to be convoluted by the IRF to describe the measured data*[95] *(equation 5.2).*

$$\int_{-\infty}^{t} \text{IRF}_{(u)} \cdot \text{MRF}_{(t-u)} \, \mathrm{d}u \tag{5.2}$$

Note that in the convolution integral goes from $-\infty$ to t as derived in reference 95.

The presence of an IRF does not only smear out the true MRF; it also shifts the maximum signal intensity of the measured pump-probe signal compared to the MRF as can be seen in fig. 22. The exact determination of the IRF helps to decrease the error when the experimental spectra are analyzed.
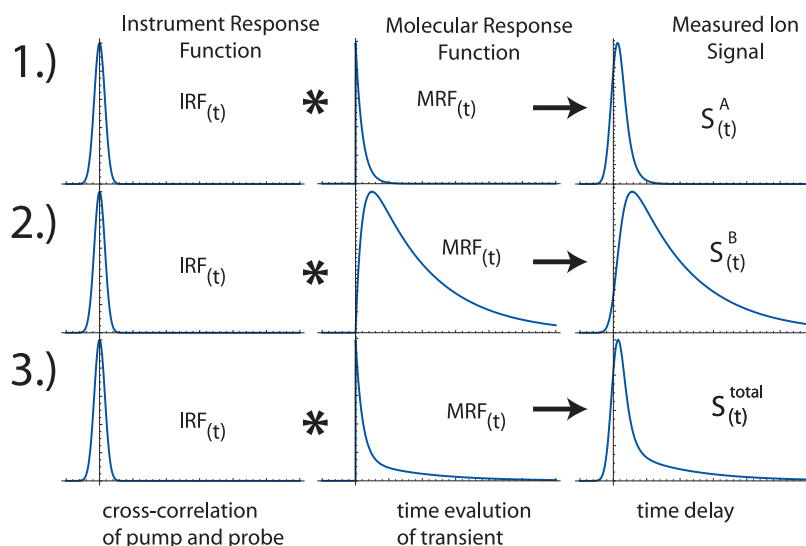
Figure 22: Three example cases of measured transient signal responses: 1.) The molecular response function (MRF) is monoexponential (compare section 5.2). The convolution with the instrument response function (IRF) gives the signal $S_{(t)}^{A}$, which is fit to experimental data. 2.) The MRF is biexponential. There is only one detectable transient state and it is populated and then depopulated. $S_{(t)}^{B}$ describes the experimental signal in this case. 3.) Two states are involved in the MRF and contribute to the ion signal as illustrated in fig. 24. The measured signal will look like $S_{(t)}^{total}$.

Due to signal noise in all scientific experiments a direct deconvolution algorithm of the recorded spectrum is a very unstable operation and does not give reliable results. Thus for most cases it is senseful to first generate the convolution of a known test molecular response function and a known instrument response function and fit the convolution itself to the experimental data. Analytic solutions for such convolutions are presented in this chapter. Numerical[96] as well as the analytic solutions were incorporated into a LabView program to analyze the data (compare section 14.8 and fig. 108).

In the simplest case a molecule is excited into a state Ψ_A and relaxes after some time to a no longer ionizable state Ψ_{dark} with a time constant τ_1 (fig. 23). Some of the molecules in state Ψ_A are ionized by the probing pulse. Since the present ions (or electrons) are detected regardless of the time delay between the laser pulses, the dynamics of the intermediate state is reflected in the dynamics of the measured ion signal (compare fig. 23). The pulses only excite (or ionize) a small fraction of the molecules present. The ion signal $I_{(t)}$ of the molecule in the time-resolved mass spectra is proportional to equation 5.3.

$$I_{(t)} \propto \rho_1 [A]_{(t)} + \rho_2 [B]_{(t)} \tag{5.3}$$

Herein ρ_1 and ρ_2 represent the ionization cross sections[2] of state A and B, respectively. $[A]_{(t)}$ and $[B]_{(t)}$ resemble the concentrations of the corresponding species in the ionization region. In case state B is not ionizable by the probe wavelength, then ρ_2 equals zero and the ion intensity is given by $I_{(t)} \propto \rho_1 [A]_{(t)}$. Hence state B is a so called "dark state" (Ψ_{dark}). If we don't take into account the additional temporal behavior induced by the laser pulse and state A depopulates monoexponentially, then $[A]_{(t)}$ is described by equation 5.4.

$$\frac{\mathrm{d}[A]_{(t)}}{\mathrm{d}t} = -k_1 \cdot [A]_{(t)} \rightarrow [A]_{(t)} = [A]_0 \cdot e^{-kt} \tag{5.4}$$

Hereby k represents the rate constant, t the evolving time and $[A]_0$ the starting population. But due to the finite time-resolution of the pump-probe laser experiment, the measured time-dependent ion signal does *not* strictly follow the molecular response function (MRF), which is only reflected by $I_{(t)} \propto H_{(t)} \cdot \rho_1 [A]_0 \cdot \exp(-kt)$. Herein the *Heaviside* function ($H_{(t<0)} = 0$, $H_{(t\geq 0)} = 1$) accounts for the fact that before zero in time no transient A is present. To describe the measured time-dependent signal adequately, this function has to be convoluted by the IRF. The cross-correlation of two laser pulses is usually assumed to have a Gaussian shape and the IRF can thus be described by function 5.5.

$$\mathrm{IRF}_{(t)} = \int_{-\infty}^{\infty} P_{\mathrm{pr}}(u) \cdot P_{\mathrm{pu}}(t-u)\,\mathrm{d}u = Ag \cdot \exp\left(\frac{-t^2}{2\sigma^2}\right) \tag{5.5}$$

In this equation Ag represents the amplitude of the Gaussian function (maximum laser intensity) and σ stands for the half of the distance between both abscissas of inflection of the Gaussian.[3] Hence according to equation 5.2 for transient molecules following a "state $A \rightarrow$ state B" model and with $\rho_2 = 0$, the measured signal $S_{(t)}$ can be described by equation 5.6[95].

$$S_{(t)} \propto \rho_1 [A]_0 Ag \int_{-\infty}^{t} H_{(t-u)} \exp(-k_1(t-u)) \exp\left(\frac{-u^2}{2\sigma^2}\right) \mathrm{d}u \tag{5.6}$$

Ψ_i^+ Ion

λ_{probe}

Ψ_A τ_1

λ_{pump}

Ψ_X

Figure 23: Ψ_A relaxes after some time to a no longer ionizable state Ψ_{dark} with a time constant τ_1

---

[2] Cross section: Probability of absorption of one photon by one molecule in the interaction region at a given wavelength, laser intensity etc. It is a characteristic constant for each state transfer (e.g., from state A to the ion).   [3] The value 2σ equals 0.849 times the full width at half maximum of the Gaussian (FWHM $= \frac{2 \cdot \sigma}{0.849}$), $\sigma = \frac{\mathrm{FWHM}}{2(2\ln 2)^{0.5}}$. The FWHM of the IRF is given by the FWHM of the two Gaussian shaped laser pulses: $\mathrm{FWHM}_{IRF} = \sqrt{FWHM_{\mathrm{pu}}^2 + FWHM_{\mathrm{pr}}^2}$
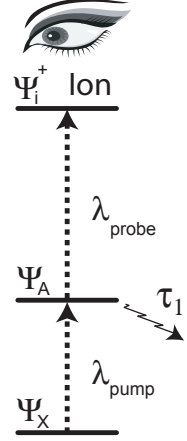
The analytic solution to this convolution is given in equation 5.7. By fitting this expression[4] to the experimental data in a least squares fit, the time constant $\tau_1 = 1/k_1$ can be extracted and conclusions can be drawn, whether this relaxation process takes place in a monoexponential $A \rightarrow B$ fashion (compare figure 22 first trace).

$$S_{(t)} = F \times \exp\left[\frac{1}{2}k_1\left(\sigma^2 k_1 - 2t\right)\right]\left[1 + \text{Erf}\left(\frac{-\sigma^2 k_1 + t}{\sqrt{2}\sigma}\right)\right]$$

with (5.7)

$$F = \alpha\sqrt{\frac{\pi}{2}}\sigma\rho_1[A]_0 Ag$$

ⓘ *The error function Erf(x) is defined as $\frac{2}{\sqrt{\pi}}\int_0^x \exp\left(-t^2\right)dt$ and is tabulated in most scientific programs, e. g., Origin and LabView*

Since the values for $[A]_0$, Ag and ρ_1 are not explicitly known in most pump-probe experiments and only have an effect on the amplitude of $S_{(t)}$, they can all be summarized into one prefactor F, which is a free variable fitting parameter. The factor α in F is an arbitrary proportionality constant. The analytical solution for the monoexponential deactivation ($\Psi_A \rightarrow \Psi_B$) in equation 5.7 is related to solutions found for describing signals from neutron emission time detectors[97,98].

5.3 THE THREE-STATE MODEL

Many electronically excited molecules do not deactivate directly from a bright detectable state ($\rho_1 \neq 0$) to a dark non-detectable state ($\rho_2 = 0$). The excited molecule can deactivate through a cascade of states, e. g., $A \xrightarrow{\tau_1} B \xrightarrow{\tau_2} C$ with ($\rho_1 \neq 0$) *and* ($\rho_2 \neq 0$). If two of the states are ionizable and the third has a negligible cross section, then two states are observed simultaneously but most likely with different efficiencies as illustrated in figure 24. In this case the observed dynamics are more
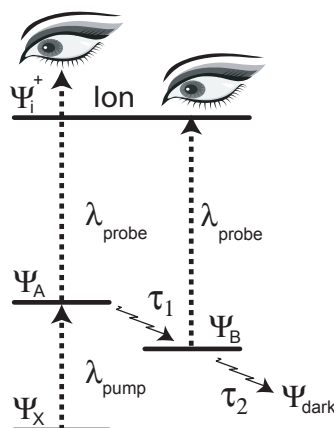
Figure 24: In case two states are ionizable simultaneously, a "state A to state B to state C model" has to be applied, rendering it more difficult to simulate the pump, probe signal.

sophisticated. Since two species A and B are ionizable both contribute to the ion signal $I_{(t)}$ and both have to be accounted for (equation 5.8).

$$I_{(t)} \propto \rho_1[A]_{(t)} + \rho_2[B]_{(t)} + \rho_3[C]_{(t)} \tag{5.8}$$

4 The convolution integrals in this chapter were solved using the technical computing software *Mathematica* and *Mathcad*.

$[A]_{(t)}$ and $[B]_{(t)}$ resemble the populations of molecules in the ionization region corresponding to state A and B as a function of time. The variables τ_1 and τ_2 denote the time constants for the elementary transitions of state A to state B (τ_1) and B to C (τ_2), respectively. In the easiest case, state C will be undetectable and thus $\rho_3 = 0$. Two differential equations must be solved in order to find a solution for $I_{(t)}$. These are presented in equation 5.9.

$$\frac{\mathrm{d}[A]_{(t)}}{\mathrm{d}t} = -\frac{1}{\tau_1} \cdot [A]_{(t)}$$

$$\frac{\mathrm{d}[B]_{(t)}}{\mathrm{d}t} = \frac{1}{\tau_1} \cdot [A]_{(t)} - \frac{1}{\tau_2} \cdot [B]_{(t)}$$

(5.9)

The solution of the first differential equation for $[A]_{(t)}$ was presented in equation 5.4. The solution for the inhomogeneous differential equation of second order ($[B]_{(t)}$) was taken from the references 95, 99 and is shown in equation 5.10 ($\tau_i = 1/k_i$).

$$[B]_{(t)} = \frac{[A]_0 \cdot \tau_2}{\tau_2 - \tau_1} \cdot \left(e^{\frac{-t}{\tau_2}} - e^{\frac{-t}{\tau_1}} \right)$$

(5.10)

In this case the *total amount of ions* which is produced in the probe step results from two different states. Hence the depopulation of state A as well as the population and depopulation of state B are reflected by the ion yield as a function of time. For a proper description of the measured signal $S_{(t)}$, the total molecular response function has to be convoluted by a Gaussian shaped IRF. The convolution of function 5.11 with function 5.5 yields equation 5.12. *As visible and shown in ref. 95, the MRF of each detectable state can be convoluted separately by the IRF and then added together in form of a linear combination to yield the total signal* $S_{(t)}^{total} = F_A \cdot S_{(t)}^A + F_B \cdot S_{(t)}^B$.

$$I_{(t)} \propto H_{(t)} \left[\rho_1 [A]_0 e^{\frac{-t}{\tau_1}} + \rho_2 \frac{[A]_0 \cdot \tau_2}{\tau_2 - \tau_1} \cdot \left(e^{\frac{-t}{\tau_2}} - e^{\frac{-t}{\tau_1}} \right) \right]$$

(5.11)

$$S_{(t)}^{total} \propto$$

$$Ag \int_{-\infty}^{t} H_{(t-u)} \left[c_1 e^{\frac{-(t-u)}{\tau_1}} + c_2 \left(e^{\frac{-(t-u)}{\tau_2}} - e^{\frac{-(t-u)}{\tau_1}} \right) \right] e^{\left(\frac{-u^2}{2\sigma^2} \right)} \mathrm{d}u$$

(5.12)

In equation 5.12, $\rho_1 [A]_0$ is contracted into prefactor c_1 and $\rho_2 \frac{[A]_0 \cdot \tau_2}{\tau_2 - \tau_1}$ summarized in c_2. This integral is solvable under the following physical senseful assumptions: $\sigma > 0$, $\tau_1 > 0$ and $\tau_2 > 0$. The analytical solution utilizing these assumptions in the *Mathematica* software (*Wolfram Research*) is given in equation 5.13. The parameters c_1 and c_2 should not be confused with the ionization cross sections of the states A and B. As shown for the "A to B" model in section 5.2, some of the factors are usually not precisely known and exclusively affect the amplitude, hence they can again be contracted into prefactors F_i. The amplitude correction factors F_i have no effect on the dynamics and are variable fit parameters. The factors are, however, proportional to the ionization cross sections. Thus the time-dependent signal of the A to B to C process in figure 24 can be described by $S_{(t)}^A + S_{(t)}^B = S_{(t)}^{total}$ (see

third trace of figure 22). The experimental signal of an *A* to *B* to *C* problem, in which state *A* and state *B* are detectable, can be fit to $S^{total}_{(t)}$ and the time constants τ_1 and τ_2 reflecting the molecular response can be extracted.

$$
S^A_{(t)} = F_A \cdot \exp\left[\frac{1}{2\tau_1}\left(\frac{\sigma^2}{\tau_1} - 2t\right)\right]\left[1 + \mathrm{Erf}\left(\frac{t - \frac{\sigma^2}{\tau_1}}{\sqrt{2}\sigma}\right)\right]
$$

$$
S^B_{(t)} = \left[F_B \cdot e^{\frac{\sigma^2 - 2t\tau_2}{2\tau_2^2}}\left(1 + \mathrm{Erf}\left(\frac{t - \frac{\sigma^2}{\tau_2}}{\sqrt{2}\sigma}\right)\right)\right] - \tag{5.13}
$$

$$
\left[F_B \cdot e^{\frac{\sigma^2 - 2t\tau_1}{2\tau_1^2}}\left(1 + \mathrm{Erf}\left(\frac{t - \frac{\sigma^2}{\tau_1}}{\sqrt{2}\sigma}\right)\right)\right]
$$

In the case where only state *B* is detectable (figure 25)[5], the experimental signal can be properly described by $S^B_{(t)}$ as illustrated in the second trace of figure 22. By performing linear combinations of the presented $S^i_{(t)}$-functions (e. g., $S^A_{(t)} + S^B_{(t)} + S^C_{(t)}$) many of the experimental pump-probe signals can be adequately described.
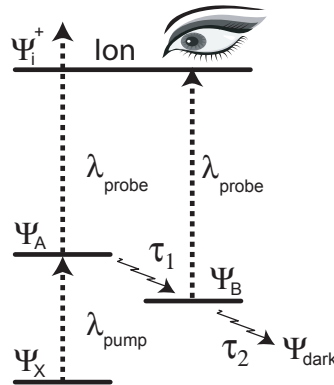
Figure 25: In case only state *B* is detected, a "state A to state B to state C model" has to be applied also. The measured signal is then describable by $S^B_{(t)}$ alone.

---

[5] This, e. g., would be the case if state *B* gives a well separated band in a photoelectron spectrum and the time dependence of the peak is to be described.

PHOTODISSOCIATION DYNAMCIS OF 2-PROPYL

6.1 INTRODUCTION AND STATE OF KNOWLEDGE

In this chapter the investigation of the photodissociation dynamics of the 2-propyl radical, C_3H_7, by time- and frequency resolved detection of the H-atom photofragments is presented. The work was motivated by preceding efforts to rationalize the reaction dynamics of alkyl radicals and to identify the general principles that determine their photochemistry[100,101]. Studies on the dissociation dynamics of isolated radicals provide the knowledge necessary for modeling the kinetics[102,103] of combustion processes, hydrocarbon cracking and planetary atmospheres. The most important unimolecular reaction channel in many radicals is the loss of a hydrogen atom and formation of a closed-shell molecule. In the case of 2-propyl, propene is likely to be formed. Earlier work on partially deuterated 2-propyl showed that the photodissociation is associated with a regioselective loss of a hydrogen atom in α position to the radical center[104] (fig. 26). However, only limited information on the mechanistic details was provided.

The unimolecular dissociation of radicals can be investigated by depositing a sufficient amount of energy into the molecules by laser excitation[105–108]. The dissociation dynamics and kinetics can then be studied by time-resolved detection of H atoms and photofragment Doppler spectroscopy (chapter 2.2).

The interpretation of such chemical reaction dynamics within statistical theories relies on a conversion of electronic to internal energy and a subsequent redistribution in the electronic ground state that is fast compared to the dissociation rate. While this assumption was confirmed in the case of allyl[105] and propargyl[106], it has to be questioned for other alkyl radicals such as ethyl (C_2H_5)[107] and *tert*-butyl $(t\text{-}C_4H_9)$[108]. In ethyl the observed dissociation rates were 3–4 orders of magnitude lower than expected from simple RRKM calculations while in *tert*-butyl a decrease was observed in the reaction rate at excitation wavelengths below 329 nm, i.e., upon increasing the excitation energy. This discrepancy motivated the experiments on propyl radicals in order to gain insight into the photodissociation dynamics of further alkyl radicals. The unimolecular dissociation rates of *thermally* prepared 2-propyl radicals can be well described by RRKM theory between 700–850°C[109].

Similar to other alkyl radicals, the UV spectrum of 2-propyl shows a broad and unstructured band between 260 and 220 nm[110]. A fast internal conversion (IC) to the electronic ground state as the initial process following photoexcitation was suggested to explain the diffuse appearance of the spectra.

2-propyl has two α positions

1-propyl has an α & β position
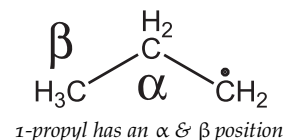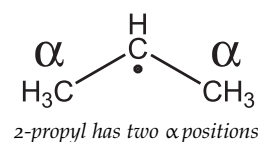
Figure 26: Definition of α & β for 2-propyl and 1-propyl

In contrast to the other studied intermediates, commercially available 2-bromopropane (*Aldrich*) was used without further purification as precursor for free 2-propyl radicals. Thermal decomposition proceeds according to scheme 2. Typical mass spectra of the 2-bromopropane precursor are presented in figure 28. The spectra were taken with the
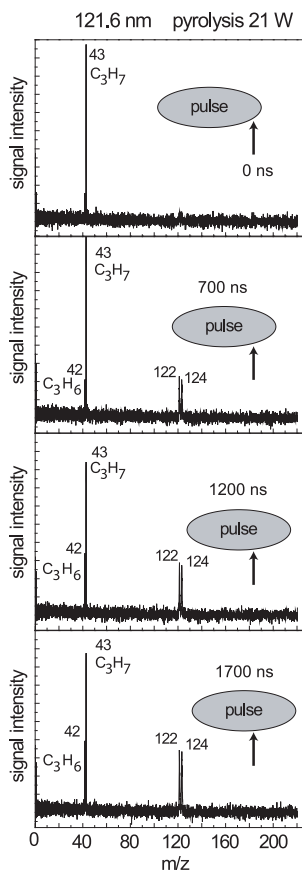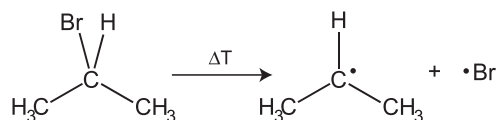
Scheme 2: Pyrolytic generation of propyl radicals

electrodes of the pyrolysis 2 cm apart and at a distance of 2 cm from the skimmer (orifice diameter 1.5 mm). The pressure of the first chamber lay at 1.6×10^{-4} mbar and the ionization chamber at 2.2×10^{-6} mbar. The background pressure of the inert gas was 1.9 bar absolute. The pulse voltage of the solenoid valve was set to 350 V with a pulse duration of 2.0 units on the pulse generator (approx. 160 µs). The 121.6 nm VUV radiation was produced with 14 mJ pulses of 364.8 nm radiation and a krypton pressure of 0.1 bar. A very high ratio (approx. 100/1) of propyl/propene was found at the leading edge of the molecular beam pulse. At non-optimal pyrolysis conditions propene can already be formed as a side product in the pyrolysis source.

The upper trace in fig. 28 was taken with the pyrolysis turned off, resulting only a small propyl signal ($m/z = 43$) induced by dissociative photoionization of 2-bromopropane at 121.6 nm[111]. Two relatively strong peaks of the precursor are present at $m/z = 122$ and $m/z = 124$, showing the typical isotopic distribution of elementary bromine (^{79}Br/^{81}Br : 51%/49%). The optimal conversion power for the pyrolysis was found to lie at 21 W (24 V, 0.88 A) as shown in the middle trace of the illustration. At these conditions the propyl signal increased by a factor of twenty, whereas the precursor was completely converted. Note that the conversion was strongest at the leading edge of the molecular pulse as demonstrated in fig. 27. In case of the 2-bromopropane it was of utmost importance to optimize pyrolysis conditions (temperature, pulse duration, pulse delay, skimmer distance etc.) carefully in order to suppress any propene background. In an additional experiment, the intensity of the hydrogen signal was measured while scanning the excitation wavelength from 255 nm to 230 nm. The action spectrum showed a similar shape as the absorption spectra recorded by *Wendt and Hunziker*, confirming that the H-atom photofragments originate from the neutral 2-propyl radical[110]. The power of the excitation laser was around 0.7 mJ/pulse in the region of 235 nm, whereas the power lay at 1.5 mJ/pulse in the region of 250 nm. Because of the lower absorption coefficient of 2-propyl in this spectral region, higher laser intensities had to be employed around 250 nm in order to achieve a sufficient two-color to one-color contrast. The laser spot size lay around 0.35 cm in diameter. The experiments showed a strict linear dependence between the hydrogen signal intensity and the excitation laser intensity in the range of 0.0–2.0 mJ/pulse. Thus higher order processes, such as dissociative photoionization, cannot account for the signal.

Figure 27: TOF spectra at different delay times of the molecular pulse. Only the leading edge of the pulse carries pure C_3H_7.
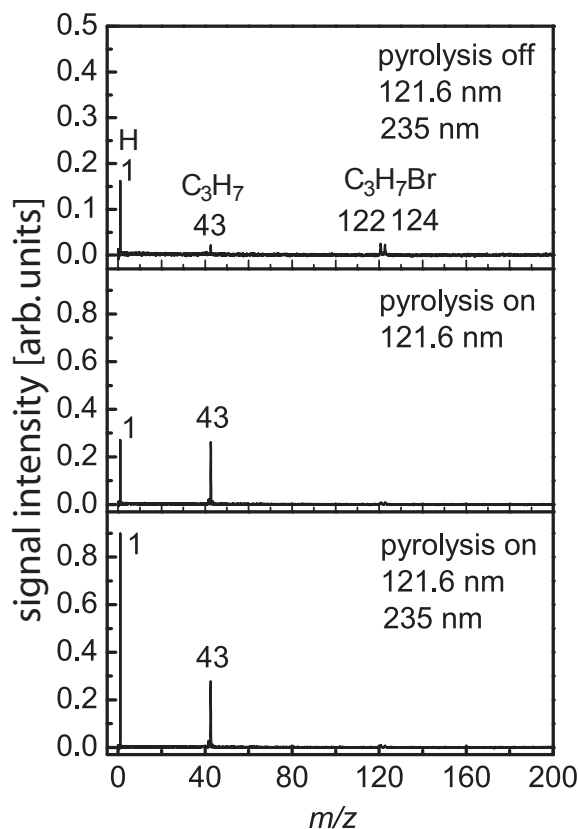
Figure 28: Typical TOF mass spectra of 2-bromopropane at different conditions.

6.3 DOPPLER PROFILES

Doppler profiles of the Lyman-α transition of hydrogen were taken at several excitation wavelengths in the region of 230–255 nm (compare chapter 3.3). Thus the excitation laser induced a transition into the electronically excited 3p Rydberg and/or 3s state of the propyl radicals[110]. Hydrocarbon radicals are known to have broad absorption bands. In case of the propyl radical the 3s band and the 3p band overlap strongly. It can therefore not be ruled out that a distribution of molecules in the 3p and molecules in the 3s state was generated by the excitation laser. The excited states of alkyl radicals are assumed to deactivate quickly after excitation[30,112] and the dissociation process is likely to take place from the hot ground state surface (scheme 3). Nevertheless, this is still a matter of debate.
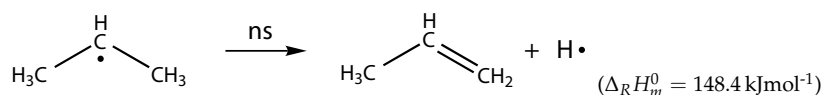
Scheme 3: The optically prepared hot 2-propyl radicals dissociate after a few ns to yield propene and hydrogen atoms with considerable kinetic energy.

According to ref. 113, the standard dissociation enthalpy for the loss of hydrogen can be calculated to 148.4 kJmol^{-1}. Analysis of the recoil

induced Doppler broadening of the Lyman-α transition revealed an isotropic distribution of ejected hydrogen atoms. The measurements concluded that approx. 20% of the excess energy ($E_{exc} = E_{phot} - E_{diss}$) are transferred into kinetic energy of the extracted H-atom. This value is typical for statistical photodissociation processes of hydrocarbon radicals[105,106]. In contrast, for C–H-photodissociation processes of aromatic compounds, which yield radicals rather than closed shell molecules, expectation values lie considerably lower (10%–12%)[36,114]. This can partially be explained by the negligible reverse barrier of the reaction[1].

Figure 29 shows six typical Doppler profiles of the Lyman-α transition of photo detached H atoms. As can be seen in fig. 28 a background signal with the excitation laser turned off was present at all times and was subtracted before the Doppler profiles were processed. The exper-
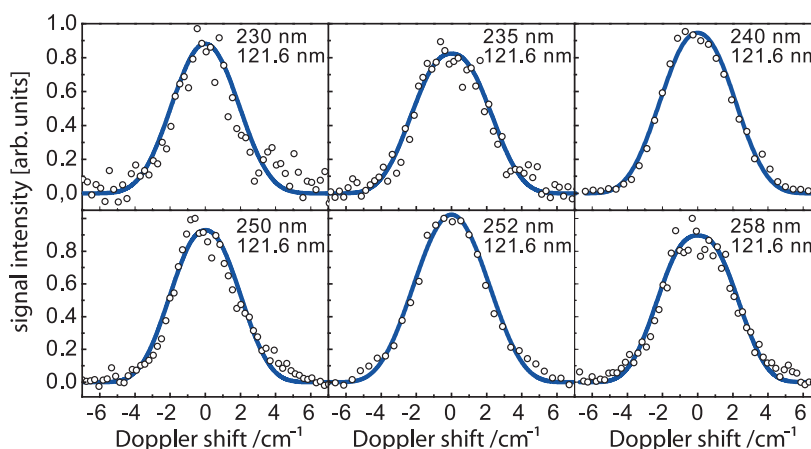
Figure 29: Typical Doppler profiles after subtraction of the background signal.

imental profiles were then analyzed by the method of *S. North, et al.* in order to evaluate the speed distribution of the ejected hydrogen atoms and to calculate the average value of energy release[116–118]. Hereby a trial translational distribution is created by the empirical equation 6.1.

$$P_{(E_t)} = \left[\left(\frac{E_t}{E_0} \right)^a \left(1 - \frac{E_t}{E_0} \right)^b \right] \tag{6.1}$$

$E_{(t)}$ represents the available translational energy and E_0 the total available excess energy of the hydrogen atoms. The exponents *a* and *b* are variable fit coefficients. A Doppler profile is calculated from a starting distribution with arbitrary *a* and *b* values and then compared to the experimental profile. The coefficients *a* and *b* were iteratively optimized until the sum of least-square deviations between the calculated and the experimental Doppler profile had converged. The laser bandwidth, natural line broadening, the fine structure splitting of the Lyman-α transition and the convolution with the parent velocity distribution was omitted in the analysis. Nevertheless, these effects will be small compared to the velocity distribution of the fragment. Since ex-

---

[1] The energy corresponding to the reverse barrier is preferentially transferred into kinetic energy of the fragment[115].

periments were carried out perpendicular to the molecular beam, the parent velocity distribution is very narrow.

The calculated energy distributions using the numerical analysis on the experimental profiles of fig. 29 are depicted in illustration 30. The translational energy release lay typically in the region of $70\,\mathrm{kJmol^{-1}}$ after excitation between 230 nm and 258 nm. The released kinetic energy did not significantly increase with shorter excitation wavelengths. However, the experimental values are within the limited accuracy of the employed method (approx. $\pm10\%$).
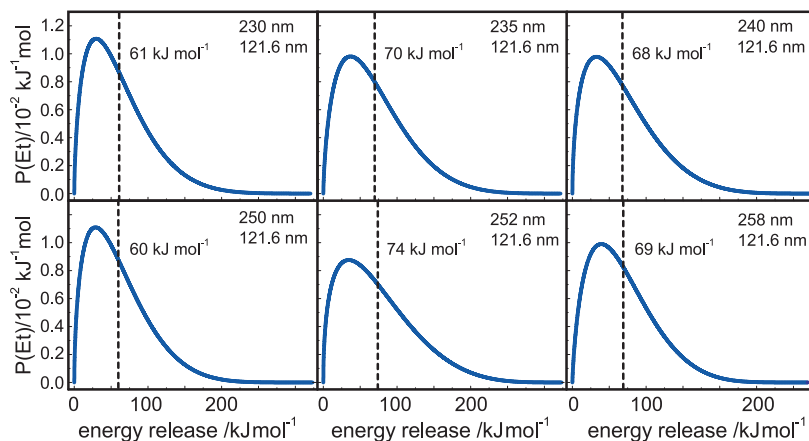
Figure 30: Kinetic energy release distributions corresponding to the Doppler profiles in figure 29.

In order to verify that the recorded Doppler profiles are in agreement with a statistical dissociation process, the calculated energy distribution at 240 nm excitation wavelength was compared to the one-parameter distribution 6.2. This equation was derived by *M. Quack* and tested on a set of other molecules[119]. Hence it enables to draw conclusions on the mechanism, depending on the value of n.

$$P_{(E_t)} = CE_t^n \rho_{(E_{ee}-E_t)} \tag{6.2}$$

C is a normalization factor, ρ represents the convoluted vibrational and rotational density of states of the products at combined internal energy and is thus a function of the released translational energy E_t and the excess energy E_{ee} (in this case only $\rho_{rot,vib}$ of the propene fragment, since H is an atom). The density of states was calculated using MP2/6-311G** frequencies of propene (see appendix A.4, page 148) by the method described in ref. 120. The result of the qualitative calculation, by varying n to give the same expectation value $\langle E_t \rangle$ as in the experiment, is depicted with dashed lines in fig. 31. The model yielded a factor n of 2.2. As discussed in the literature[119], a value of n between 0 and 3 indicates a statistical reaction. The agreement of the one-parameter distribution (6.2) with the two-parameter distribution (6.1) is reasonable. The dotted curve represents a simple prior distribution ($n = 0.5$) for comparison, which describes an ideal statistical process. It yields an expectation value of $32\,\mathrm{kJmol^{-1}}$, considerably smaller than the experimental one. The discrepancy between the prior distribution and the one derived from the experimental Doppler profiles is at least partially due to the existence of a reverse barrier for the C–H bond rupture as will be discussed later.
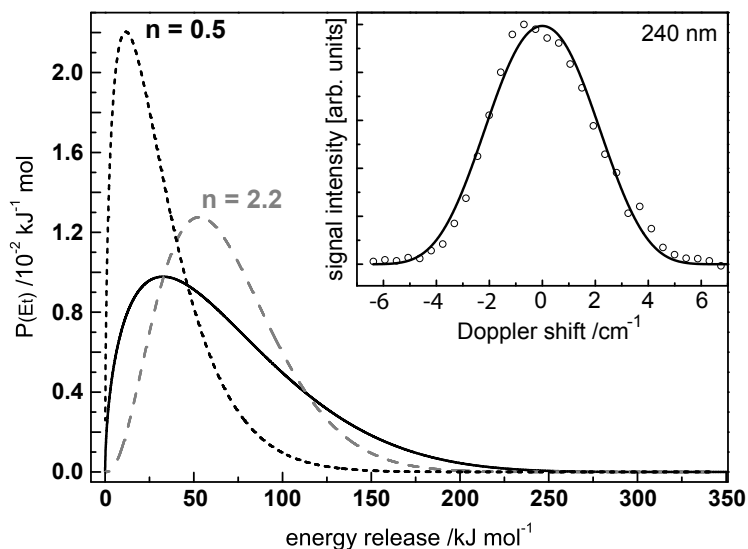
Figure 31: The translational energy release distribution (solid line) corresponds to a two-parameter fit (eq. 6.1) of the experimental Doppler profile recorded at 240 nm (inset). A prior distribution (dotted line) and the results from an one-parameter fit (dashed line, eq. 6.2) are given for comparison.

6.4 UNIMOLECULAR RATE CONSTANTS

Unimolecular rate constants for hydrogen loss were measured by integrating the H-atom signal as a function of the time delay (Δt) between the excitation and the detection laser. The acquired time-delay scans were analyzed by performing the least square fit algorithm of *Levenberg and Marquardt*[121,122] on equation 6.3. The algorithm was implemented in a *LabVIEW* program which is presented on page 136.

$$I_{(\Delta t)} = N \times \left[e^{-k_d(\Delta t - t_0)} - e^{-k_H(\Delta t - t_0)} \right] \times S_{(\Delta t)} + Y_0 \qquad (6.3)$$

In this equation, N is an empirical constant resembling the amplitude of the signal I, k_d is the decay constant [s^{-1}] of the signal due to the movement of the H atoms out of the ionization region, t_0 is the zero in time [s], k_H is the constant of interest [s^{-1}], giving the rate constant for the rise time of the H signal after excitation and Y_0 is the ordinate offset of the H background signal [arb. units]. The entire function was multiplied by a step function $S_{(\Delta t)}$ defined in equation 6.4, which gives the value zero for $\Delta t < t_0$ and one for $\Delta t > t_0$.[2] A convolution with an instrument response function was not performed.

$$S_{(\Delta t)} \approx \frac{1}{2} \left[1 + \tanh \left(b \left(\Delta t - t_0 \right) \right) \right] \qquad (6.4)$$

Analyzing the experimental data with equation 6.3 resulted rate constants for the rising time of the H signal (k_H) of around 5.8×10^7 s^{-1} after excitation at 254 nm and 8.0×10^7 s^{-1} at around 240 nm. Figure 33 shows three representative time-delay scans at excitation wavelengths of 240, 250 and 256 nm. Note that the power of the excitation laser lay typically at 0.7 mJ/pulse in the region of 235 nm whereas the power lay

---

[2] The factor b should be chosen bigger than 1×10^4. Larger values give a sharper step function.

at 1.5 mJ/pulse in the region of 250 nm. Higher laser intensities had to be employed around 250 nm in order to achieve a sufficient two-color to one-color contrast. Additional experiments showed a linear dependence between the hydrogen signal intensity and the laser intensity in the range of 0.0–2.0 mJ/pulse, indicating an one-photon process (fig. 32).

From −5 ns to 50 ns delay time 230 sweeps[3] were usually taken every 2 ns. The same number of sweeps were taken every 5 ns for all other delay times. As can be seen in fig. 33, the rates tend to increase

Figure 32: H signal intensity as a function of laser power
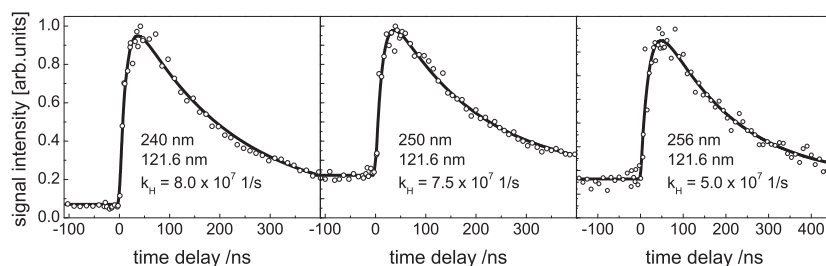
Figure 33: Hydrogen signal intensity as function of the delay between excitation of 2-propyl and ionization of hydrogen.

continuously from 256 nm to 240 nm excitation. The differences nevertheless are relatively small and already close to the time resolution of the setup.

6.5 RRKM CALCULATIONS

Unimolecular rate constants for detachment of a H atom in α position were calculated by RRKM theory, which was described in chapter 4.6 (see fig. 26). The transition state and reactant vibrational frequencies needed for performing RRKM calculations were computed by B3LYP/6-311G** and MP2/6-311G**(QST3) method of theory, respectively (Gaussian 03). Both methods predict similar frequencies for the reactant as well as for the transition state (TS). The geometry of the TS for the B3LYP calculation was taken from the maximum of a relaxed potential energy surface scan (one internal coordinate was varied while all other coordinates were optimized). As comparison the right side of table 4 shows the frequencies of the TS obtained by a QST3 MP2/6-311G** calculation. The frequencies of the TS are similar to those of propene as predicted by the postulate of Hammond[123] (see appendix A.4). The frequencies of the reactant (2-propyl) were calculated by performing a full optimization at the same levels of theory mentioned before. The frequencies are listed in table 3 and 4. The $\langle S^2 \rangle$ value was close to 0.75 for all calculations.

The ground state equilibrium geometry of 2-propyl is C_s symmetrical with the mirror plane cutting H1, C1 and the center between both C2 carbons (see right side figure).

For computation of the unimolecular rate constants by RRKM theory, the wavenumbers of the B3LYP calculations were taken for the TS and the equilibrium geometry. The two lowest vibrational modes (approx.

ⓘ QST3 stands for "quadratic synchronous transit" with three starting structures. It is a very reliable method for finding transition states. Three geometries are given to the calculation, the reactant geometry, the TS geometry guess and the product geometry. The program then searches the saddle point along this coordinate.

Table 2: Equilibrium geometry of 2-propyl

	MP2	B3LYP
C1-C2 [Å]	1.505	1.490
C1-H1 [Å]	1.087	1.085
C2-H2 [Å]	1.093	1.095
C2-H3 [Å]	1.104	1.104
C2-H4 [Å]	1.099	1.097
C2C1C2 [°]	120.7	121.1
H1C1C2H2 [°]	25.0	26.8

---

[3] Sweep: The laser system produces 10 shots per second. Thus every 0.1 s a signal is registered by the oscilloscope. This cycle is referred to as one sweep.

Table 3: Vibrational wavenumbers [cm⁻¹] of the propyl radical and symmetry. Left side: B3LYP/6-311G**, right side: MP2/6-311G**

105.8 (A″)	116.2 (A′)	354.0 (A′)	108.1 (A″)	140.0 (A′)	362.9 (A′)
395.5 (A′)	883.0 (A′)	939.2 (A″)	415.3 (A′)	890.9 (A′)	976.6 (A″)
945.0 (A″)	1028.6 (A′)	1146.3 (A″)	992.5 (A′)	1084.9 (A′)	1177.0 (A″)
1177.4 (A′)	1367.8 (A″)	1408.7 (A″)	1229.3 (A′)	1430.3 (A″)	1471.2 (A″)
1413.2 (A′)	1469.5 (A″)	1478.4 (A″)	1484.7 (A′)	1512.4 (A″)	1522.8 (A″)
1480.0 (A′)	1491.7 (A′)	2930.9 (A″)	1544.2 (A′)	1554.8 (A′)	2942.6 (A″)
2935.3 (A′)	3011.0 (A″)	3012.5 (A′)	2944.4 (A′)	3018.9 (A″)	3019.1 (A′)
3080.9 (A′)	3081.8 (A″)	3161.6 (A′)	3079.7 (A′)	3080.3 (A″)	3161.9 (A′)

Table 4: Vibrational wavenumbers [cm⁻¹] of the transition state and symmetry. Left side: B3LYP/6-311G**, right side: QST3 calculation MP2/6-311G**

i-885.9 (A)	178.8 (A)	342.7 (A)	i-1142.9 (A)	160.1 (A)	313.3 (A)
429.8 (A)	482.5 (A)	685.1 (A)	445.7 (A)	490.9 (A)	730.2 (A)
919.5 (A)	940.0 (A)	980.0 (A)	936.2 (A)	982.2 (A)	1071.4 (A)
1000.3 (A)	1050.8 (A)	1191.1 (A)	1105.1 (A)	1126.0 (A)	1240.3 (A)
1299.5 (A)	1405.7 (A)	1437.0 (A)	1351.5 (A)	1479.6 (A)	1499.6 (A)
1477.3 (A)	1491.4 (A)	1603.3 (A)	1518.0 (A)	1553.8 (A)	1645.4 (A)
3004.4 (A)	3046.6 (A)	3094.1 (A)	2988.7 (A)	3059.4 (A)	3084.5 (A)
3131.4 (A)	3136.8 (A)	3220.2 (A)	3117.3 (A)	3140.4 (A)	3220.2 (A)

110 cm⁻¹) for the equilibrium geometry of 2-propyl and the lowest real vibrational mode of the TS (approx. 180 cm⁻¹) were replaced by free internal rotors. The internal methyl rotors (two for the reactant and one for the TS) were simulated by using the reduced moment of inertia reported in a study on internal rotors (6.97 cm⁻¹)[124]. Directly utilizing the (not reduced) moments of inertia of the methyl groups $(3m(\mathrm{H}) \times (R(\text{C-H}) \sin \alpha)^2)$ in the RRKM calculations would result in an error[4]. This is because the correct reduced moment of inertia should be calculated about the axis connecting the center of masses of the rotating group *and* the rest of the molecule. More precise calculations also include coupling with all other rotations of the molecule[125]. For the activation energy the zero point energy corrected B3LYP value was used (158 kJmol⁻¹). The moments of inertia of the reactant and TS correspond to 1.25, 0.28, 0.25 cm⁻¹ and 1.16, 0.28, 0.26 cm⁻¹, respectively, and were taken from the same calculation.

The wavelengths for exciting 2-propyl radicals lay between 230 nm and 258 nm which correlates in depositing 520 kJmol⁻¹ and 464 kJmol⁻¹ of energy into the molecule. Some unimolecular rates in this region predicted by performing simple RRKM calculations with the QCPE 291 program are listed and depicted in figure 34. An important parameter for performing RRKM calculations is the so called statistical factor, which describes the reaction path degeneracy of the reaction. It is easily understood that the reaction will be faster if the same reaction can proceed to the same product on several equivalent reaction paths. Nevertheless, the derivation of the statistical factor can be somewhat

---

[4] In the equation $m(\mathrm{H})$ represents the atomic mass of hydrogen, $R(\text{C-H})$ the C–H bond distance and α the tetrahedron angle.

unintuitive as the example of 2-propyl shows[5]. A formula to calculate statistical factors (s) can be derived from a complete permutation and inversion group formalism and is shown as equation 6.5[126].

$$s = \frac{m^\dagger \sigma}{m \sigma^\dagger} \tag{6.5}$$

In formula 6.5, s represents the statistical factor, m is the number of different optical isomers and σ stands for the symmetry number (order of largest rotational subgroup). The daggers mark the TS. For 2-propyl

λ [nm]	Rate [s^{-1}]
230	5.8×10^{11}
235	5.1×10^{11}
240	4.4×10^{11}
245	3.9×10^{11}
250	3.4×10^{11}
255	3.0×10^{11}
260	2.7×10^{11}
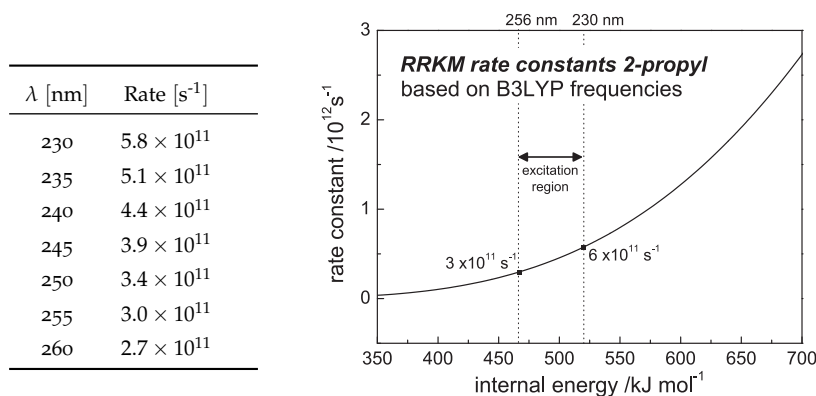
Figure 34: Calculated unimolecular rate constants

the symmetry number should be chosen as two (σ=2), since the lowest vibrational level is above the inversion barrier for the radical center[127] leading to a C_{2v} symmetry which does not have different optical isomers ($m = 1$). But since the 2-propyl radical has two only slightly hindered rotors these should be accounted for[128]. Each rotor has a symmetry number of 3. Thus for the 2-propyl radical the σ value of the numerator in equation 6.5 equals $2 \times 3 \times 3 = 18$. The reaction shown in scheme 3 has a TS with no symmetry and the order of the largest rotational subgroup of the TS molecule equals one. There is only one free methyl rotor left in the TS[6] with a symmetry number of 3. Thus in equation 6.5, $\sigma^\dagger$ equals 1×3. In contrast to the 2-propyl radical itself, the TS has two different optical isomers ($m^\dagger = 2$). The overall reaction degeneracy for the unimolecular reaction shown in fig. 3 equals $2 \times 18/(1 \times 3) = 12$. This makes sense because the "planar" 2-propyl radical has two equivalent sides and 6 equivalent H atoms that can eliminate from either side of the plane. The calculations predict rate constants on the order of 4.5×10^{11} s^{-1}. A rate constant with this order of magnitude would, however, not be resolvable by the applied ns-laser setup.

6.6 CALCULATIONS ON DISSOCIATION BARRIERS

Several possible photodissociation and isomerization pathways exist after electronic excitation of propyl. Femtosecond time-resolved studies on the excited states of hydrocarbon radicals found a decay to the

---

[5] I want to thank *Prof. V. D. Knyazev* for valuable discussions on statistical factors.
[6] The TS has a specific geometry. Thus one of the methyl groups is "locked" in place.
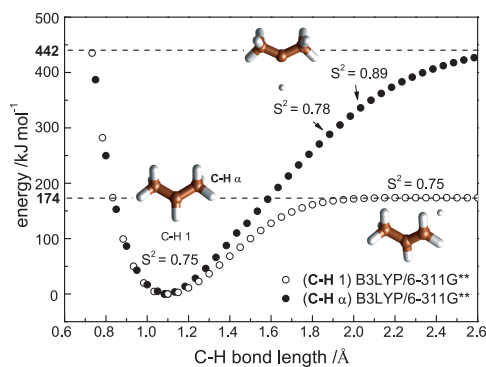
(a) Direct C–H bond dissociation pathways
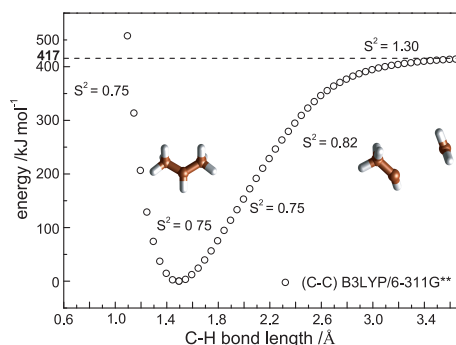
(b) Direct C–C bond dissociation pathway

Figure 35: The C–H bond at α position has the lowest barrier for bond dissociation. ZPEC is not included in graphs above.

ground state surface only few femtoseconds after excitation[30,112]. All further reactions presumably take place from there[129]. In order to acquire a qualitative picture of the relative energy barriers for the different photoinduced reactions of hot propyl radicals on the ground state surface, relaxed potential energy surface scans were performed with B3LYP/6-311G** level of theory. Note that the depicted surfaces do not include zero point energies. These were added in subsequent calculations for single optimized points. Immediate dissociation pathways of the 2-propyl radical consist of a C–C bond cleavage, a C–H bond cleavage at α position and a C–H bond cleavage at position 1. The results of the calculations are presented in fig. 35. The calculations predict that the C–H bond in α position is by far the weakest bond (174 kJmol^{-1} without and 158 kJmol^{-1} with zero point energy correction ZPEC). The calculations predict a much higher bonding energy for the central C–H bond (442 kJmol^{-1}, 429 kJmol^{-1} with ZPEC) as well as for the C–C bond (417 kJmol^{-1}, 513 kJmol^{-1} with ZPEC); it is thus most likely that the ejected H atoms correspond to the α position also taking into account that this position is statistically favored. All three reaction pathways discussed above do not show any reverse barrier by means of B3LYP theory. However, a second calculation with a different functional (BMK/6-311G** [74]) predicted a reverse barrier of 6.1 kJmol^{-1} for the hydrogen loss in α position. The BMK functional has explicitly been developed to yield correct reaction barriers[74], whereas

the B3LYP functional tends to underestimate them. However, rather than obtaining quantitative dissociation barriers, the calculations were performed to have a qualitative overview over the different reaction barriers of propyl for extracting feasible reaction paths.

Another feasible reaction path could be a [1,2]-H-shift followed by a C–C bond dissociation to ethene and methyl. Ethylene + methyl are only 108 kJmol^{-1} higher in enthalpy than 2-propyl and only 98 kJmol^{-1} higher than 1-propyl[130,131]. Thus excitation of 1-propyl should result in photodetachment of methyl. The B3LYP calculations concluded that a barrier of 185 kJmol^{-1} (177 kJmol^{-1} with ZPEC) exists for a [1,2]-H-shift as illustrated on the left-hand side of figure 36. The barrier

(a) H-shift: 1-Propyl⇌2-Propyl   (b) C–C bond dissociation pathway
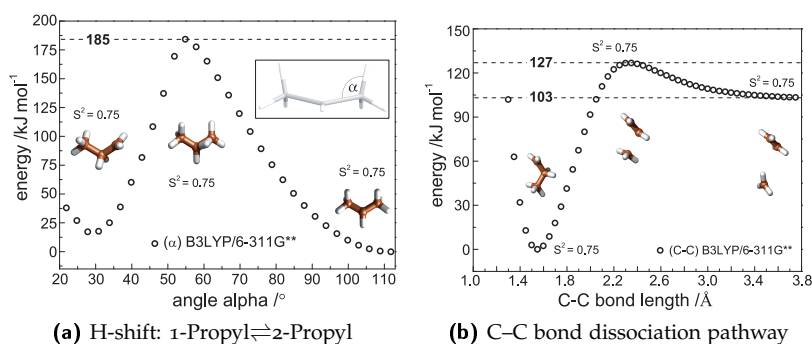
Figure 36: C–C dissociation pathway with a prefixed [1,2]-H-shift

for hydrogen migration is predicted only 19 kJmol^{-1} higher in energy than a direct C–H bond cleavage in α position and cannot be ruled out as a possible reaction pathway after excitation. The barrier for dissociation of the 1-propyl radical into ethene and methyl was calculated to be only 127 kJmol^{-1} (136 kJmol^{-1} with ZPEC). The difference in internal energy between reactants and products is predicted to be 103 kJmol^{-1} (85.5 kJmol^{-1} with ZPEC), which is consistent with experimental results[132]. If a [1,2]-H-shift takes place it is very likely that a C–C dissociation directly follows. A summary of all calculated reaction pathways with zero point corrected energies is given in figure 38.

6.7 EXPERIMENTS WITH 1-PROPYL

After having performed the qualitative B3LYP calculations one major question remained: Does the 2-propyl radical lose its hydrogen in α position after excitation or does it first undergo a [1,2]-H-shift to 1-propyl and subsequently lose the hydrogen? In order to answer this question 1-propyl radicals were produced cleanly in a free jet in a similar manner to 2-propyl. 1-Bromopropane was used as precursor. The result of the experiment is depicted in fig. 37. Note that the absorption maximum of 1-propyl lies at 209 nm (3p band) whereas the absorption maximum of 2-propyl lies at 240 nm (3p band)[110]. Thus shorter wavelengths (218 nm–255 nm) were used to excite 1-propyl. In contrast to 2-propyl the 1-propyl did not lose hydrogen atoms in measurable quantity after excitation between 218 nm and 255 nm. The consequences of the experiment are that no isomeric scrambling takes place in the pyrolysis source. The pyrolysis cleanly breaks the C–Br bond and the
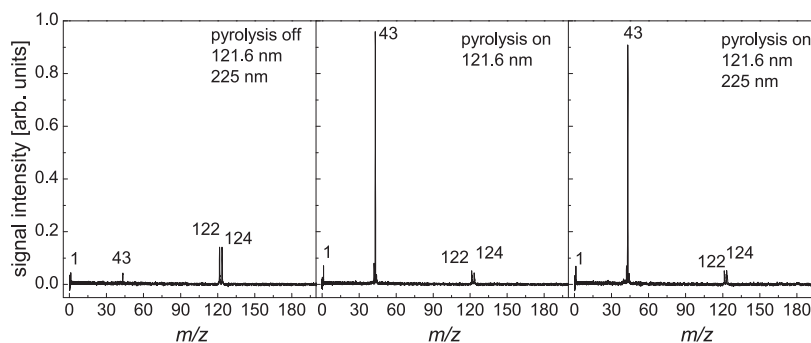
Figure 37: Typical TOF mass spectra of 1-bromopropane at different conditions. By turning on the pyrolysis source an intense propyl signal appears (middle). The hydrogen signal does not increase by turning on the excitation laser (right)

nascent pyrolysis products are conserved immediately due to the supersonic expansion. The main deactivation process of 1-propyl radicals does not seem to be the loss of hydrogen atoms as the calculations already suggested. Presumingly a C–C rupture takes place. Note that the detection efficiency of the apparatus is several orders of magnitude lower for methyl than for hydrogen. In contrast to methyl, H atoms are excited resonantly and the Lyman-α transition has a very strong oscillator strength.

6.8 DISCUSSION AND CONCLUSIONS

In agreement with chemical intuition the calculations suggest two relevant reaction pathways for 2-propyl: Direct loss of hydrogen in α position after excitation and/or isomerization to 1-propyl. The mass spectra given in figure 37 show that 1-propyl does not lose H atoms upon excitation as readily as 2-propyl. Most likely it dissociates according to the energetically most favorable product channel into ethene + methyl, as also evident from the computations. The loss of methyl is a known reaction path of 1-propyl radicals in thermal equilibrium[132,133] and has been evaluated theoretically before[134]. The mass spectra confirm that (a) the observed H atoms originate from 2-propyl and (b) that no scrambling of hydrogen atoms occurred in the nozzle during pyrolysis. The detection efficiency of the setup for methyl is considerably lower than for hydrogen. Thus if a small amount of 2-propyl radicals isomerizes to 1-propyl and subsequently undergoes C–C bond rupture, it will not be observed. A summary of the B3LYP calculated pathways is given in fig. 38. It is to assume that the reaction shown in scheme 3 is the dominant reaction pathway of 2-propyl after excitation because of the lower computed barrier as compared to [1,2]-H-shift. A regioselective dissociation was also found in earlier measurements on isotopically labeled 2-propyl radicals[104]. The barrier towards isomerization from 2-propyl to 1-propyl is predicted by the calculations to lie at 177 kJmol^{-1}. This is relatively high, especially since the B3LYP functional tends to underestimate barrier heights by around 10 kJmol^{-1}. However, the result is in agreement with the experiment, which also shows that no isomerization between the two isomers takes place in the pyrolysis nozzle. An interesting comparison can be drawn when
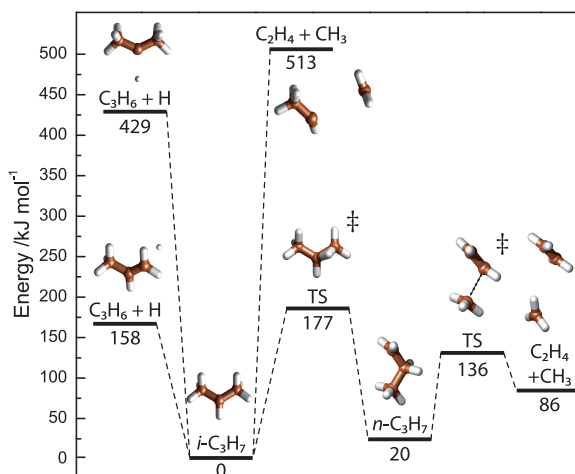
Figure 38: Summary of important reaction pathways of 2-propyl and 1-propyl predicted by B3LYP level of theory.

compared to the results on carbenes in the following chapters (e.g., page 91, fig. 77). These species show a much lower barrier towards hydrogen migration and can indeed isomerize in the pyrolysis nozzle. Thus from an purely experimental point of view, a "critical" barrier towards thermal [1,2]-H-shifts, using jet flash pyrolysis, lies between 31 kJmol^{-1} (carbenes) and 177 kJmol^{-1} (radicals).

The analysis of the nearly Gaussian-shaped Doppler profiles, the derived translational energy distribution and the expectation value of 20% of the excess energy released as translation indicate that 2-propyl dissociates in a statistical fashion after electronic excitation. This shows that excited-state deactivation is fast compared to the dissociation rate. The difference between the experimentally derived $P_{(E_t)}$ and the one obtained from a simple prior distribution can partially be explained by the presence of a reverse barrier, which was indeed found in the BMK calculation. This energy is not distributed statistically between the internal degrees of freedom of the products and is preferentially released as translation[115], delivering a qualitative explanation for the higher translational energy release of $\langle 20\% \rangle$. The remaining difference between the experimentally derived and the prior distribution is probably due to two factors: First, the BMK computations might still underestimate the reverse barrier by several kJmol^{-1}. And second, the density of states used to calculate the prior distribution was computed using harmonic frequencies, which constitutes only a crude approximation at the high excess energies present in the experiment.

An interesting result of the photodissociation of 2-propyl is the significant deviation of the observed dissociation rates from the RRKM model, which amounts to approximately three orders of magnitude. A similar deviation was also found for ethyl[107] and *tert*-butyl[108] and seems to be a general feature of alkyl radicals. In contrast, the photodissociation of the unsaturated radicals allyl and propargyl can be described well by statistical theories[106]. There are two possible explanations for this behavior in alkyl radicals. The first is an excited-state deactivation that is more complicated than the assumed simple

internal conversion to the ground state. From the femtosecond studies during my "master's thesis", it is known that the initially excited 3s Rydberg state of the *tert*-butyl and the ethyl radical deactivate within roughly 100 fs[30,112], but the final state of the deactivation was not identified. For *t*-butyl the 3p Rydberg state is longer lived and showed a lifetime of 2 ps. This, however, is still short when compared to the measured rate constants for H loss. Considerations using a valence bond picture suggest that upon stretching one C–C bond, leading to dissociation into a methyl radical and a carbene, the energy of the lowest excited valence state decreases significantly for alkyl radicals[30] along this coordinate (see appendix A.5). It correlates to the closed shell singlet state of the carbene and crosses the 3s and 3p Rydberg states. Therefore, the initially populated excited state might deactivate in a multi-step process. Since the role of this valence state in the photochemistry of alkyl radicals remains unclear so far, further theoretical and time-resolved experimental studies are essential to obtain a complete understanding of all photophysical processes involved in the alkyl radical photochemistry.

A second explanation for the large discrepancy between experimental rates and simple RRKM computations was recently provided by *Bach et al.* for the ethyl radical[129]. In a classical trajectory study of ethyl dissociation it was found that around 20% of trajectories showed quasiperiodic behavior, leading to population trapping for extended periods of time. In a frequency-domain picture, quasiperiodic trajectories correspond to resonances that are only weakly coupled to the remaining degrees of freedom. In this picture the surprisingly slow photodissociation of ethyl can thus be explained by a slow randomization of energy in the electronic ground state, rendering one of the major assumptions of statistical theories invalid. Whether a similar mechanism applies to the 2-propyl radical as well has yet to be shown. However, with regard to the excited-state calculations mentioned above, it is likely that conical intersections lead to a deactivation of the electronically excited species far away from the ground state equilibrium geometry, increasing the probability of reaching quasiperiodic trajectories on the ground state surface.

7

PHOTOIONIZATION STUDIES OF DIAZIRINES AND THEIR CATIONS

7.1 INTRODUCTION AND GOALS

Diazirines are known to be ideal precursor molecules for carbene generation[135]. Two diazirines, 3-phenyl-3-(trifluoromethyl)diazirine and 3-chloro-3-phenyldiazirine (fig. 39), were employed for studying phenylcarbenes in the forthcoming chapters. These molecules were additionally investigated by PEPICO spectroscopy, which gives insights into the dissociative photoionization (DPI) of such species. To know the behavior of these diazirines upon irradiation is important information, since DPI can lead to signals in the mass spectrum that are difficult to distinguish from signals originating from the intermediates that are under investigation in the following chapters.

Additionally, diazirines have become important compounds for photoaffinity labeling in which the compounds are cleaved photochemically to produce covalent bonds with acceptor molecules[29]. Especially TFPC-N_2 entities have become the standard in this field due to their chemical and physical properties. In contrast to many other diazirines these moieties are a) not explosive, b) their absorption spectrum has its maximum in a spectral region in which biological samples do not strongly absorb and c) the resulting carbenes do not isomerize[29]. So far, only relatively small diazirine (e. g., R_1=CH_3, R_2=H) model compounds with less practical importance have been studied by photoelectron spectroscopy[136].

3-chloro-3-phenyldiazirine (CPC-N_2)

3-phenyl-3-(trifluoromethyl)diazirine (TFPC-N_2)

Figure 39: CPC diazirine & TFPC diazirine

7.2 DERIVING THERMOCHEMICAL PROPERTIES

The synchrotron experiments enabled insights into the dissociative photoionization of diazirines and yielded appearance energies (AEs) for the corresponding ionized carbene fragments. By determining the appearance energies for fragments and measuring the IP of the same, thermodynamic cycles can be drawn as illustrated in fig. 40. Missing thermodynamic parameters can then be complemented according to equation 7.1. The figure also illustrates the dependence of the reverse barrier (X) on two different reaction pathways in the cation. The light gray pathway shows an exothermic dissociation (BDE$^+$ < 0 eV), whereas the black solid line describes an endothermic dissociation (BDE$^+$ > 0 eV). Thus the more exothermic the dissociation is (BDE$^+$ < 0 eV), the larger the back barrier X will be. *Note the direction of the arrows in fig. 40.*

$$AE_{(R_2N, R_2^+)} = BDE_{(R_2N)} + IP_{ad(R_2)} + X \qquad (7.1)$$

In the case of many hydrocarbon radical *cations*, the circle can be further simplified. These species usually have endothermic bond dissociations as well as negligible reverse barriers (X $\approx$ 0 kJmol^{-1}) and hence the activation energy (E‡) nearly equals the bond dissociation energy

ⓘ *The bond dissociation energy (BDE) is defined as the enthalpy at 0 K that is required to homolytically break a bond of some specific molecular entity. If new bonds are formed upon cleavage and only weak bonds are broken, the enthalpy (heat at constant pressure) can be exothermic. Thus the BDE can be < 0 kJmol^{-1}. A BDE can also be exothermic if the dissociation relieves bond strain. The BDE should not be confused with the activation energy E‡, which is always $\geq$ 0 kJmol^{-1} (fig. 40).*
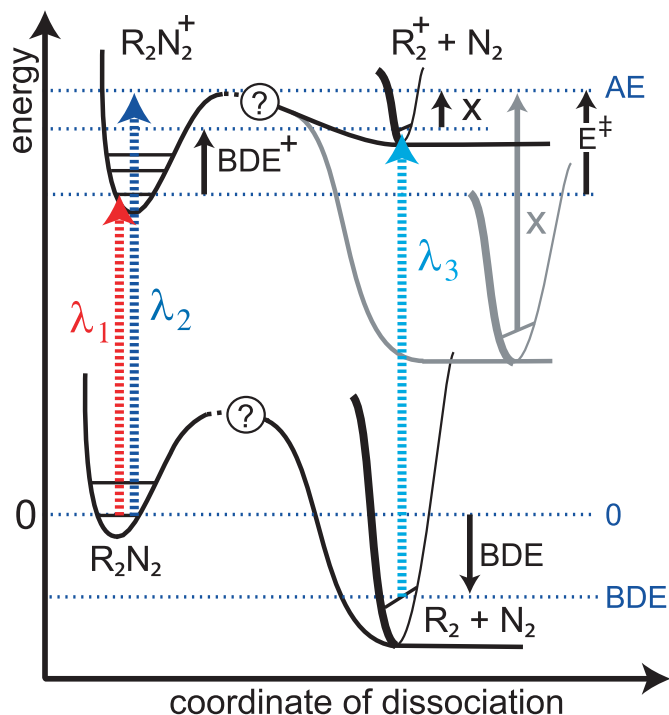
Figure 40: General thermodynamic circle: A cycle can be drawn incorporating the IP of the fragment (λ_3), the bond dissociation energy (BDE) of the neutral parent molecule, the appearance energy (AE) of the cationic fragment (λ_2) when irradiating R_2N_2 and the reverse barrier (X) of the dissociated cation. *Note the arrow directions: up > 0, down < 0.*

(BDE$^+$) of the cation[137]. The BDE of the parent in these cases can then be calculated according to equation 7.2.

$$\text{BDE} = \text{AE}_{(R_2N,\ R_2^+)} - \text{IP}_{ad(R_2)} \tag{7.2}$$

For the diazirines a similar simple picture is not likely to be assumable. The abstraction of the very stable N_2 is known to be exothermic and a reverse barrier will exist for the neutral. The N_2 abstraction might follow a related potential energy surface in the cation. This will be underpinned by forthcoming calculations. Hence a direct conclusion on the BDE of the neutral diazirine cannot be extracted without the knowledge of the reverse barrier in the cation. However, the experimentally determined values for IP and AE nearly complete the circle.

Additionally, the activation energy (E‡) for the dissociation of the diazirine *cations* can simply be calculated by taking the difference between adiabatic IP of the of the diazirine and the appearance energy of the fragment R_2^+ according to equation 7.3 (see fig. 40).

$$E^\ddagger = \text{AE}_{(R_2N,\ R_2^+)} - \text{IP}_{ad(R_2N)} \tag{7.3}$$

Only if the dissociation of the cation is endothermic (BDE$^+$ > 0) *and* there is no reverse barrier (X = 0), the activation energy (E‡) equals the bond dissociation energy of the cation (BDE$^+$).

IPs and AEs are very important thermodynamical properties that can help to identify reactive species (see fig. 12 on page 15).

The experiments were performed at the new storage ring *Soleil* in France. The setup was described in chapter 3.5. PEPICO as well as TPEPICO spectra (chapter 2.5) were recorded together with conventional photoelectron spectra via VMI. The diazirines were synthesized according to procedures found in the literature[138–140].

The mass spectra of TFPC-N_2 and CPC-N_2 are presented in fig. 53 and 54 on page 68. Without the pyrolysis turned on, the photon energy dependence of the ion yields of the photofragment (TFPC), the precursor (TFPC-N_2) as well as the dimer (TFPC-$N_2)_2$ are presented in fig. 41 (acquisition time 7 s per photon energy). The signal of the diazirine and the carbene photofragment both set in slightly above 9 eV. Thus the diazirine partially shows dissociative photoionization already at the ionization threshold (AE_{0K} taken from fig. 44):

$$TFPC\text{-}N_2 \xrightarrow[AE_{0K}\,=\,9.3\,eV]{h\nu} TFPC^+ \;+\; N_2 \;+\; e^-$$
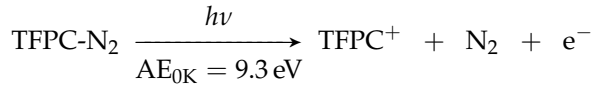
At around 8.9 eV, the ion signal of the precursor dimer was found to set in earlier as the diazirine itself. It has a low signal level up to 9.5 eV. More accurate ionization thresholds can be obtained when exclusively ions detected in coincidence with near-threshold electrons are taken into account as was explained in chapter 2.5. The inset in figure 41
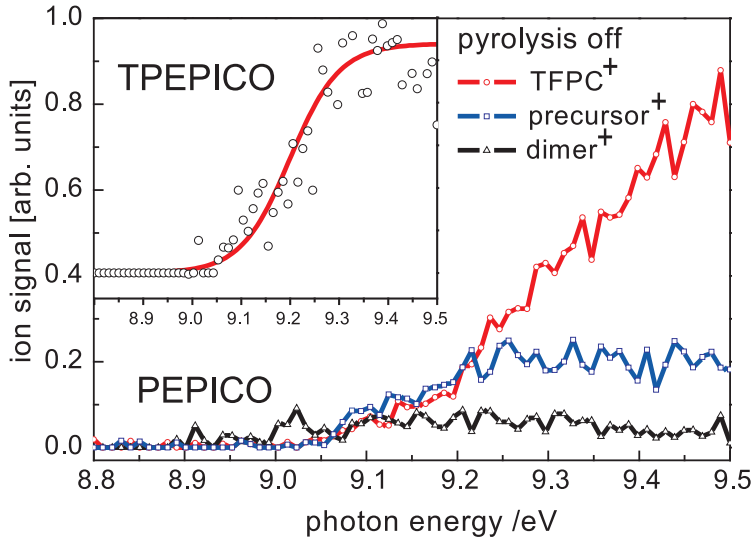
Figure 41: Photoion yields of the diazirine (TFPC-N_2), its dimer cluster and the TFPC$^+$ ion fragment recorded by PEPICO spectroscopy. The inset shows the TPEPICO spectrum of the photofragment TFPC$^+$.

shows the TFPC$^+$ ion signal that could be associated with electrons corresponding to a maximum kinetic energy of 10 meV (red line drawn to guide the eye). The rise of the threshold signal is much steeper and does not increase any further beyond 9.4 eV.

Spectra obtained for CPC are similar in appearance and are depicted in figure 42. At each photon energy data were averaged for 25 s. In contrast to CPC-N_2, no signal from the precursor was observed even

with the pyrolysis turned off because of a complete and direct dissociative ionization of the diazirine at the ionization threshold (threshold taken from fig. 44):

$$\text{CPC-N}_2 \xrightarrow[> 8.8\,\text{eV}]{h\nu} \text{CPC}^+ + \text{N}_2 + \text{e}^-$$

The inset in figure 42 shows the measured CPC ion signal corresponding to threshold electrons as a function of the photon energy. The
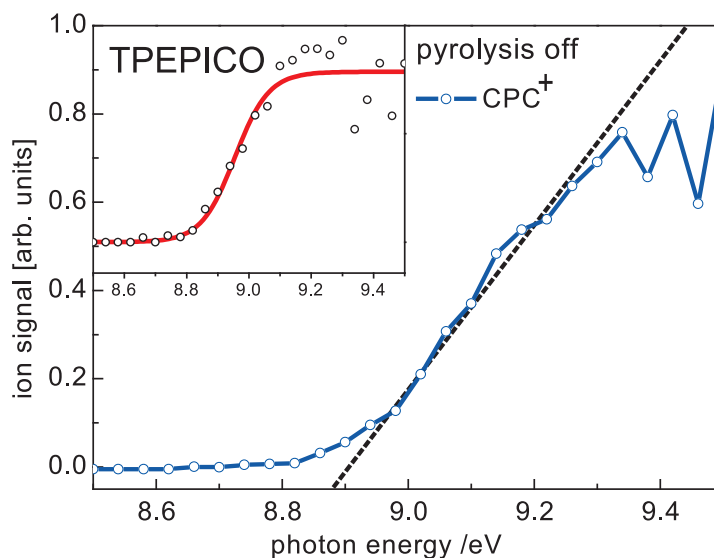
Figure 42: Photoion yield of the CPC$^+$ ion fragment recorded by PEPICO spectroscopy. The inset shows the corresponding TPEPICO spectrum.

threshold signal remains constant above 9.1 eV in the measured energy region.

The PEPICO spectra of the TFPC$^+$ fragments were further analyzed using a model developed by *Asher et al.* [141]. Due to a thermal temperature of the molecular beam above 0 K, the correct AE$_{0K}$ is not found directly at the position where the signal first appears in the spectrum. The molecules in the beam still have some thermal energy. Thus a signal can appear slightly before the actual 0 K appearance energy, since the thermal energy of the parent is available for fragmentation. These "hot bands" can be accounted for by analytical expressions. In brief, the density of states of the parent diazirine (TFPC-N$_2$) was calculated from its vibrational (and rotational) constants, which were taken from the calculations presented in section 7.4. From the density of states $\rho_{(E)}$, a temperature dependent internal energy distribution $P_{(E,T)}$ was calculated according to equation 7.4[1].

$$P_{(E,T)} = \rho_{(E)} \times \exp\left(\frac{-E}{kT}\right) \tag{7.4}$$

---

[1] The integral over $P_{(E,T)}$ is normalized to 1. Only vibrational states were counted. $k = 1.380\,650\,4 \times 10^{-23}$ J/K

This function was then fitted with the empirical equation 7.5, which can be easily convoluted (compare chapter 5) and is continuous and well behaved in contrast to equation 7.4.

$$P_{(E,T)} = A \times E^{\kappa} \times \exp\left(-aE\right) \tag{7.5}$$

Herein E represents the internal thermal energy of the parent and the coefficients A, a and κ are variable fitting parameters. After determination of the best coefficients, function 7.5 is convoluted by an arbitrary "kernel" function $K_{(E_{phot})}$. The kernel function would describe the rise of the ion signal correctly if the molecular beam was at zero Kelvin. Since the true experimental kernel function is usually unknown, approximations have been proposed in the literature[141] (fig. 43). The most common functions used are given in equations 7.6 and 7.7. K_l is a simple linear kernel with a slope m and K_e accounts for an exponential rise to a plateau which is often seen in experimental spectra. Both kernels are exemplified in fig. 43.

$$K_l = m \times \left(E_{phot} - \mathrm{AE}_{0K} \right) \tag{7.6}$$

$$K_e = m_e \times \left[1 - \exp\left(-B\left(E_{phot} - \mathrm{AE}_{0K} \right) \right) \right] \tag{7.7}$$

Figure 43: Examples of common kernels

The prefactors m_e corrects for intensity, E_{phot} stands for the irradiated photon energy and AE_{0K} is the appearance energy of the fragment at absolute zero. In the present work, the exponential kernel K_e was chosen, since this model is more adequate for fragment yield curves that level off at higher energy[141]. In order to simulate the true experimental spectrum $S_{(E_{phot})}$, these kernel functions have to be convoluted with the internal energy distribution $P_{(E,T)}$ of the parent according to equation 7.8. The procedure is exemplified in equation 7.9 with K_e and accounts for the thermal energy already present inside the parent before it dissociates into its fragments.

$$S_{(E_{phot})} = \int_{x_0}^{\infty} K_{(x)} \times P_{(x-E_{phot})}\, \mathrm{d}x \tag{7.8}$$

$$S_{(E_{phot})} = \int_{x_0}^{\infty} m_e \left[1 - \exp\left(-B\left(x - \mathrm{AE}_{0K} \right) \right) \right] \times \\ A\left(x - E_{phot} \right)^{\kappa} \exp\left(-a\left(x - E_{phot} \right) \right)\, \mathrm{d}x \tag{7.9}$$

The integral 7.9 was solved numerically and fit to the experimental data to determine corrected values for AE_{0K}[2]. However, analytic solutions to the integral are given in ref. 141.

This analysis was performed for the PEPICO ion yield curve of TFPC-N_2 as depicted in fig. 44. The upper trace presents the total ion yield, whereas the lower trace only counts ions corresponding to electrons with low kinetic energy (compare chapter 2.5). The photoion yield curves of the TFPC$^+$ radical fragment, which were recorded employing 3-phenyl-3-(trifluoromethyl)diazirine as precursor, are depicted on the right side of figure 44. After ionizing TFPC-N_2^+, the fragment becomes visible at slightly higher photon energies as was found

Figure 44: Both diazirines (TFPC-N_2 and CPC-N_2) show dissociative photoionization. The appearance energy of their radical fragments TFPC$^+$ and CPC$^+$ were elucidated by analyzing the ion yield curves according to the method of *Asher et al.*

for the chlorinated diazirine. A value for the AE_{0K} was determined by the analysis of *Ascher et. al.* to lie at $9.27 \pm 0.1\,\text{eV}$ for TFPC$^+$.

The left side of fig. 44 shows the ion yield curves obtained when using CPC-N_2. Here the radical fragment CPC$^+$ starts to appear already around $\approx 8.8\,\text{eV}$ at the temperature of the molecular beam. No parent is visible for CPC-N_2. Thus the onset for CPC$^+$ is strongly determined by Franck-Condon factors associated with the photoionization process, and an analysis according to *Asher* is not precise for CPC-N_2. Since internal energy will also shift this value compared to the a true 0 K measurement, the threshold for dissociative photoionization of CPC-N_2^+ can only be estimated to lie at around $9.1 \pm 0.2\,\text{eV}$ when assuming a similar shift of roughly 0.3 eV.

In contrast to CPC-N_2, the parent is indeed visible for TFPC-N_2 and hence a breakdown diagram can be plotted to determine the appearance energy[142]. Such a diagram is formed by dividing the integral of each mass channel (Int_1 and Int_2) by the total integral (Int_1+Int_2), yielding the fractional abundances[143]. The plot is given in fig. 45 and gives an AE_{0K} at $9.28 \pm 0.1\,\text{eV}$. In this diagram a 3 point smooth was performed and electrons taken into account with 0–10 meV of kinetic energy. Hence the resolution can be determined to lie in the region of 20 meV. The AE_{0K} can be estimated by subtracting the shift, which is induced by the smoothing process and the finite energy resolution of the measurement, from the position where the fractional abundance of the mother reaches a constant level: $9.30\,\text{eV} - 0.02\,\text{eV} = 9.28\,\text{eV}$. The method of *Asher et al.* and the breakdown diagram give very similar values.

Note that in the breakdown diagram the data points between 9.00 and 9.15 eV have a very poor signal-to-noise ratio and should be disregarded. However, in the interesting region above 9.15 eV the signal quality is sufficient to extract a reliable value for the appearance energy.
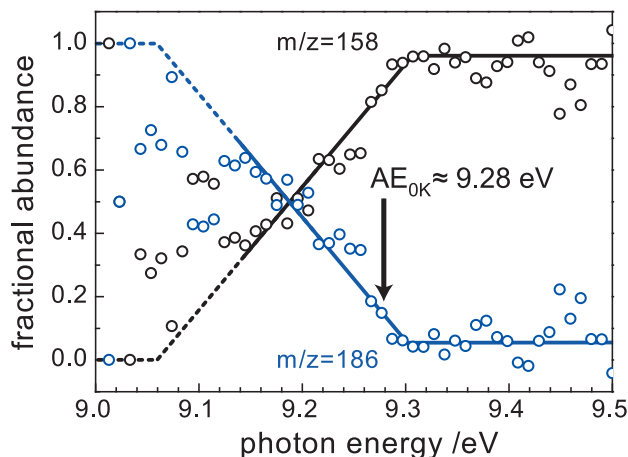
Figure 45: Breakdown diagram of TFPC-N$_2$. By plotting the fractional abundance[144] of parent and daughter, breakdown diagrams[142] enable the determination of AEs.

7.4 COMPUTATIONAL RESULTS

Hybrid density functional theory (DFT) computations were employed using the B3LYP functional with a 6-311^{++}G** basis set as implemented in the Gaussian 03 program package[145]. Tight convergence criteria with a threshold of 1×10^{-10} ha and a pruned (99,590) grid were used. The geometry optimizations were done using the GDIIS algorithm. For both diazirines the geometry of the neutral and the ionic ground state was computed. The vibrational frequencies of the two *neutral* diazirines are listed in table 5. These were used to calculate the

Table 5: Vibrational wavenumbers [cm^{-1}] of the diazirines. Left side: CPC-N$_2$, right side: TFPC-N$_2$

3210.4	3199.3	3189.4	3214.9	3201.0	3190.4	3179.0
3178.0	3168.3	1689.2	3169.3	1732.6	1645.3	1618.9
1641.7	1618.0	1527.4	1534.6	1480.4	1378.2	1337.4
1476.5	1363.7	1326.7	1326.3	1228.5	1225.2	1189.2
1267.7	1215.8	1186.8	1161.7	1130.4	1125.2	1076.8
1118.7	1065.8	1038.3	1052.5	1014.2	1008.6	987.4
1014.0	1009.9	990.5	942.9	938.4	888.5	850.2
942.7	902.0	900.2	776.9	738.8	710.1	658.7
852.0	782.3	711.0	633.2	607.4	567.5	547.3
675.3	632.8	561.4	447.3	447.3	415.5	378.8
453.3	417.0	414.5	332.4	319.5	263.2	237.7
394.1	372.1	293.6	138.3	131.1	65.2	28.0
180.7	141.9	30.8				

density of states of the neutral molecule needed for analyzing the AE of the fragments according to the method of *Asher*[3].

---

[3] Note that the vibrational frequencies of the diazirines have to be taken in this model[141] and not those of the cationic species. The internal energy distribution of the neutral is transposed into the ion and shifts the AE.

The HOMO of the diazirines was found to extend over the entire molecule, including the N=N double bond of the nitrogen ring as well as the phenyl ring and is presented in figure 46. The HOMO and
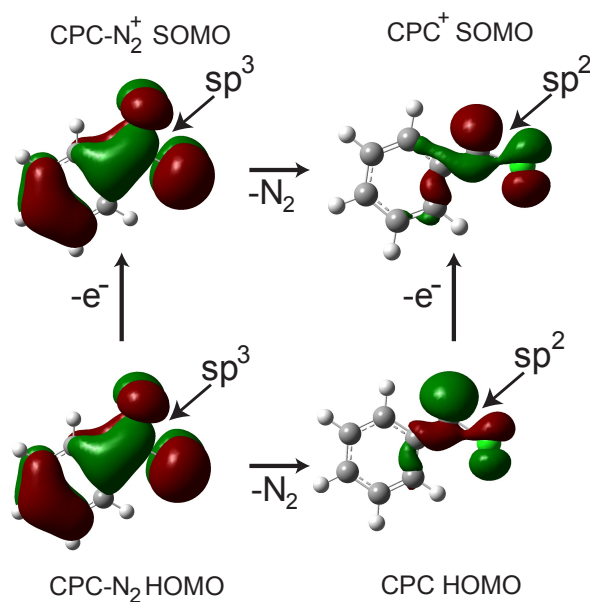
Figure 46: The HOMO and SOMO of CPC-N_2 and CPC-N_2^+ are similar and the same holds for CPC and CPC$^+$. Analog observations were made for the TFPC case. The reactivity of the neutral is also reflected by the cationic species.
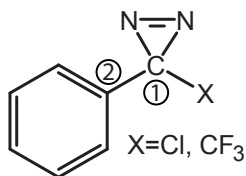
Figure 47: Definition of C1 and C2

SOMO of CPC-N_2 and CPC-N_2^+ have a similar appearance. Same holds for the corresponding fragments CPC and CPC$^+$. Similar observations were also made when calculating TFPC (R=CF_3). Hence the reactivity pattern of neutral diazirines is also found in the cationic species as will be discussed later.

Important geometrical parameters of the diazirines (explained in fig. 47) and their corresponding ions are given in table 6. The table includes parameters that show the strongest change in geometry upon

Table 6: Geometric parameters with strong change upon ionization.

	CPC-N_2	CPC-N_2^+	TFPC-N_2	TFPC-N_2^+
C1-N_2 [Å]	1.46	1.57	1.48	1.56
C1-C2 [Å]	1.49	1.43	1.49	1.43
C1-X [Å]	1.77	1.71	1.51	1.53
N=N [Å]	1.23	1.18	1.22	1.18

ionization and hence are likely to have the highest impact on the photoelectron spectra. In CPC-N_2, the distance (D) between C1 and the N=N moiety increases upon ionization from 1.46 Å to 1.57 Å. In addition D(C1–C2), D(C1–X) and D(N=N) shorten significantly, indicating a tendency to lose the N_2 group. In TFPC-N_2 the same trend is observed. However, the C1–CF_3 bond length increases slightly upon ionization, whereas in CPC-N_2 a decrease in the C1–Cl bond length is predicted.

Figure 48 shows electron density plots of the two diazirines. As already mentioned in the results section, CPC-N_2 and CPC-N_2^+ dissociate more easily than the corresponding trifluoro compounds (TFPC-N_2 and TFPC-N_2^+). This fact can be partially explained by comparing the density plots in fig. 48 as will be discussed below. CPC-N_2 has the highest electron density on the two nitrogen atoms of the diazirine ring. Compared to the Cl group, the CF_3 group in TFPC-N_2 has a much stronger $-I$-effect on carbon C1 and the F atoms carry high charge densities. Crude bond dissociation energies (BDEs) of both diazirines can be estimated by comparing the sum of vibrational and zero point energies of N_2 and the carbenes calculated in chapter 9.4 with those of the corresponding diazirines:

$$CPC\text{-}N_2 \longrightarrow CPC \ + \ N_2 \quad BDE = -21.5\,\text{kJmol}^{-1}$$

$$TFPC\text{-}N_2 \longrightarrow TFPC \ + \ N_2 \quad BDE = -7.6\,\text{kJmol}^{-1}$$

For the corresponding cations (R_2C-N_2^+) the B3LYP calculations predicted dissociation energies for the loss of nitrogen to lie at $BDE^+ = -79.0\,\text{kJmol}^{-1}$ (TFPC-N_2^+) and $BDE^+ = -136\,\text{kJmol}^{-1}$ (CPC-N_2^+), respectively. Note that the dissociation energies of the cations are considerably more exothermic than those obtained for the neutrals. Hence removing one electron from the diazirines destabilizes these systems. However, both parent cations are still predicted as stable molecules with zero imaginary frequencies.

By comparing the sum of vibrational and zero point energy of the diazirines (R-N_2) with their corresponding cations R-N_2^+, a crude estimation of the IP_{ad} can be drawn. The B3LYP calculations yielded an $IP_{ad} = 8.59\,\text{eV}$ for CPC-N_2 and an $IP_{ad} = 8.83\,\text{eV}$ for TFPC-N_2, respectively.

CPC

TFPC

Figure 48: Electron density plot of TFPC-N_2 and CPC-N_2: blue = high density, orange = low density

7.5 DISCUSSION

The comparison of the behavior of TFPC-N_2 and CPC-N_2 upon ionization is interesting and gives insights into the stability of diazirine moieties. *Robinson et al.* have published a conventional photoelectron spectrum[136] of the small 3,H-diazirine (H_2CN_2) and identified numerous ionic states. The much larger CPC, on the other hand, undergoes complete dissociative photoionization directly after the loss of its electron (fig. 42), while for TFPC some molecular ions are formed at the ionization threshold and remain visible beyond 9.5 eV (fig. 41). The hybrid-DFT computations *yielded a stable minimum on the ionic ground state surface* for both of the diazirines$^+$. This is in agreement with the photoion images recorded during the femtosecond experiments with polarized laser light (see fig. 64 on page 80) and to similar images recorded with synchrotron radiation. These are all unpolarized and hence give no evidence of a direct dissociation. The images suggest that the diazirines survive at least one rotational period.

The 3,H-diazirine, known from the literature, loses an electron from a nitrogen lone pair at the lowest ionization energy. In contrast, the HOMO of the phenyldiazirines was computed to extend over the entire molecule (fig. 46) and the ionization process induces a single occupied orbital as depicted in the upper left of fig. 46. Hence the ionization

process proceeds out of a completely different orbital as compared to 3,H-diazirine.

Table 6 gives an overview of several bond lengths that change significantly upon ionization. The C–N bonds are weakened, while the N=N bonding strength increases. Thus nitrogen loss is simplified in the ion and the IP comes energetically closer to the AE in accord with the experimental results. The geometry change upon ionization is larger for CPC-N_2 than for TFPC-N_2. In particular a significant decrease in the C_1–Cl bond length is computed. This gives a reasonable explanation for the immediate dissociative photoionization of the CPC-N_2 compared to the TFPC-N_2. The PEPICO experiments give no evidence of the existence of a stable CPC-N_2^+ cation. Strong geometry changes lead to a strong shift of the cationic and neutral potential energy surfaces. Thus FC factors will only be large at a position of the cation far away from its equilibrium geometry, inducing an excitation into vibrational states well above the zero point energy of the cation (fig. 49 case ② to ④). Hence the FC factors directly have influence on how
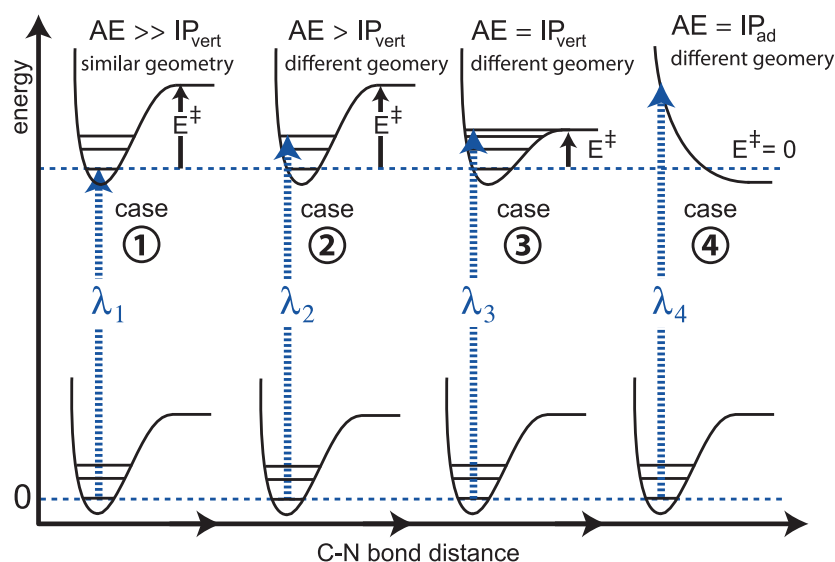
Figure 49: Four different borderline scenarios: ① The geometry of the neutral and cation are similar and the cation has a high activation barrier (E‡); ② geometry of cation and neutral differ, high E‡; ③ geometry of cation and neutral differ, low E‡; ④ E‡ = 0, direct dissociation

much energy is transposed into the ion. Therefore, it can be assumed that for CPC-N_2 sufficiently large Franck-Condon factors exist only for states close to or above the threshold for dissociative ionization.

In TFPC-N_2 the geometry change is not as pronounced. Thus the picture is shifted into the direction of the first border line case in fig. 49 and subsequently some molecular ions can be observed. In addition to the FC factors, the stability of the cation, which is determined by the activation energy (E‡) of the dissociation, has a strong effect on the AE. The higher this barrier is, the more photon energy is needed to observe dissociative photoionization.

There are several arguments that conclude that the TFPC-N_2^+ cation (as well as its neutral) has a higher E‡ than CPC-N_2^+. The first ques-

tion one has to ask in order to qualitatively estimate the value $E^{\ddagger}$ in the cation is: How does the loss of nitrogen proceed mechanically? According to ref. 146 the cleavage of the C–N bonds happens not concerted but in a two-step process over a diradical species in case of a neutral diazirine which is cleaved thermally (scheme 4). It is impor-
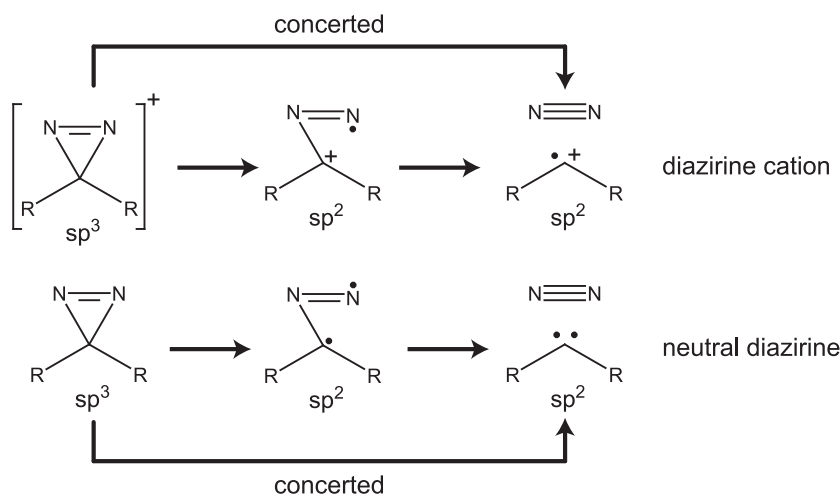
Scheme 4: Upon C–N bond cleavage the diazirine and its corresponding cation are formed sp^2 hybridized. Same argument would hold if the reaction proceeded in a concerted manner.

tant to note that upon opening of the diazirine ring (scheme 4, middle), the carbon C1 will change from a sp^3 to a sp^2 center. In case of the neutral the remaining not-hybridised p orbital at this center will hold the unpaired electron (compare fig. 119 of *t*-butyl in chapter A.5, page 154). In case of the cation the electron will be removed from this orbital. The $E^{\ddagger}$ will depend on how efficiently the functional group of the diazirine (CF_3 vs. Cl) can stabilize this intermediate species, i. e., its transition state (TS)[4]. Even if the reaction would proceed mechanistically in a concerted way, the carbene (and its cation) would also have an sp^2 center at C1 (compare right-hand side of fig. 46). In all cases for the cationic and neutral species, the chlorine atom will stabilize the product as well as the pathway to product formation through its mesomeric effect (fig. 50, +M-effect). Thus it will facilitate the loss of nitrogen by lowering the barrier to dissociation. Such a strong stabilization of the *open valence* sp^2 center can, however, not be performed by the CF_3 group, which in contrast has a very strong electron withdrawing effect (fig. 48). In fact the CF_3 will *de*stabilize the carbocation center. This qualitative approach to understand the different behavior concerning dissociative photoionization of TFPC-N_2^+ and CPC-N_2^+ is in perfect agreement to the neutral species: TFPC-N_2 is relatively stable and has wide applications for photo labeling[29,147], while CPC-N_2 is explosive. The decomposition of neutral diazirines into carbenes and nitrogen also transforms the center from a sp^3 carbon to a sp^2 carbon.

Figure 50: The free electron pairs of Cl stabilize the central vacant p obital of the sp^2 center.

---

[4] Since the *first* C–N bond cleavage will be endothermic in a two-step mechanism (nitrogen is not formed yet) the reaction will have a late TS according to the *Hammond* postulate[123].

Reasonable potential energy surface for TFPC-N$_2^+$:
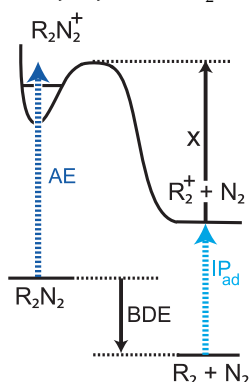
Reasonable potential energy surface for CPC-N$_2^+$:
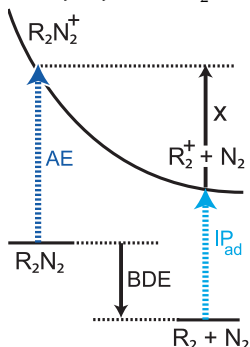
Figure 51: The experiments and calculations conclude that a reverse barrier for TFPC-N$_2^+$ and CPC-N$_2^+$ exists.

The thermodynamic circle in fig. 40 is almost complete using the measured IP$_{ad}$ of chapter 8 for the carbenes and the AEs of the corresponding radical cations presented in fig. 41 and 42 of this chapter. The one missing parameter is either the back barrier of the dissociative photoionization in the cation (X) or the bond dissociation energy (BDE) of the neutral. By taking the calculated B3LYP BDEs of the neutrals, the reverse barriers in the dissociative photoionization step can be estimated[5]:

$$X = AE_{(R_2N, R_2^+)} - \left(BDE_{(R_2N)} + IP_{ad(R_2)} \right)$$

For TFPC-N$_2^+$:

$$X = 9.27\,\text{eV} - (-0.079\,\text{eV} + 8.47\,\text{eV}) = 0.88\,\text{eV} = 84.9\,\text{kJmol}^{-1}$$

For CPC-N$_2^+$:

$$X = 9.1\,\text{eV} - (-0.223\,\text{eV} + 8.15\,\text{eV}) = 1.17\,\text{eV} = 113\,\text{kJmol}^{-1}$$

Note that the reverse barrier does not mean that an activation energy is necessary for the dissociation of the cation. It merely states that energy is needed to reverse the dissociation process in the cation (fig. 51). For CPC-N$_2^+$ the value X is more properly described as the *negative* $-\text{BDE}^+$ of the cation than a true back barrier, since no activation energy exists (fig 51, bottom). Once knowing the reverse barrier in the cation, other parameters of the diazirine cations can be calculated (fig. 40), e.g., the BDE$^+$ of the diazirine cation. The difference between the back barrier X and the BDE$^+$ of the diazirine cation consists only in the activation energy E‡ for the dissociation of the cation (compare fig. 40 and 49). E‡ can be estimated by taking the difference of the adiabatic IP measured for the diazirine and the appearance energy of the fragment. Since no parent signal was measurable for CPC-N$_2$, the value for E‡ will be approximately $\approx 0\,\text{kJmol}^{-1}$ and the bond dissociation energy[6] can be estimated to lie at around $-113\,\text{kJmol}^{-1}$ (case 4, fig. 49 and bottom trace of fig. 51). Note that an activation energy of precisely $0\,\text{kJmol}^{-1}$ contradicts the B3LYP calculations, since the CPC-N$_2^+$ cation was predicted as a stable species with zero imaginary frequencies. However, the energy surface might be very shallow and lie between case 3 and 4 of fig. 49; hence no parent is visible in the mass spectrum. Further experimental evidence of a small E‡ is given by the unpolarized photoion images (fig. 64, page 80), which indicate that a direct dissociation on the cationic potential energy surface does not take place and suggests that a dissociation proceeds over a metastable state with an (presumably very small) activation barrier.

For TFPC-N$_2$ the difference between its IP$_{ad}$ and the AE of the TFPC$^+$ fragment is difficult to determine, since a fit according to *Asher* was only possible for the fragment and both the fragment and the mother appear at the same photon energy. However, extrapolating the TFPC-N$_2^+$ in a *Wannier*-type fitting procedure (compare chapter 8,

---

[5] A positive X means energy is needed to reverse the dissociation reaction in the cation from the point of view of the products. [6] A negative BDE means that heat is released upon dissociation from the point of view of the reactant (exothermic reaction). The BDE should not be confused with the activation energy E‡.

page) yields an $IP_{ad} \approx 9.05\,eV$. Hence $E^{\ddagger} = AE_{(R_2N,\,R_2^+)} - IP_{ad(R_2N)}$ will lie between 0–0.2 eV ($< 19\,kJmol^{-1}$). Over the relation:

$$E^{\ddagger} = BDE^+ + X = AE_{(R_2N,\,R_2^+)} - IP_{ad(R_2N)}$$

a bond dissociation energy in the cation of $BDE^+ < -65.9\,kJmol^{-1}$ can be extracted. This is in agreement with the B3LYP calculations for the cation. The determination of $E^{\ddagger}$ of the TFPC-N_2^+ dissociation depends on a correct value for the IP_{ad}. Since the $TFPC^+$ is always visible simultaneously to its parent, the value for $E^{\ddagger}$ will be very low if present and an assignment of an IP_{ad} is not straightforward. As was done for CPC, taking an $E^{\ddagger}$ of $0\,kJmol^{-1}$ for the TFPC-N_2^+ yields a lower limit for the BDE^+ of $-84.9\,kJmol^{-1}$ *in the cation*.

An explanation why the parent (TFPC-N_2^+) is visible in contrast to CPC-N_2^+ is the formation of a metastable cation. Hence even though some of the parent cations are stable during the drift towards the detector, it is just a question of time before they dissociate by an accumulation of enough energy in the critical C–N mode. This scenario also could move TFPC-N_2^+ closer from case 3 to case 4 in figure and the calculated lower-limit BDE^+ has to be taken. Under the assumption that the B3LYP predicted BDEs for the neutrals are afflicted with only a small error as compared to the radical cations, the B3LYP functional predicts the trends correctly but slightly overestimated the BDEs of the cation.

As a conclusion it can be said that the reactivity of the diazirine cations has a similar functional group dependence as the neutral diazirines and can be explained by the same qualitative chemical intuition. However, upon ionization the reactivity increases significantly and the loss of nitrogen is facilitated.

8

PHOTOIONIZATION STUDIES OF
PHENYLCARBENES

For the interpretation of the time-resolved photoelectron spectra in the forthcoming chapter 9, which presents femtosecond studies of phenylcarbenes, it was of utmost importance to know the ionization potentials (IPs) of chlorophenylcarbene (CPC) and trifluoromethylphenylcarbene (TFPC). These are depicted in fig. 52. The determination of chemically exact ionization potentials for reactive intermediates by high level of quantum chemical (q. c.) theory is still limited to small molecular entities[70]. Hence an experimental approach was chosen. This chapter shows experimental studies on the photoionization of TFPC and CPC employing synchrotron radiation, which permitted a determination of the vertical as well as adiabatic IPs. These measurements in turn can serve as benchmark values for future q. c. approaches, since carbenes are referred to as testing grounds for computational chemistry[11]. Additionally, ionization potentials are very useful to derive other thermochemical properties such as dissociation energies (BDE) and heats of formations as was discussed in chapter 7 on the example of the corresponding precursors.

chlorophenylcarbene (CPC)

trifluoromethylphenylcarbene (TFPC)
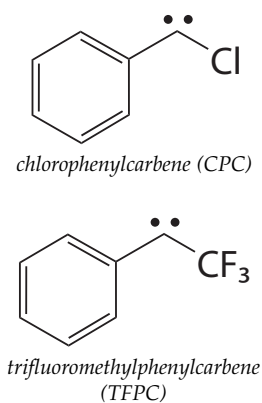
Figure 52: CPC & TFPC

8.1 EXPERIMENTAL DETAILS

The measurements were performed at the storage ring *Soleil* in France. The setup was described in chapter 3.5 in more detail. PEPICO as well as TPEPICO spectra (chapter 2.5) were recorded together with conventional photoelectron spectra via VMI. Free carbenes were produced from diazirine compounds (fig. 39, page 53) according to the reaction illustrated in scheme 5 on page 76. In contrast to the laser experiments, a continuous molecular beam was used. The electrodes of the pyrolysis source were 1–2 mm apart and the tube was only weakly heated, which was sufficient for a full conversion of the diazirines. As will be fully discussed in chapter 9.3.1 and is demonstrated in fig. 64 on page 80, the conversion efficiency of the pyrolysis could be monitored by the VMI spectrometer also using synchrotron radiation.

8.2 EXPERIMENTAL RESULTS

Mass spectra of the precursors, recorded at photon energies above the ionization threshold, are presented in figures 53 and 54. Figure 53 shows mass spectra of TFPC-N$_2$ recorded at a photon energy of 9.2 eV. With pyrolysis off (upper trace) an intense peak of the diazirine precursor ($m/z = 186$) is visible. At this photon energy dissociative photoionization is already partially occurring as shown by the signal at $m/z = 158$, which corresponds to the ionized carbene fragment TFPC$^+$. The small signal at $m/z = 372$ is attributed to a weakly bound diazirine dimer which shows that the temperature in the beam is sufficiently low to permit cluster formation. The mass signal at $m/z = 40$
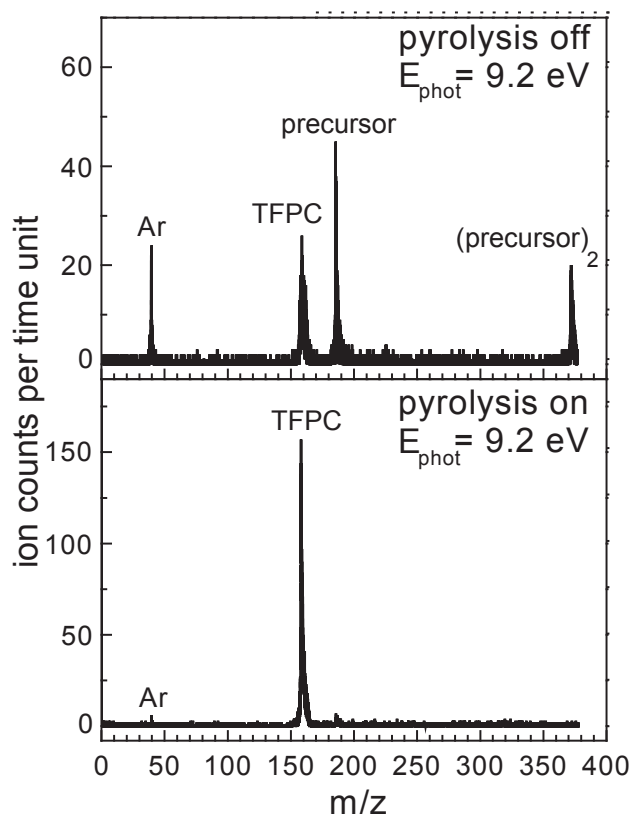
Figure 53: Mass spectra of TFPC-N$_2$ recorded at different conditions with a photon energy of 9.2 eV.

is assigned to argon, since some second harmonic radiation, which was not completely absorbed by the gas filter, was still present (see fig. 20 on page 23). Hence this mass served as a reference for calibration. When the pyrolysis is turned on (lower trace), the carbene signal increases strongly and dominates the mass spectrum. Note the different ordinate scale in the two traces of figure 53. The conversion of the diazirine precursor is nearly quantitative and no side products are formed.

The mass spectra in figure 54 were taken with the second precursor (CPC-N$_2$) seeded in the molecular beam. However, the signal-to-noise ratio is significantly lower than in the case of TFPC due to a shorter acquisition time[1]. In contrast to TFPC-N$_2$, no precursor signal is visible for CPC-N$_2$ in the mass spectra despite the pyrolysis source being turned off (upper trace). The mass of the ionized carbene ($m/z = 124$) immediately appears already at 8.85 eV and strongly increases when moving to higher photon energy 9.10 eV. This indicates that CPC-N$_2$ shows direct dissociative photoionization, forming CPC$^+$. When the pyrolysis is turned on, an additional signal at mass $m/z = 41$ appears which is attributed to allyl, $C_3H_5^+$. The allyl signal is formed from residual C_3H_5I still present in the beam. It had been used in preceding calibration experiments and can be used for mass and VUV energy calibration[53]. The small signal appearing at $m/z = 89$ corresponds to

---

[1] It was the last day of our run at the synchrotron.
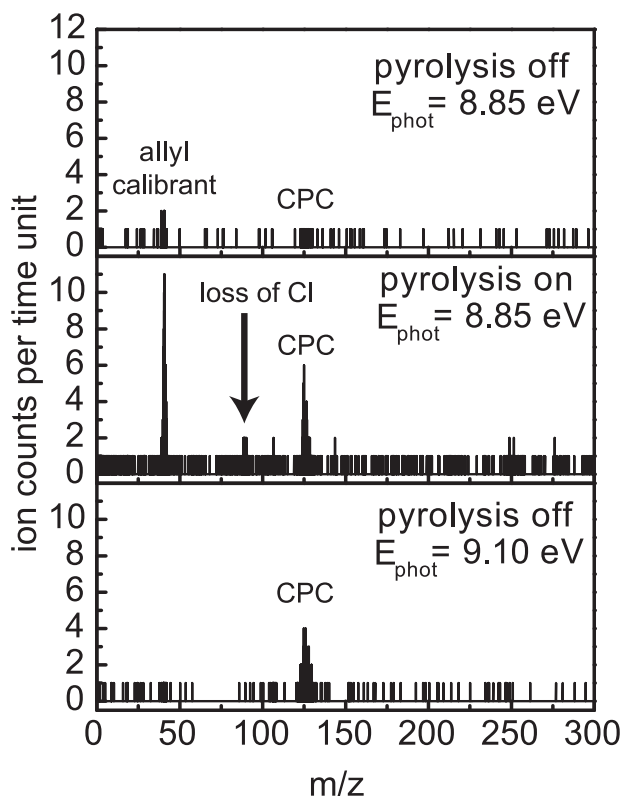
Figure 54: Mass spectra of CPC-N_2 recorded at different conditions with a photon energy of 8.85 eV and 9.10 eV.

$C_7H_5^+$, which is formed from CPC by the loss of a Cl atom. This side product is likely to be formed in the pyrolysis and does not originate from dissociative photoionization of the precursor. The same signal was detectable in the femtosecond laser experiments in chapter 9. Due to an insufficient signal-to-noise ratio it was not possible to extract conclusive PEPICO spectra from this mass channel.

To differentiate between pyrolytically produced carbenes and those originating from dissociative photoionization, several additional control experiments were performed on the diazirines with the pyrolysis source turned off. These results were already presented in chapter 7, which also discussed the dissociative photoionization of diazirines. Additionally, photoion images showed that with pyrolysis off, the velocity distribution of the CPC^+ signal was broad as will be discussed in detail for the femtosecond experiments (forthcoming chapter). This enables to draw conclusions on the origin of the ions.

From static velocity map images recorded at a fixed photon energy, conventional photoelectron spectra can be calculated as was described in chapter 2.3. Note that the synchrotron experiments were performed by measuring coincidences of ions and electrons. Hence the recorded photoelectron spectra are "mass selected" and can be recorded even if side products or molecules for calibration (such as allyl) are present in the beam. Figure 55 depicts the static photoelectron spectrum of the TFPC. It was recorded with an acquisition time of 22.5 min. No anisotropies were visible in the static photoelectron image. Hence it

was processed using the pBASEX method with a P0 basis set expansion as was described in chapter 2.3.1; this basis set averages over all angles and converts the image into a conventional photoelectron spectrum with no angular information. The vertical ionization potential can be derived from the maximum intensity of the spectrum ($IP_{vert} = 8.95 \pm 0.05$ eV). The spectrum was also compared to a FC
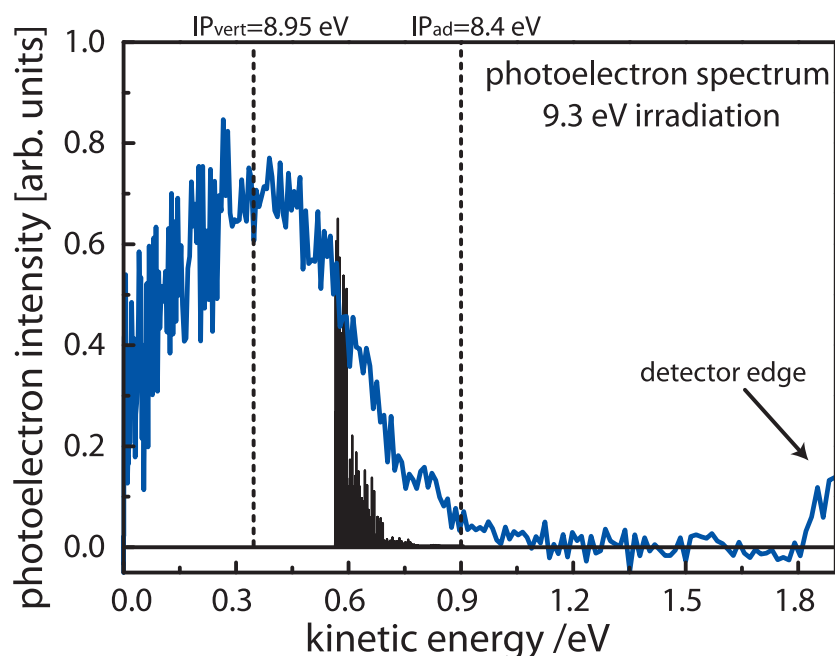
Figure 55: Conventional PES of TFPC. The Spectrum is compared to a FC simulation in the region of the adiabatic IP.

simulation[2] in the region of the adiabatic IP and is depicted in fig. 55 in black as a stick diagram. A FC simulation can help to identify the adiabatic IP[148]. The parameters needed for the simulation, such as Hessians, equilibrium geometries and vibrational frequencies of the adiabatic cation and the neutral, were taken from B3LYP/6-311^{++}G** computations. The prediction of the stick spectrum was only possible in a relatively small energy window at a reasonable computational cost because of the very high density of transitions[3]. The simulation hence explains why no vibrational resolution could be resolved in the spectrum. Due to presence of several low frequency modes and combination bands and the finite vibrational temperature, a resolution of the vibrational structure was not possible. Thus even though the resolution of the PEPICO spectra was not at the limit of the used monochromator, it is unlikely that vibrational resolution could have been achieved by taking smaller steps in the ion yield PEPICO spectra in fig. 56 (and 57a). The simulation also predicted that the main activity is found in the C_1–C_2–CF_3 bending vibration, but in addition other low

---

[2] The software *FCfit 2.7*, programmed by *D. Spangenberg, P. Imhof and S. Schumm* from the university of Düsseldorf/Germany, was used for the simulation. Note that it was not explicitly developed for the simulation of photoelectron spectra and hence some parameters, like how many quanta are allowed, are not straightforward to determine.
[3] Processor: AMD Athlon XP 2000, 1 Gb RAM

frequency modes showed large contributions to the transition probability, including the CF_3 torsion and combinational vibrations. The simulation yielded only very weak transitions up to $0.17\,\text{eV}$ over the true adiabatic IP. Hence the estimated IP_{ad} in fig. 55 has to be taken as a rough approximation, since a measurable photoelectron signal will only arise if the FC factors are large enough. However, since the intermediate was produced in a continuous expansion, the cooling efficiency of the pyrolysis source is known to be weaker than in pulsed mode. Hot bands can mediate the spectrum from ionization out of vibrationally excited neutral molecules. This, on the other hand, would artificially increase the signal intensity before the true IP_{ad} is reached. These two effects might compensate each other. With this measurement an $IP_{ad} = 8.4 \pm 0.2\,\text{eV}$ for TFPC can only roughly be estimated.

A more accurate value for the IP_{ad} of TFPC was obtained from the PEPICO ion yield spectrum given in figure 56. An important point to mention is that at the ionization threshold autoionizing states are easily populated and contribute to the ion signal[149], which leads to an enhancement of the measured signal around the IP_{ad}. Thus an ion signal can often be observed even when the Franck-Condon factors are small in contrast to the conventional photoelectron signal in fig. 55. In the conventional photoelectron spectrum, the photon energy ($9.3\,\text{eV}$) is significantly higher than the ionization energy and autoionizing states close to threshold are not significantly populated.

The ion signal of TFPC in figure 56 was analyzed using the *Wannier-type* threshold law[150,151], which states that the electron (or ion) yield rises nearly linearly in the threshold region of an one-electron photoionization process. Hence a linear interpolation around the threshold is a simple way of distinguishing hot band artifacts in the spectra. These rise exponentially in contrast to the real threshold signal. The least squares fit of the experimental data in the threshold region to a linear equation is indicated by the solid line. Its crossing point with the baseline, marked by an arrow, yields the adiabatic ionization energy $IP_{ad} = 8.47 \pm 0.1\,\text{eV}$. The remaining signal to the left of the line can be assigned to ionization of intermediates which were still vibrationally excited after the expansion. With regard to the size of the molecule, the IP_{ad} obtained from the ion yield spectra is in reasonable agreement with the one derived from the photoelectron spectrum via the FC simulation.

For CPC a static photoelectron image was recorded at $9.5\,\text{eV}$ photon energy. Only electrons arriving in coincidence with CPC^+ are considered. An IP_{vert} of $9.3\,\text{eV}$ can be derived from the photoelectron spectrum (fig. 57b). The signal to noise ratio, however, is considerably lower as for TFPC due to the shorter acquisition time. To derive an adiabatic IP for TFPC, the photoionization efficiency curve was analyzed by applying the *Wannier* threshold law, which is depicted as a solid line in figure 57a. From the crossing of the line, which was obtained in the *Wannier-fit*, with the baseline of the spectrum, an adiabatic ionization potential of $IP_{ad}=8.15\,\text{eV}$ is extracted. The difference between the adiabatic and the vertical ionization energy is thus larger for CPC than for TFPC, indicating an even stronger change in geometry upon ionization.

ⓘ *Near the threshold, the yield σ of photoelectrons from a photoionization process scales with the photon energy E_{phot} according to:*

$$\sigma \propto E_{phot}^{\mu}$$

μ is the threshold index, which is in a zeroth-order picture the number of extracted photoelectrons (n) in the ionization process[150]. This approximation neglects the electron correlation.

$$A + h\nu \rightarrow A^{n+} + ne^- \quad (n \approx \mu)$$
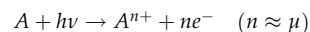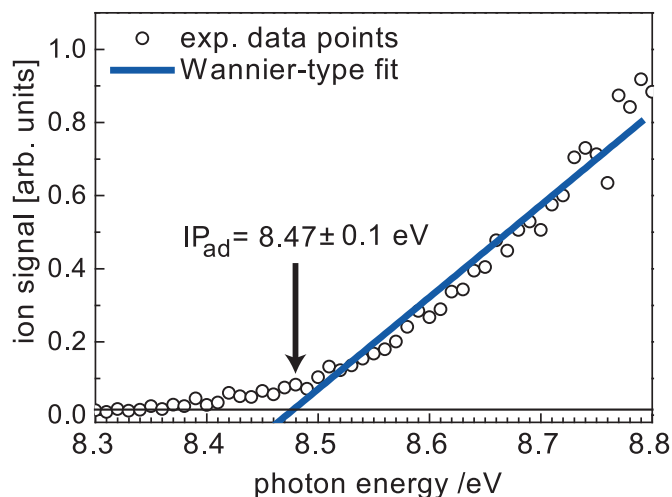
Figure 56: Photoion yield of TFPC obtained by PEPICO spectroscopy. TFPC was produced by pyrolysis of the corresponding diazirine. The adiabatic IP is identified using the *Wannier* law.

(a) Ion yield spectrum of CPC   **(b)** Photoelectron spectrum of CPC
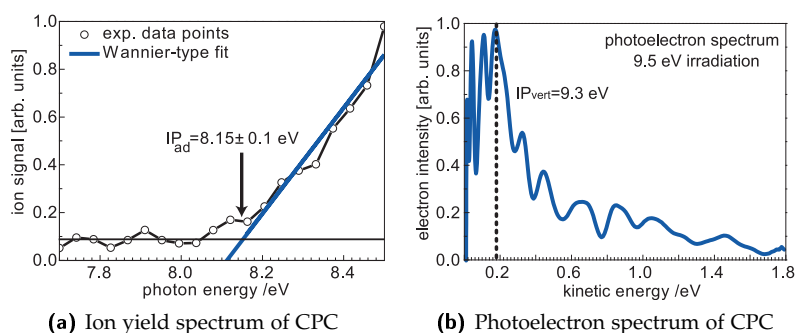
Figure 57: By recording ion yield curves and conventional photoelectron spectra using the PEPICO technology, the IP_{vert} and IP_{ad} of CPC can be measured. The adiabatic IP is identified using the *Wannier* law.

8.3 COMPUTATIONAL RESULTS FOR INTERPRETATION

For aiding the interpretation of the experimental data, simple hybrid density functional theory (DFT) computations were employed using the B3LYP functional with a 6-311^{++}G** basis set. B3LYP is known to give good results for calculations on phenylcarbenes at low cost[152] and showed negligible spin contaminations in the computations. Cs symmetry was found in both neutral and cationic ground state of CPC. TFPC showed a *slight* torsion of the CF$_3$ group out of the mirror plane. However, the torsional barrier of the CF$_3$ group is low and both the radical cation as well as TFPC can be assumed to have an effective Cs symmetry as well. In CPC the highest occupied molecular orbital (HOMO) can be described as a sp^2 orbital at the carbene center[152] (see, e.g., fig. 46 on page 60). In contrast to CPC, the TFPC is found to have a triplet ground state (table 9, page 90). Hence one electron is promoted to a p-like orbital which is stabilized mesomerically by

Table 7: Geometric parameters with strong change upon ionization (phenyl-carbenes).

	CPC	CPC$^+$	TFPC	TFPC$^+$
C$_1$-C$_2$ [Å]	1.45	1.37	1.39	1.35
C$_1$-X [Å]	1.75	1.62	1.46	1.50
C$_1$-C$_2$-X [°]	112.5	137.3	137.5	142.5

the aromatic π system. Upon ionization, the electron is removed from this orbital. The geometric parameters of both carbenes, which show a relatively large change when comparing the equilibrium geometry of the neutral and the corresponding radical cation, are summarized in table 7. Thus these parameters have the largest impact on the shape of the spectra in agreement to the FC simulations. The parameters of table 7 are defined in figure 58. According to the calculations, the geometrical changes of the phenyl group seem to be of minor importance in the photoionization process. The vibrational wavenumber of the C$_1$-C$_2$-X bending mode decreases for CPC from 200.4 cm^{-1} to 144.6 cm^{-1} upon ionization. For TFPC, however, an increase is predicted from 89.1 cm^{-1} to 113.7 cm^{-1}.

Upon removal of an electron, the angle β increases significantly from 112.5° to 137.3° in CPC. In TFPC on the other hand, β increases only from 137.5° to 142.1°. In addition one finds changes in the bond length upon ionization. Both bond lengths C$_1$–C$_2$ and C$_1$–Cl shorten in CPC. This is in contrast to TFPC where the bond length between C$_1$ and the CF$_3$ group increases while the C$_1$–C$_2$ bond length also decreases. Based on the calculations, it is to expect that the C$_1$–C$_2$–X bending vibration has the most influence on the spectra in both species. Due to a distinct change in angle upon ionization, this mode has strong influence on the Franck-Condon factors. Wavenumbers for this mode were computed to lie at 114 and 145 cm^{-1} for the cationic species TFPC$^+$ and CPC$^+$, respectively. There are other low-wavenumber vibrations in both carbenes and cations, but most of them cannot be assigned to a simple bond changes and some incorporate rotational modes of functional groups (e. g., the CF$_3$ group in TFPC). To acquire crude adiabatic ionization energies the zero point energies of the fully optimized structure of the neutral carbene and its cation were subtracted from one another. Additionally, the vertical IPs for both species were approximated by taking the neutral ground state equilibrium structure in a single point calculation for the ion. The computed adiabatic and vertical ionization energies are 7.41 eV and 8.20 eV for CPC and 7.93 eV and 8.15 eV for TFPC. The experimental and theoretical results are summarized in table 8.

The carbocations of both carbenes are radical species. Hence low-lying excited electronic states can be expected as found for almost all hydrocarbon radicals. Simple TD-DFT calculations at B3P86/6-311^{++}G** level of theory predict a number of electronically excited states between roughly 2 and 3 eV above the ionic ground state for both carbenes. However, none of them is energetically low enough to have influence on the spectra in the investigated energy region.
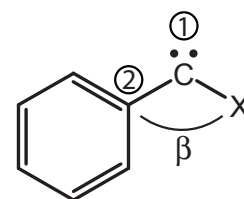
Figure 58: Definition of C$_1$, C$_2$ and β

Table 8: Experimental and calculated adiabatic IPs (vertical IPs in brackets).

	Exp. ±0.1 [eV]	*B3LYP [eV]*
TFPC	*8.47 (8.95)*	*7.93 (8.15)*
CPC	*8.15 (9.3)*	*7.41 (8.20)*

The measurements show that using synchrotron radiation as a broadly tunable VUV light source is ideally suited to investigate the ionization thresholds of reactive intermediates in combination with the pyrolysis source. DFT calculations at B3LYP level of theory underestimate the IP for both carbenes by over 0.5 eV. For this size of molecules, chemical accurate calculations at higher level of theory are still computationally too demanding and can only be performed on smaller carbene species[70]. The measured values for IP_{ad} and IP_{vert} are precise enough to be used for interpreting the time-resolved photoelectron in the femtosecond studies of the forthcoming chapter 9.

The photoelectron spectra are all unstructured and broad in agreement with the high transition density predicted in the qualitative FC simulation and with respect to the strong change in geometry of the carbenes upon ionization. Especially the C1–C2–X angle varies considerably. Since this mode possesses a low vibrational wavenumber and the equilibrium geometries of cation and neutral differ along this coordinate, it is likely to have a strong influence on the spectrum in consistence with the simulation. The change in bond angle is stronger in the case of CPC than for TFPC. This can be understood in terms of the spin multiplicity of the carbenes in their neutral ground state. CPC is a singlet[152,153] carbene and TFPC has a triplet ground state[154] (compare page 89); the corresponding ions, however, are both doublet radical species with similar electronic structure. The distinct change of the C1–C2–X angle can thus be explained in a simple VSEPR model[155] (fig. 59). An electron pair will need more space and reduce the C1–C2–X angle (β) stronger than a single occupied molecular orbital. Consistent with the calculations, this model predicts a smaller β angle in the neutral CPC ground state than for TFPC.

Another strongly changing parameter (table 7) is the C1–C2 bond distance, which shortens in the ion when compared to the neutral. This result can be explained by a delocalization of the positive charge over the aromatic ring, enforcing more double bonding character of the C1–C2 bond. Interestingly, the change in C1–X is opposite in the two carbenes. In CPC the nonbonding electrons of the chlorine atom can interact with the empty p orbital on C1 by mesomerization. This stabilizes the positive charge (see fig. 50, page 63) and leads to an increase of the C1–Cl bond strength as well as a shortening of the bond length. This sort of strong interaction is not possible for the electron withdrawing CF_3 group (compare fig. 48, page 61). The positive partial charge of the carbon in the CF_3 group introduces a repulsion in the cation which cannot be compensated by any hyperconjugative interaction of the C–F bond with the cationic center. This leads to an increased C1–CF_3 bond length.

A smaller difference between IP_{ad} and IP_{vert} was found for TFPC as for CPC. This indicates that the geometry of TFPC changes less strongly upon ionization, which is fully consistent with the B3LYP computations and suggests that the TFPC is indeed formed in a triplet state. The alternation of the C1–C2–X bond angle will not be as big for TFPC as for CPC according to the calculations and the simple VSEPR model when removing an electron. If TFPC would have a singlet ground state the difference between IP_{ad} and IP_{vert} should lie closer to the value measured for CPC.

Figure 59: The angle β depends on the spin state of the carbene ($\beta_s < \beta_t$ according to VSEPR).

ULTRAFAST EXCITED-STATE DYNAMICS OF PHENYLCARBENES

9.1 INTRODUCTION AND STATE OF KNOWLEDGE

This chapter gives insights into the primary photophysical processes of phenylcarbenes after photoexcitation. The excited state deactivation was elucidated by femtosecond time-resolved pump-probe spectroscopy, since little is known about the photochemistry of *isolated* phenylcarbenes[156]. Arylcarbenes play important roles in rearrangements of alkylated aromatic compounds at high temperatures and might be important in industrial cracking processes[157]. Depositing a well-defined amount of energy into the molecule by laser excitation and following the evolving photophysics in real time can help understanding the nature of such rearrangements and physical processes initiating them[1]. The photochemical induced isomerization of CPC to 1-chlorocyclohepta-1,2,4,6-tetraene (CCHT) has been studied by matrix isolation techniques[159]. Femtosecond time-resolved experiments in the liquid phase document the photolysis of diazirines and give detailed insight into the photochemical formation of arylhalocarbenes[160]. But, so far, no information has been available on the primary photophysical processes of isolated arylcarbenes themselves. However, such primary photophysical processes as internal conversion (IC), intersystem crossing (ISC) and relaxation over conical intersections (CIs) initiate almost all photoreactions, and photochemistry rarely takes place from the initially excited state[50]. The elucidation of such processes is thus of considerable importance for understanding phenylcarbene photochemistry.

Whereas CPC has a singlet ground state[152,153], ESR spectra show that TFPC has a triplet ground state[154]. No computational results on the singlet-triplet gap of TFPC were available in the literature yet. DFT calculations, however, predict TFPC to have a triplet ground state (see section 9.4.2 below) in accordance to the experiments. Hence the present chapter explores and compares dynamics on singlet and triplet potential energy surfaces of structurally very similar molecules.

Velocity map imaging (VMI) was used in combination with the pyrolysis source and has proven to be a powerful tool for studying intermediates. It enables to distinguish between pyrolytically generated intermediates and intermediates produced by dissociative photoionization of the precursor, which is an issue that is important for the interpretation of spectroscopic data[161]. The method thus greatly simplifies the optimization of the pyrolysis conditions and seems to be of general interest for efficiently studying reactive intermediates as will be discussed in detail below.

---

[1] Possible thermal and photochemical isomerizations of arylcarbenes directly depend on the substituents at the aryl ring as well as the second substituent linked to the carbene center[158].

The phenylcarbenes were produced from diazirines by supersonic jet flash pyrolysis (compare section 3.1.1). Diazirines are known to be ideal precursors for generating free carbenes[135] and are important compounds for photoaffinity labeling[147]. The diazirines (3-phenyl-3-(trifluoromethyl)diazirine, 3-methyl-3-phenyldiazirine and 3-chloro-3-phenyldiazirine)² were synthesized according to procedures found in the literature[138–140]. The precursor was seeded in 3 bar of argon and expanded through a short, weakly heated silicon carbide (SiC) tube attached to the water cooled solenoid pulsed valve operating at 20 Hz (chapter 3.1.1). Details on the nanosecond and femtosecond laser systems as well as on the apparatus are found in sections 3.3 and 3.4, respectively. In the femtosecond studies the intermediates were excited at 265 nm and ionized with 795 nm in a multiphoton process. For analyzing the time-resolved spectra, good starting values for zero time delay as well as the instrument response function were taken from experiments on C_7H_5 (see figure 68). In the time-delay scans 256 shots were averaged per data point. The time-resolved spectra reported here typically constitute an average of four to five such scans. VMI[38] was used to monitor the kinetic energy distributions of the ions and electrons in real time. The method and the spectrometer were introduced in chapters 2.3 and 3.4.3 in detail.

The REMPI spectra were recorded utilizing the dye laser setup described in section 3.3. For excitation, the unfocused frequency-doubled output of a tunable nanosecond dye laser was used (beam diameter around 0.35 cm). In the nanosecond experiments the carbenes were produced under the same conditions as in the femtosecond experiments.

9.3 EXPERIMENTAL RESULTS

9.3.1 *Clean Phenylcarbene Generation*

Several diazirines with different functional groups were tested for generating the phenylcarbenes (R=CH_3, CF_3, Cl). The pyrolytic generation of the phenylcarbenes is illustrated in scheme 5. The precursors, corresponding to R=Cl and R=CF_3, show full conversion to the carbene already at low pyrolysis temperatures. Only a small amount
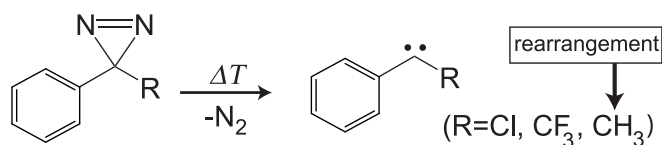
Scheme 5: Carbene generation by supersonic jet flash pyrolysis of diazirines.

of one-color background and negligible quantity of side products are observed in the mass spectra. However, supersonic jet flash pyrolysis was unsuccessful when R=CH_3, as determined experimentally on page 81 below. Typical time-of-flight (TOF) mass spectra obtained in the femtosecond experiments using 3-chloro-3-phenyldiazirine (R=Cl) are depicted in figure 60 at different conditions. The spectrum in the

---

² However, as will be shown below, 3-methyl-3-phenyldiazirine yields styrene rather than the carbene.
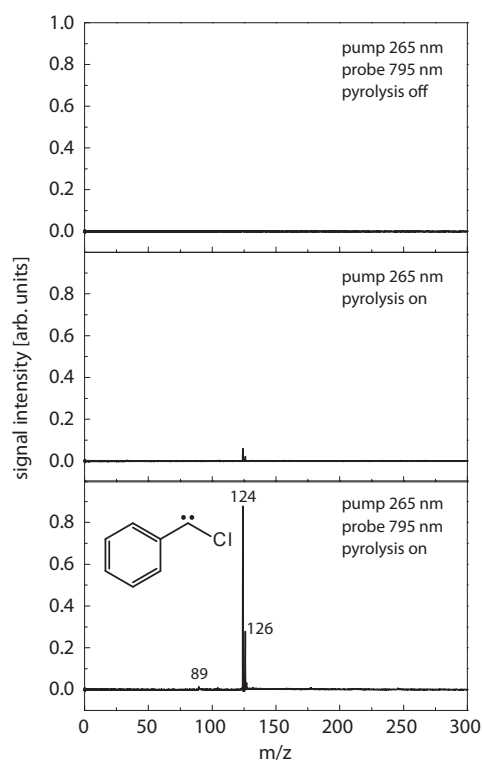
Figure 60: Mass spectra of 3-chloro-3-phenyldiazirine recorded at zero time delay at different conditions. When turning the pyrolysis on, the carbene signal ($m/z = 124/126$) increases strongly (bottom trace). In two-color experiments a strong pump-probe contrast is achieved.

upper trace has been recorded with the pyrolysis source turned off and both excitation (265 nm) and probe (795 nm) laser arriving at around zero time delay. Only when strongly zooming into the mass spectrum (not shown) a negligible signal at the mass of the carbene ($m/z = 124$) was visible under these conditions due to dissociative photoionization (DPI) of the precursor. This observation agrees with the studies on the DPI of diazirines using synchrotron radiation (chapter 7). The amount of fragments originating from DPI depends on the position in the molecular beam pulse. At the leading edge of the pulse only pyrolytically generated carbenes are present and none resulting from dissociative photoionization of the precursor. When turning the pyrolysis on, the carbene signal increases by a factor of 100–1000 (bottom trace), depending on the position in the molecular beam[3]. CPC shows the typical chlorine isotopic distribution ($^{35}Cl/^{37}Cl$: 76%/24%) as well as a small ^{13}C isotopic peak. The center trace is recorded with the pump laser alone. A comparison of the center and bottom trace illustrates the pronounced pump-probe contrast of the CPC signal. Note that the pump laser was attenuated to produce a very small one-color signal, whereas the probe laser was adjusted to give no one-color signal at all in the delay scans. The second product of the pyrolysis is N_2, which

---

[3] At the leading edge of the molecular beam pulse, the conversion efficiency is nearly 100%

is neither excited nor ionized at the chosen wavelengths. Experiments using the second harmonic of the Ti:Sa laser (398 nm) as probe wavelength did not result in a sufficient pump-probe contrast. A very small signal is also present at $m/z = 89$. The time dependence of this mass signal, corresponding to C_7H_5, is different from the time dependence of CPC as will be discussed below. The mass spectra of 3-phenyl-3-
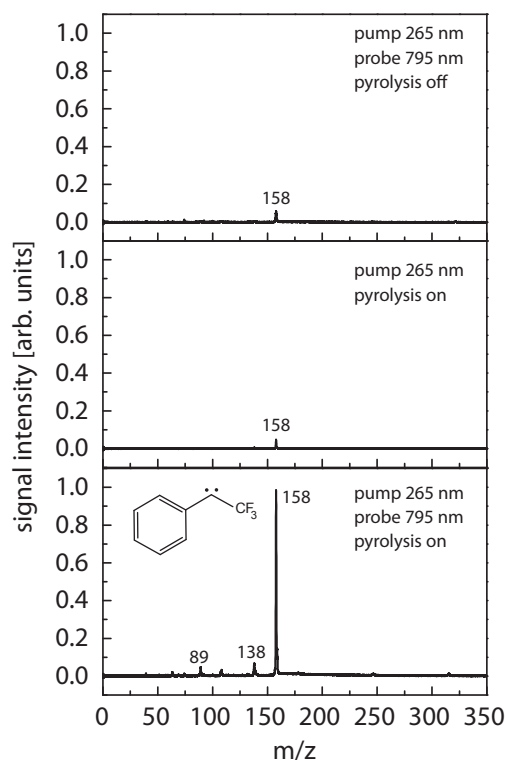
Figure 61: Mass spectra of 3-phenyl-3-(trifluoromethyl)diazirine recorded at zero time delay at different conditions. When turning the pyrolysis on, the carbene signal ($m/z = 158$) increases strongly (bottom trace). With two colors, a pronounced pump-probe contrast is achieved.

(trifluoromethyl)diazirine (R=CF$_3$) are presented in fig. 61. Again the diazirine is cleaved efficiently at low pyrolysis temperatures. Similarly clean spectra were also obtained using the nanosecond setup for the REMPI experiments as well as for control experiments with 118 nm VUV light (not depicted). When turning the pyrolysis on, the carbene signal ($m/z = 158$) increases by a factor of 10. Adding the probe laser induces a significant pump-probe contrast as visible in the bottom trace of fig. 61. For the pump-probe experiments the laser power of the 795-nm probe was attenuated to give no one-color signal in the TOF-MS. The fragments with $m/z = 138$ and $m/z = 89$ correspond to the loss of HF and CF$_3$, respectively. Both masses show the same time dependence and thus originate from dissociative photoionization, which is discussed in more detail below (see fig. 70). This fragmentation pattern is presumably linked to the multiphoton probe step and was not observed in one-color VUV experiments when applying synchrotron radiation up to 9.5 eV [162].

A [1+1]-REMPI spectrum was recorded for TFPC using the tunable nanosecond dye laser setup and a resolution of $4\,cm^{-1}$. Due to the large region of the scan, three different laser dyes were used and the spectrum was merged together from three successive scans. A three point smooth was applied in between 36000–38500 cm^{-1}, and a six point smooth was used above 38500 cm^{-1} because of the lower signal-to-noise ratio in this region. The spectrum is presented in fig. 62 and shows two broad and unstructured bands. The first band is peaked at 36650 cm^{-1} and a second weaker band is peaked at around 41140 cm^{-1}. For CPC, all attempts to record a [1+1]-REMPI spectrum using the nanosecond dye laser setup failed. As visible TFPC absorbs strongly at 265 nm, allowing femtosecond pump-probe experiments using the Ti:Sa third harmonic for excitation of TFPC. The recorded REMPI spec-
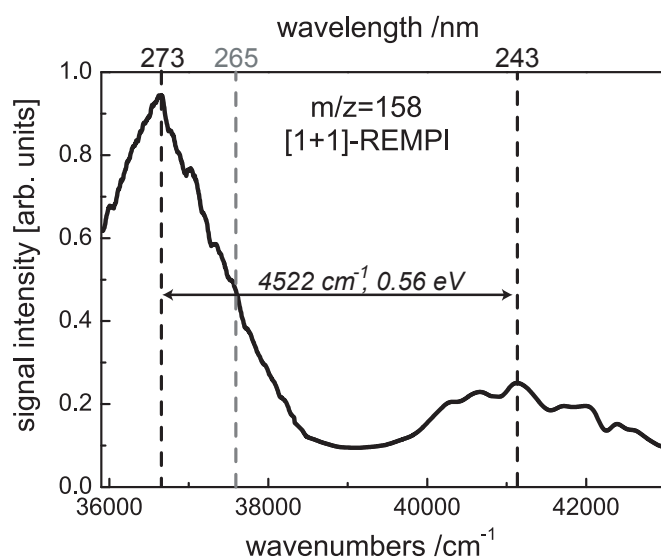
Figure 62: REMPI spectrum of TFPC recorded using a nanosecond dye laser setup.

trum of TFPC has similarities to the UV/VIS spectrum recorded in matrix experiments[163] of a closely related phenylcarbene (TFPC-COOH), which was produced by the irradiation of 4-(1-azi-2,2,2-trifluoroethyl)-benzoic acid (ATEBA). The two carbenes only differ in the presence of a COOH group at the aryl ring. No UV/Vis absorption spectrum of TFPC is available in the literature. The REMPI spectrum of TFPC has a strong absorption band at 36650 cm^{-1} and a second weaker band is peaked at around 41140 cm^{-1}. A strong absorption around 36000 cm^{-1} seems to be characteristic for trifluoromethylphenylcarbene entities, since the UV/Vis absorption spectrum obtained after irradiation of ATEBA in ethanol[163] shows an intense band at 35714 cm^{-1}. This band of the corresponding carbene (TFPC-COOH) is red shifted compared to TFPC due to the presence of a -COOH group. The weaker band of TFPC appearing at 41136 cm^{-1} in the REMPI spectrum is not visible in the UV/Vis spectrum of TFPC-COOH reported in the literature, since it is superposed by a much stronger absorption band of the remaining ATEBA precursor in this spectral region.

intensity 500 arb. units

beam direction

pyrolysis off

zoom x 100

intensity 500 arb. units

beam direction

HOT

carbenes from dissociative photoionization

pyrolysis off

$m/z = 124$

beam direction

COLD

pyrolytically generated carbenes

pyrolysis on

intensity 50 000 arb. units

zoom x 100

beam direction

detector saturation

pyrolysis on

intensity 50 000 arb. units
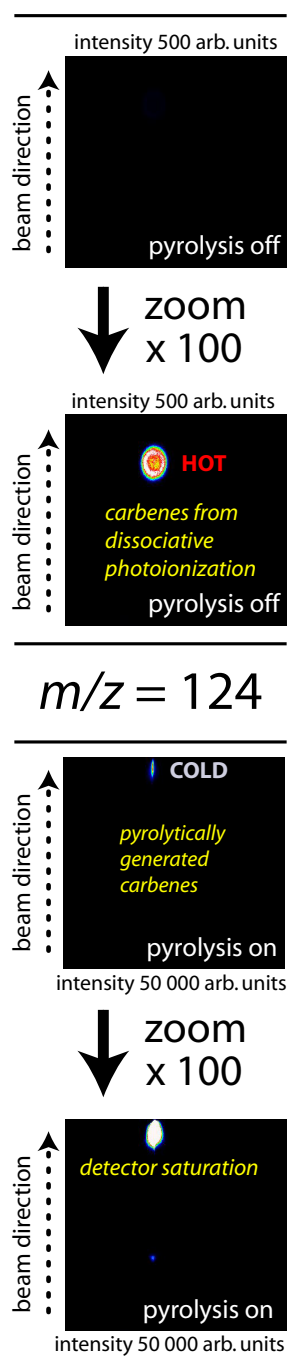
Figure 63: Photoion images at different conditions

As a second detection method, photoion imaging was applied. In contrast to conventional TOF mass spectrometry, this mass selective method does not only register the different ion masses but also at which position they collide with the detector. Thus particles with higher kinetic energy will hit the detector on a bigger radius. By processing the raw images via the pBASEX algorithm, the kinetic energy distribution of the particles is accessible (for details refer to chapter 2.3). Typical photoion images of 3-chloro-3-phenyldiazirine, which was irradiated by 265 nm only (150 μJ), are depicted in fig. 63 and 64. Note that these images were recorded later in the molecular beam as compared to the TOF spectra in fig. 60 and the laser power at 265 nm was considerably higher than in the pump-probe experiments. Later in the molecular beam, the concentration of diazirines is higher, whereas the maximum concentration of pyrolytically generated intermediates is found at the leading edge of the gas pulse. When the pyrolysis is turned off, the 3-chloro-3-phenyldiazirine yields a ring of fragments at the mass of the CPC ($m/z = 124$, left) in the images. The corresponding kinetic energy distribution of these fragments is peaked at 90 meV. Their energy distribution and the corresponding raw image (inset) are presented in fig. 64. The comparison with the synchrotron
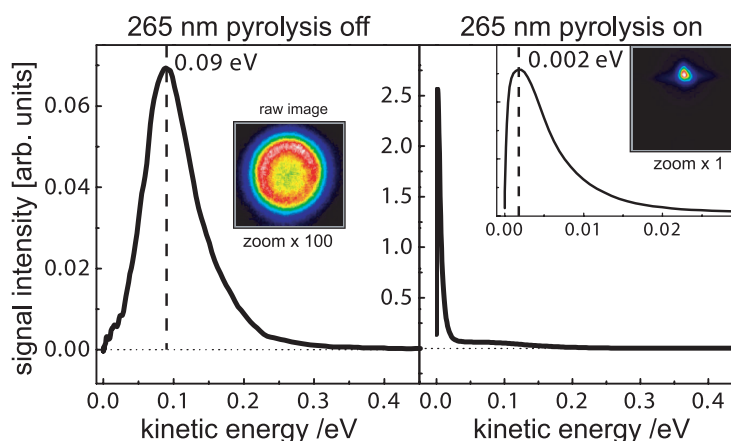
Figure 64: Kinetic energy distributions of the carbene ions ($m/z = 124$) with pyrolysis source off (left) and on (right) recorded by VMI. The raw images are depicted as insets. The intensity of the signal strongly increases with pyrolysis on and the kinetic energy distribution becomes very narrow (note the same x-axis scale). The magnified kinetic energy distribution with pyrolysis on (0.00 eV–0.03 eV) is given as inset in the upper right corner.

experiments presented in chapter 7 and 8 proves that the fragments are formed by dissociative photoionization of the precursor by two 265 nm photons[162]. The VUV synchrotron measurements show that dissociative photoionization of CPC-N_2 is visible above > 8.8 eV. Because of the excess energy (≈ 0.56 eV) of 2×265 nm photons deposited into the precursor and the presumably exergonic bond dissociation energy of the diazirine cation, it dissociates upon ionization into nitrogen and CPC$^+$ with considerable kinetic energy despite CPC$^+$ being the heavier fragment. When turning the pyrolysis on, the ring continuously fades out and an intense spot appears at the same mass ($m/z = 124$, CPC). These particles have a higher velocity in the direction of the mo-

lecular beam (fig. 64, right) and a very narrow kinetic energy spread with its maximum peaked at 2 meV. A magnified plot of the narrow energy distribution is shown as an inset on the right-hand side of fig. 64 together with the raw image. These ions are no longer produced by dissociative photoionization of the precursor in the ionization region but by a [1+1]-REMPI process of pyrolytically generated carbenes in the beam. Thus by monitoring the speed distribution of the ions as a function of the pyrolysis temperature, the conditions of intermediate generation can easily be optimized. The method allows distinguishing between carbenes originating from the pyrolysis source (spot) and carbenes formed by dissociative photoionization (or photodissociation) of the precursor (ring). This simplifies the interpretation of spectroscopic data, since dissociative photoionization or photodissociation processes, which lead to fragments, can safely be discriminated from intermediates originating from the pyrolysis source. Similar observations were made when using 3-phenyl-3-(trifluoromethyl)diazirine (R=CF$_3$) and 3-methyl-3-phenyldiazirine (R=CH$_3$). Hence optimization of the TFPC generation (and 3-methyl-3-phenyldiazirine dissociation) can be done in the same way.
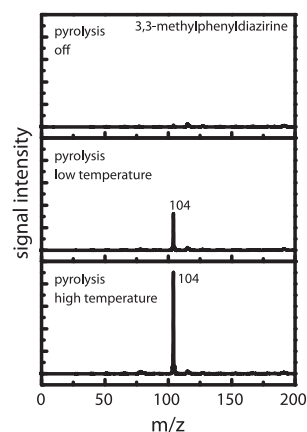
Figure 65: TOF mass spectra of 3-methyl-3-phenyldiazirine at different pyrolysis conditions recorded with the nanosecond laser setup at 35715 cm^{-1}.
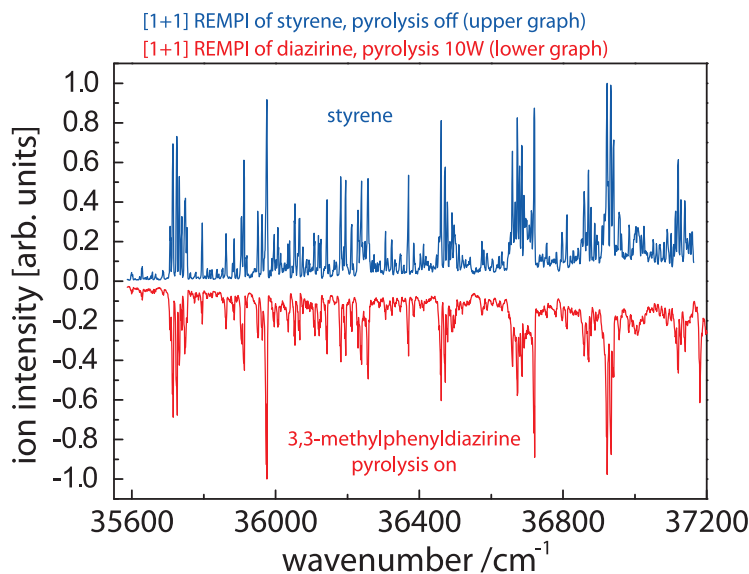
Figure 66: [1+1] REMPI of authentic styrene compared to the pyrolysis product of 3-methyl-3-phenylcarbene. Pyrolysis of 3-methyl-3-phenyldiazirine produces styrene in high concentrations.

REMPI spectroscopy was performed to experimentally determine the absorption spectrum of the product obtained by supersonic jet flash pyrolysis of 3-methyl-3-phenyldiazirine (TOF mass spectra in fig. 65). The result is presented in figure 66 (bottom trace) and compared to the spectrum obtained when using authentic styrene (upper trace). Between 35600 cm^{-1} and 36000 cm^{-1} the REMPI spectrum of styrene shows the same structure that was also acquired by fluorescence spectroscopy reported in the literature[164]. The REMPI spectrum augments it up to 37200 cm^{-1}. The experiment shows that styrene has a major contribution in the molecular beam. Hence a barrier of

only 31 kJmol^{-1} (see computational section) is insufficient to generate a clean beam of MPC. This control experiment also proves that jet flash pyrolysis produces a vibrationally cold molecular beam using diazirines. Further experiments using deuterated 3-methyl-3-phenyl-diazirine (R=CD$_3$) showed no conclusive evidence of deuterated MPC in the beam (see fig. 67), which is known to have a higher barrier towards isomerization as compared to non-deuterated MPC[165] due to a reduced possibility of tunneling.

(a) TOF mass spectra   **(b)** Pump-probe signals
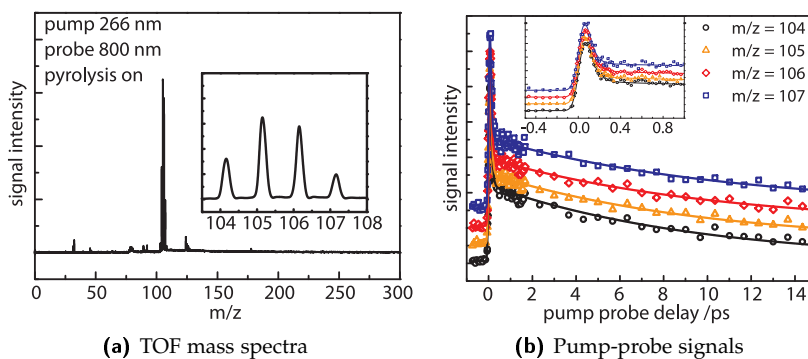
Figure 67: TOF mass spectra of partially deuterated 3-methyl-3-phenyldiazi-rine (R=CH3,CDH2,CD2H,CD3) at different pyrolysis conditions using femto-second lasers (left). The synthesis yielded a mixture of all four combinations of deuteration at the methyl group. In the time-resolved pump-probe experiments (right) all four peaks showed the same excited-state dynamics already known from authentic styrene in ref. 166.

9.3.2 *Time-Resolved Measurements*

Three different experimental techniques were used to elucidate the excited-state dynamics of the phenylcarbenes:

1. measurements of the time-dependent ion signal by TOF-MS

2. time-resolved ion imaging

3. time-resolved photoelectron imaging

After optimization of the pyrolysis source, methods (1) and (2) yielded identical results.

The ionization potential (IP) of the CPC is low, and the excited states form a dense band between 3.9 and 6 eV[152]. Thus elucidating the primary photophysical processes of the 3 $^1A'$ state with a single probe photon is unlikely to yield sufficient pump-probe contrast because the photons of pump (265 nm) and probe would lie energetically too close. For example, in a [1+1'] process a 275-nm probe would be necessary to reach the IP. Thus the available 795 nm were used in a multiphoton probe step. A probing wavelength of 795 nm gave a good alternative and produced a very strong two-color contrast. However, due to the large density of excited states of arylcarbenes, applying a multiphoton probe can lead to photoelectron spectra which are mediated by intermediate resonances and can sophisticate their interpretation[167–169].

Typical mass selected delay scans obtained for CPC and TFPC are depicted in figure 68 and figure 70, respectively (both lower trace). The
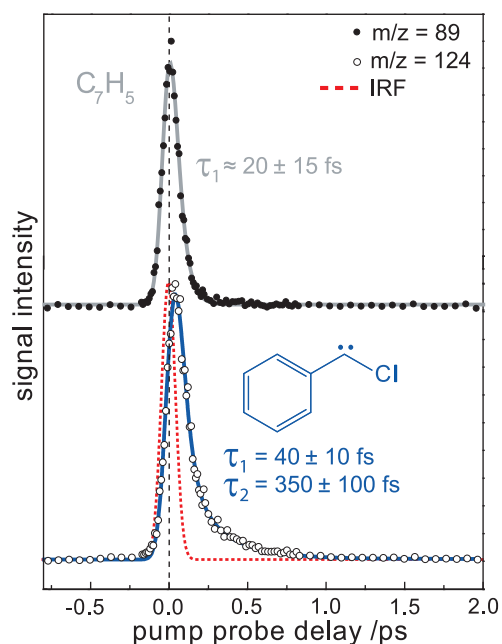
Figure 68: Ion signal of CPC (R=Cl, lower trace) and C_7H_5 (top trace) as a function of the time delay (pump 265 nm, probe 795 nm). The signal is described by a two-step decay for CPC, whereas the C_7H_5 can be described by a monoexponential decay. The IRF is presented as a dotted red line.

carbene signals are compared with delay curves of other fragments present in small quantities in the mass spectra (upper traces). The time-dependent ion signals of both carbenes indicate a two-step decay. Hence a two-step molecular response function was convoluted by a Gaussian shaped instrument response function (FWHM=105 fs for CPC, 95 fs for TFPC) to describe the spectra. The IRF was optimized in a global fitting procedure. Dynamic models were fitted simultaneously to both delay scans shown in figure 68. The zero time delay and the FWHM of the laser cross correlation was shared in this procedure. The model for CPC reflects a two-step deactivation process between three states (I $\rightarrow$ II $\rightarrow$ III) as was described in chapter 5.3 [95]. Both signals apparently decay to zero at long time, suggesting that state III is not efficiently ionizable in the probe step using 795-nm photons. Hence the experimental time-resolved ion signal was described by a linear combination of $S_{(t)}^A$ and $S_{(t)}^B$ derived in equation 5.13 on page 38. $S_{(t)}^A$ describes the monoexponential decay of state I with a time constant of τ_1, and $S_{(t)}^B$ describes the monoexponential rise (τ_1) and monoexponential decay (τ_2) of state II. Hence the mass-resolved spectra reveal that both carbenes show an ultrafast initial relaxation process in the order of $\tau_1 = 30$–70 fs, followed by a second relaxation process, which is about ten times slower. However, as will be described below, two time constants are not sufficient to describe the complete dynamics of CPC.

Figure 69: Mesomeric structures of phenylcarbyne

When recording the time-resolved spectra for CPC a small mass peak was present at $m/z = 89$ (C_7H_5). Its time dependence is presented in the top trace of figure 68 and differs strongly from the signal of CPC. The time dependence is adequately described by a single exponential convoluted with the IRF (state I to state II model, chapter 5.2). The state lifetime was measured to lie around 20 fs. Due to the difference in dynamics, it is likely that this species is formed from CPC during pyrolysis by an irreversible loss of Cl· and not due to dissociative photoionization from CPC. It might correspond to phenylcarbyne (fig. 69), which is formed upon C–Cl bond cleavage in CPC. However, several minima on the ground state potential energy surface of C_7H_5 are known in the literature from quantum chemical calculations[170]. It is thus not clear which of these isomers is generated by the pyrolysis, and due to the small signal size it is not considered in the discussion of the photoelectron spectra below.

In contrast to CPC, the small mass peaks observed at $m/z = 89$ and $m/z = 138$ while studying TFPC (fig. 61) show the exact same time-dependent signal as was found for TFPC. The mass channels
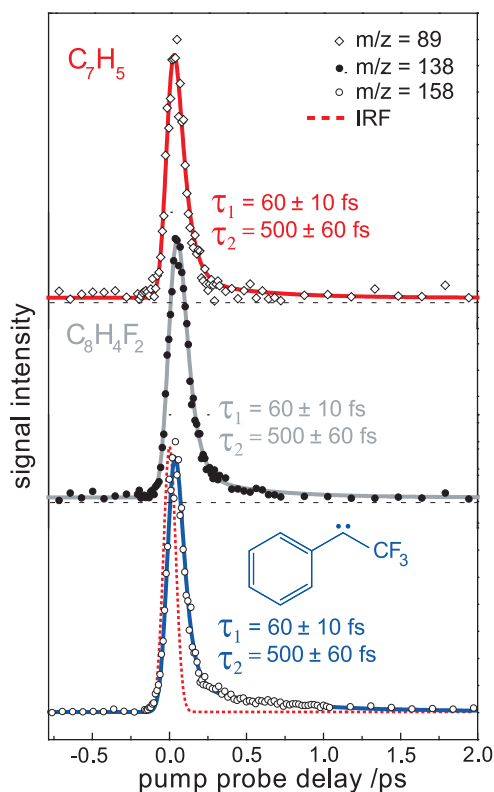
Figure 70: Ion signal of TFPC (R=CF$_3$, bottom trace), $C_8H_4F_2$ (middle trace) and C_7H_5 (top trace) as a function of the time delay (pump 265 nm, probe 795 nm). The signal is well described for all species by using the same model and equal time constants.

correspond to the loss of CF$_3$ and HF, respectively (fig. 70). These fragments are likely to result from dissociative photoionization of the parent TFPC$^+$ in the probe step.

Time-resolved PE Imaging

A deeper insight into the excited-state dynamics of polyatomic molecules was obtained by time-resolved photoelectron spectroscopy (TR-PES)[50]. The time-resolved photoelectron spectra, which were extracted using velocity map electron imaging of CPC and TFPC, are depicted in fig. 71 and 73, respectively. The images show a contour plot of the photoelectron intensity as a function of kinetic energy (horizontal axis) and time delay (vertical axis). The bottom PES in fig. 71 consists of an average over all delay times, showing diffuse broadened structures in the electron spectra. The photoelectron spectra were examined using the integration software described in chapter 14.7. The spectra of CPC and TFPC are rather similar in appearance and can be described by a superposition of three Gaussian functions (G1, G2, G3) and one exponential function for electrons with very low kinetic energy. This choice of describing the photoelectron spectrum does not intend to reflect a possible mechanism in this case. It was chosen for convenience in order to assign reliable time constants to different electron energy envelopes. The photoelectron spectrum of CPC shows one very sharp peak around zero kinetic energy (0.00–0.04 eV, EXP1), one broad band extending from 0.00–0.25 eV (G1), one very broad unstructured band around 0.51 eV (0.45–0.58 eV, G2) and a third broad band at 0.92 eV (G3). The two broad bands to the right (0.51 eV and 0.92 eV)
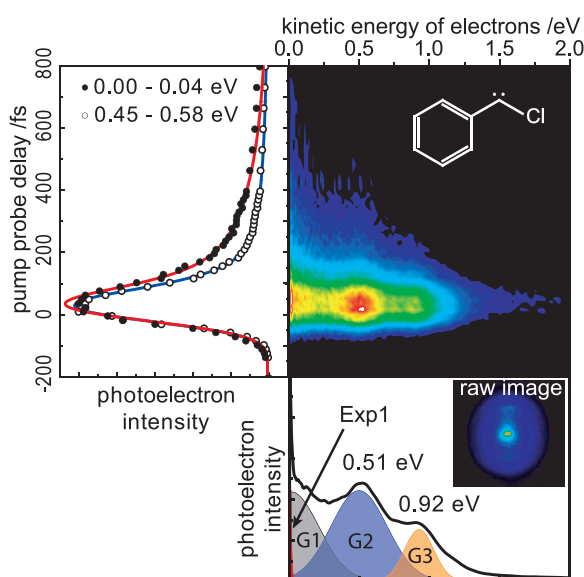
Figure 71: TRPES of CPC (pump 265 nm probe 795 nm). The photoelectron spectrum shows the unpolarized (Po) part of the images. Photoelectrons with low kinetic energy do not fully decay to zero after 1 ps (left). The averaged photoelectron spectrum shows three bands (bottom).

in the PES yield the same time dependence as the mass-resolved ion signal presented in the lower trace of fig. 68. The two-band structure can be described by two overlapping Gaussians G2 and G3 (fig. 71, bottom). These two bands show the largest contribution to the intensity of the photoelectron spectra. The sum of Exp1 and G1 nicely fits the structure of the low kinetic electrons.

On the left-hand side of fig. 71, the time-dependent photoelectron signal of electrons with low kinetic energy (0.00–0.04 eV) is compared to the signal originating from photoelectrons between 0.45 and 0.58 eV without using a fitting procedure to Gaussian and exponential functions. The decay curves were normalized to the same maximum signal intensity, and differences at long delay times are apparent. In contrast to the high energy electrons, the signal of the photoelectrons with low kinetic energy is not well described by a fit with only two time constants.

For comparison the time-dependent PES were additionally fit to the linear combination (Exp1+G1+G2+G3) while optimizing the amplitudes of each function. With this procedure the spectra can be adequately described at all delay times. The integral of each of the four basis functions was then determined as a function of the time delay between pump and probe. In all recorded spectra the G1 integral (as well as the Exp1 integral) did not decay to zero in the recorded time period as can be seen on the left hand side of fig. 72. Here the time dependence of the G1 integral is compared to the time dependence of the G3 integral. Note that the contribution of Exp1 is small compared to G1. The time-dependent integrals of G2 and G3 yield the same delay curve as the mass peak of CPC. However, the dynamics of G1 (and Exp1) show significant deviations. The time-dependent signal is no longer well described by a two-step deactivation scheme. A model transient I→transient II→transient III→transient IV is required in order to properly describe the dynamics of G1 (fig. 72). A third time constant in the order of 3 ps appears when plotting the integral of G1 (or Exp1) as a function of the delay time.
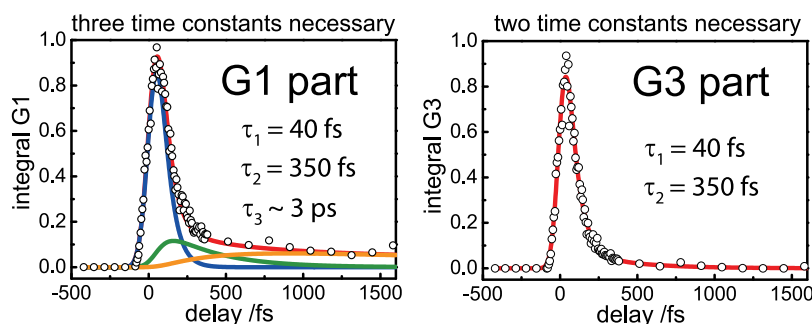
Figure 72: Time-dependent integrals of the functions G3 and G1 of CPC. Both integral functions were normalized to the maximum intensity for ease of comparison. G3 decays to zero, whereas for G1 a third time constant is necessary in order to describe the time evolution.

The time-dependent photoelectron spectra of TFPC can be analyzed the same way as was done for CPC. The spectra are rather similar in appearance and only differ in the positions of G2 and G3 as well as in the magnitude of the time constants. The G3 part is well described by two time constants (τ_1=60 fs, τ_2=500 fs), whereas for the G1 part again an additional time constant is required ($\tau_3 \approx$ 3 ps, see fig. 74). The time-dependent ion signal of TFPC, depicted in the lower trace of fig. 70, revealed only two time constants (τ_1=60 fs, τ_2=500 fs). The same time constants are also found in the G3 part of the TRPES.
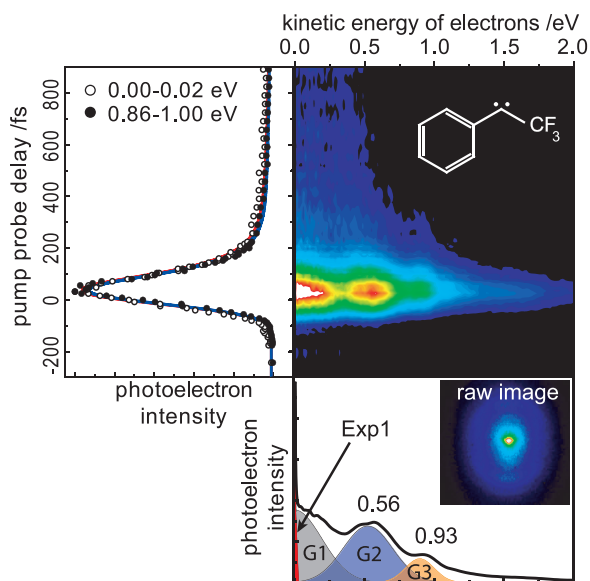
Figure 73: TRPES of TFPC (pump 265 nm, probe 795 nm). The photoelectron spectrum shows the P0 part of the images. Photoelectrons with low kinetic energy do not fully decay to zero after 1 ps (left). The averaged photoelectron spectrum shows one sharp peak and three bands (bottom).
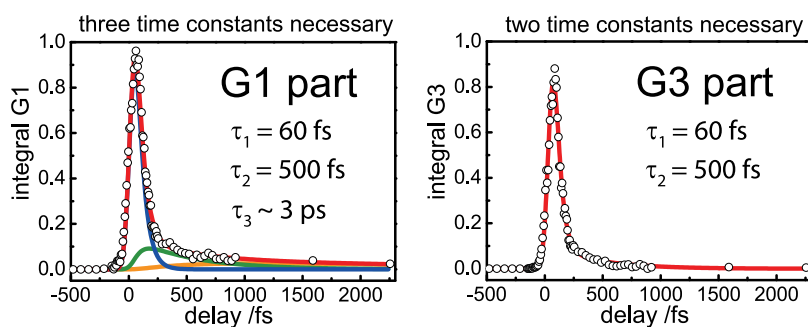
Figure 74: Time-dependent integrals of the functions G3 and G1 of TFPC. Both integral functions were normalized to the maximum intensity for ease of comparison. G3 decays to zero, whereas for G1 a third time constant is necessary in order to describe the time evolution.

The electron images also carry information about the angular distribution of the electrons. The pBASEX algorithm used for analysis of the photoelectron images also analyzes the angular distribution and can distinguish polarized (P2) and unpolarized (P0) parts in the photoelectron images[38] (compare chapter 2.3). Figure 71 and 73 depict only the time evolution of the isotropic P0 part of the images, which holds a much higher contribution to the overall electron signal. The P2 part, which is not shown, has significant contributions from electrons with a non-zero kinetic energy only. The Exp1 and G1 function are no longer required in the description of the PES for the polarized (P2) part of the photoelectron images. This indicates that the low kinetic energy electrons (Exp1+G1) originate from autoionization processes. In contrast, the polarized P2 contribution to electrons above 0.25 eV suggests that such electrons originate from a direct ionization process.

9.4 COMPUTATIONS

9.4.1 *Procedures, Goals and Methods*

Isomerizations

Depending on the functional groups, some phenylcarbenes are known to perform a ring expansion to cycloheptatetraenes. Hence the [1,2]-C-shift reaction coordinate was examined with DFT calculations using BMK/6-311^{++}G** level of theory (see scheme 6 and figure 76) to help estimate which reactive isomer is produced in the pyrolysis nozzle. For
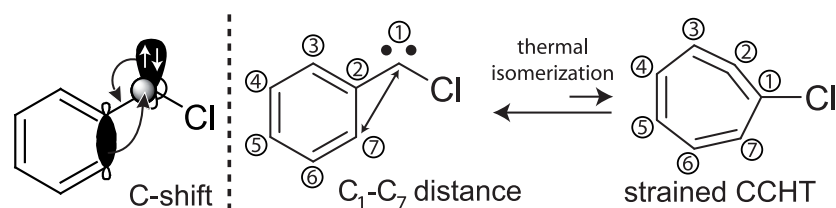
Scheme 6: C-shift of CPC to CCHT with an illustration of the scanned coordinate.

the theoretical study the BMK functional, explicitly developed for modeling thermochemical kinetics, was chosen (compare chapter 4)[74]. It was used as implemented in the Gaussian 03 set of programs[145]. The distance between C_1–C_7 is considerably smaller in 1-chlorocyclohepta-1,2,4,6-tetraene (CCHT) than in CPC (scheme 6). Hence for finding a first good approximation of the transition state, a relaxed potential energy surface scan was performed along this coordinate as suggested in reference 171 for the ring expansion. The geometry at the maximum potential energy of the scan was used as a guess for the transition state of the isomerization and was subsequently used in a QST3 calculation[77] for further improvement. The transition state, the reactant (CPC) as well as the product (CCHT) were optimized separately with tight convergence criteria[1], and the electronic energies were zero point energy corrected (ZPEC).

---

[1] Predicted change in energy smaller than $< 1 \times 10^{-10}$ ha

For CPC extensive *ab initio* and DFT calculations on the singlet-triplet gap have been performed by the *M. Platz* group[152], showing the B3LYP functional to be a cost effective method to estimate this important parameter[172]. No calculations existed on the singlet-triplet gap of TFPC, even though experimental evidence concludes that it has a triplet ground state[154]. In order to acquire a value for the S-T gap of TFPC, full optimizations with the UB3LYP/6-311^{++}G**, UBLYP/6-311^{++}G**, BVWN5/6-311^{++}G** and BVWN5/6-311^{++}G(2df,2p) DFT functionals were carried out for the singlet as well as for the triplet carbene. The sum of electronic and ZPE was compared for each method (table 9). The UBLYP and BVWN5 functionals were used, since they were found to yield good values for the singlet-triplet gaps of other carbene systems[173].

Electronic States

The location of the first excited states of CPC was calculated by time-dependent DFT calculations (TD-B3P86/6-311^{++}G**). In these calculations the UB3LYP/6-311^{++}G** optimized ground state geometry was used, and ZPEC was omitted. Similar to the TDDFT calculations on the neutral CPC, the location of the first excited-state energy of the CPC$^+$ ion was estimated (vertical geometry) by TD-B3P86/6-311^{++}G** level of theory using the same geometry.

9.4.2 Computational Results

Isomerizations

Figure 76 summarizes the results of the BMK calculations for the isomerization of CPC to CCHT. The ordinate represents the sum of electronic and zero point energy and the abscissa represents the reaction coordinate of the isomerization to CCHT. The sum of electronic and zero point energy of CPC was arbitrarily set to 0 kJmol^{-1} as reference point. The QST3 calculation[77] predicts an isomerization barrier for CPC to CCHT of 96 kJmol^{-1}. The reverse barrier lies at only 26 kJmol^{-1} and the carbene CPC is situated 70 kJmol^{-1} lower in energy than the highly strained CCHT. The $\Delta_R G_m^0$ value for the CPC to CCHT reaction was calculated to lie at 69.1 kJmol^{-1}.

In order to see how low a barrier can be before supersonic jet flash pyrolysis no longer generates the desired product out of the diazirine, 3-methyl-3-phenyldiazirine (R=CH$_3$) was employed in the experiments (fig. 67). This precursor in principle could yield 3-methyl-3-phenylcarbene (MPC). MPC is known to have only a very small barrier towards isomerization[165] to the thermodynamic considerably more stable styrene via a [1,2]-H-shift. BMK/6-311G** (QST3) calculations employing the same procedure as described above for CPC predict the barrier to lie at only 31 kJmol^{-1} (fig. 77). The preceding relaxed potential energy surface scan was performed along the C–C–H angle. The value for the isomerization barrier is close to the value retrieved by BPW91/cc-pVDZ level of theory (23 kJmol^{-1}) reported in the literature[174].

energy levels

energy /eV		
5.03	4 ¹A''
4.76	3 ¹A''
4.46	3 ¹A'
4.09	2 ¹A''
3.94	2 ¹A'
1.54	A ¹A''
0.00	X ¹A'

265 nm

relevant orbitals

MO 34 (a'')

MO 33 **LUMO** (a'')

MO 32 **HOMO** (a')

MO 31 (a'')

MO 30 (a'')

MO 29 (a')
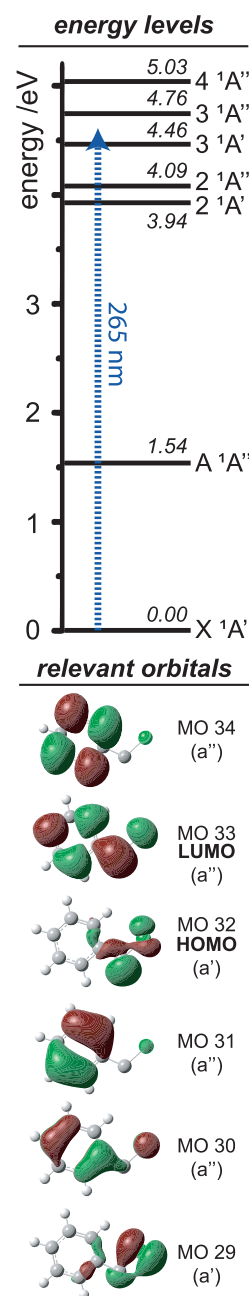
Figure 75: Border orbitals of CPC and its excited states predicted by TDDFT
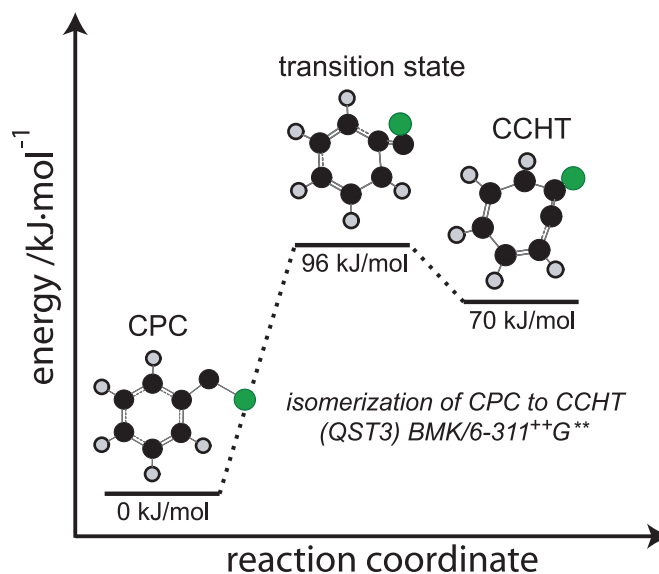
Figure 76: Energy diagram of the ground state isomerization of CPC. The barrier was calculated using the BMK functional with 6-311^{++}G** basis set. The transition state was found by applying the QST3 method along the C–C distance coordinate. The energy corresponds to the sum of zero point and electronic energy.

Singlet-Triplet Gaps

The UB3LYP/6-311^{++}G** calculations yield that TFPC has a triplet ground state. According to the B3LYP functional the first singlet state is located 17.4 kJmol^{-1} higher in energy. For comparison the same level of theory gave a singlet-triplet gap of -23.5 kJmol^{-1} for CPC, which predicts the CPC correctly as a singlet in its ground state and closely reproduces the benchmark result obtained from ref. 152. Values for the S-T gap using other functionals are given in table 9. The B3LYP result for the TFPC fits nicely into a series of calculations reported in ref. 175, performed on carbenes with varieties of different electronegative substituents.

Table 9: Singlet-triplet gaps [kJmol^{-1}]:

Method	TFPC	CPC
B3LYP	17.4	-23.5
BLYP	10.8	–
BVWN5	13.8	–
benchmark[2]	–	-27.7

Electronic States

Ab initio calculations on the excited states of CPC are available[152]. The corresponding energy diagram was reproduced by time-dependent density functional theory (TD-B3P86/6-311^{++}G**) and is shown in fig. 75 (top). The latter calculation provides a zeroth-order picture of the 265-nm excitation of CPC that is consistent with that of ref. 152. Excitation takes place into the fourth excited singlet state (3 $^1A'$). This transition holds by far the largest oscillator strength in the calculations and is predominantly described by a transfer of an electron from a π orbital of the aromatic ring (MO 30) into the LUMO (MO 33) of the molecule, which contains a contribution of the p orbital at the carbene center. Note that there is a relatively large energy gap between the A $^1A''$ and the 2 $^1A'$ state of 2.4 eV, whereas the states from 2 $^1A'$

---

[2] The benchmark value is taken from ref. 152. It was calculated by: UCCSD(T)/6-311G(2df,p) + ZPE (UB3LYP/6-31G*)
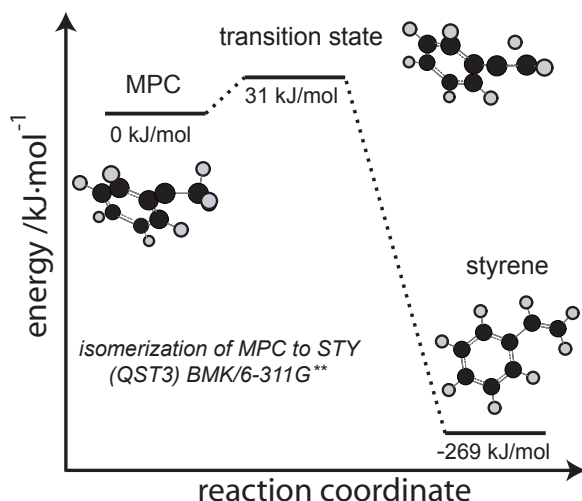
Figure 77: Energy diagram of the ground state isomerization of MPC (singlet potential energy surface). The barrier was calculated using the BMK functional with 6-311G** basis set. The transition state was found by applying the QST3 method along the C–C–H angle coordinate. The energy corresponds to the sum of zero point and electronic energy.

to $4\,^1A''$ are close in energy and presumably strongly coupled. The $A\,^1A''$ state has a dominant electronic configuration corresponding to the promotion of an electron at the carbene center (MO 32 to MO 33). Several electron configurations contribute to the levels $2\,^1A'$ to $4\,^1A''$. They involve the promotion of an aromatic electron.

At TD-B3P86/6-311^{++}G** level of theory, the first excited state of the CPC$^+$ ion is predicted at around 1.7 eV above the vertical ionization potential of CPC (same geometry as CPC in the ground state). For the adiabatic case (geometry of the ground state cation), the method yields a value of 1.9 eV.

9.5 DISCUSSION

9.5.1 *Pyrolysis of Diazirines*

Producing a clean molecular beam of intermediates is associated with a considerable experimental challenge. Velocity map imaging (VMI)[38] simplifies the discrimination between fragments formed by the source and fragments originating from dissociative photoionization or photodissociation by laser light as shown in figure 64. Pyrolytically generated intermediates show a higher velocity along the expansion of the molecular beam and a very narrow velocity spread. Further VMI experiments on iodoalkanes showed that this approach is generally applicable also with other precursors for generating free radicals (compare chapter 12). The method thus aids clean intermediate generation of reactive intermediates in combination with the pyrolysis source as illustrated in fig. 78. For the diazirines the pyrolysis conditions could easily be optimized by following the images in real time. The diazirines cleave via dissociative photoionization when irradiated. This observation is in agreement with the synchrotron studies presented
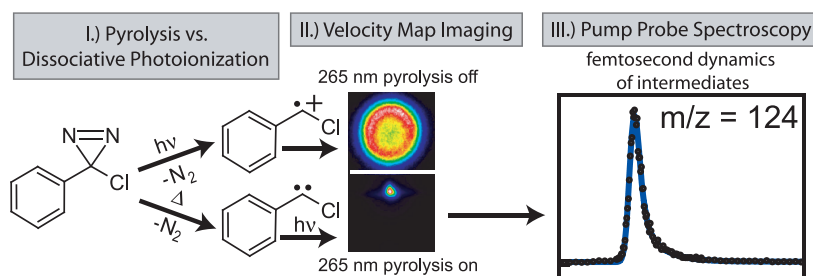
Figure 78: By analyzing the photoion images (in real time) conclusions on the origin of the different masses detected in the TOF spectra can be drawn. Pyrolytically generated intermediates show a higher velocity along the expansion of the molecular beam and a very narrow velocity spread as compared to their counterparts originating from dissociative photoionization.

in chapter $7^{[162]}$. With 265-nm laser light the CPC$^+$ fragments carry away 0.09 eV of kinetic energy. As visible in figure 64, the images are not polarized. This might be linked to a small barrier towards dissociative photoionization in the cation, and dissociation occurs after at least one rotational period of the diazirine$^+$, indicating that the diazirines do not directly dissociate. However, since no information on the electronic character (and rotational angular momentum) of the intermediate state of the diazirine and its cation is available, nonadiabatic interactions of the accessible ionic states might also induce unpolarized photoion images[176].

Due to the high reactivity of the carbenes, the possibility of isomerizations inside the pyrolysis has to be excluded. However, the thermodynamic stability of phenylcarbenes, with regard to isomerization, strongly depends on functional groups of the phenyl ring[158] as well as on the second substituent in alpha position to the carbene center. While flash vacuum thermolysis of phenyldiazirine (R=H) can produce cycloheptatetraene (CHT) thermally[177,178], depending on the trapping method, TFPC (R=CF$_3$) is known to be inert towards isomerizations[147]. Note that the technique of jet flash pyrolysis, applied in this study, achieves much shorter contact times, faster cooling and can be optimized in real time while monitoring the pyrolysis products in the TOF-MS in contrast to earlier studies using vacuum thermolysis of diazirines. The second phenylcarbene (CPC, R=Cl) is known to be stable in condensed phase at room temperature[153]. The CPC is stabilized mesomerically by the free electron pairs of the chlorine atom[171]. The BMK calculations predict the carbene CPC to be 70 kJmol^{-1} lower in energy than chlorocyclohepta-1,2,4,6-tetraene (CCHT). Thus CPC will be strongly favored on thermodynamic grounds. According to $\Delta_R G_m^0$ = 69.1 kJmol^{-1} = $-RT \ln K$ and a pyrolysis temperature of approx. 800 K, the ratio of CPC/CCHT will be at around 40000. In contrast to the equilibrium between CHT and phenylmethylene, reported in ref. 177, the chlorine atom considerably stabilizes the carbene rendering it thermodynamically favored over CCHT. Hence it can be concluded that neither TFPC nor CPC isomerize during the pyrolytic generation from the corresponding diazirine precursors shown in scheme 5. On the other hand, barriers of only 31 kJmol^{-1} are not sufficient and MPC isomerizes to styrene when generated pyrolytically from the corresponding precursor.

In case of the CPC *ab initio* calculations of the excited states are available[152] and are well reproduced by time-dependent DFT (TDDFT) calculations. The TD-B3P86/6-311^{++}G** energies of the excited states are depicted in fig. 79. All available calculations predict a large energy gap between the $A\,^1A''$ state and the next higher excited state. A dense assembly of electronic excited states exists between 3.9 and 6 eV, which are likely to be strongly coupled. This makes precise quantum chemical calculations challenging, since many electronic configurations contribute to the description of the electronically excited states in this energy region[152]. However, taking the CASPT2 values for the location of the excited states from *Platz et al.*[152] instead of TDDFT values does not significantly change the picture. When using the CASPT2 values, the $A\,^1A''$ level rises by 0.2 eV and thus would predict electrons with 0.2 eV kinetic energy when detecting this state rather than 0.08 eV when using the TDDFT values. Due to the broad bands in the experimental TRPES, shown in figure 71, it is not clear whether TDDFT or CASPT2 gives the best description on the location of the excited states. In all calculations reported in the literature, the transition that
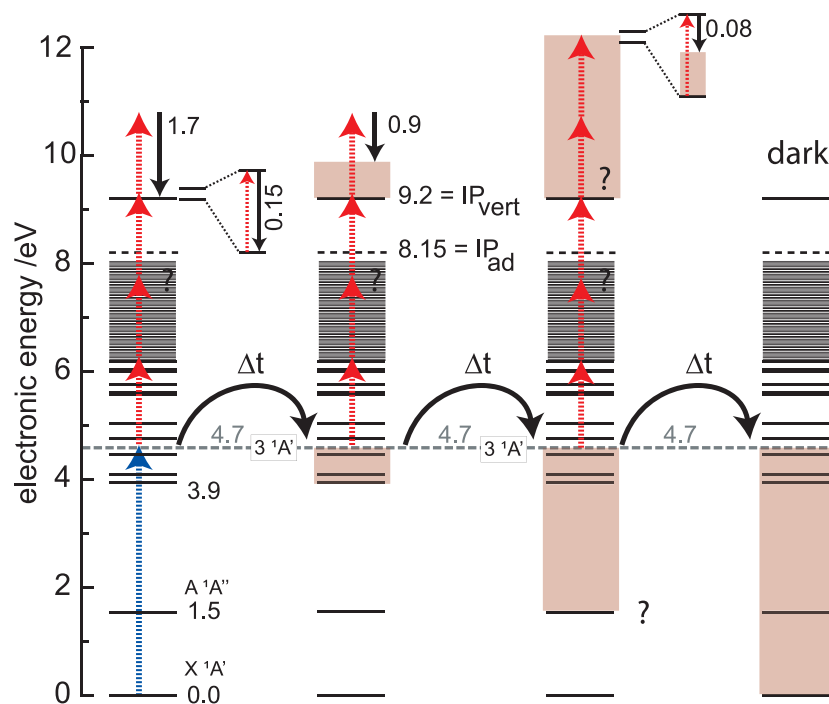
Figure 79: Excited states of CPC calculated by TDDFT. The IP is taken from synchrotron experiments (chapter 8). Most likely the initial excitation takes place into the 3 A' state which holds by far the largest oscillator strength. The red boxes mark internal rovibrational energy.

carries the by far strongest oscillator strength in the energy region of 4.7 eV (265 nm) corresponds to the excitation of an electron from a π orbital of the phenyl ring into the LUMO of the molecule (state 3 $^1A'$). The relevant orbitals are depicted in fig. 75. The LUMO contains a

considerable contribution of the p orbital at the carbene center which conjugates with the aromatic ring. The excitation energy of the $3\,^1A'$ state is very sensitive to the details of the excited-state calculation and it varies according to ref. 152 between 4.01 eV (309 nm) and 5.85 eV (212 nm). However, the experiment shows that a photon energy of 4.7 eV (265 nm) can be used for exciting the molecule.

The femtosecond time-resolved pump-probe experiments reveal that the initially excited state of the phenylcarbenes deactivates in a multi step fashion. When analyzing the TRPES of CPC (figure 71), most of the photoelectrons possess a kinetic energy of around 0.50 eV (open circles, left side), and a second broad peak is visible at around 0.91 eV. Both of the peaks show the same time dependence as the mass selected delay curve of figure 68. Thus they are likely to correspond to the same photophysical processes. Since the dense manifold of excited states depicted in figure 79 is not expected to result in well separated bands in the TRPES, it can be assumed that these unstructured bands result from ionization out of dense manifold of excited states around 4.7 eV. The structure of the PES (G2 and G3) is not visible when static one-color photoelectron spectra are taken at higher laser intensities with 265 nm only ([1+1] REMPI) as shown in figure 80. In this one-color
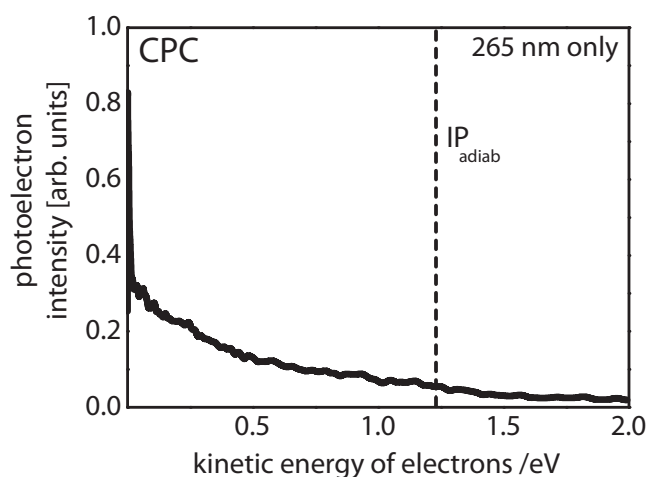
Figure 80: One-color PES recorded by VMI with 265 nm only. No structures are visible.

spectrum the band has its maximum at 0.05 eV and slowly falls off towards 1.25 eV in accord with the adiabatic and vertical IP measured in the synchrotron experiments (compare chapter 8), showing that FC factors are large for transitions in high-lying states of the ion. Nevertheless, radical cations are known to possess low-lying electronically excited states and TDDFT calculations predict the first excited state of the CPC ion to lie 1.7 eV above the IP in case of a vertical transition. It can be assumed that the two bands (G2 and G3) in the TRPES originate from two ionization processes involving a different number of probe photons. Taking an adiabatic IP of 8.15 eV, a [1+3'] process corresponds to a maximum possible kinetic energy of 1.19 eV and a [1+4'] process to 2.75 eV, respectively. A clear assignment of the two bands in

the TRPES is not straightforward, and low-lying electronically excited states of the cation or intermediate resonances mediate the spectra. As apparent from the comparison of figure 71 and 80 the structure in the TRPES is linked to the multiphoton probe.

In contrast to the photoelectrons around 0.5 eV, the time-dependent signal at low kinetic energies is not well described by two time constants. If the relaxation proceeds via internal conversion, the electronic energy will be converted to internal vibrational energy of the molecule and distributed in several vibrational modes. When ionizing the molecule in the probe step, this energy does not contribute to kinetic energy of the photoelectrons. Under the assumption that the geometry of the species does not strongly change while relaxation to the a lower-lying state takes place, the time dependence of the low kinetic energy electrons can be explained by following picture: Taking the $IP_{vert} = 9.2$ eV of CPC into account, ionization from the $A\,^1A''$ state (located at 1.54 eV in TD-B3P86/6-311^{++}G** calculations) would produce a band of electrons at around 0.08 eV when probing with five 795-nm photons (5×795 nm $\equiv 7.79$ eV). Thus ionization out of this state will produce electrons with low kinetic energy and suggests that observing these electrons (G1) is a possibility of following the time dependence of the $A\,^1A''$ state. This picture can explain why the dynamics of the $A\,^1A''$ state becomes visible in the decay curve for G1 and the signal no longer decays to zero in the measured delay time. The signal will be weak, since more probe photons are necessary to probe from lower lying electronic states. In a [1+3'] ionization the primary populated $3\,^1A'$ state will also produce low kinetic energy electrons, since highly excited levels above the ionization limit can autoionize. Autoionization uses up some of the internal energy to overcome the ionization threshold and usually produces electrons with low kinetic energy[179]. The 795-nm multiphoton ionization is likely to populate high-lying autoionizing states when probing the dense manifold of excited states illustrated in fig. 79. Therefore, all three time constants are visible in the photoelectron energy range of G1. Because the $A\,^1A''$ state is the lowest electronically excited state, the remaining time constants have to be linked to the dynamics of energetically higher lying states. Hence the first decay constant $\tau_1 = 40$ fs of CPC can be assigned to a relaxation within the dense manifold of initially excited states at around 4 eV. Subsequently, an internal conversion with a time constant of 350 fs takes place into the $A\,^1A''$, converting the excess electronic energy into internal energy. Due to the existence of intermediate resonances, the ionization efficiency of the excited states between 3.67 eV and 4.01 eV will be much higher than the ionization efficiency of the $A\,^1A''$ with the 795-nm probe (1.56 eV). Thus the time-dependent ion signal in the lower trace of figure 68 apparently decays to zero.

9.5.3   *Excited-State Dynamics of TFPC*

Electronic spin resonance (ESR) indicates that the TFPC has a triplet ground state[154] in contrast to CPC[153]. The calculations compute the singlet state to be 17.4 kJmol^{-1} higher in energy than the triplet state by DFT calculations. Thus the photophysics of the carbene will take place on the triplet potential energy surface. Interestingly, both car-

benes show similar dynamics in the time-resolved experiments regardless of their ground state spin multiplicity. Time-dependent density functional theory (TDDFT) calculations on the excited states of triplet TFPC did not produce reliable results due to a large number of electronic configurations contributing to each excited state at TD-B3P86/6-311^{++}G** level of theory. Singlet TFPC gave a similar picture of the excited states as for CPC when applying TDDFT. In order to acquire a more detailed explanation for the relaxation process of the triplet TFPC, higher level excited-state calculations by *ab initio* methods are necessary. Nevertheless, the data for TFPC indicate that the excited-state deactivation of TFPC follows a related mechanism to the deactivation of CPC. The initially prepared state decays within 60 fs, which is followed by a relaxation occurring within 500 fs. A third time constant in the order of several picoseconds was also extracted. The deactivation cascade again follows a "state I→state II→state III→ground state" scheme. The time dependence of electrons with low kinetic energy again differs from high kinetic energy electrons and indicates a third deactivation process.

9.5.4 *Conclusions*

TFPC and CPC can be cleanly generated by supersonic jet flash pyrolysis out of their corresponding diazirines. However, the isomerization barrier of MPC to styrene (only 31 kJmol^{-1}) is not high enough to use the corresponding diazirine as a precursor for examination of MPC. The BMK functional is a cost effective method for estimating whether side reactions in the pyrolysis source can take place or not.

The following model for the photochemistry of CPC can be suggested: With short wavelength irradiation[159] an electron from the π system of the aromatic ring is excited into the LUMO of the molecule[152]. This initially excited electronic state (3 $^1A'$) is most likely coupled to several other close-lying electronic states. The experiments presented in this chapter conclude an ultrafast relaxation of around 40 fs within this dense manifold of the initially prepared state. Since the electronic states are energetically very close, the pump pulse will likely produce a wave packet composed of a superposition of electronic as well as vibrational states. The movement of the wave packet out of the FC region, due to geometric deformations or a relaxation process between the close-lying states, explains the first 40 fs time constant. The remaining time constant of 350 fs has to be assigned to a subsequent relaxation to the A $^1A''$ state. From the present experiments no information is available on how the A $^1A''$ deactivates. Photoinduced isomerization at short wavelengths ($\lambda > 254$ nm) of CPC to 1-chlorocyclohepta-1,2,4,6-tetraene (CCHT) has been reported in matrix experiments[156]. In principle, the photoreaction of CPC to CCHT could take place on the A $^1A''$ state potential energy surface and the third time constant may correspond to this process. However, due to the lack of diluents and the missing cage effect it is most likely that after the primary photophysical relaxation processes have taken place, the C–Cl bond fission of CPC dominates over an isomerization to CCHT at isolated conditions. The loss of halides via predissociation has been observed for several isolated halocarbenes[180]. Since no

fragments of lower masses grow in as a function of the time delay, and internal conversion to the ground state will be fast because of the many vibrational degrees of freedom of the molecule, it can be assumed that the third time constant represents the relaxation of the $A\,^1A''$ state into the hot ground state. Any further reactions will thus take place on the hot ground state surface.

In matrix experiments the large amount of excess energy deposited into the molecule by irradiation with $\lambda > 254\,\text{nm}$ enables isomerization to CCHT until the internal energy has been transferred to the diluents. Since CCHT is not reverted back to CPC at $\lambda > 254\,\text{nm}$, all CCHT is preserved at matrix conditions. Further continuous irradiation of the matrix with $\lambda > 254\,\text{nm}$ transfers all remaining CPC successively to CCHT[159]. Nevertheless, CCHT formation will only be of importance in condensed phase and most likely not in the isolated carbene.

Even though TFPC has a triplet ground state the experiments give evidence that a similar deactivation pattern of the excited states takes place.

EXCITED-STATE DYNAMICS OF PROPADIENYLIDENE

10.1 INTRODUCTION AND STATE OF KNOWLEDGE

In this chapter the investigation of the primary photo physical processes and photodissociation dynamics of the linear C_3H_2 isomer[1] by femtosecond time-resolved pump-probe spectroscopy and H-atom photofragment spectroscopy is presented. Small carbenes, such as the l-C_3H_2, play key roles in the chemistry of the interstellar space[4,181–183], hydrocarbon cracking[10] and in combustion processes[2]. They are also important model systems for theoretical chemistry due to the large number of low-lying and strongly coupled electronic states[11]. Propadienylidene itself, depicted on the right-hand side of scheme 7, was characterized by microwave spectroscopy[76], discovered in translucent clouds[128] and observed in a cyclopentene flame by VUV photoionization[184]. Due to its importance in high energy environments, there is considerable interest in elucidating its photochemistry and excited-state dynamics upon interaction with high energy radiation. Hence l-C_3H_2 was examined by laser spectroscopy in the laboratory under isolated conditions. Propadienylidene has C_{2v} symmetry and

Scheme 7: Supersonic jet flash pyrolysis of 3-bromo-1-iodopropyne

a singlet ground state, X $^1A_1$ [185] (see scheme 9, page 107). The transition into the symmetry forbidden A $^1A_2$ state was observed in a cavity ringdown experiment[186,187]. The B $^1B_1$←X $^1A_1$ transition was observed in noble gas matrix experiments (Ar, Ne) and was assigned by comparison with calculations[184,188] (see scheme 8). However, most relevant for the photochemistry of the carbene is the transition into the C $^1A_1$ state around 240 nm[181]. It can be considered to be a $\pi \rightarrow \pi^*$ transition, and its femtosecond dynamics are presented in this chapter.

Even though one procedure existed in the literature[189] on how to pyrolytically generate this important intermediate by means of jet flash pyrolysis of 1,3-dibromopropyne (BrC$_3$H$_2$Br), this method soon showed to be inappropriate for measurements employing the standard setup especially for long scans. It is thus not surprising that only a conventional photoelectron spectrum of pyrolytically generated C_3H_2 exists in the literature, since this is a measurement that can be performed in a very short period of time[189]. The 1,3-dibromopropyne precursor is pyrophorus and had to be synthesized several times in order to find a procedure for seeding the precursor into inert gas with-

---

[1] Propadienylidene (l-C_3H_2) is alternatively referred to as vinylidenecarbene.

out decomposition and contact to the atmosphere. The precursor also decomposed faster on metallic surfaces, and thus special glassware was developed (see section 3.2). It consisted of a metallic body with a glass flask inlay and the precursor could be injected by a syringe from the top through a septum. The hermetically sealed container was then connected to the apparatus and the precursor was directly seeded into the inert gas without contact to the atmosphere. Very high pyrolysis temperatures had to be applied for cleaving both C–Br bonds of the precursor. The source was not constructed to withstand such high temperatures and the poppets of the General Valve (material: peak) were degenerating within one day. No stable operation of the pulsed molecular beam was possible under such conditions. Thus a high vacuum compatible water cooling system was developed in order to augment the pyrolysis source developed by *Chen et al.*[18] (see section 3.1.1). Even though this improvement tremendously enhanced the conversion efficiency for generating C_3H_2, the precursor still was requiring too high pyrolysis temperatures so that the SiC tubes of the source broke within several days. Thus new precursors were synthesized with lower C–Hal binding energies: 3-bromo-1-iodopropyne (IC_3H_2Br) and 1,2-diiodopropyne (IC_3H_2I). It showed that IC_3H_2Br was the best possible precursor and led to a breakthrough being able to perform measurements on C_3H_2 under stable conditions as will be explained below.
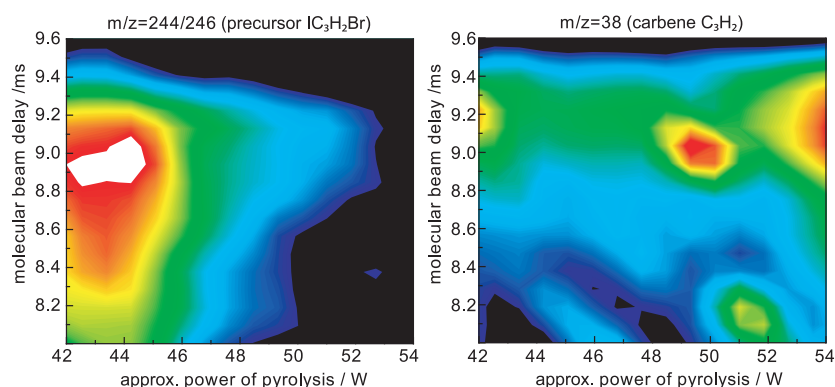
Figure 81: By computer assisted variation of pyrolysis parameters and recording the TOF spectra ($\lambda = 118\,\text{nm}$), 3D contour plots can be drawn. These aid the preparation of intermediates. Left: IC_3H_2Br precursor intensity as a function of pulse delay and pyrolysis wattage. Right: Intensity of C_3H_2.

The software described in chapter 14.6, which plots the intensity of different mass channels as a function of the most important pyrolysis parameters, was used to aid the optimization of pyrolysis conditions (fig. 81). As visible the precursor still needs high pyrolysis temperatures when compared to other precursors. Time-of-flight mass spectra, which were recorded using VUV light, are given in fig. 86 on page 111 and document a clean generation of the intermediate. It was found that the Doppler width of the H-atom photofragments depended on the pyrolysis temperature. Due to this observation over 120 spectra were recorded in total[190]. Since only little information on gas phase experiments of C_3H_2 is available in the literature, many laser experiments were performed over a large energy range (i. e., REMPI, photo-

fragment Doppler spectroscopy, pump-probe spectroscopy). H-atom photofragment spectroscopy showed to be a sensitive tool for examining the photochemistry of C_3H_2 and will be presented in chapter 11.

10.2 DISSOCIATION OF THE PRECURSOR

The thermal dissociation of the IC_3H_2Br precursor behaved differently compared to other precursors used with the pyrolysis source so far. Usually only one C–X bond had to be cleaved, whereas in IC_3H_2Br two bonds had to be cleaved thermally in a successive manner. Hence the bond dissociation energies of $I–C_3H_2–Br$ were investigated by DFT studies to get a deeper insight. Over several experimentally tested precursors for l-C_3H_2 (BrC_3H_2Br, IC_3H_2Br, IC_3H_2I), the I-Br-variation interestingly showed to be the most efficient C_3H_2 precursor. This observation gave the thrust for a computational investigation.

For this study, the ground state of the precursor (3-bromo-1-iodo-propyne) and the pyrolysis intermediates IC_3H_2 and C_3H_2Br were calculated using B3LYP/6-311G** level of theory. Additionally the BMK functional[74] with a 6-311G** basis set on iodine[192] and a 6-311++G(2df,2p) basis set on all other atoms was employed. However, the heavy atoms bromine and iodine are influenced by relativistic effects, not included in simple DFT calculations using all electron basis sets[192]. Hence some of these effects were taken into account by using

ⓘ *SO coupling gets important for heavy atoms. The coupling is partially quenched in molecules and thus plays a smaller role there. In this study it was neglected for IC_3H_2Br, IC_3H_2 and C_3H_2Br. SO coupling induces for atomic Br and I two no longer degenerate states: $P_{1/2}$ and $P_{3/2}$. The $P_{1/2}$ is lower in energy and the total SO splitting is asymmetrical according to the degeneracy of states $(2J+1) \rightarrow P_{1/2}$ "weighs" 2 units and $P_{3/2}$ "weighs" 4 units. Hence the $P_{1/2}$ is lowered in energy by $\frac{2}{6}$ (see ref. 191).*

Table 10: Bond dissociation enthalpies [kJmol⁻¹] of the precursor using different methods and basis sets. The SO coupling is not yet taken into account.

	B3LYP 6-311G**	BMK 6-311++G(2df,2p)	BMK/MWB AUG-pVTZ	BMK/MDF AUG-pVTZ
IC_3H_2Br	0	0	0	0
IC_3H_2+Br	231.6	226.5	204.4	224.1
I+C_3H_2Br	379.2	376.1	375.1	397.2
I+C_3H_2+Br	460.2	470.9	450.1	493.3

relativistic effective core potentials[193] in additional BMK calculations. These calculations used a 28MDF or 28MWB effective core potential on bromine with an AUG-cc-pVTZ basis set for the valence electrons, a 46MDF/AUG-cc-pVTZ or 46MWB/AUG-cc-pVTZ combination for iodine[194] and an all electron AUG-cc-pVTZ basis set for other atoms. These potentials, however, do not take into account spin-orbit (SO) coupling of the unpaired valence electron[192], which is large for atomic bromine and iodine (SO_I = 90.95 kJmol⁻¹, SO_{Br} = 40.09 kJmol⁻¹)[113]. This can be accounted for afterwards over an approximation by following the procedure described in ref. 191. Hereby the SO splitting is only taken into account for the atomic species². Table 10 summarizes computed dissociation enthalpies at 298 K *without* spin orbit correction. Figure 82 depicts the BMK/MDF/AUG-cc-pVTZ results *including* the empirical correction for SO coupling. The fully nonrelativistic results, which were calculated at BMK level using all electron basis sets, are added in brackets. Hence the figure illustrates the two borderline cases.

---

² Many thanks to *Prof. M. Kaupp and H. Bahmann* for very helpful discussions on SO splitting and pseudo potentials.
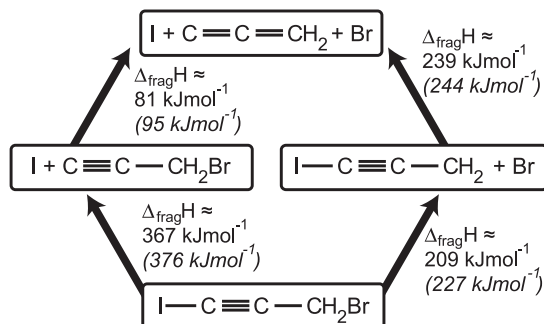
Figure 82: Bond dissociation enthalpies at BMK/MDF/AUG-cc-pVTZ level of theory with SO correction for the free atoms. The fully non relativistic results (BMK/6-311^{++}G(2df,2p)) are given in brackets and do not include an empirical SO correction.

The calculations demonstrate why IC_3H_2Br is the best precursor out of the XC_3H_2X series. The weakest bond is not, as would be intuitively expected, the C–I bond but the C–Br bond. The intermediate IC_3H_2 radical can be stabilized by interaction of the radical site with the π system of the triple bond, whereas the corresponding C_3H_2Br radical has sigma character and is thus thermodynamically disfavored. When moving from BrC_3H_2Br to IC_3H_2Br the "critical" bond is weakened. This renders IC_3H_2Br more suitable as a precursor for C_3H_2. As found in the nanosecond laser experiments, IC_3H_2I does not help to further improve the efficiency[3].

A second useful information is to know when the precursor shows dissociative photoionization (DPI). This can lead to fragmentation patters in the mass spectrum that complicate their interpretation. Hence the IC_3H_2Br precursor was also studied by TPEPICO spectroscopy at the synchrotron light source *Soleil* (see chapter 2.5). The result is shown in figure 83a. The blue curve describes the threshold electron/ion yield of the parent IC_3H_2Br as a function of the photon energy. The IP_{ad} of the precursor could be determined to 9.27 ± 0.1 eV. No values were available in the literature yet. At around 10.3 eV the signal starts to diminish due to DPI, and the IC_3H_2 daughter becomes visible. As found for the neutral, the cation loses the bromine atom first.

A breakdown diagram plots the fractional abundances for each channel[143] and enables a more precise determination of the appearance energy. It is formed by dividing the integral of each mass channel (Int_1 and Int_2) by the total integral (Int_1+Int_2). The diagram[142] is given in fig. 83b and yields an AE_{0K} at 10.4 ± 0.1 eV ($BDE^+ = AE_{0K} - IP_{ad} \approx 1.13$ eV)[4].

Hence it is important for the investigations on C_3H_2, in which the photon energy exceeds 10.1 eV and DPI can start to set in, to assure that the precursor is fully converted in the pyrolysis source. Above this threshold DPI will lead to a source of $IC_3H_2^+$ cations. These can be confused with IC_3H_2 radicals that are produced in the pyrolysis source and are subsequently ionized.

---

3 In contrast IC_3H_2I had such a low vapor pressure that it is difficult to vaporize.   4 The lines are drawn to guide the eye and not by performing a fit to a thermally convoluted 0 K breakdown diagram.
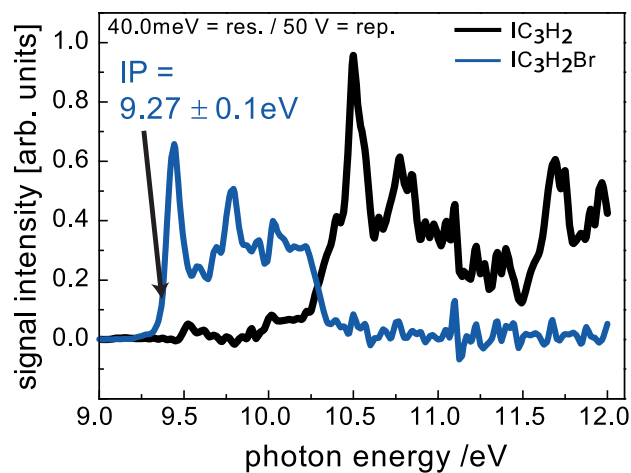
(a) TPEPICO of IC_3H_2Br
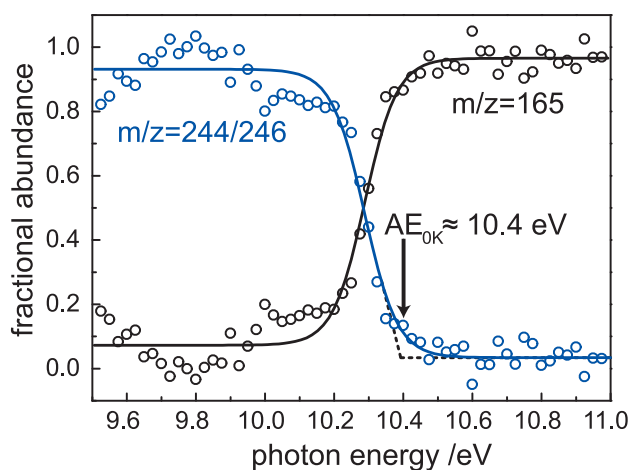
(b) Breakdown diagram of IC_3H_2Br

Figure 83: Top: TPEPICO spectrum of IC_3H_2Br shows the signal intensity of threshold photoions corresponding to the mass of IC_3H_2Br (blue) and its fragment IC_3H_2 (black). Bottom: By plotting the fractional abundance[144] of parent and daughter, breakdown diagrams[142] enable the determination of AEs.

This section presents results on the excited-state dynamics of C_3H_2, which were followed on a femtosecond time scale. These give insights into the deactivation of the initial optically prepared excited state. These experiments ideally precede further investigations presented in the forthcoming chapter 11, which discusses the subsequent reaction pathways of the carbene taking place on a nanosecond time scale.

10.3.1   *Specific Experimental Details*

The measurements were performed at the *Max-Born-Institut in Berlin* in a collaborationwith *T. Schultz et al.* A standard molecular beam apparatus was used. It was equipped with a time-of-flight mass spectrometer. The laser system consisted of a commercial Ti:Sapphire oscillator regeneratively amplified to mJ levels at 1 kHz. For excitation, the frequency mixed and doubled output of an optical parametric generator giving 0.5–1 µJ pulses at 250 nm was used. The transients were ionized by a fraction of the amplified 800-nm fundamental. For pump-probe contrast optimization, the laser beams were attenuated by factors of 3–30 using neutral density filters. The two beams were focused with a 750 mm focal mirror to spot sizes of > 100 µm. The instrument response function (IRF $\approx$ 140 fs FWHM) and the zero in time were determined by measuring the time-dependent signals of molecules with a very slow decay rate (time constant > 10 ps)[95]. Data points were recorded typically every 10 fs. At each delay time the ion signals were counted over 200 laser shots.

10.3.2   *Experimental Results*

Since the two halogen bonds of the precursor have to be broken in a stepwise fashion, the excited-state lifetimes of several intermediates could be studied in the experiment (IC_3H_2, C_3H_2Br and C_3H_2). However, both monohalogenated compounds absorb UV radiation and can yield C_3H_2 by photodissociation. Hence reliable data on the carbene require high pyrolysis temperatures and a complete conversion not only of the precursor but also of the halogenated intermediates. Photodissociation of the intermediate species is an alternative source of C_3H_2 carbenes, which are formed vibrationally hot. Their dissociation dynamics differ from those of carbenes cooled in the adiabatic expansion as will be explained in more detail when discussing the nanosecond time-resolved experiments in section 11.

Figure 84 shows the time-dependent mass signals of IC_3H_2, C_3H_2Br and C_3H_2 upon excitation at 250 nm and subsequent ionization with 800-nm pulses. All three species give rise to a monoexponential decay of the pump-probe signal within < 100 fs and could be adequately described by function 5.7 derived in chapter 5 (page 36). However, for C_3H_2 a slight offset remains after a time window of 600 fs as can be seen when comparing the horizontal line drawn in fig. 84, which marks zero signal intensity, with the residual transient signal (bottom trace). This line indicates the one-color background ion signal in each mass
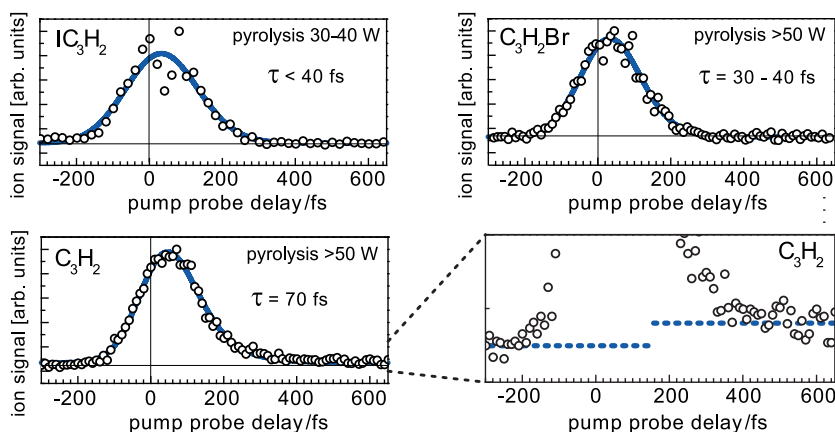
Figure 84: Time-dependent ion signal of mass channels $m/z = 165$, $m/z = 117/119$, $m/z = 38$. Dependent on the pyrolysis temperature different mass channels were investigated. The bottom trace corresponds to C_3H_2.

channel. The signals of IC_3H_2 and C_3H_2Br decay to the background signal intensity.

As a control experiment, time-dependent ion signals of the 3-bromo-1-iodopropyne precursor were measured with the pyrolysis turned off (not depicted). A reverse time dependence with a sub-100-fs decay time showed that it is excited by 800-nm pulses, possibly in a multi-photon process, and ionized by 250 nm. The different temporal behavior of the precursor and propadienylidene shows that the carbene does not originate from dissociative photoionization of IC_3H_2Br.

10.3.3   *1-Iodopropyne and 3-Bromopropyne Radicals*

For IC_3H_2 the vertical and adiabatic ionization energies of 7.73 eV and 7.67 eV were estimated by B3LYP/6-311G** level of theory; hence the ionization takes place in a $[1 + 2']$ pump-probe process. Relativistic pseudo potentials were, however, not used in these estimations of ionization energies.

The decay of IC_3H_2 (upper left of fig. 84) deviates only slightly from the instrument response function. Only an upper bound for the life time of 40 fs could be gained from the averaged data of several experiments. Many iodine containing compounds show an absorption in the region of 250 nm. The excitation takes place into an absorption band (A-band)[195] composed of several directly dissociative states. This is reflected by the broad and unstructured absorption spectra of these molecules. Consequently, the measured excited-state lifetime of the IC_3H_2 radical is short and no signal remains at long delay times. Upon photoexcitation the C–I bond is cleaved and C_3H_2 is formed as was also seen in the nanosecond time-resolved VUV/UV experiments in the forthcoming chapter (fig. 86). Similar observations were made for C_3H_2Br shown in the upper right of fig. 84. The predicted vertical/a-diabatic ionization energies (B3LYP/6-311G**) of 12.94 eV and 10.82 eV would require at least a $[1 + 4']$ ionization process. This is supported by a low signal intensity of this mass channel. Nevertheless, the C_3H_2Br

showed a pronounced pump-probe contrast when excited with 250 nm. An excited-state lifetime of 30–40 fs again only constitutes an upper bound but is consistent with a direct excited-state dissociation of the radical.

10.3.4 Excited-State Dynamics of Propadienylidene
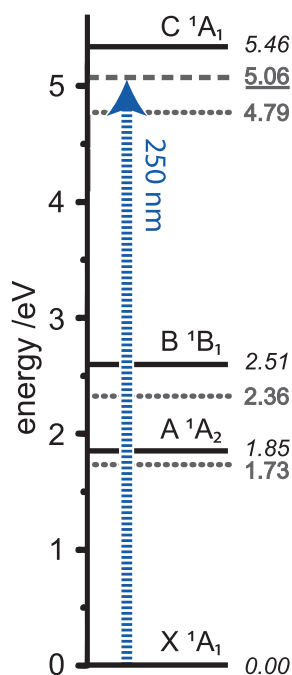
The time-dependent mass signal of l-C_3H_2 is shown in the bottom trace of fig. 84. Corresponding mass spectra are depicted in fig. 86 on page 111 using 118 nm VUV and nanosecond lasers. The ionization potential of propadienylidene lies at 10.43 ± 0.02 eV[189]. Thus a $[1 + 4']$ ionization process is expected. A cyclic isomer, c-C_3H_2, exists which has a lower adiabatic ionization energy of 9.15 eV[189]. However, studies showed that when using BrC_3H_2Br as precursor, only the linear isomer is formed in the pyrolysis nozzle and no isomerization takes place[189].

In fig. 84 the kinetics of the relaxation were described by a monoexponential decay (state A to B model) with a life time of $\tau = 70 \pm 10$ fs. The small offset visible after 500 fs seems to last for a few ps, but the signal was too small to extract a reliable second time constant. The time constant $\tau = 70$ fs can be assigned to the lifetime of the excited $C\ ^1A_1$ state of propadienylidene. An excited state level diagram is given in scheme 8. The italic numbers are calculated by TDDFT (vertical energies). Literature values[184,188] are added for the adiabatic transition energies (dotted lines) and the vertical transition energies ($C\ ^1A_1$ state only, dashed line, underlined value). The TDDFT values are in good agreement with earlier computational and experimental results[184]. A short time constant is in agreement with the structureless H-atom action spectrum, which was observed in photofragment spectroscopy (forthcoming chapter 11).

At lower pyrolysis temperatures the measured time-constants were generally smaller. This discrepancy can be explained by photolytically produced carbenes. These are produced when the pyrolysis is incomplete and some precursor remains in the beam, which is cleaved by photolysis. Further evidence for this hypothesis is given in the experiments of the forthcoming chapter using nanosecond lasers. Photolytically produced carbenes will carry more internal energy, which influences the excited-state lifetime.

Vibronic progression observed in matrix isolation experiments were assigned to a C–C stretching mode. The structure, however, is not detailed and broad, which seems be linked to the very short lifetime of the excited state. Due to the time-energy uncertainty the reported vibronic resolution is close to the possible limit, set by the lifetime of 70 fs, in consistence with the nanosecond experiments in chapter 11. Here the recorded action spectra also provided no structural information.

The pump-probe experiments suggest that the excited carbenes deactivate via internal conversion to the hot ground state on a femtosecond time scale. From the highly vibrationally excited ground state further dissociation reactions can occur. In principle, a multistep-deactivation via lower-lying excited electronic states is possible. As mentioned above, the time-delay scans of the C_3H_2 mass channel show a very

Scheme 8: Energy diagram of the excited states of C_3H_2

small offset for longer delay times that might originate from ionization from a lower electronic state. Thus the experiments are in consistence with a multistep deactivation mechanism.

Another question arises from the experiments: To which state does the initially populated state deactivate? Since only time-resolved ion signals were recorded, a multiphoton ionization (800 nm) chosen and no time-resolved photoelectron spectra recorded, this question cannot be clearly answered. Still, assumptions can be drawn on the basis of correlations between neutral and ionic states[50], even if the analysis is not as straightforward compared to single photon probe experiments. A multiphoton probe process does not necessarily terminate in the ionic ground state, and accidental resonances in the probe step can mediate the ionization probabilities. Scheme 9 shows the important border orbitals needed to describe the electron configuration of the states. According to the DFT calculations, the electronic ground state can be described by the following molecular orbital configuration: ... $(1b_1)^2(7a_1)^2(2b_2)^2(2b_1)^0$ (compare scheme 9).

B3LYP/6-311^{++}G** calculations do not yield a C_{2v} ground state symmetry for the radical cation as found for the neutral carbene but a slightly bent geometry (c_s symmetry). However, the orbitals are similar in appearance and thus characterized by C_{2v} convention (vertical ionization). Ionization into the cationic ground state ... $(2b_2)^1(2b_1)^0$ requires the detachment of an electron from the $2b_2$ orbital. The electronically excited $C\,^1A_1$ state of the neutral corresponds to a $(1b_1)^2 \to (2b_1)^0$ excitation (63%). Ionization of the resulting excited state does not lead to the ionic ground state, and a low ionization probability is expected. However, the TDDFT calculations yield that the $(2b_2)^2 \to (2b_1)^0$ also contributes (18%) to the $C\,^1A_1$ state. This may lead to a significant ionization cross section into the ionic ground state. The lower-lying $A\,^1A_2$ and $B\,^1B_1$ states are dominated by single excitations, $(2b_2)^2 \to (2b_1)^0$ and $(7a_1)^2 \to (2b_1)^0$, respectively (scheme 9). When ionizing the B state an electron is removed from the $7a_1$ orbital, and ionization into the ionic ground state is not expected. This renders the ionization probability negligible. As for the $A\,^1A_2$ state and/or the electronic ground state ($X\,^1A_1$) a large amount of electronic energy is transferred to vibrational energy after relaxation of the C state. This vibrational energy of the intermediates does not contribute strongly to the ionization probability, and the detection efficiency by photoionization will be low as well. The small signal offset at long delay times may be linked to the low ionization probability of the A state. However, it is to expect that internal conversion between B, A and ground state will be fast as found for other intermediates with close-lying electronic states[30]. Hence a further reasonable explanation is that the signal at long delay times originates from the hot electronic ground state. This hypothesis could be elucidated in further state selective time-resolved photoelectron measurements. However, the nanosecond time-resolved experiments in chapter 11 will give further indications that the carbene indeed deactivates to the hot ground state surface.
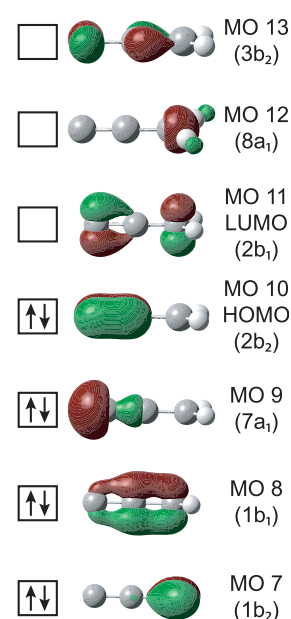
Scheme 9: Boarder orbitals of propadienylidene.

PHOTODISSOCIATION DYNAMCIS OF PROPADIENYLIDENE

Following the femtosecond experiments on the excited-state dynamics, the l-C_3H_2 was excited using nanosecond dye lasers at excitation wavelengths between 260 and 230 nm, corresponding to 460–520 kJmol^{-1}. Hence a sufficient amount energy for dissociation was deposited into the molecule by optical excitation. The dissociation dynamics and kinetics can then be studied by time-resolved detection of H atoms and by Doppler spectroscopy[27,196] (refer to chapter 2.2 for more details). The detection of hydrogen atoms by Lyman-α radiation is a sensitive tool for the observation of photoreactions of reactive intermediates as was discussed in chapter 6 for the 2-propyl radical in detail. This method was also applied to investigate the photochemistry of l-C_3H_2. Note that this approach is only sensitive to reaction channels shown in equation 11.2 and 11.3 and not to the loss of H_2 (equation 11.1). The most important reaction channels, accessible at these photon energies, are summarized in fig. 85. All energies are given in kJmol^{-1} relative to l-C_3H_2 and are based on computations. Most of the energies are taken from the a publication by *Mebel et al.*[76]. The energy difference between the cyclic and linear isomer of C_3H was derived from computations of *Ochsenfeld et al.*[197]. As visible, the lowest dissociation threshold corresponds to the loss of H_2 as shown in equation 11.1.

$$\text{l-C}_3\text{H}_2 \longrightarrow \text{C}_3 \ (X^1\Sigma_g^+) + \text{H}_2 \quad \Delta_R H^0 = +250 \text{ kJmol}^{-1} \tag{11.1}$$

However, there is a considerable barrier (+357 kJmol^{-1}) associated with this channel. This brings it energetically close to H-atom loss and formation of either the cyclic or the linear isomer of C_3H shown in equations 11.2 and 11.3.

$$\text{c-C}_3\text{H}_2 \longrightarrow \text{c-C}_3\text{H} \ (X\ ^2B_2) + \text{H} \cdot \quad \Delta_R H^0 = +423 \text{ kJmol}^{-1} \tag{11.2}$$

$$\text{l-C}_3\text{H}_2 \longrightarrow \text{l-C}_3\text{H} \ (X\ ^2A') + \text{H} \cdot \quad \Delta_R H^0 = +374 \text{ kJmol}^{-1} \tag{11.3}$$
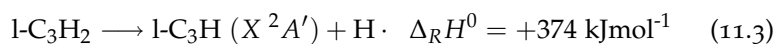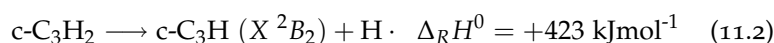
According to recent anion photodetachment spectra, the A $^2A_1$ state of c-C_3H (463 kJmol^{-1}) could in principle also be energetically accessible[198]. Rupture of a C–C bond constitutes an alternative pathway, but dissociation into acetylene and a ground state carbon C (^3P), corresponding to +395 kJmol^{-1} [76,199], is prohibited by spin conservation. Neither formation of C (^1D) plus acetylene (+568 kJmol^{-1}), nor formation of C_2H + CH (+550 kJmol^{-1}) are energetically possible after optically preparing excited propadienylidene between 260 and 230 nm[76]. These pathways will thus not be further considered in these experiments, although crossed-beam experiments of acetylene and C (^3P) yielded evidence for the minor role of spin-forbidden reactions[200,201].
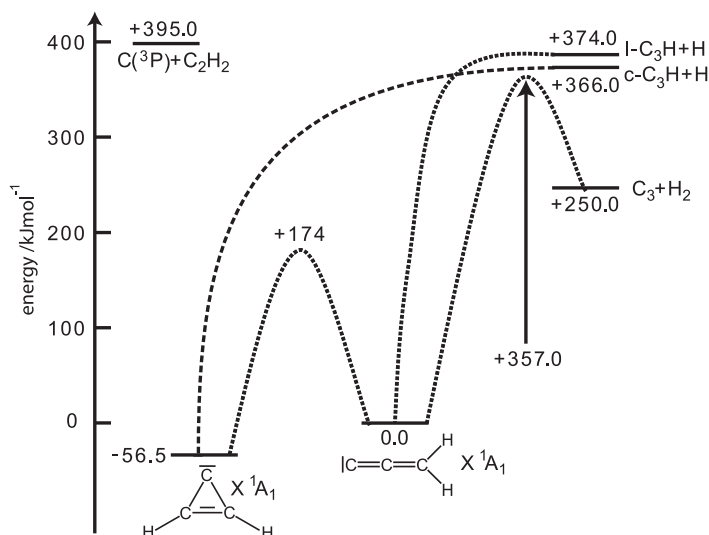
Figure 85: Energetically accessible reaction channels for propadienylidene. The energies are given in kJmol^{-1}. Loss of a H$_2$ molecule and formation of C$_3$ is the energetically lowest dissociation channel, but it is associated with a considerable barrier. Therefore, loss of an H atom becomes competitive.

11.1 EXPERIMENTAL DETAILS AND MASS SPECTRA

A detailed description of the experimental setup, used for performing these nanosecond time-resolved measurements, is given in chapter 3.3. Photoionization mass spectra were recorded at 118 nm in addition to 121.6 nm used for detection of the hydrogen fragments, since the ionization energy of l-C$_3$H$_2$ lies at around 10.43 eV[189] and is thus slightly above the energy of a single 121.6 nm photon (10.2 eV). In fig. 86 several photoionization mass spectra, recorded at 118 nm (10.5 eV), are presented. With the pyrolysis source turned off the signal of the precursor 3-bromo-1-iodopropyne ($m/z = 244/246$) is detected (top trace). All masses and fragments containing bromine can easily be recognized by the ^{79}Br/^{81}Br isotopic pattern. In addition, signals at mass $m/z = 165$ (IC$_3$H$_2$) and $m/z = 38$ (C$_3$H$_2$) are present. The synchrotron results depicted in fig. 83a and 83b prove that these fragments originate from dissociative photoionization of the precursor. When the pyrolysis source is turned on (center trace), the intensity of the signal at mass $m/z = 38$ increases significantly (see also 3D plots in fig. 81 on page 100). In addition a strong I$^+$ signal appears. As visible, the precursor is not converted completely at medium pyrolysis temperatures, and a signal of IC$_3$H$_2$ is present as well. The signal at the mass of C$_3$H$_2$Br is negligible. Obviously the C–Br bond in the precursor is cleaved more easily than the C–I bond as was deduced from further experiments employing BrC$_3$H$_2$Br and IC$_3$H$_2$I in compliance to the augmenting calculations presented in section 10.2. When the pyrolysis nozzle is heated further (bottom trace) the precursor is almost completely converted, and only a very small IC$_3$H$_2$ signal is present when zooming into the mass spectrum. In addition, a very small HI signal was observed as well. It has been shown before in experiments utilizing synchrotron radiation that bimolecular reaction products can be formed in the nozzle[202]. However, their concentration is comparatively small in pulsed laser ex-
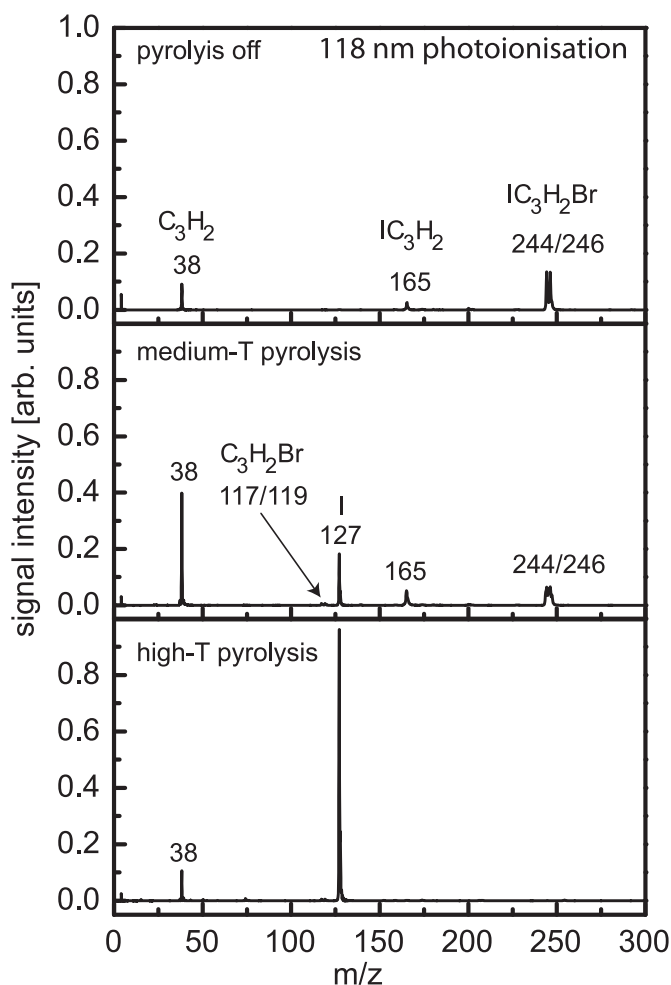
Figure 86: Photoionization mass spectra of propadienylidene relevant for the conditions taken at 118 nm (10.51 eV). The 118 nm spectra show that quantitative conversion of the precursor is only achieved at very high pyrolysis temperatures.

periments that are carried out on the leading edge of the gas pulses of the molecular beam. Same holds for HI, which is a common side product of iodoalkanes in the pyrolysis. In several other pulsed laser experiments, pyrolytically generated intermediates were always found at the leading edge of the gas pulse in high concentrations. Here only a negligible amount of side products are present (compare chapter 6). In case of the IC_3H_2Br precursor, the pyrolysis parameters were varied over a large range. The best conversion efficiency, with smallest number of side products, was observed by mounting the heating electrodes as close together as possible (1 mm) and heating the SiC tube to the maximum possible temperature (white color).

The experiments showed that recording additional mass spectra at 121.6 nm (10.20 eV) aids the optimization of the pyrolysis conditions for a clean carbene generation. They are presented in figure 87. The spectra in the top and center trace were recorded without the excitation laser present. At low and medium temperature pyrolysis (top trace), a small amount of l-C_3H_2 is discernible in the spectra recorded
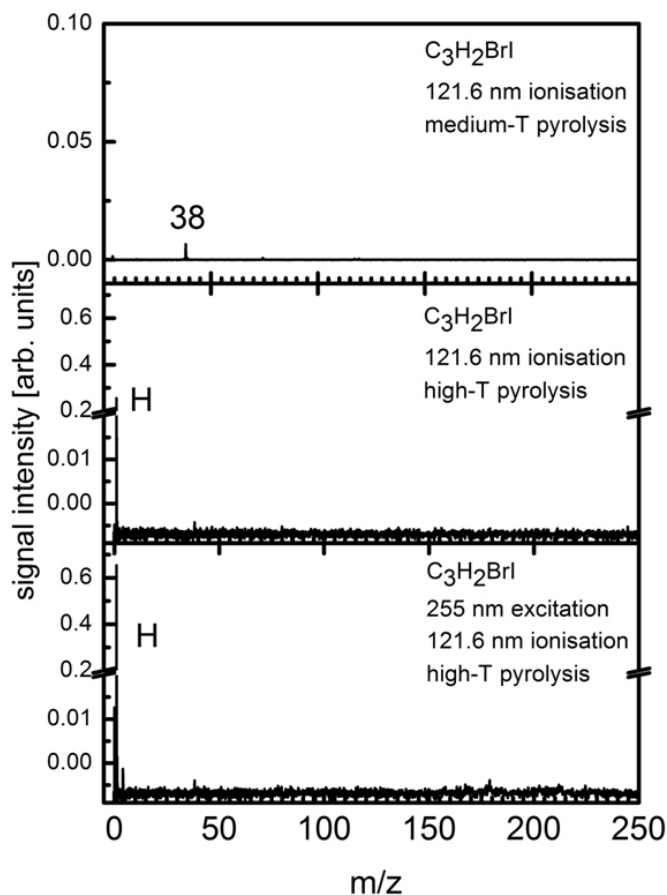
Figure 87: Photoionization mass spectra of IC$_3$H$_2$Br under various conditions taken with 121.6 nm irradiation (10.20 eV). Insufficient pyrolysis temperatures (top trace) yield C$_3$H$_2$ in the spectrum, despite its ionization energy[189] of 10.43 eV. Only at high pyrolysis temperatures (center and bottom trace) IC$_3$H$_2$ is fully converted and all C$_3$H$_2$ is produced pyrolytically. A H-atom background is present without excitation (center trace), but the signal increases significantly when the excitation laser is turned on (bottom trace).

at 121.6 nm despite its high ionization energy of 10.43 eV. When the temperature of the pyrolysis nozzle is increased further (center trace) the carbene signal ($m/z = 38$), originating from dissociative photoionization of IC$_3$H$_2$, disappears. The precursor (IC$_3$H$_2$Br) differs from many earlier experiments on radicals (compare, e. g., chapter 6) in an important aspect: Since two bonds have to be cleaved sequentially in order to produce l-C$_3$H$_2$, a second intermediate (IC$_3$H$_2$ in this case) appears in the carbene formation process. Most likely even after complete conversion of the precursor, C$_3$H$_2$ can be formed by photodissociation of some IC$_3$H$_2$ intermediate that is still present. Such carbenes will contain a significant amount of internal energy and can perturb the photodissociation experiments described below, since the velocity of the H fragments will be convoluted by the speed distribution of the parent and the internal energy contributes to the C–H bond breakage. As was experimentally proven using synchrotron radiation (fig. 83 on page 103), the precursor can produce other fragments by dissociative photoionization. Thus it is essential to increase the pyrolysis up to the

point where the 118 nm mass spectrum indicates complete conversion of the precursor and the carbene signal, resulting from photodissociation of IC_3H_2, disappears at 121.6 nm. To achieve this very high pyrolysis temperatures are needed. However, an isomerization to c-C_3H_2 in the pyrolysis nozzle is unlikely, since the latter has an ionization energy of 9.15 eV[189]. It would thus be ionized and detectable with 121.6 nm (fig. 87). The spectrum in the center trace shows the presence of a H-atom background signal at high pyrolysis temperature which is subtracted before interpreting the Doppler profiles listed below. The one-color background appears due to H atoms formed in the pyrolysis source. Since it is almost absent at lower pyrolysis temperatures it does not originate from dissociative photoionization of the precursor or side products with the 121.6 nm or the 365 nm radiation alone. In the bottom trace a two-color spectrum is depicted, using 121.6 nm for detection and the 255 nm excitation laser in addition. As visible, a strong enhancement of the signal at $m/z = 1$ was achieved, indicating that H-atom loss is an important reaction channel of C_3H_2. The magnitude of the H-atom signal depended linearly on the excitation laser power (fig. 88).
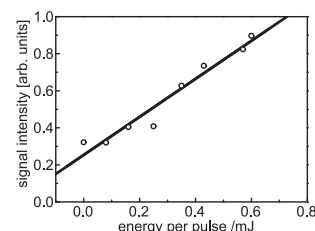
Figure 88: H signal intensity as a function of laser power

11.2 H-ATOM PHOTOFRAGMENT SPECTROSCOPY

The H-atom loss was then investigated as a function of the excitation wavelength between 260 and 230 nm (460 to 520 kJmol^{-1}), corresponding to excitation into the C $^2A_1$ state. In a simple molecular orbital picture an electron is excited from the 1b$_1$ orbital into the 2b$_1$ orbital[203,204] (compare scheme 9, page 107).

Information on the product energy distribution was obtained from Doppler profiles of the hydrogen fragments. Most of the energy released into translation will be carried away by the hydrogen atom on account of momentum conservation, leading to a Doppler broadening of the Lyman-α absorption line. By examining the Doppler broadening of the Lyman-α transition, information on the kinetic energy distribution can be drawn (compare page 42). In figure 89 three Doppler profiles, recorded at 255 nm under different pyrolysis conditions, are presented. The one-color background signal, which is also visible without the excitation laser, was subtracted in all spectra. All three absorption profiles are described well by a Gaussian function (solid line), indicating a *Maxwellian* speed distribution. The contributions to the total broadening of the profiles induced by the fine structure splitting, the laser bandwidth and the speed distribution of the parent was neglected. As evident from figure 89, the full width at half maximum (FWHM) of the Doppler profile counter intuitively *decreases* with increasing pyrolysis temperature. This dependence was observed at all excitation wavelengths and indicates the possible presence of a second source of hydrogen atoms in addition to the pyrolytically produced l-C_3H_2.

An explanation for the decreasing FWHM of the Doppler profile is obtained by comparing the mass spectra presented in figure 86 and 87 as discussed above. They document that conversion of the precursor is incomplete at low and medium temperatures, and some IC_3H_2 intermediates are still present. Presumably due to the residual fundamen-
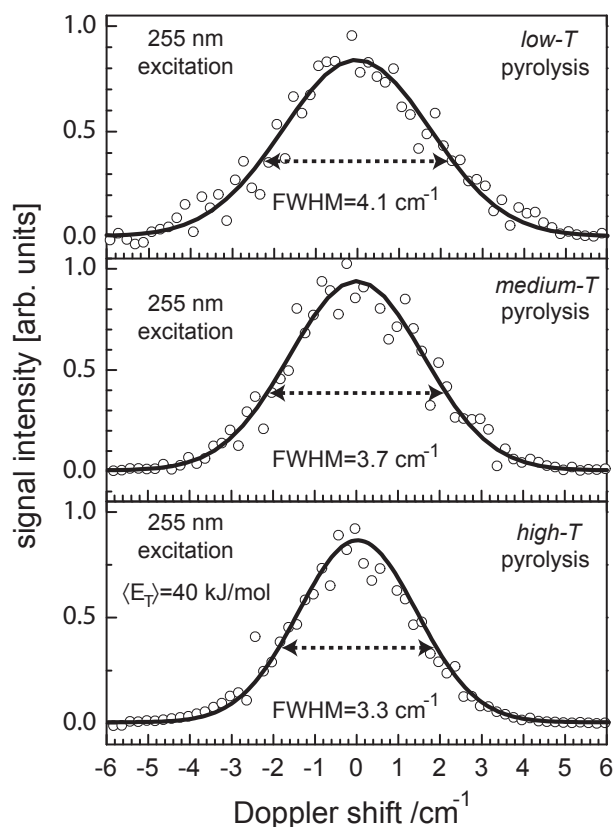
Figure 89: H-atom photofragment Doppler profiles (255 nm excitation). The FWHM decreases with increasing temperature of the pyrolysis source. At the highest pyrolysis temperature (bottom trace), where quantitative conversion of the precursor is achieved, a translational energy release of 40 kJmol^{-1} is obtained.

tal wavelength used to generate the VUV light, these intermediates are partially converted to the carbene by photolysis in the interaction region. This photolytically produced carbene will possess significant internal energy as indicated by the appearance of a broadened carbene signal in the TOF spectrum recorded at 121.6 nm (fig. 87, top trace). H atoms generated from such photolytically produced carbenes will carry away more translational energy, leading to a broader Doppler profile. Therefore, only the profiles recorded at high pyrolysis temperature are considered for interpretation of the dissociation process. Using formula 2.1 presented on page 7[35], an expectation value for the translational energy release of $\langle E_T \rangle = 40$ kJmol^{-1} could be extracted from the FWHM of 3.3 cm^{-1}.

Another possibly interfering species might be HI, which is present in small amounts in the mass spectrum and is known to be a source of fast H atoms[205]. However, in the energy range of interest its absorption cross section is continuously decreasing to the red and has its maximum at around 222 nm[206]. At 255-nm excitation HI contributions will be negligible as mentioned above. Therefore, a rather long excitation wavelength at the red edge of the absorption band was chosen for a detailed analysis of the dependence of the Doppler profile on the pyrolysis temperature.

The loss of a hydrogen atom can lead to two products, linear (l-) and/or cyclic (c-) C_3H. As both channels are energetically very close and do not exhibit a reverse barrier (see fig. 85), it is not possible to securely distinguish them. At first glance l-C_3H seems to be the most probable reaction product, but inspection of figure 85 reveals that the lowest reaction barrier is the isomerization to c-C_3H_2. Thus energized l-C_3H_2 is able to access the c-C_3H reaction channel as well. In a thermal reaction, a dissociation on the c-C_3H_2 part of the ground state surface will lead to c-C_3H, while dissociation on the l-C_3H_2 part of the surface will lead to l-C_3H. In agreement to the preceding femtosecond experiments, this picture assumes a fast internal conversion of propadienylidene to the electronic ground state. IC is then followed by a statistical dissociation. The almost perfect Gaussian shape of the Doppler profile also supports a statistical mechanism and no anisotropies were found when applying different laser polarizations. The measured translational energy release of $\langle E_T \rangle = 40\,\mathrm{kJmol^{-1}}$, corresponding to 37% of the excess energy and based on the computed heat of reaction of path shown in equation 11.3, is comparatively large.

When the maximum observed H-atom velocity is extracted from the wavenumber of the Doppler profile, at which the signal has decayed to zero, an upper limit for the excess energy of 115–120 kJmol^{-1} is calculated (fig. 90). For deriving this value, the formula for Doppler broadening on the margin of page 7 was rearranged and substituted into $E_{max} = 0.5\,m_H\,v_{max}^2$. This yields equation 11.4.

$$E_{max} = \frac{1}{2}m_H\left(c - \frac{(\widetilde{\nu}_0 + \widetilde{\nu}_{max})c}{\widetilde{\nu}_0}\right)^2 \approx 6.688\,\frac{\mathrm{kJcm^2}}{\mathrm{mol}} \times (\widetilde{\nu}_{max})^2 \quad (11.4)$$

Herein E_{max} is the maximum possible excess energy, m_H is the mass of hydrogen, c is the speed of light, $\widetilde{\nu}_0$ is the wavenumber of the Lyman-α transition of H at rest and $\widetilde{\nu}_{max}$ is indicated in figure 90. The computational value, however, lies at 104 kJmol^{-1} for c-C_3H + H. Even at the highest pyrolysis temperature the experimental and theoretical value showed this discrepancy. Typical vibrational temperatures of pyrolytically generated radicals are 100–200 K, corresponding to only 1–2 kJmol^{-1} of internal energy[1]. Thus there are two possible reasons for these discrepancies: Either (a) the dissociation energy is slightly lower than computed or (b) even at the highest pyrolysis temperatures still a small amount of carbenes is present that contain some internal energy. If it is assumed that the true dissociation energy is only 12 kJmol^{-1} smaller than computed, the translational energy release corresponds to $\langle E_T \rangle = 34\%$. This translational energy release is relatively high for a statistical reaction but not unusual when compared to other reactive species[100,207].

Figure 90: An upper limit for the excess energy can be calculated from the point where the profile reaches the baseline.

11.3 RATE CONSTANTS FOR THE LOSS OF HYDROGEN

Recording the H-atom signal as function of the delay time between excitation and ionization laser gives information on the rate constant of the dissociation process. Reaction rates can be extracted afterwards from the rise time of the signal according to equation 6.3 (page 44).

---

[1] The vibrational temperature is estimated by comparison of simulated spectra with rotationally resolved REMPI spectra of allyl radicals.

As visible in figure 91, the signal rises within a few nanoseconds or less at all excitation wavelengths; thus the rate of H-atom loss is faster than the time resolution of the ns-laser setup (5–10 ns). Note that the
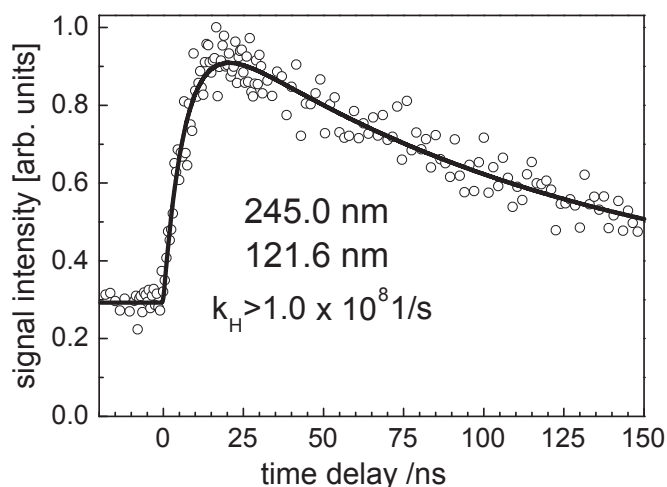
Figure 91: H-atom signal as a function of the time delay between excitation (245 nm) and ionization (121.6 nm) laser pulse, giving a rise time that is faster than the time resolution of the ns-laser setup. The H-atom loss occurs within less than a few nanoseconds (analysis using eq. 6.3 on page 44).

signal decay is due to the drift of the H atoms out of the observation region and has no chemical significance and reflects the recoil velocity of the photofragments, which was already analyzed by Doppler spectroscopy.

To support the experiments, simple RRKM calculations were performed utilizing the B3LYP frequencies as well as the CCSD(T) barriers of *Mebel et al.*[76]. These calculations were augmented by B3LYP/6-311G** frequency calculations for some of the transition states. The frequencies[2] are listed in table 11.

Table 11: Important vibrational frequencies for modeling the unimolecular rate constants of C_3H_2. All values are given in cm^{-1}.

l-C_3H_2:[2]	3168, 3091, 2043, 1485, 1147, 1052, 1042, 293, 233
TS: l-$C_3H_2 \rightarrow$ c-C_3H + H:	3252, 1677, 1252, 956, 892, 869, 616, 593, i-869
TS: l-$C_3H_2 \rightarrow$ l-C_3H + H:	3301, 2032, 1237, 847, 744, 662, 348, 224, i-842
TS: l-$C_3H_2 \rightarrow C_3$ + H_2:[2]	3133, 2388, 1747, 1124, 903, 520, 427, 259, i-1064

The rotations of the reactant and the TS were neglected in the RRKM calculations. The results indicate that H-atom loss of l-C_3H_2 is the dominant reaction channel in the energy range investigated in the present study. In table 12 the calculated rates are summarized for two excitation wavelengths. At 230 nm excitation the calculations predict a rate constant of 8.2×10^{10} s^{-1} for the formation of l-C_3H, 3.5×10^{10} s^{-1} for the loss of H_2 and 2.0×10^{10} s^{-1} for the formation of c-C_3H, following a fast isomerization to cyclopropenylidene. At 260 nm the rates

---

[2] Note that the frequencies for l-C_3H_2 and for the TS of the reaction l-$C_3H_2 \rightarrow C_3$ + H_2, were taken from ref. 76.

Table 12: RRKM rate constants

Product	260 nm	230 nm
c-C_3H+H	$3.0 \times 10^9\,s^{-1}$	$2.0 \times 10^{10}\,s^{-1}$
l-C_3H+H	$9.8 \times 10^9\,s^{-1}$	$8.2 \times 10^{10}\,s^{-1}$
C_3+H_2	$6.1 \times 10^9\,s^{-1}$	$3.5 \times 10^{10}\,s^{-1}$

are calculated to be $9.8 \times 10^9\,s^{-1}$, $6.1 \times 10^9\,s^{-1}$ and $3.0 \times 10^9\,s^{-1}$, respectively. The ratios of the calculated rates indicate that the channel for the loss of H_2 decreases in importance at shorter wavelengths when compared to the loss of H atoms. It thus seems that l-C_3H is the dominant reaction product. However, the numbers are very close together and even small changes in the barriers or frequencies will have a significant impact on the relative order. Nevertheless, the measured subnanosecond rate is indeed in agreement with the RRKM computations as expected in the case of a statistical dissociation. This is in contrast to nanosecond time-resolved experiments on several alkyl radicals which give rates that are slower than expected by means of RRKM theory[100,107,208] (compare chapter 6). It is therefore interesting to note that propadienylidene, like unsaturated radicals[106,209], does not show such an unexpectedly slow H-atom loss.

Additionally, H-atom photofragment excitation (action) spectra were recorded by integrating the signal intensity of the H^+ ions as a function of the excitation wavelength. These, however, did not show any structure. In the energy range used for excitation in this study, the only available absorption spectra were recorded in a rare gas matrices[184,188]. The matrix spectrum reaches its maximum around 237 nm. Only a very broad vibronic structure is observable. Several possibilities could be responsible for the differences between the observed structureless action spectrum and the matrix spectrum: a.) The hydrogen detection is sensitive to only one possible reaction channel (loss of *atomic* hydrogen) and no conclusions can be drawn on the loss of H_2 molecules after excitation. b.) A further explanation might be that the very high temperatures needed for fully converting the precursor[3] negatively influence the stability of the pyrolysis source. This might have a large impact on the action spectra, which require long acquisition times. Thus a complete conversion of both precursor and IC_3H_2 intermediate cannot be assured over an entire scan.

The results obtained for l-C_3H_2 are relevant for earlier work on the propargyl radical, C_3H_3. *Fahr et al.* examined the absorption spectrum of propargyl in the UV range[210] and reported a maximum at around 242 nm. In later work on the photodissociation dynamics of the radical a H-atom action spectrum was recorded with similar appearance[106]. The data were confirmed by photofragment translational energy spectroscopy[211]. Computational work questioned this

---

[3] The spectra shown in fig. 91 and fig. 89 (bottom trace) could be recorded at very high pyrolysis temperatures due to the considerably shorter acquisition time needed for such measurements as compared to action spectra.

assignment and suggested a C_3H_2 isomer to be the carrier of the H-atom signal[212,213]. In principle, propadienylidene might be formed by overheating propargyl in the nozzle. However, the data presented here indicate that this is not the case. The Doppler profile at the highest temperature shows a FWHM of $3.3\,cm^{-1}$ and is thus significantly broader than the one obtained for propargyl at the same wavelengths (FWHM $= 2.4\,cm^{-1}$). A sub-nanosecond dissociation time was measured (fig. 91) for l-C_3H_2, thus H-atom loss occurs at least two orders of magnitude faster than after exiting propargyl. Additionally, neither the action spectrum nor the earlier matrix absorption spectrum of propadienylidene resemble the H-atom action spectrum recorded for propargyl. Therefore, propadienylidene is unlikely to contribute to the absorption[210] or the H-atom action spectrum of the propargyl radical[106].

As a conclusion, the combined study of l-C_3H_2 by nanosecond- and femtosecond-resolved laser experiments shows that after optical excitation the electronically excited $C\,^1A_1$ state of the carbenes deactivates to the hot ground state with a time constant of 70 fs. From the ground state surface the loss of hydrogen atoms occurs with a rate constant greater than $1 \times 10^8\,s^{-1}$ and $\langle E_T \rangle = 34\%$ of the excess energy are released into the H fragment. The reaction proceeds statistically and is well described by simple RRKM estimations.

EXCITED-STATE DYNAMICS OF THE 2,3-DIMETHYLBUT-2-YL RADICAL

12.1 INTRODUCTION

Considerable interest in the excited-state dynamics arises not only for free carbenes but also for radical species. Ultrafast investigations on the excited states have been performed for the *t*-butyl radical, the benzyl, the ethyl and the propargyl radical during my "Master's Thesis"[30,112]. Today's investigations of excited-state deactivations go into the direction of polyatomic molecules as has, e. g., been demonstrated with multiple examples by the *A. Stolow* group[50,214,215]. Exploring the dependence of the molecular dynamical response on different functional groups[166] is a systematic way of elucidating the new field of the femtochemistry[216] for polyatomics. A deep understanding of the functional group dependence, as has been developed for the ground state surface of molecules, still has to be evaluated for excited-state reactivity. In a recent publication the excited-state dynamics of the 3s and 3p Rydberg states of *t*-butyl have been presented[30].

In this chapter, the results on the closely related 2,3-dimethylbut-2-yl (DMB) are summarized, which was produced by jet flash pyrolysis from 2-iodo-2,3-dimethylbutane according to scheme 10. The experimental approach and setup was described in detail in chapters 3.4 and 9.2. Both the *t*-butyl as well as DMB are tertiary radicals that only differ by two methyl groups at the side chain (fig. 92). As pre-

t-butyl radical

2,3-dimethylbut-2-yl radical

Figure 92: The *t*-butyl and the 2,3-dimethylbut-2-yl radical are closely related and only differ in the presence of two methyl groups.

Scheme 10: Pyrolytic generation of 2-iodo-2,3-dimethylbutane

sented in the pioneering work[110] of *H. R. Wendt et al.*, the absorption spectrum of 2,3-dimethylbut-2-yl has its maximum at around 266 nm (fig. 93) conveniently enabling excitation with the third harmonic of a Ti:Sa oscillator. At a wavelength of 265 nm the radical was excited into the 3p Rydberg state. The excited state was then ionized with pulses of 795 nm central wavelength using femtosecond time-resolved pump-probe spectroscopy as was introduced in chapter 2.4. The C_{3v} symmetrical *t*-butyl radical shows only a rel. weak absorption band for the excitation into 3p Rydberg state. It is symmetry forbidden according to ref. 110. On the other hand, for the DMB radical this transition is allowed by symmetry[110], and the 3p absorption band is very strong. Already the absorption spectra of both closely related tertiary radicals deviate from one another. Thus it is interesting to compare their excited-state deactivation and see how it is affected by the aliphatic side chains.

Despite the importance of hydrocarbon radicals, the photochemistry of alkyl radicals is not fully understood. Although few radicals exist

Figure 93: Gas phase absorption spectra of the *t*-butyl (upper trace) and the 2,3-dimethylbut-2-yl radical (lower trace), recorded by *Wendt and Hunziker*. The spectrum was taken and adapted from ref. 110.

such as allyl which show dissociation rate constants in agreement to statistical RRKM theory, many alkyl radicals show strong deviations from the theoretical values as has been discussed for the propyl radical in chapter 6. Two hypotheses try to give an explanation for these observations: 1.) The deactivation of the excited state proceeds to regions on the ground state surface which do not randomly distribute the thermal energy of the molecule[129], and/or 2.) the excited states are long lived and hence the slow deactivation detains the dissociation of the molecules. Experimental approaches have so far yielded relatively short time constants for the excited-state deactivation times of radicals, which lie in the region of 30 fs to 2 ps[30,112]. However, these studies are limited to detectable ("bright") states.

New approaches for fortifying the two hypotheses go in the direction of varying functional groups (R_1, R_2) of the radicals and measuring the changes in dissociation rates for reactions exemplified in equation 12.1. This has been demonstrated recently for the allyl radical and its derivative the 2-methylallyl radical[14,207].

$$RH_2C\text{–}\dot{C}R_2 \xrightarrow[-H\cdot]{h\nu} RHC\text{=}CR_2 \tag{12.1}$$
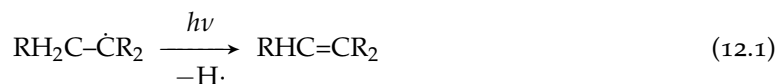
Although this chapter is focused on excited-state dynamics, rather than on elucidating further photochemical dissociation processes, it also aims to examine the functional group dependency of alkyl radical femtochemistry in a systematic way.

The experiments were performed with the apparatus described in chapter 3.4. It was the same setup as was used for studying the excited-state dynamics of phenylcarbenes in chapter 9 and similar conditions were used. The precursor was synthesized according to ref. 217.

The upper trace of figure 94 shows the time-of-flight spectrum obtained when employing the precursor with the pyrolysis turned off. Mass peaks are visible at $m/z = 43$, $m/z = 84$, $m/z = 85$, $m/z = 128$ and $m/z = 212$ corresponding to propyl, 2,3-dimethyl-2-butene, DMB, HI and 2-iodo-2,3-dimethylbutane. As known from other halides, the precursor already shows partial photodissociation[218] or dissociative photoionization[219] (DPI). These processes yield a signal at $m/z = 85$ in the mass spectrum. The intensity of the mass peak at $m/z = 84$ (2,3-dimethyl-2-butene) increased over the day and could be strongly reduced by pulling vacuum on the seeding line for $\approx 1\,\mathrm{min}$. Hence it is produced from decomposition of the precursor forming HI as well. The precursor changed its color from colorless to red after around $1\,\mathrm{h}$ at room temperature. The decomposition yields the volatile 2,3-dimethyl-2-butene that can be evaporated easily and is not linked to the pyrolysis or DPI. Propyl ($m/z = 43$) seems to be formed from DPI
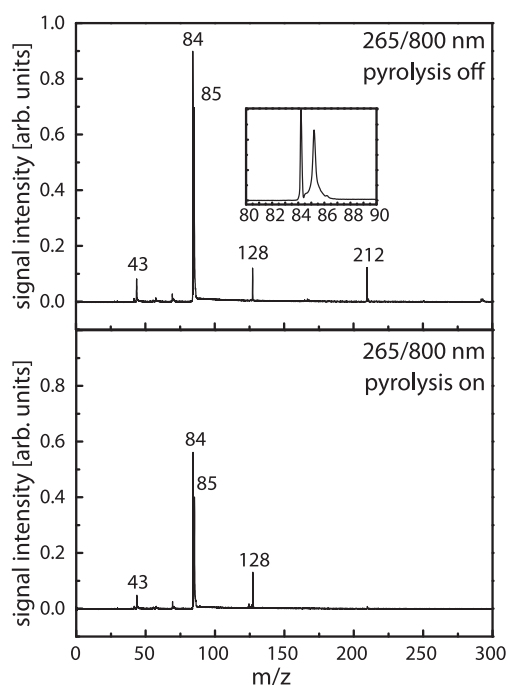
Figure 94: Time-of-flight spectra of 2-iodo-2,3-dimethylbutane at different pyrolysis conditions. With pyrolysis on the precursor is fully converted. However, the signal of the radical also diminishes and further examination with VMI is necessary.

of the DMB radical by homogeneously cleaving the central C–C bond. Upon turning on the pyrolysis, the precursor is fully converted (fig. 94, bottom trace). Unfortunately the radical signal decreases as well. However, this situation is also found for other precursors[161] and can arise if the cross section for the precursor is higher than for the intermediate. Thus the cations with $m/z = 85$ produced by DPI give a stronger signal than ions of the same mass produced by ionization of the radical.

Referring to chapter 9.3.1, VMI showed to be an efficient method to distinguish pyrolytically generated intermediates from those produced by DPI. This chapter gives a further proof of concept that analyzing the photoion images enables to optimize the pyrolysis conditions. Fig-
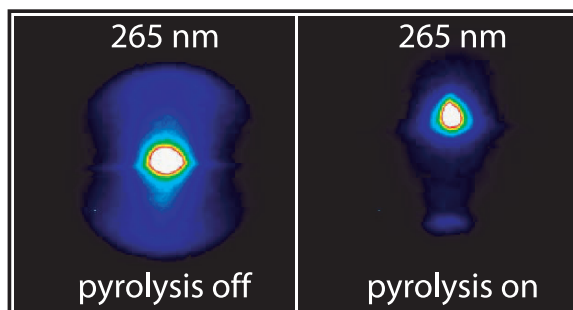
Figure 95: Velocity map images taken with a mass gate around $m/z = 85$ at different pyrolysis conditions. The intensity of the 265 nm was increased creating an one-color signal.

ure 95 presents velocity map images of 2-iodo-2,3-dimethylbutane at different pyrolysis conditions. These were recorded at an increased laser intensity (150 μJ) with horizontal polarized 265-nm light alone. The images only include masses around $m/z \approx 85 \pm 2$. Note that the mass selectivity of the photoion images is limited by the duration of the voltage pulse applied to the front MCP of the detector. Hence in contrast to the TOF spectra in fig. 94, the mass resolution is not sufficient to separate the two mass peaks at $m/z = 85$ and $m/z = 84$. However, since $m/z = 84$ corresponds to 2,3-dimethyl-2-butene and is not formed by dissociative photoionization, it will appear as a sharp central spot in the image and does not disturb the interpretation. With pyrolysis off, the image shows a sharp central spot and two polarized hour-glass-shaped extensions (fig. 95, left-hand side). When turning the pyrolysis on, the polarized part disappears, the central peak shifts in the direction of the molecular beam and the signal slightly intensifies to a sharp spot. Even though the difference is not as pronounced as was demonstrated for the diazirines in chapter 9.3.1 (page 80), the images enable a differentiation between bond fissions induced by laser radiation and those induced pyrolytically. With the pyrolysis turned off the 2-iodo-2,3-dimethylbutane dissociates and due to momentum conservation picks up a considerable amount of kinetic energy, which leads to the polarized extensions. By turning on the pyrolysis no precursor is further introduced into the molecular beam and the signal with $m/z = 85$ loses the extended part. Hence it can be concluded that DPI and/or photodissociation of the precursor is reduced and the mass signal at $m/z = 85$ must have a high contribution of the pyrolytically produced DMB radical at these conditions. In contrast to the diazirines, examined in the same way (page 80), the laser induced dissociation does not lead to an unpolarized ring of photofragments but to a polarized image. This indicates that the dissociation of the precursor proceeds in a direct way and suggests a photodissociation with a low barrier.

The mass spectrum recorded with pyrolysis on shows that several different species are present. The DMB radical cannot be produced cleanly from its precursor. On the one hand, this has the disadvantage that no time-resolved photoelectron spectra can be recorded without contributions from other masses, since the apparatus was not designed for coincidence measurements. Thus the examination was restricted to time-resolved TOF mass spectra. These, on the other hand, can easily be calibrated due to the many reference peaks, and the IRF can be deduced more precisely by analyzing the time dependence of other masses. In this examination the 2,3-dimethyl-2-butene was ionized nonresonantly by the 265-nm pump and 795-nm probe pulses. Hence the IRF as well as the exact zero in time could be determined by fitting the time-dependent signal of mass $m/z = 84$ to a Gaussian function. The result is given in the top trace of fig. 96 and yields a FWHM of 119 fs ($\sigma = 51$ fs).
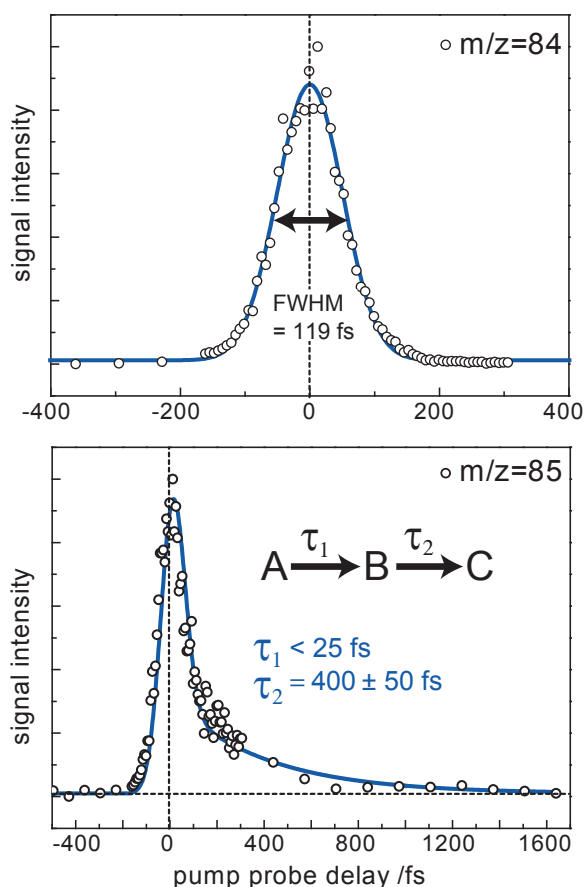
Figure 96: Signal intensity of mass $m/z = 84$ and $m/z = 85$ as a function of the time delay between excitation and ionization (pump 265 nm, probe 795 nm).

For extracting the decay time-constants of the DMB radical, the IRF was convoluted with a monoexponential molecular response function (see equation 5.7 on page 36) and the convolution compared to the experimental results by a least squares fit. Exclusively the time

constant and amplitude of the function were optimized, whereas the FWHM and the zero in time were held fixed and taken from the time-dependent ion signal of 2,3-dimethyl-2-butene. As visible in figure 97,
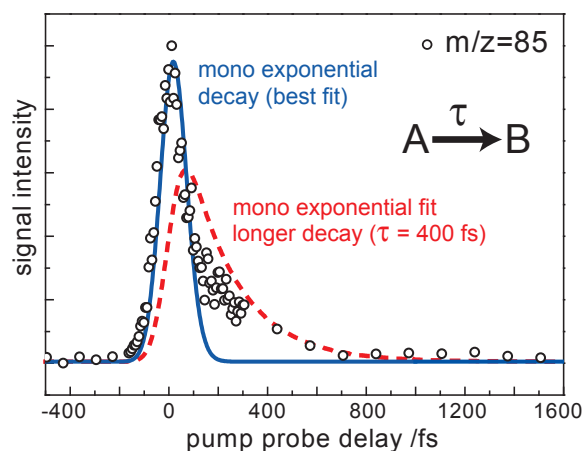
Figure 97: Signal intensity of mass $m/z = 85$ as a function of the time delay between excitation and ionization (pump 265 nm, probe 795 nm). The experimental data was fit to a monoexponential model.

the monoexponential model does not adequately describe the experimental data and a second fit was performed utilizing a biexponential deactivation mechanism as described by function 5.13 on page 38. In this function, the linear combination of $S_{(t)}^A$ and $S_{(t)}^B$ reflects a decay of the initially prepared state with a time constant τ_1. Additionally, an exponential rise of a lower-lying state also with τ_1 and its consecutive deactivation with a second time constant τ_2 are added by introducing $S_{(t)}^B$. This model very nicely describes the experimental data and time constants of $\tau_1 < 25$ fs and $\tau_2 = 400 \pm 50$ fs could be extracted as shown in the bottom trace of figure 96.

12.4 CONCLUSIONS AND DISCUSSION

In contrast to *t*-butyl, the excitation at 265 nm is symmetry allowed for the DMB radical[110]. Hence the excitation has a much higher oscillator strength and former by C_{3v} symmetry forbidden transitions become accessible[110].

The 3p state of the DMB radical deactivates in a two-step process. This observation is different when compared to the deactivation of the 3p state of the closely related *t*-butyl radical[30]. For the *t*-butyl radical the deactivation of the 3p Rydberg state was surprisingly slow ($\tau = 2$ ps), especially when compared to the lower-lying 3s state, which deactivated on a time scale of 100 fs. In the DMB radical one methyl group was replaced by a more "floppy" *i*-propyl group. This increases the vibrational state density of the molecule and breaks the C_{3v} symmetry. These aspects might explain an accelerated deactivation of the DMB radical when compared to *t*-butyl. A similar effect of functional groups on the deactivation times of excited states has recently been reported for several benzenes[166].

An interesting point to discuss is the two-step deactivation of the 3p state when compared to *t*-butyl. Since the reported time-dependent ion signal of *t*-butyl in ref. 30 has a lower signal-to-noise ratio in the region between 0–500 fs, it is possible that the first deactivation step is simply not resolved. The first time constant ($\tau_1 < 25$ fs) might originate from a quick deformation and the movement of the induced wave packet out of the FC region. If the replaced side group of DMB opens or accelerates the passage through a deactivation funnel, the shorter time constants might reflect this process. This then could enable a faster excited-state deactivation (see fig. 10 on page 13). When analyzing the potential energy surfaces of *t*-butyl in the appendix A.5, a conical intersection to the ground is apparent along the asymmetric C–C stretching mode (fig. 122 on page 156). By adding the *i*-propyl group the "3p $\rightarrow$ 3s" or "3p $\rightarrow$ ground-state" transition becomes accelerated. The measured second time constant ($\tau_2 = 400 \pm 50$ fs) is in the order of the excited-state lifetime reported for the 3s Rydberg state of *t*-butyl.

SYNTHESIS

13.1 1,3-DIBROMOPROPYNE

The synthesis is based on ref. 220 with minor modifications. 17.85 g (111.67 mmol, 5.72 ml) bromine were slowly added to a solution of 25.06 g (447.67 mmol) potassium hydroxide in 170 ml water at 5°C. After 10 min at 5°C, 13.28 g (111.67 mmol) propargyl bromide (Aldrich) diluted with toluene (20%) was added drop wise to the prepared solution of hypobromite while stirring. The yellow solution was stirred for 1 h at 0–5°C and the product extracted with 3×50 ml Et$_2$O and dried over magnesium sulfate. 1,3-Dibromopropyne was distilled under argon atmosphere using a Vigreux column and is not stable in air after purification but can be stored under argon at -20°C for one month without noticeable decomposition.

b.p.: 55°C (15 mbar); 52-55°C (13.3 mbar)[220]
^{1}*H-NMR* (250 MHz, CDCl$_3$): $\delta = 3.8$ (s, 2H, CH$_2$) ppm
MS/TOF-PI(+) 118 nm: *m/z* (%) = 200 (49), 198 (100), 196 (51) [M]$^+$; 119 (70), 117 (70) [M-Br]$^+$

13.2 3-BROMO-1-IODOPROPYNE

Two solutions were prepared separately: 9.66 g propargyl bromide solution (80%) in toluene (7.73 g pure propargyl bromide, 65.0 mmol) and a solution of 16.49 g iodine (65.0 mmol) in 16 ml of saturated KI solution in water[221]. Both solutions were added within one hour simultaneously from separate dripping funnels to a solution of 14.55 g (260 mmol) NaOH in 98 ml of water with agitation at 0–5°C. After 3 h the product is extracted from the yellow reaction mixture with 3 times 20 ml diethyl ether, dried over MgSO$_4$ and distilled under inert gas over a Vigreux column. The yield of the colorless product was 28% (4.48 g, 18.3 mmol) and can be stored at -20°C under argon.

b.p.: 59–60°C (3 mbar); 62°C (4 mbar)[221]
^{1}*H-NMR* (250 MHz, CDCl$_3$): $\delta = 4.02$ (s, 2H, CH$_2$) ppm
MS/TOF-PI(+) 118 nm: *m/z* (%) = 246 (97), 244 (100) [M]$^+$; 165 (40) [M-Br]$^+$; 38 (45) [M-BrI]$^+$

13.3 1,3-DIIODOPROPYNE

1,3-diiodopropyne was prepared from 3-bromo-1-iodopropyne by the Finkelstein reaction[222]. 1.00 g (4.08 mmol) of 3-bromo-1-iodopropyne was slowly added at 5°C to 20 ml of a saturated solution of KI in acetone. Immediate precipitation of KBr was noticeable. After 1 h at 5°C the reaction mixture was distilled over a Vigreux column under argon. The yield of the colorless product was quantitative and can be stored at -20°C under argon.

b.p.: 52–55°C (2 mbar)
MS/TOF-PI(+) 118 nm: *m/z* (%) = 38 (100) [M-2I]$^+$

All steps were performed under argon atmosphere[223]. Note that inhalation of 3-chlorocyclopropene causes headaches and dizziness. 50 ml of mineral oil for IR spectroscopy (suitable for nujol mull preparations, Sigma-Aldrich CAS:8042-47-5) was purified by removing volatile components at 0.1 mbar and 90°C. After cooling 20°C and flushing with argon, 2 ml (3.00 g, 16.9 mmol) of tetrachlorocyclopropene were added. The reaction flask was connected to a special trap that could be attached to the seeding line of the molecular beam apparatus after the synthesis (see chapter 3.2). With a syringe 17.2 ml (17.2 g, 59.1 mmol) of tributyltin hydride were slowly added through a septum over a period of 30–50 min and the mixture was kept at 20°C. After tributyltin hydride was added, the mixture was heated for 30 min to 80°C and then shock frozen with liquid nitrogen. At 30°C and 0.1 mbar the product was distilled for 5–8 min into the trap held at −196°C. Longer distillation times increase the yield at the cost of purity.

MS/TOF-PI(+) 118 nm: *m/z* (%) = 74 (100), 75 (3), 76 (32) $[M]^+$

13.5 ACETONE ISOHYDRAZONE

8.71 g (11.0 ml) acetone and 40 ml (0.534 mol) of a 25% NH_3 solution are stirred for 30 min at room temperature[224]. The solution is then cooled down to 0°C and 12.4 g (0.11 mol) of hydroxylamine-O-sulfonic acid (HOSA) are slowly added so that the temperature of the mixture does not exceed 10°C. After stirring for one hour, NH_3 and acetone are evaporated under reduced pressure for about 3 min. 36 g of NaOH are dissolved in 21 ml of water at approx. 60°C. This solution is then added very slowly to the reaction mixture, which should not exceed 10°C. The two layers are separated and the upper layer (approx. 80% product) is transferred into a second separatory funnel. After one to two hours the layers are separated again. The upper layer (> 80% product) can now be stored at −20°C for about one month. Further purification can be achieved by storing the crude product over molecular sieves (4 Å) and/or solid KOH and subsequent distillation with a 40 cm packed column at 1 atm over solid KOH. The colorless product then crystallizes after approx. one hour at RT. If crystallization does not take place the distillation must be repeated. Note that the boiling point is dependent on how dry the acetone isohydrazone is, since it forms an azeotrope mixture with water which boils at 98°C.

b.p.: 102–103°C (1.01 bar); 106°C (1.01 bar)[225]
^{1}*H-NMR* (250 MHz, acetone D6): δ = 1.32 (s, 6H, CH$_3$), 1.84 (s, 2H, NH) ppm
MS/TOF-PI(+) 118 nm: *m/z* (%) = 72 (20) $[M]^+$; 42 (100) $[M-N_2H_2]^+$

13.6 3.3-DIMETHYLDIAZIRINE

3.3-Dimethyl-diazirine is explosive, and *the reaction procedure was performed with protective gear!* A small reaction flask, was continuously flushed with argon and connected to a trap held at −78°C (that could

directly be connected to the molecular beam apparatus later on, see fig. 17 on page 19).
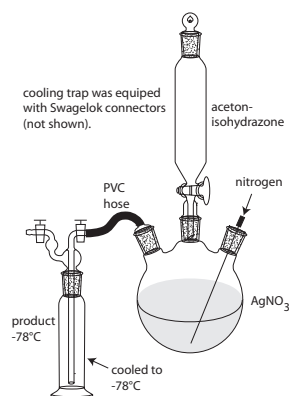
Figure 98: Trapping apparatus (traps shown on page 19)

1 g of acetone isohydrazone was dissolved in 15 ml of 2M NaOH and added at RT within 3 min to 5.5 g of fresh AgNO$_3$ (VWR Normapur grade) diluted in 7 ml of water. The reaction mixture immediately turned black and formation of gas was noticeable. The mixture was warmed to 50°C for 10 min after the formation of gas had receded.

MS/TOF-PI(+) 118 nm: *m/z* (%) = 42 (100) [M-N$_2$]$^+$

13.7 3.3-PENTAMETHYLENEDIAZIRIDINE

37 ml (0.49 mol) 25% aq. NH$_3$ solution and 16.3 g (17.3 ml, 0.17 mol) cyclohexanone were stirred at RT for 30 min. At 5°C 13.9 g (0.111 mol) of 80% hydroxylamine-O-sulfonic acid (Aldrich) were added slowly in approx. 45 min[226]. After one hour the mixture was stored at −16°C for several hours. The crude product was filtered, washed with diethyl ether, dried under reduced pressure (15 mbar) and purified by vacuum sublimation (10 mbar, bath temperature 76°C) with a yield of 29% (3.66 g).

m.p.: 105–107°C; 104–107°C[226]

13.8 3.3-PENTAMETHYLENEDIAZIRINE

3.40 g (20.1 mmol) AgNO$_3$ were diluted in 10 ml of water. While stirring 10 ml of 2 N NaOH were slowly added. The brown precipitate (Ag$_2$O) was filtered and washed with water, methanol and ether[226].

1.00 g (8.9 mmol) 3.3-pentamethylenediaziridine were dissolved in 22 ml diethyl ether at 34°C. At RT the Ag$_2$O was added in 4 min with agitation. A silver precipitate was noticeable on the inner side of the flask. After one hour the solution was filtered and dried over Na$_2$SO$_4$. Diethyl ether was evaporated at 0°C and 40 mbar and the product distilled at 33°C (41 mbar) with a yield of 68% (0.68 g). The product can be stored diluted in Et$_2$O at −16°C.

b.p.: 33–35°C (41 mbar); 33°C (40 mbar)[226]
MS/TOF-PI(+) 118 nm: *m/z* (%) = 82 (100) [M-N$_2$]$^+$

13.9 3-chloro-3-phenyldiazirine
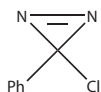
The reaction was performed under dim light. 5 g (31.9 mmol) benzamidine hydrochloride and 12.8 g (0.302 mol) LiCl were dissolved in 190 ml DMSO[138]. Under agitation 400 ml aq. 10% sodium hypochlorite solution with 20 g of NaCl were run into the reaction mixture, while the product was *continuously* evaporated (20 mbar) into a cooling trap held at −126°C (duration approx. 20 min). The reaction is strongly exothermic. The product and water solidify in the cooling trap. At atmospheric pressure the cooling trap was allowed to warm to room temperature and 2 g of LiCl were added under agitation. The two phases were separated. The upper water phase was discarded. The pale yellow lower phase was isolated with a yield of 82% (4.1 g). The product can be stored at −16°C for several months.

MS/TOF-PI(+) 265 nm: *m/z* (%) = 124 (100) $[M-N_2]^+$

13.10 3-phenyl-3-(trifluoromethyl)diazirine
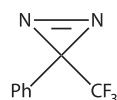
The synthesis was performed without modifications as presented in ref. 139. The product can be stored in the dark at −20°C when diluted with 50% diethyl ether. Before starting the experiment the diethyl ether was partially evaporated and the remaining Et_2O was removed by shortly pumping the seeding line of the molecular beam apparatus.

MS/TOF-PI(+) 265 nm: *m/z* (%) = 158 (100) $[M-N_2]^+$

13.11 N-benzylacetophenone imine
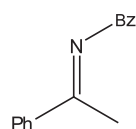
10 g (83.2 mmol) of acetophenone, 8.93 g (83.3 mmol) of benzylamine and 10 mg (52.6 µmol) of p-toluenesulfonic acid monohydrate were dissolved in 23 ml of toluene, which had been dried over $MgSO_4$[227]. The mixture was refluxed for ≈ 2 h with a *Dean-Stark* trap until ≈ 1.5 ml (83.2 mmol) of H_2O had separated and then cooled down to 0°C, washed with 2 × 8 ml of $NaHCO_3$ solution, 1 × 8 ml water and dried over Na_2SO_4. Toluene was evaporated at 77 mbar (≈ 60°C) and the residue distilled with reduced pressure (0.3 mbar); boiling point 122–135°C. The liquid product was then filled into a longish glass tube and allowed to crystallize at 0°C. The upper fraction is discarded and the crystallization can be repeated for further purification by "zone" crystallization. The yield was 75% (13.1 g).

b.p.: 122–135°C (0.3 mbar); 125–126°C (0.5 mbar)[227]

13.12 3-methyl-3-phenyl-diaziridine
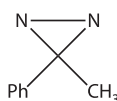
10.45 g (50 mmol) of N-benzylmethylphenyl ketimine were dissolved in 100 ml of methanol[140]. This solution was dripped over 3 h to 75 ml of liquid ammonia at −78°C, under agitation. 8.5 g (90%, 7.95 g pure, 67.6 mmol) of technical grade hydroxyl amine-O-sulfonic acid (HOSA) were dissolved in 50 ml of MeOH and slowly added to the reaction mixture over 2 h. Afterwards the solution was stirred over night at

room temperature. The mixture was extracted with $3 \times 50\,ml$ of diethyl ether, dried over Na_2SO_4 and the Et_2O was evaporated. While evaporating the white precipitate was filtered off several times and extracted with Et_2O. After evaporating the diethyl ether the yield of the yellow raw product was 96% (6.45 g), which was used without further purification in the following synthesis.

13.13   3-METHYL-3-PHENYLDIAZIRINE

16.5 g (97.1 mmol) of $AgNO_3$ were dissolved in 50 ml of water at 100°C, 100 ml of 1 M NaOH were added, the brown precipitate was filtered off, washed with acetone and Et_2O, dried under reduced pressure for 5 min and immediately used. 6.45 g ($\approx$ 48.1 mmol) of the raw product from synthesis 13.12 were dissolved in 130 ml of Et_2O, the freshly prepared silver oxide added and stirred for 4 h at room temperature *in the dark*. The yellow solution was filtered and the 130 ml of Et_2O evaporated at room temperature. The synthesis yielded 67% (4.28 g, 32.38 mmol) of a yellow oil.
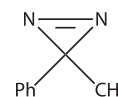
MS/TOF-PI(+) 266/800 nm: *m/z* (%) = 104 (100) $[M-N_2]^+$

13.14   3-(DEUTEROMETHYL)-3-PHENYLDIAZIRINE

The deuterated species was synthesized by a similar synthesis route as was described in the procedures 13.11 to 13.13. However, in step 13.11 D_3-acetophenone was used and the reaction mixture was not washed with a $NaHCO_3$ solution or water, but immediately distilled after evaporation of toluene. Procedures 13.12 and 13.13 were not modified. The product was a mixture of all four different isotopologues (R=CH_3, CDH_2, CD_2H, CD_3) in the ratio $\approx$ 1:2:2:1.
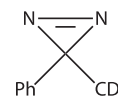
MS/TOF-PI(+) 266/800 nm: *m/z* (%) = 104 (50), 105 (100), 106 (95), 107 (45) $[M-N_2]^+$

13.15   2-IODO-2,3-DIMETHYLBUTANE

3.5 g (41.6 mmol, 4.94 ml) of 2,3-dimethyl-2-butene were added to a solution of 17.3 g 99% H_3PO_4 (175 mmol) and 0.73 ml of water[217]. 20.8 g (1.25 mol) of KI were added and the solution heated to 80–100°C under agitation for 4 h. The solution turned red. The reaction mixture was washed with 12.5 ml of water and the raw product extracted with 22 ml of Et_2O, discolored by adding sodium tetrathionate ($Na_2S_2O_3$), washed 3× with 20 ml of a saturated NaCl solution and dried over Na_2SO_4. The product can be distilled (without column) at atmospheric pressure with partial decomposition, but reduced pressure (30 mbar) increases the yield. Yield: 80.5% (7.10 g, 33.5 mmmol).

b.p.: 120–140°C (1.013 bar)
MS/TOF-PI(+) 265/800 nm: *m/z* (%) = 212 (20) $[M]^+$; 127 (20) $[I]^+$; 85 (80) $[M-I]^+$; 84 (100) $[M-HI]^+$; 43 (14) $[M-IC_3H_6]^+$

Many different azo compounds were synthesized during this thesis and several synthesis procedures were tested from the literature that did not give a reasonable yield. Due to the importance of these compounds as radical precursors, synthesis 13.16 and 13.17 show a route that was taken successfully many times. Experimental results employing these precursors will be published separately. The procedure is based on reference 228. However, the use of pyridine as a catalyst should be strictly avoided.

Since the product and the reactant (methyl amine) are gaseous, this synthesis route is the most challenging in the series of R–N=N–R azo compounds and can be transferred to other azo compounds (R$\neq$CH$_3$) with minor modifications. 39 ml ($\approx$ 0.88 mol) of methyl amine were condensed at -78°C and 125 ml of -78°C cold pentane were added. In an open apparatus (only sealed with CaCl$_2$ drying tubes), a solution of 30 g of sulfuryl chloride and 100 ml of pentane were added over 3 h to the reaction mixture held between -60 and -15°C. A white precipitate is formed consisting of the ammonium salt and the N,N′-dimethylsulfamide. The pentane is evaporated and the precipitate extracted over night with Et$_2$O using a *Soxhlet* extractor. After evaporating the ether, the yield was 52% (27.6 g) of a crystal colorless product.

^{1}*H-NMR* (250 MHz, CDCl3): $\delta = 2.72$ (s, 6H, CH$_3$), 4.23 (s, 2H, NH) ppm

13.17   AZOMETHANE
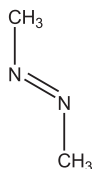
Azomethane is explosive. *The reaction procedure was performed with protective gear!* 0.9 g (7.25 mmol) of N,N′-dimethylsulfamide were dissolved in 4 ml of a 2 M aq. solution of NaOH at 0°C, in a similar apparatus as depicted in fig. 98, which was flushed by nitrogen. However, the dripping funnel was replaced by septum and a syringe and a CaCl$_2$ drying tube was fixed in between the trap held at -196°C and the reaction flask. 5.2 ml of *freshly ordered* (Sigma-Aldrich) 10% aq. solution of NaOCl were slowly added through a syringe, the reaction mixture was allowed to stir for 15 min, 1.5 ml of 6 M HCl were added (pH = 1) and the flask heated to 50–60°C for 30 min. The reaction mixture turned yellow. At room temperature 7 ml of 2 M NaOH were added. While continuously gently flushing the apparatus with N$_2$, 15 ml of 10% NaOCl solution were slowly added through the septum[1] and the gaseous product condensed in the trap, which was directly connected to the molecular beam apparatus.

MS/TOF-PI(+) 118 or 121 nm: *m/z* (%) = 58 (100) [M]$^+$; 43 (71) [M]$^+$-CH$_3$

---

[1] Note that NaOCl can only be added in abundance for gaseous azo compounds that are continuously removed.

DEVELOPED SCIENTIFIC SOFTWARE

All programs were developed with *LabView 6.0*, *8.0*, *8.2* and *8.5*, respectively. This list of programs considers exclusively new programs[1]. Modified and improved programs are not included.

14.1 G-READER 3.5

The G-Reader 3.5 is a program designed to read out the most important information of *Gaussian 03* output files (frequencies, rotational constants, energies etc.). The program also includes the possibility to read out stationary points of relaxed potential energy surface scans and plots the energy as a function of the desired coordinate. The program works for normal potential energy scans (opt=z-matrix) as well as for *mode-redundant* scans and gives out a coordinate vs. energy ASCII code to easily import into *Origin* and other scientific plotting programs. Another function of the program is to read out Cartesian coordinates of all stationary points after a successful potential energy surface scan and create a list of these geometries including the corresponding energy needed for supplementary material in publications.

Figure 99: *Gaussian 03* output reader

---

[1] The software is available upon request:
bastian.noller@phys-chemie.uni-wuerzburg.de

Further Options and Features:

- Extracts frequencies and symmetries into LaTeX table format

- Extracts selected geometries along a potential energy surface scan

- Generates input files for further *Gaussian* calculations

- Generates *.csh files for submitting *Gaussian* jobs

- Generates potential energy surface scans for TDDFT calculations

- Extracts excited-state energies of TDDFT calculations for entire coordinate scans

14.2 MOLCAS-READER 3.5

Molcas-Reader was programmed to accelerate the calculation of excited states along nuclear coordinates. The program greatly simplifies combining the strengths of the *Gaussian* program package with the CASSCF program of *Molcas*. The program takes the converged geome-
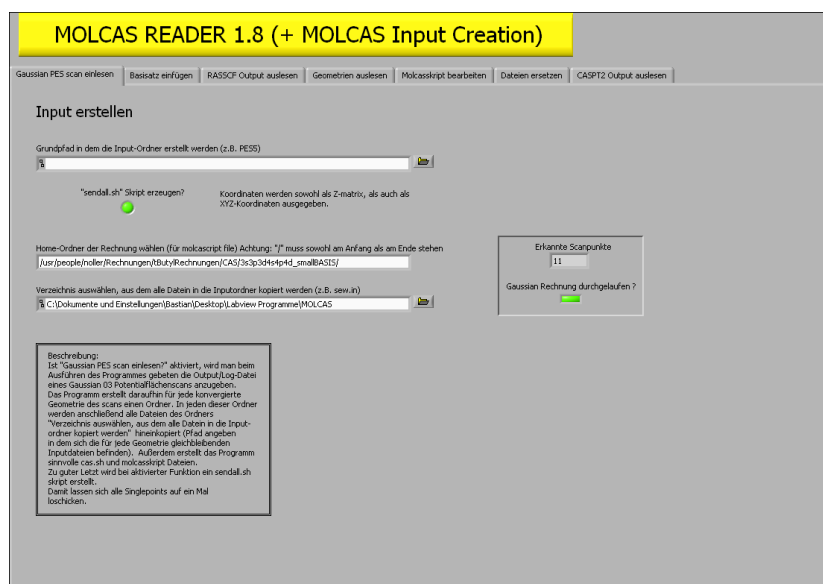
Figure 100: Molcas-Reader 1.8

tries of a potential energy surface scan performed by *Gaussian 03* and creates a new directory with proper input files for *Molcas* at each stationary point. An entire input for all geometries along the scanned nuclear coordinate is automatically created. Since some of the input files (e. g., rasscf.in containing information on the active space, sew.in, scf.in, rasread.in, caspt2.in) should be the same for all coordinates of one potential energy scan, a folder can be chosen containing these files, which will be copied into every directory of a stationary point calculation.

14.2.1 Output Files

- *information.txt:* Gives information on the method of the Gaussian scan applied to calculate the geometries.

- *gXname.xyz:* Gives out the Cartesian coordinates of the stationary point number X, which are needed for the *Seward* input of *Molcas*. It is not immediately included into the sew.in file in case symmetry adjustments have to made. "Name" corresponds to name of the output file of Gaussian.

- *molcasscript:* This file contains an automatically generated script file for the "bash" shell of unix operating systems. The working path is included into every *Molcas* script file. By starting the script the calculation for the single point is started. Note that no adjustments have to be made for this file. It is generated in a way to automatically have an unique working directory for *Molcas* for every calculated point.

- *cas.sh:* A shell script created to send the *Molcas* script file into the queue. The name for the job is created automatically and is unique for every stationary point.

The procedure of performing CASSCF or CASPT2 calculations in *Molcas*, respectively is the following: Seward→SCF→RasRead→RASSCF→CASPT2. All of these steps are included into the *Molcas* script and can be stopped after the SCF calculation (compare section 14.2.2) or after the RASSCF calculation by activation the option in *Molcas-Reader 1.7*.

14.2.2 Rydberg States

A special feature of *Molcas-Reader 1.8* is to include and position diffuse basis functions (i. e., to describe Rydberg states) at the center of charge of a molecule. Typically the complete Rydberg orbital shell should be placed at a position corresponding to the center of charge[229]. In order to achieve this in *Molcas* one would have to do a Seward calculation and SCF calculation for every single point, augment the basis set in every sew.in file by a Rydberg orbital shell and add the calculated center of charge from the scf.out file to position the Rydberg functions. *Molcas-Reader 1.8* automates this process and batch edits all directories containing the single point geometries after SCF calculations were performed as a batch with *Molcas* (option include basis set).

14.2.3 Further Options

- *readout rasscf:* Reads all energies of all roots along the coordinate for easy plotting of the potential energy surfaces.

- *readout geometries:* Does the same for the corresponding coordinate of choice.

- *readout caspt2:* Does the same for the energies of the CASPT2 calculations.

- *edit molcas:* Feature to quickly edit very many *Molcas* script files. One option is to increase the number of successive rasscf calculations performed in case of slow convergence.

- *replace files:* Option to quickly replace all the input files, i. e., to change the active space for all coordinates.

14.3 GUIRRKMQCEP 1.4

Graphical user interface (GUI) for the RRKM program by the *Indiana University Department of Chemistry* QCPE 291[230]. The input for the QCPE programs is needed in Fortran terminology. The GUI takes care of this without the need to learn this terminology. Just fill out the required information on the reaction, molecule and transition state. *GUIrrkmQCEP 1.4* can import frequencies directly from *Gaussian 03* frequency calculations. The information is sent to the QCPE 291 program and its created output is read and converted to the energy unit of choice.
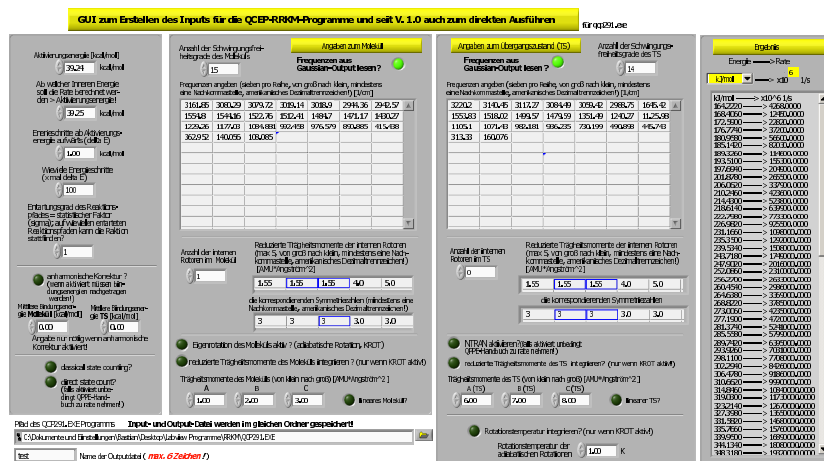
Figure 101: GUI for QCPE 291

14.4 DOMYDELAYS 2.5

Since version 2.8 of the program *Delay-Scan* mainly written by *M. Schneider*, I implemented a procedure to automatically generate systematic names for the output files containing information on the measurement (e. g., date, wavenumber of excitation etc.), which can be batch processed by *DoMyDelays 2.5* (fig. 102). By selecting a folder containing the delay scans (i. e., scan001, scan002, etc.) the program opens these files successively, and performs a least square fit with function 6.3 (compare, e. g., chapter 6.4). Good starting parameters can be automatically detected. Afterwards the program runs *Origin 7.5* and directly produces nicely formatted *Origin* OPJ files in publication quality by sending LabTalk commands to *Origin*.
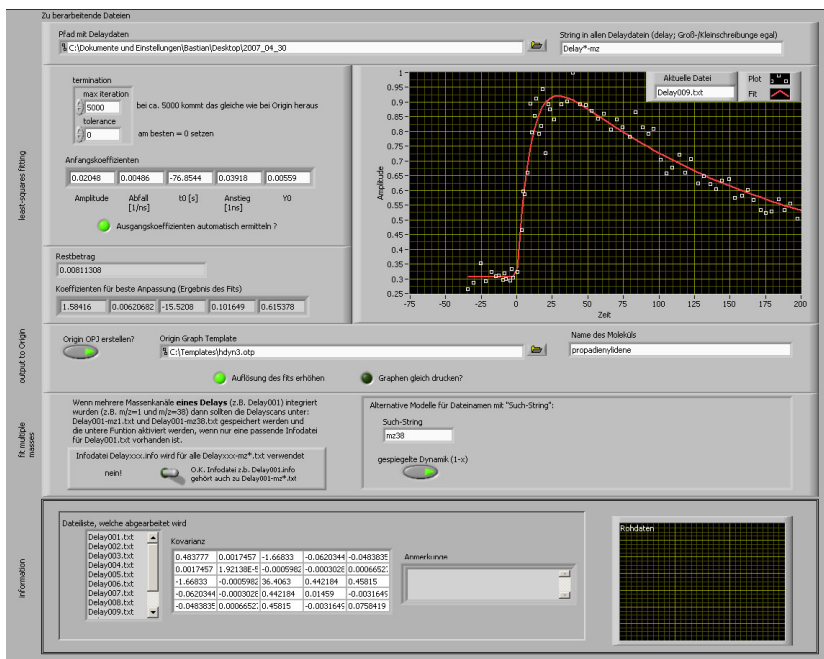
Figure 102: DoMyDelays 2.5

14.5 DOMYDOPPLERS 2.9

This program is closely related to *DoMyDelays* since it performs almost the same tasks for recorded Doppler profiles rather than for delay scans. The fitting procedure is not directly implemented in the program itself. The analysis of the profiles and the calculation of the speed distribution function is done by calling upon *QTDopplerfit* by *J. Buback*. The output is then sent to *Origin*.
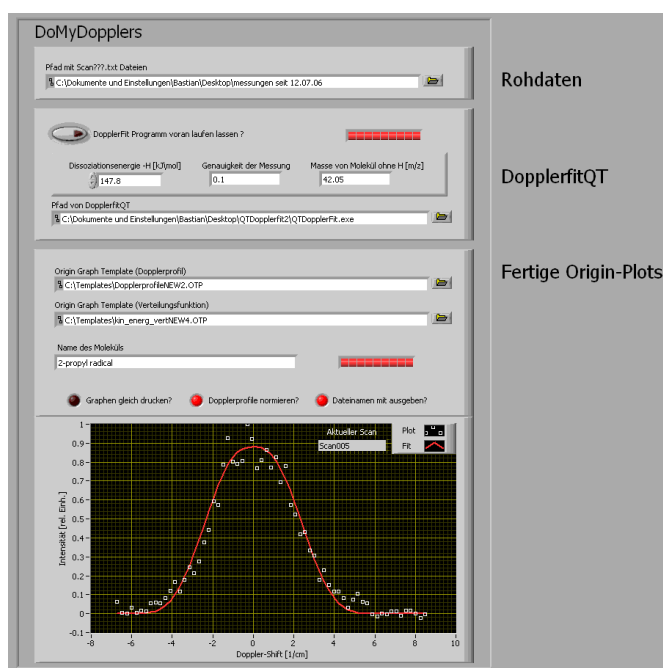
Figure 103: DoMyDopplers 2.9

m/z=82 (carbene/cyclohexene C_6H_{10})

m/z= 67 (side product C_5H_7)
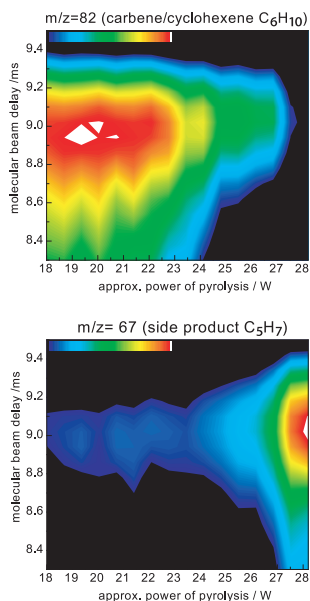
Figure 104: Top: Signal intensity of C_6H_{10} as a function of power and pulse delay. Bottom: C_5H_7

One of the most time consuming tasks for generating a clean molecular beam of intermediates is the optimization of both the pulse delay of the General Valve as well as finding the ideal temperature for the pyrolysis. Thus this program was developed to automate this task. The program slowly ramps the voltage of the power supply energizing the pyrolysis source and waits until the temperature has stabilized. With a constant temperature the program then starts scanning different delays of the valve. As output the experimentalist receives a three dimensional plot of the mass signal intensity, which he is trying to optimize, as a function of the applied voltage and the delay between laser and molecular beam pulse. This method is an efficient and systematic way to optimize the signal intensity of intermediates as can be seen in figure 105 and is demonstrated, e. g., in chapter 10 (page 100) on the example of propadienylidene. It also enables to clearly identify temperature thresholds, where side products start to appear. An example is given in figure 104. In this figure cyclohexyldiazirine ($C_6H_{10}N_2$) was pyrolyzed. The pyrolytic product (C_6H_{10}) appears already at low temperatures as can be seen in the top trace. However, further increase of the temperature lets the C_6H_{10} signal decline, whereas a new mass appears (C_5H_7) at around 30 W that interestingly might correspond to the cyclopent-1-ene-3-yl radical.
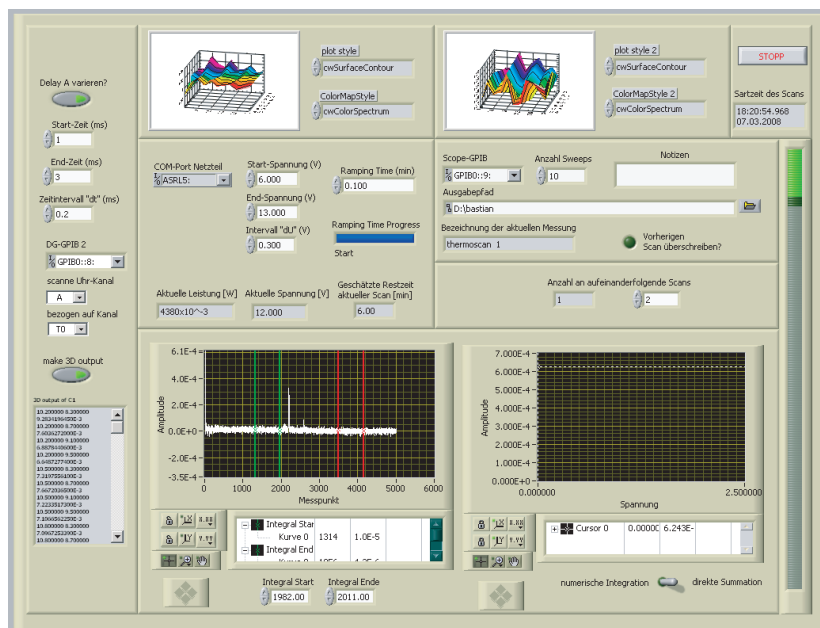
Figure 105: ThermoMap 1.1

The program *PES-Fitter* was developed to analyze time-resolved photoelectron spectra (TRPES) as well as photoion spectra (fig. 106). Often PES recorded by imaging techniques have overlapping band structures that are difficult to separate by direct integration. Thus this program first simulates a PES as a basis set expansion of several functions (e. g., $1\times$ exponential function Exp1 and three Gaussians G1, G2 and G3). The amount of functions used can be adjusted according to the experimental spectrum. In a least squares fitting procedure the amplitudes (or if wanted all parameters, such as position and FWHM) are optimized to give the best fit to the experimental spectrum. The program

Quantum chemical calculation programs often use so called "Gaussian type obitals" (GTOs) and "Slater type orbitals" (STOs). While basis sets using Gaussian functions are more efficient to calculate, STOs are exponential functions and are better for describing the "cusp" of orbitals close to the nucleus.

Figure 106: PES-Fitter 1.6

automates this fitting procedure for all delay times of a time-resolved scan and integrates each of the basis function separately as a function of the time delay between pump and probe pulse. Hence the dynamics of overlapping bands can be distinguished and elucidated. The basis set expansion includes exponentials as well as Gaussian type functions. Whereas Gaussian type functions are usually perfect for describing the bands in the PES, electrons with very low kinetic energy are not well described. Such electrons can be produced from autoionizing states and result a very intense and sharp peak at around 0.00 eV. In order to account for this sharp "cusp" an exponential is added into the expansion, enabling a good description of this part of the spectrum.

Further Features:

- Autodetection of zero in time

- Intensity correction for starting amplitudes for faster convergence

- Autosave feature

- Set boundaries for all parameters, locking of single and multi parameters

14.8 FURTHER SOFTWARE

- *Plot3D-PES:* Plot and export 3D photoelectron spectra from raw data (see fig. 107)

- *ConvolutionFit 4.6:* Performs least square fits to different models in order to analyze time-delay scans of femtosecond experiments (fig. 108). The program performs convolutions of a Gaussian shaped instrument response function analytically as well as numerically with kinetic models (compare chapter 5).

- *Add-Up-Spectra:* Program to merge and average multiple spectra (e. g., REMPI) even if they are recorded at different resolution (not depicted).

- *Erwartungswert 3.0:* Program for quickly extracting the expectation value of the kinetic energy release of Doppler profiles and generating an excel spread sheet (not depicted).

- *Fluxcorrektator-Soleil 2.0:* Program for correcting ion yield spectra for photon flux and gold grid response at the synchrotron Soleil (not depicted).
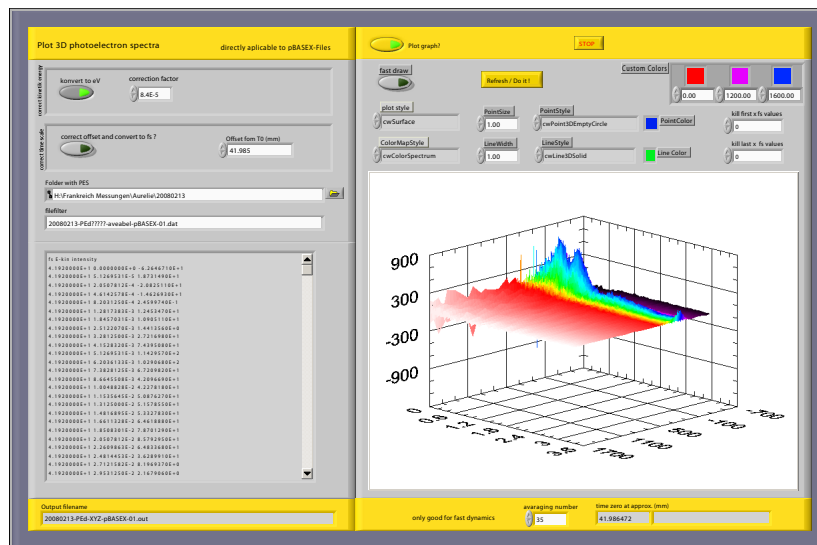
Figure 107: Plot3D-PES
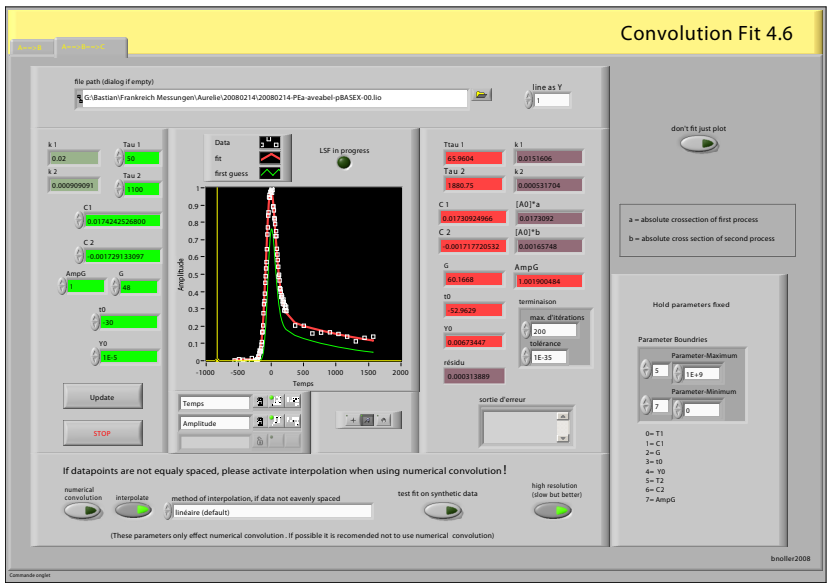
Figure 108: ConvolutionFit 4.6

APPENDIX

A.1 ZEKE DETECTOR

A.1.1 *Description of the Detector*

A photoelectron detector following the concept of *Wurz et al.*[231] was designed for measuring highly resolved zero kinetic energy electron (ZEKE) spectra. Due to the high energy resolution, ZEKE spectroscopy enables to resolve vibrational and rotational energy levels. The method is used in particular for cations correlating to Rydberg states[232]. A short introduction to ZEKE spectroscopy is given in chapter A.2. Removing an electron from a hydrocarbon radical produces carbocations, which are of considerable interest in organic chemistry[233]. The new MCP detector provided a signal response time comparable to latest state-of-the-art electron detectors applied in spacecrafts[234] and expensive commercial detectors[235] as demonstrated in figure 109. Note that the full width at half maximum (FWHM) of the recorded signal was close to the time resolution of the oscilloscope and has to be regarded as the upper limit.
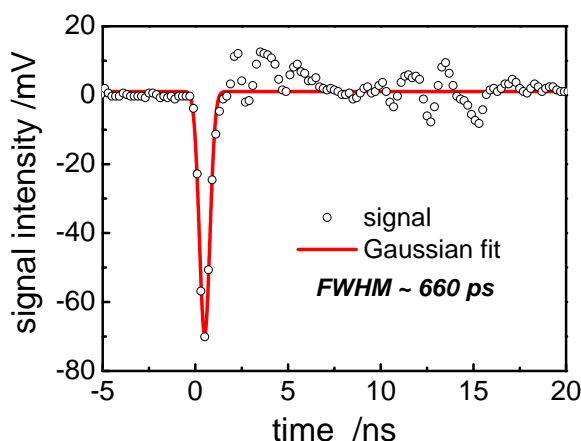
Figure 109: The electron detector shows a very short instrument response function (IRF). The FWHM of the signal was determined to 660 ps.

In this section the electron detector is described in more detail. While a photoion detector is relatively straightforward to build, an electron detector is considerably more complicated. The electron signals are very short and fast (ps regime). Hence it is of importance that the signal path is carefully designed to suppress any signal reflections before reaching the oscilloscope — a problem known in high frequency technology such as radio or television. The second challenge is to find a possibility to safely decouple the highly charged electron anode from the oscilloscope without losing signal transmittance or causing reflections. The detector is shown schematically in figure 110. For near ZEKE spectroscopy by pulsed field ionization (PFI-ZEKE) it is advan-

(a) Scheme (side view)   **(b)** Photo (side view)
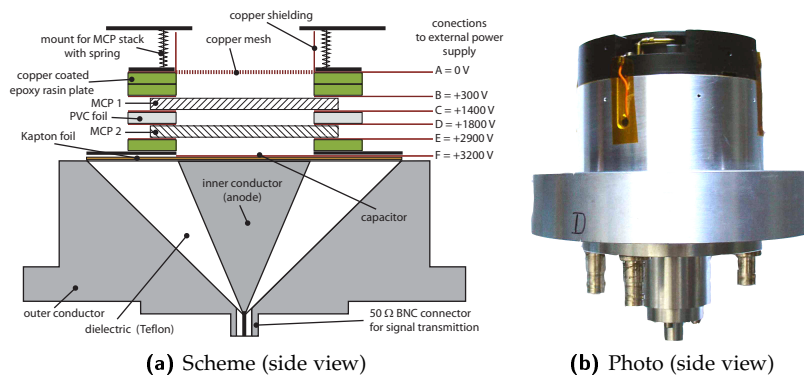
Figure 110: The ZEKE detector was build directly into a standard CF flange and incorporates a conical anode to suppress signal reflections

tageous to design a detector with a field of $0\,\mathrm{Vcm^{-1}}$ toward the ionization region, otherwise the ionization of Rydberg states will already take place without applying the pulsed field. On the other hand, the detection efficiency of a MCP detector strongly depends on the kinetic energy of the incoming electrons[236]. Thus a copper mesh with 80% transmittance (*Buckby Mears*) was fixed in front of the first MCP and put to the same potential as the molecular beam apparatus. The potential applied to the front of the first MCP was set to 300 V to accelerate the electrons onto its surface for higher detection efficiency. The potential applied the back of MCP1 was set to 1400 V. A potential difference of approx. 1100 V per MCP achieves the best possible amplification as well as a long lifetime of the MCP[237]. The detector includes a second MCP for further amplification and is mounted in a chevron orientation. The two MCPs in the chevron stack are separated by a 70 µm thick ring-shaped PVC foil, which is coated with copper from both sides (total thickness 150 µm). A distance of approx. 150 µm achieves a better signal gain as if both plates are in direct contact[237]. The time resolution is hereby further improved by applying an additional potential between the back of MCP1 and the front of MCP2 of 400 V[231,237]. The second MCP is also driven by 1100 V. The amplified electron signal is transferred to the oscilloscope through a capacitor directly included in the transmission line (compare figure 110). This capacitor was built on top of a conical anode. Hereby the anode was covered by Kapton tape. A thin adhesive copper foil was then fixed on top of the Kapton tape to form an anode//Kapton//copper capacitor. Hence the anode is electrically separated from the high voltage applied to the copper foil. The capacitor decouples the DC voltage applied to the copper foil from the oscilloscope but lets AC signals pass. Between the back of MCP2 and the copper foil the electrons are collected by applying a potential difference of 300 V. Hence the copper foil is held at a potential of +3200 V. The entire detector voltages are supplied by a single high voltage power supply, using a resistive voltage divider depicted schematically in figure 111.

Unwanted signal reflections occur when high frequency signals are transported along transmission lines that vary in the characteristic wave impedance. For coaxial cables the characteristic wave impedance
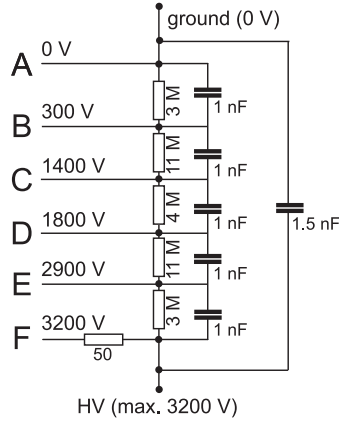
Figure 111: Circuit diagram of the resistive voltage divider used for powering the detector (compare figure 110).

depends on the ratio between the diameter of the outer shield and the diameter of the inner conductor. Hence the conical anode was designed to behave as a perfect $50\,\Omega$ coaxial transmission line that slowly reduces its diameter to the diameter of a standard commercial coaxial cable. The diameter ratio of the central anode to the surrounding mantle was calculated according to equation A.1[238] to give an independence of $50\,\Omega$ when separated by the solid dielectric (Teflon, $\epsilon_r = 2.05$).

$$Z = \frac{60\,\Omega}{\sqrt{\epsilon_r}} \ln \frac{D}{d} \tag{A.1}$$

A.1.2 *Assembly of the ZEKE detector*

It is important to safely and easily exchange the MCP plates of a particle detector if necessary. Hence a detector design was chosen that assures an easy assembly as demonstrated in figure 112. *The MCPs are not included in the figure.* Inset ① shows the plane anode (top view). The anode is covered by Kapton tape (inset ②). A thin adhesive copper foil is fixed on top of the Kapton tape to form an anode//Kapton//-copper capacitor. On top of the capacitor a mount for the MCPs is attached (inset ③). The connections to the front and back side of the MCPs is achieved by epoxy resin plates which are coated from one side by copper. In inset ④ the epoxy resin ring for the connection to MCP2 is inserted. The two MCPs in the chevron stack are separated by a $70\,\mu m$ PVC foil which is coated with copper from both sides (total thickness $150\,\mu m$, inset ⑥). After putting a second mounting ring in place to support the second MCP (inset ⑦), the last epoxy resin plate is inserted (⑧). The entire stack of detector components is then locked in place by a plastic ring that slightly places pressure onto the stack by four springs (compare scheme (a) on the left of figure 110). This ring is also equipped with a grounded copper mesh to shield fields, originating from the detector, from entering the molecular beam apparatus. This locking system is held in place by the lid of the detector shown in inset ⑨ of figure 112.
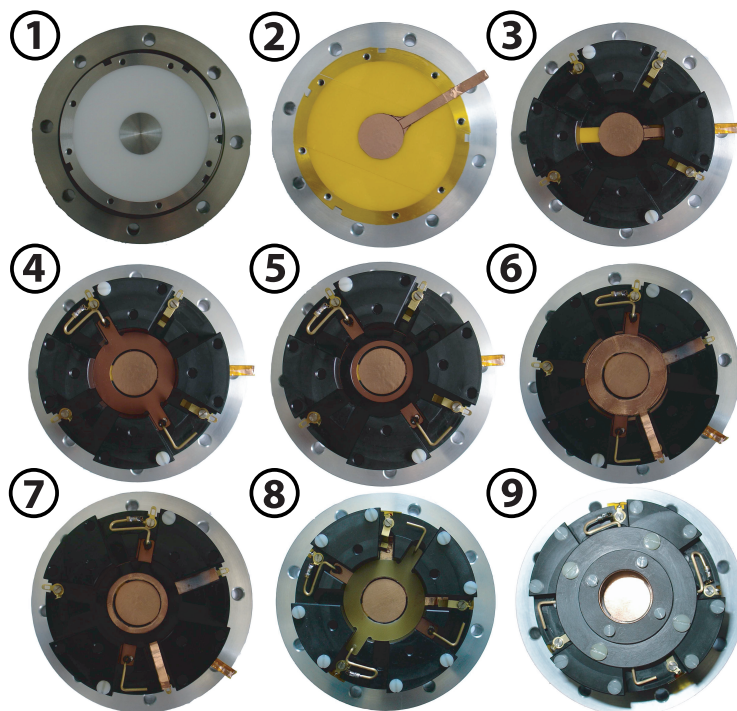
Figure 112: Top view on the detector. The ZEKE detector is build on top of a conical anode. The MCP assembly is build up of several layers (compare text).

A.2 ZEKE SPECTROSCOPY

This section is intended to give a brief description of the ZEKE detection method [232,239] with regard to the detector described in section A.1, and since it is closely related to TPEPICO spectroscopy presented in chapter 2.5.1. In ZEKE spectroscopy a laser is tuned near the threshold of ionization of the molecules in the molecular beam. The threshold can either be reached by applying VUV light sources or using REMPI schemes and UV/VIS light. In conventional photoelectron spectroscopy (PES) [240] the kinetic energy of the photoelectrons is measured at constant photon energy, and the photon energy is held fixed; whereas in ZEKE spectroscopy the light source is tuned. In contrast to TPES, not the electrons with near zero kinetic energy that result from direct ionization are detected. In ZEKE spectroscopy the photon energy lies slightly below the ionization threshold, and the ionization takes place by applying a pulsed field. Thus it is more correctly described as pulsed field ionization spectroscopy (PFI-ZEKE). The molecules are excited to Rydberg states [241]. Rydberg states are highly excited electronic states of molecules, and the excited electron is far away from the molecular nucleus framework. Similar to the Rydberg formula for hydrogen, these states converge to an eigenstate of the ion [242]. The ZEKE states are then field-ionized and the electrons accelerated to the detector by applying a pulsed electric field only few microseconds after the excitation took place [239]. This method of delayed extraction usually assures that most "spontaneous" electrons from the top Rydberg states, free electrons with zero kinetic energy and other free electrons have drifted out of the detection region due

🛈 After preparing ZEKE states it is also possible to extract the corresponding ions rather than the electrons. The advantage of this method (mass analyzed threshold ionization, MATI) is its mass selectivity.

146

to electric stray fields in the apparatus. The externally applied pulsed field then ionizes further Rydberg states, the amount depending on the extraction voltage. These extracted electrons are then detected. The advantage of ZEKE spectroscopy over conventional photoelectron spectroscopy is its high resolution at moderate experimental expense. The high resolution is achieved by pinning down two parameters simultaneously: The energy of the photoelectrons *and* the excitation wavelength are fully determined. In conventional photoelectron spectroscopy all ionic rovibrational states below the irradiated photon energy contribute to the electron signal. Thus usually many ionic states give rise to the photoelectron signal. This prohibits a resolution of the energy levels. ZEKE spectroscopy overcomes this drawback by detecting Rydberg states in a small energy window, which correlate to the ionic states. Additionally, the frequency of the light source can be measured more easily in contrast to the kinetic energy of the electrons in conventional PES.

TPEPICO presented in chapter 2.5.1, on the other hand, selects "real" zero kinetic energy electrons which were not generated by field ionization.

A.3 HOW TO MAKE MOLECULAR BEAM SKIMMERS

A highly polished aluminum mandrel was used and cleaned thoroughly with ethanol and water before use. The mandrel was inserted
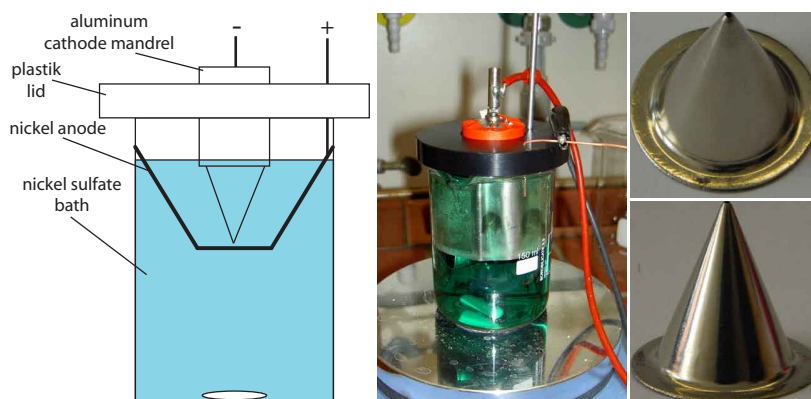
Figure 113: Setup for electroforming molecular beam skimmers

into a solution of 150 ml water, 6.40 mg (2.25×10^{-5} mol) sodium dodecylsulfate (SDS), 40 mg sodium saccharin, 15 mg (0.174 mmol) 2-butyne-1,4-diol, 5.62 g H_3BO_3, 45.0 g ($\approx$ 0.167 mol) $NiSO_4$ x $(H_2O)_{6-7}$ and 1.00 g (4.24 mmol) $NiCl_2$ x $(H_2O)_6$ at 50°C (pH = 4–5). The solution has to be well stirred to prevent agitation of gas on the surface, leading to pits in the skimmer and rendering it unusable. An improvement would be to rotate the mandrel by an electrical motor instead of stirring the solution. For the first three hours the voltage was held at 0.3–0.4 V (3–6 mA) and afterwards slowly increased within one hour to 0.8–1.3 V ($\leq$ 80 mA). Every 2 hours the electroformed nickel layer was washed with acetone and water in order to reduce pitting. The electrolysis was finished after approx. 12 h. The outer surface of the skimmer can now be polished. The electroformed nickel skimmer is removed from the

template by repeatedly (approx. 10×) completely cooling the template with liquid nitrogen down to −196°C and heating with a hot water bath[243]. The skimmer can then usually be pulled off. The nickel sulfate solution can be reused after filtration.

A.4 VIBRATIONAL FREQUENCIES OF PROPENE

To verify the correct prediction of the TS frequencies of the reaction shown in fig. 3 on page 41, the frequencies of the product molecule (propene) were computed by the same method used to calculate the TS frequencies (table 13).

Table 13: Vibrational wavenumbers [cm^{-1}] of propene (MP2/6-311G**).

3276.7	3188.3	3175.7	3163.5	3143.6	3067.9	1705.6
1514.9	1498.1	1462.7	1419.8	1323.9	1198.7	1075.1
1025.9	949.7	942.0	907.1	581.4	423.6	199.1

According to the postulate of Hammond the geometry of the TS should be similar to the product in an endothermic reaction[123]. As can be seen, the frequencies are indeed close to the frequencies predicted for the TS (compare table 3). The frequencies were also used to calculate the combined density of states of the products needed for equation 6.2 (page 43).

During my *diploma thesis*[1] the excited-state dynamics of the *t*-butyl radical were investigated in the gas phase by femtosecond time-resolved pump-probe experiments[30,244]. These experiments showed that in the region of 330 nm (3.76 eV) excitation, the lifetime of the excited 3s Rydberg state changes spontaneously from 80 fs (< 330 nm) to 150 fs (> 330 nm). A reasonable explanation for this observation is a change in the deactivation process due to an interaction between electronic excited states. Thus extensive *ab initio* calculations on the excited states of the *t*-butyl radical were preformed to describe the run of the most important potential energy surfaces (fig. 114)[2].

Four degrees of freedom were selected:

1. [1,2]-H-shift (fig. 115)

2. C–H stretching mode (fig. 116)

3. asymmetric C–C stretching mode (fig. 117)

4. symmetric C–C stretching mode/umbrella mode (fig. 118)
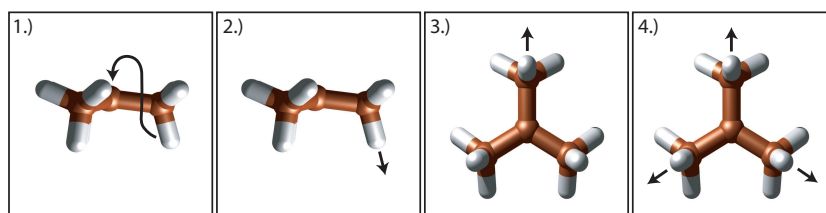
Figure 114: Most important degrees of freedom.

A.5.1 *Employed Methods*

MP2/6-311** and B3LYP/6-311** calculations for the ground state potential energy surfaces were performed using the *Gaussian 03* program package[145]. The potential energy surface scans were done by starting from the ground state equilibrium geometry of the molecule and increasing (or decreasing) one bond length and/or one angle step by step. Simultaneously *all other* internal coordinates were optimized without restrictions for every new single point geometry (relaxed potential energy surface scan). The molecule was held in C$_s$ symmetry during the relaxed potential energy surface scan in order to accelerate the subsequent calculations on the excited states (both MP2 and B3LYP conclude a C$_{3v}$ equilibrium geometry as can be seen in table 14).

In figure 115 the barrier calculated for a [1,2]-H-shift (MP2/6-311**) is depicted. Note that one of the methyl groups was flipped by 60 degrees from the ground state equilibrium geometry in order to maintain the molecule in C$_s$ symmetry along the scan[3]. The $\langle S^2 \rangle$ value (expectation value of the total spin) was near 0.75 for all geometries along

Table 14: Equilibrium geometry of *t*-butyl

	MP2	B3LYP
C-C [Å]	1.508	1.500
C-H (a) [Å]	1.107	1.104
C-H (b) [Å]	1.097	1.093
angle β [°]	25.33	20.68

---

[1] German equivalent to master's thesis   [2] Many thanks to *Dr. M. Arnone* and *Prof. B. Engels* for supervising the calculations.   [3] The torsional barrier will be small compared to the barrier for the hydrogen migration.
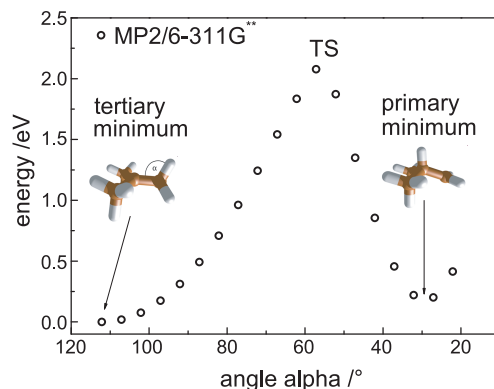
Figure 115: [1,2]-H-shift calculated by MP2 method of theory.

the pathway. The barrier for hydrogen migration of this rotatiomer was calculated to lie at 2.08 eV. Since the rotatiomer was calculated to be 0.06 eV higher in energy than the correct ground state equilibrium geometry, the barrier of a [1,2]-H-shift in *t*-butyl can be estimated to be 2.14 eV. Note that in these qualitative calculations, no zero point energy correction was performed as for the other calculations in the former chapters. The calculation was repeated using density functional theory (DFT) with method and basis set mentioned above. The barrier lay at 2.03 eV for the rotatiomer and thus the actual barrier at 2.09 eV. The primary radical (fig. 115 right-hand side) lay 0.18 eV higher in energy in the MP2 calculation than the tertiary rotatiomer, whereas the DFT calculation predicted an energy difference of 0.29 eV. The barrier for hydrogen migration is known to be 1.76 eV at G2(PU//QCISD) level of theory (and 2.11 eV at MP2/6-31G* level of theory) for the ethyl radical[245].

For the C–H stretching mode shown in figure 116, MP2 calculations resulted $\langle S^2 \rangle$ values much larger than 0.75 for long bond lengths. Thus the potential energy surface along the coordinate was calculated by DFT. Hereby the expectation value of the total spin lay very close to
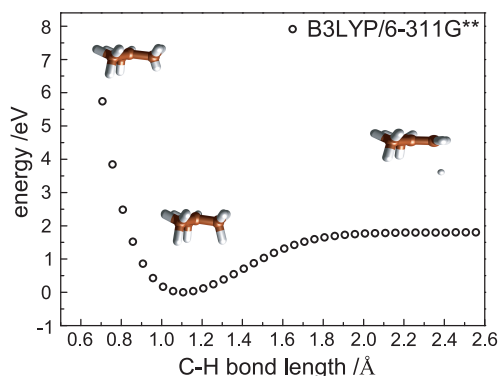
Figure 116: C–H stretching mode calculated by B3LYP method of theory.

0.75. Note that the predicted geometries of the MP2 and B3LYP calculations only slightly differed even at spin contaminated MP2 geometries.

150

The B3LYP calculations predict a dissociation barrier of 1.80 eV for the C–H bonds of *t*-butyl.

The probably most interesting degree of freedom (see discussion) of the *t*-butyl radical is its asymmetric stretching mode. Figure 117 shows the potential energy surface (B3LYP) for the asymmetric stretching mode (one C–C bond length was varied). Again MP2 calculations provided $\langle S^2 \rangle$ much larger than 0.75 for long bond lengths. Surprisingly the geometries along this coordinate were nevertheless close to those calculated by DFT. The C_s restriction on the geometry of the molecule led to discontinuities in the ground state potential energy scan at 2.75 Å and 4.00 Å, as can be seen in figure 117. Thus the cal-

(a) Calculated in C_s symmetry   **(b)** Calculated in C_1 symmetry
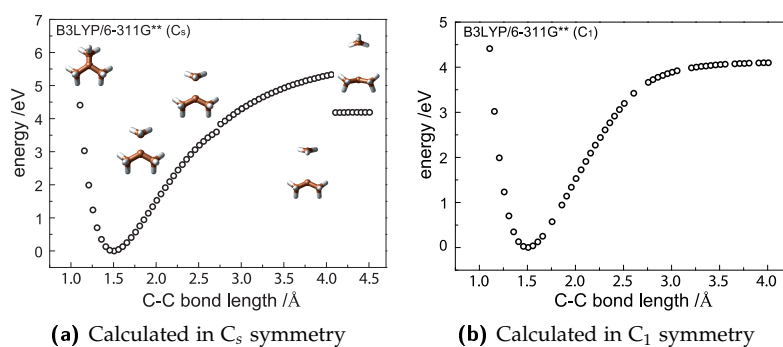
Figure 117: Asymmetric C–C stretching mode calculated by B3LYP method of theory.

culations were also performed without symmetry restrictions (fig. 117, right-hand side), resulting no discontinuities along the run of the potential energy curve. Note that the calculations were done starting with a single radical and thus a doublet ground state. For long bond lengths the system is better described as a methyl radical (CH_3) and a dimethylcarbene (C_3H_6). This complete system will still be regarded as a doublet by the program package. Thus the pathway leads to a singlet carbene and a doublet methyl radical in the calculation. This is correct, since dimethylcarbene indeed processes a singlet ground state with a small triplet-singlet energy gap of ≈ 0.04 eV [246,247]. Without symmetry restrictions the C–C dissociation barrier of *t*-butyl can be estimated to 4.10 eV by the performed DFT calculations.

The symmetric stretching mode (all three C–C bonds stretching simultaneously) was calculated with the umbrella mode being scanned concurrently. The calculation was only performed with MP2 level of theory. The $\langle S^2 \rangle$ values lay close to 0.75 for bond lengths smaller than 1.9 Å. For bigger bond lengths the expectation value increased slowly to 1.5. The comparison of the results from B3LYP and MP2 calculations above do indeed show that geometries acquired by MP2 calculations are reliable even with $\langle S^2 \rangle$ being larger than 0.75 for the *t*-butyl radical. MP2 calculations predict very exact geometries for molecules consisting of only carbon and hydrogen atoms [248]. Thus these optimized geometries were employed in the *Molcas* calculations below. Figure 118 shows the potential energy as a function of the angle β and the C–C bond length. The MP2 calculations predict an angle β of 25° for the molecules equilibrium geometry. A cut through the PES

(a) 3D PES: Angle β and C–C bond length vs. energy

(b) cut through 3D PES at 1.508 Å (upper trace)
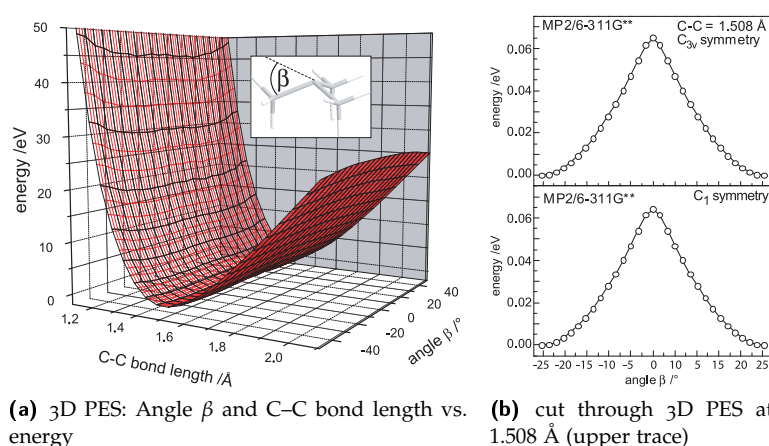
Figure 118: Symmetric C–C stretching mode and umbrella mode calculated by MP2 method of theory.

at a bond length of 1.508 Å (bond length at equilibrium geometry) is shown in the upper trace of figure 118 (b). The barrier of inversion can be estimated to 0.065 eV (6.3 kJmol^{-1}). For comparison, the angle β was scanned with the same computational method but without symmetry restrictions and with a variable C–C bond length. Very tight convergence criteria were employed to assure a correct description of the low frequency mode. The result is shown in the lower trace of figure 118 (b), showing nearly the same inversion barrier as in the approximation above, which is in good agreement with early calculations[249].

The vertical excitation energies were calculated with CASSCF[248,250] level of theory using *Molcas* 5.0[251]. For the vertical excitation energies from the ground state equilibrium geometry CASPT2[252] calculations were performed as reference. The optimized geometries (single points) of the *Gaussian 03* MP2 and B3LYP surface scans were used for the *Molcas* CASSCF calculations. Thus CASSCF was only utilized in order to determine the vertical excitation energies of each point. Dunning-cc-pVDZ basis sets were hereby employed for each atom. Since the excited states of the *t*-butyl radical are known to be Rydberg in character[253], diffuse 3s3p3d4s4p4d basis sets "[10s5p]-(3s2p)" were added to the center of charge of every geometry[254]: $\xi_s = 0.023$, 0.0055; $\xi_p = 0.021$, 0.0049 and $\xi_d = 0.015$, 0.0032. Calculations with Dunning-cc-pVTZ basis sets were found to be too time consuming for the purpose of finding a qualitative picture of the excited state potential energy surface (PES) of the *t*-butyl radical and did not significantly lower the state energies. Note that only the energies of the roots (vertical excitation energies) were calculated with *Molcas*, while the optimized molecular geometries were taken from the *Gaussian* calculations. When employing C$_s$ symmetry the electronic ground state as well as the first excited state (3s Rydberg) are of A′ symmetry, whereas the p Rydberg states (A$_1$ and E in C$_1$ symmetry) transform into two A′ and one A″ state. A CAS was chosen with 7 active electrons in 13 orbitals (nine of a′ symmetry and four of a″ symmetry) for roots with total

Table 15: CASSCF electron configurations for A′ states

state	configuration in AS		weight	energy [eV]	character
	orbitals a′	orbitals a″			α electr. in
GS	22α000000	2000	97%	$\equiv 0$	p
ES 1	220α00000	2000	84%	3.25 (4.36)	3s Rydberg
ES 2	22000α000	2000	95%	3.76 (5.10)	3p Rydberg
ES 3	2200α0000	2000	96%	3.90 (5.17)	3p Rydberg
ES 4	22000000α	2000	48%[1]	4.41 (5.69)	3d Rydberg
ES 5	2200000α0	2000	36%[1]	4.43 (5.74)	Rydberg
ES 6	220000α00	2000	65%	4.46 (5.79)	3d Rydberg
ES 7	2α2000000	2000	97%	7.23 (6.95)	valence

symmetry A′. The orbitals were optimized to minimize the average energy of all included states.

A.5.2 *Excited States*

All calculations on the excited states were performed in order to elucidate a qualitative picture of the excited-state interactions and yielded information on the character of the electronically excited states as well as on possible curve crossings (compare fig. 10 on page 13).

The energy of the excited states reduced after having augmented the cc-pVDZ basis set by diffuse Rydberg like functions at the center of charge, showing the necessity of this procedure. When employing the active space mentioned above, almost all excited states are well described by a single electron configuration. The excited state electron configurations in the CASSCF are listed in table 15 (The ground state geometry of the MP2 calculations was used). Double occupied orbitals are denoted with "2" and single occupied orbitals with alpha spin are denoted with "α". As can be seen, nine orbitals of a′ and four orbitals of a″ were used as active space for calculations run in A′ total symmetry. The states are characterized according to the orbital occupied by the unpaired electron.

Four important averaged orbitals for the present study are depicted in figure 119. In agreement with earlier work[253], the SOMO consists of a p orbital at the carbon center in the ground state (lower left) and in the first excited state the unpaired electron is transferred to a 3s Rydberg orbital (upper left). A CASPT2 single point calculation was also done at the same ground state equilibrium geometry; the results are listed in table 15 in brackets. The CASPT2 energies are closer to those of *Lengsfield III et al.* and experimental results[110]. The method nevertheless was too time consuming to apply for entire potential energy surface scans. While the CASSCF results underestimate the excitation energies significantly, the CASPT2 results are consistently higher than the experimental values. States with a total symmetry of A″ were also calculated utilizing four orbitals of a′ symmetry and nine of a″ symmetry for the active space (AS) and seven electrons. Due to the different

---

[1] Excited states with contributions of other configurations higher than 10%
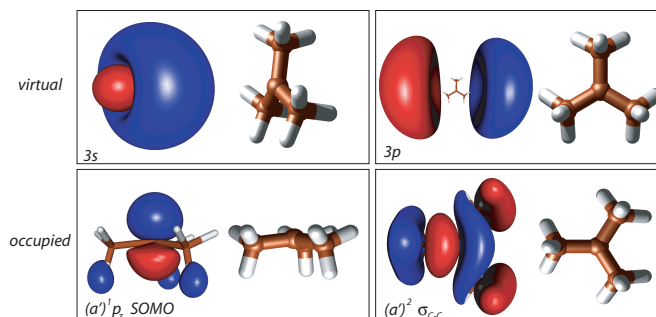
Figure 119: Some relevant orbitals for the description of the electronic structure of *t*-butyl

AS, the energies are not directly comparable to the energies in table 15 and are not listed. The lowest A″ states are exclusively of 3p and 3d Rydberg character. They behaved similar to the corresponding A′ states and will not be discussed any further.

[1,2]-H-Shift

One possible reaction pathway after excitation of the *t*-butyl radical is its isomerization into the 1-*iso*-butyl radical via [1,2]-H-Shift. Due to the relatively high isomerization barrier in the ground state a conical intersection with one of the excited states seems possible, leading to
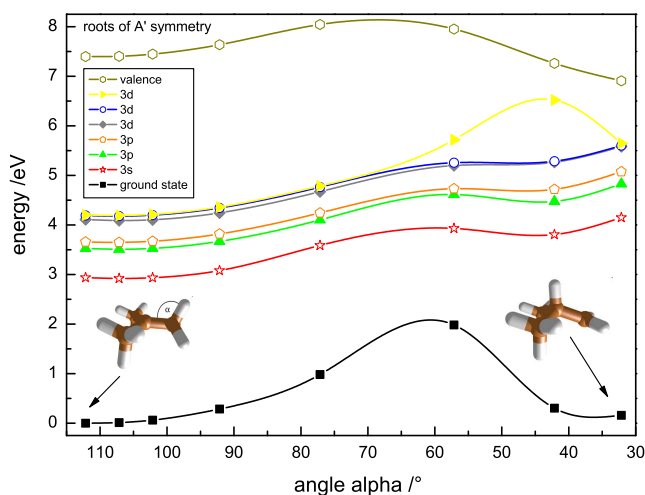
Figure 120: Potential energy as a function of the angle α, corresponding to a [1,2]-H-shift, for the lowest A′ states

a relaxation pathway of the excited state into the ground state. However, the CASSCF calculations did not show any conical intersections between the included roots; hence it is unlikely that this coordinate is a effective deactivation channel. In contrast, the excited Rydberg states seem to be relatively unaffected by a hydrogen shift in the ground state. The CASSCF calculations also conclude that the difference in

energy between the two isomers is higher in the first excited Rydberg state (0.89 eV) than in the ground state (0.20 eV). This is in agreement with a red shift of the 3s band when comparing absorption spectra of secondary versus tertiary hydrocarbon radicals[110].

C–H Stretching Mode

Stretching one of the C–H bonds and calculating the energy of the first eight electronic states also showed no conical intersections between the ground state and any electronically excited states as can be seen in fig. 121. Apparently strong nonadiabatic coupling is present between the excited states along the chosen coordinate. At approx. 1.4 Å a further state inserts into the potential energy surfaces. This changes the orbitals of the active space strong enough to show an effect even on the ground state surface. Note that the sequence of the states changes for bond lengths greater than 1.3 Å and the states can no longer be easily characterized by one electron configuration. By choosing bigger
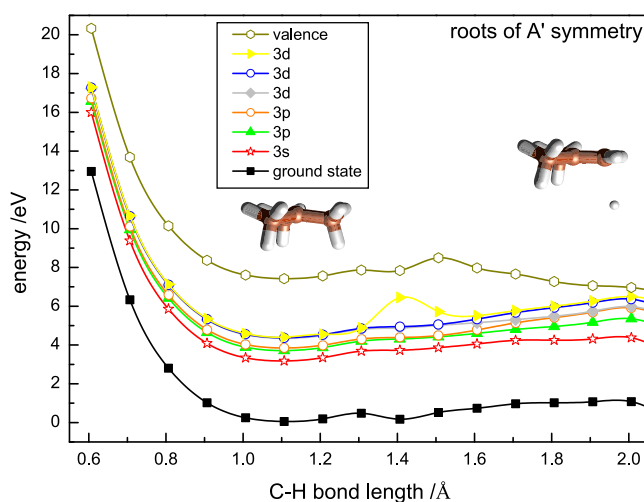
Figure 121: Potential energy as a function of one C–H bond length for the lowest eight A′ states

complete active spaces even stronger discontinuities of the potential energy surfaces were present. Nevertheless, a conical intersection of the ground state with any excited states can be excluded along this coordinate. The figure also shows that the AS is insufficient for a quantitative description of the complete potential energy surface over the range of 2 Å due to the high electronic state density. However, larger active spaces are not yet computational feasible. Unsteady potential energy surfaces predicted by CASSCF have also been reported by groups specialized on the calculation of excited states[82].

Asymmetric C–C Stretching Mode

The potential energy surfaces obtained for the asymmetric C–C stretching mode showed the strongest discontinuities of all calculated potential energy surfaces, indicating that the AS was not sufficient. Bigger active spaces up to a (7,15)-CAS increased the discontinuities. Nevertheless, all calculations showed that the 1st valance state and the
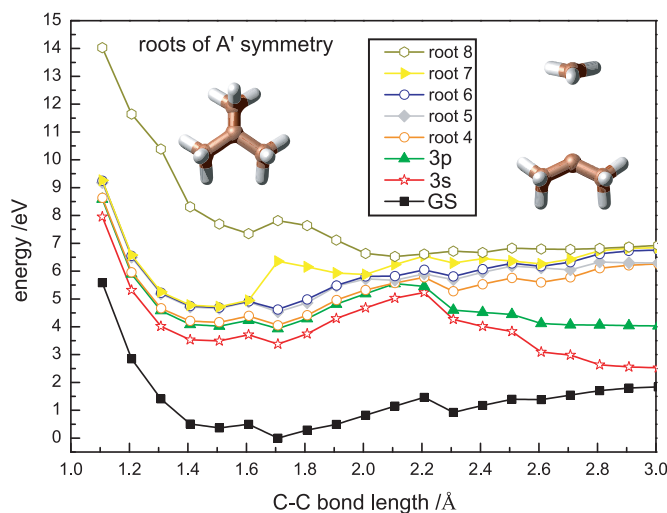
Figure 122: Potential energy as a function of one C–C bond length for the lowest eight A′ states

ground state come very close in energy for a C–C bond distance of about 3 Å. The valance and 3s Rydberg state both show strong contributions to the 2nd root shown in fig. 122 at 3 Å bond distance. This region can thus be described as a *conical intersection of three states*: The ground state, the valance state and the 3s Rydberg state. Also around 2.2 Å several excited states intersect. The asymmetric stretching mode is thus a feasible deactivation channel for optically excited *t*-butyl radicals as further discussed in section A.5.3. Calculations on a higher CI level of theory would be desirable but were too time consuming for the purposes of achieving a qualitative picture of possible deactivation channels.

Symmetric C–C Stretching Mode/Umbrella Mode

Stretching all C–C bonds simultaneously while diversifying the angle of the carbon framework β (180° minus dihedral angle) resulted well behaved potential energy surfaces for the first eight excited states in A′ symmetry. For the ease of view only the ground, 2nd, 3rd and 8th state is depicted in figure 123.

A.5.3 *Discussion*

Aside from the geometries of the neutral ground state[255], the ionic ground state[125] and the vertical excitation energies[253], no information on the excited states of *t*-butyl was available. Thus *ab initio* calculations on the ground state and a number of excited electronic states were carried out to describe the shapes of the potential energy surfaces as a function of important degrees of freedom. The calculations focus on a qualitative description of excited state rather than quantitatively correct energies. The goal was to identify possible excited-state deactivation pathways, such as intersections of excited states to the ground state. Many possible excited-state deactivation channels, such as excited-state isomerization or the symmetric C–C stretch motion,
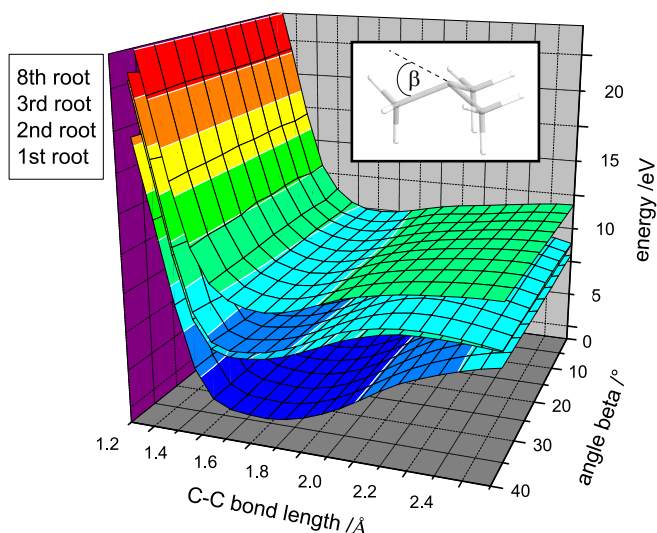
Figure 123: Potential energy as a function of all three C–C bond lengths and angle β for the ground, 2nd, 3rd and 8th state in A' total symmetry.

can be ruled out by the calculations as described above. However, the computations indicate the possibility of photochemical funnels along the asymmetric C–C stretching motion that lead to the dimethylcarbene + methyl product channel. Their presence can be qualitatively understood when considering the correlation of the *tert*-butyl electronic states with the product states, as shown in figure 124.
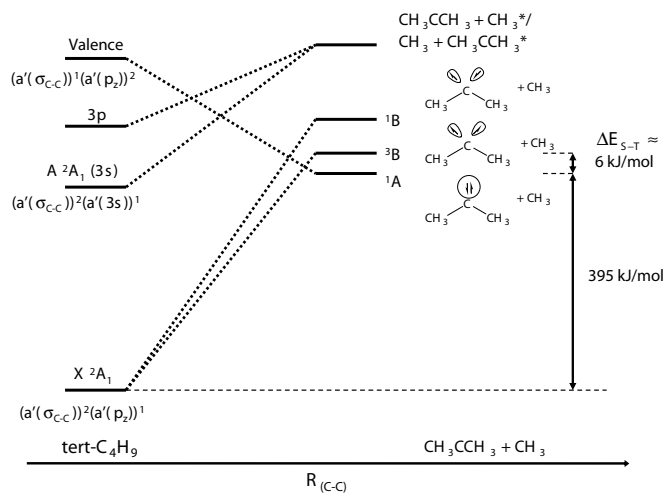
Figure 124: Correlation diagram, connecting several states of t-C$_4$H$_9$ with the H$_3$CCCH$_3$ + CH$_3$ product channel. The valence state is expected to cross both the 3s state and the ground state.

If the C–C bond of the t-butyl radical is stretched in its ground state one unpaired electron remains at the central carbon and a second unpaired electron is induced by breaking the bond. These electrons correspond to different orbitals of the nascent carbene. Consequently one arrives at triplet (^3B) or siglet carbene (^1B) with the unpaired electrons in *different orbitals* (compare fig. 124). Note that the formed products are

157

higher in energy as the carbene ground state with two electrons paired in one orbital[246,247,256]. On the other hand, an electron is transferred from a binding C–C sigma bond into the already singly occupied p orbital on the radicals carbon center if the radical is first excited to the 1st valance state. Thus the C–C bond is weakened and an electron pair is generated at the carbon center. By stretching the weakened carbon bond a singlet dimethylcarbene (^1A) is formed with a free electron pair (both free electrons in one orbital). This electron configuration (^1A) is 6 kJmol^{-1} more stable than the ^3B state described above (see fig. 124). This simple illustration indicates that a conical intersection is feasible along this coordinate. The 3s state, on the other hand, correlates to an excited electronic state of one of the products, which is presumably the 3s state of CH_3. As a consequence of this state-to-state correlation, the valence state will cross the 3p, 3s, and ground states, presumably at an extended C–C bond length. Motion along the asymmetric C–C stretching coordinate could thus provide an efficient channel for excited-state deactivation. Note that direct cleavage of the C–C bond requires 4.1 eV and is not possible upon 3s excitation. The energy range in which the state crossing is relevant for the photophysics of *tert*-butyl depends on the shape of the multidimensional potential energy surface, i.e., factors such as deformation along other degrees of freedom.

SUMMARY

SUMMARY IN ENGLISH

This thesis gives insights into the real-time dynamics of several free carbenes and radicals on a femtosecond and nanosecond time scale. The experiments were performed with radicals, singlet carbenes and triplet carbenes of various sizes. Several neutral excited states as well as the ionic ground state were characterized. Despite the relevance of such reactive intermediates in almost all chemical reactions, only relatively little experimental information on such systems is found in the literature. This is linked to the experimental challenge of producing such species under isolated conditions.

The intermediates are formed from precursor molecules under interaction-free conditions by supersonic jet flash pyrolysis. The precursor molecules were synthetically designed to show clean thermal dissociation into one specific intermediate. A large variety of spectroscopic techniques was applied to study the intermediates. Each method augments the results of the other methods. This enabled to successfully approach the main goal of this thesis: to understand the excited-state dynamics of organic intermediates. The excited states were found to deactivate rapidly to the hot ground state. The observed fast decay is presumably linked to coupled electronically excited states and relaxation takes place by internal conversion or conical intersections. Further reactions then take place on the ground state surface. Absorption spectra, photodissociation dynamics, photoelectron spectra, ionization potentials, excited-state lifetimes and dissociative photoionization were elucidated by the measurements. Pulsed and continuous light sources were used over a large spectral range (UV, Vis, VUV). A well-defined amount of energy was deposited into the molecule. After internal conversion has taken place, a microcanonical ensemble of reactive intermediates can be studied. This data helps to understand the energetics and reaction channels of intermediates. Velocity map imaging enabled to monitor the pyrolysis efficiency in real time by analyzing photoion images. This observation facilitates clean intermediate generation.

Experimental results were compared to quantum chemical calculations to aid the interpretation as well as to test the performance of theoretical approaches. Hydrocarbon radicals and carbenes are regarded as benchmark systems for computational methods due to their several low-lying electronic states and open-shell electronic configuration.

The experimental data can help to identify and understand the contributions of the examined intermediates to the chemistry of high energy environments (e. g., hydrocarbon cracking reactors, interstellar space and combustion chambers). Here increased numbers of hydrocarbon intermediates are often present and usually have a strong impact on the overall reaction mechanism. Such environments contain in general a complex mixture of several different intermediates. The more spectroscopic and dynamic properties of each isolated intermediate are known, the easier it is to identify it among multiple com-

ponents and to understand how it contributes to the overall reaction mechanism. Electronic excitation can take place by radiation, particle collisions or thermally at very high temperatures. How excited states influence the reaction mechanisms is still a matter of currant research.

Highlighted Results

- Femtosecond spectroscopy showed that the $C\,^1A_1$ state of propadienylidene (C_3H_2) deactivates after excitation at 250 nm with a time constant of 70 fs to the ground state. Photofragment spectroscopy revealed that from the hot ground state the molecule loses H atoms with a rate constant larger than $1 \times 10^8\,s^{-1}$ in agreement with RRKM theory.

- After exciting chlorophenylcarbene (CPC) and trifluoromethylphenylcarbene (TFPC) at 265 nm, both deactivate in a multistep fashion on a femtosecond time scale. TFPC was characterized by REMPI spectroscopy. The adiabatic IPs of CPC and TFPC were determined to be 8.15 eV and 8.47 eV using TPEPICO spectroscopy.

- 2-Propyl radicals were studied by photofragment spectroscopy in the excitation region of 230–260 nm. Statistical hydrogen loss occurs on a time scale of $\approx 7 \times 10^7\,s^{-1}$ and 20% of the excess energy are released into kinetic energy of the fragment. In contrast 1-propyl does not lose H and is likely to lose CH_3 instead.

- The 2,3-dimethylbut-2-yl radical is closely related to *t*-butyl and only differs by a modified side chain. This has a large effect on the excited-state deactivation of the 3p Rydberg state. The full deactivation is accelerated from 2 ps to 400 fs. The observation might be linked to symmetry breaking.

- The dissociative photoionization of several diazirines and haloalkanes was investigated by synchrotron radiation and TPEPICO spectroscopy. These molecules were employed as precursors for generating the intermediates. Thus their dynamic behavior has to be characterized to understand possible effects on the spectra of the intermediates.

Diese Arbeit gibt Einblicke in die Dynamik angeregter Zustände von mehreren isolierten Carbenen und Radikalen. Experimente wurden an verschieden großen Radikalen, singlet Carbenen und triplet Carbenen durchgeführt. Angeregte elektronische Zustände, Grundzustände von Radikal-Kationen und die Photodissoziations-Dynamik des Grundzustandes wurden charakterisiert. Obwohl beinahe alle chemischen Reaktionen über reaktive Intermediate ablaufen, ihnen Schlüsselrollen bei Verbrennungsprozessen zugesprochen werden und sie in hohen Konzentrationen in interstellaren Medien vorkommen, sind viele dieser Spezies unzureichend charakterisiert. Dies liegt hauptsächlich am hohen experimentellen Aufwand, der zur sauberen Herstellung und Untersuchung von Intermediaten nötig ist.

Die Intermediate in dieser Arbeit wurden mittels Supersonic-Jet-Flash-Pyrolysis generiert. Mit dieser Technik konnten die hoch reaktiven Moleküle konserviert und unter isolierten Bedingungen spektroskopisch untersucht werden. Hierfür wurden spezielle Vorläufermoleküle synthetisch hergestellt und auf ihre saubere thermische Zersetzung hin getestet und optimiert.

Die Intermediate wurden mit einer Reihe von spektroskopischen Methoden untersucht, die sich auf eine hervorragende Art und Weise ergänzten. Das Hauptziel der Dissertation konnte somit erfolgreich abgeschlossen werden und das Verhalten angeregten Zustände einiger wichtiger Intermediate verstanden werden. Die Zustände relaxieren auf einer Femtosekunden-Zeitskala zum heißen Grundzustand. Die schnelle Deaktivierung ist aller Wahrscheinlichkeit nach auf eine Kopplung der elektronisch angeregten Zustände zurückzuführen. Die Relaxation erfolgt über interne Konversion und konische Durchschneidungen. Photochemische Reaktionen laufen anschließend vom heißen Grundzustand aus ab. Zusätzlich konnten viele Charakteristika der Intermediate untersucht werden: Absorptionsspektren, Photochemie, Photoelektronenspektren, Ionisierungsenergien und dissoziative Photoionisation. Für die Untersuchungen wurde, über einen breiten spektralen Bereich (UV,Vis,VUV), hauptsächlich frequenz- und zeitaufgelöste Laser-Spektroskopie eingesetzt. Nachdem die Moleküle zum Grundzustand relaxiert waren, konnte die Dynamik eines mikrokanonischen Ensembles von reaktiven Intermediaten untersucht werden. Diese Untersuchungen helfen die Energetik und Reaktionskanäle der Intermediate zu verstehen. Zusätzlich wurden Messungen mit Synchrotron-Strahlung und TPEPICO-Spektroskopie durchgeführt; vorwiegend um die IPs der Spezies zu bestimmen wurde diese Technik angewandt. Velocity-Map-Imaging wurde zusammen mit der Radikalquelle erprobt. Ergänzend zu zeitaufgelösten Photoelektronenspektren konnten mit dieser Methode neue Wege zur Optimierung der Radikalerzeugung aufgezeigt werden. Die Effizienz der Pyrolyse konnte anhand der Photoionen-Images in Echtzeit verfolgt werden. Dies vereinfacht die Darstellung reaktiver Intermediate.

Die experimentellen Daten wurden mit quantenchemischen Rechnungen verglichen, um die Interpretation zu erleichtern. Des Weiteren weisen Intermediate häufig eine komplexe elektronische Struktur auf und können somit zum evaluieren quantenmechanischer Methoden verwendet werden.

Die erarbeiteten experimentellen Daten können helfen die spektroskopisch untersuchten Intermediate in komplexen Reaktionsgemischen zu erkennen und ihre dynamische Rolle darin besser zu verstehen. Je mehr Information über einzelne isolierte Intermediate bekannt ist, desto einfacher können ihre Beiträge differenziert aufgeschlüsselt werden. Eine erhöhte Anzahl von Intermediaten wird vor allem an Orten mit hoher Energiedichte beobachtet (z.B. im interstellaren Raum und in Motoren). Elektronisch angeregte Zustände der Moleküle können hier durch Teilchenstöße, Strahlung oder sogar thermisch bei sehr hohen Temperaturen angeregt werden. Wie elektronisch angeregte Zustände Reaktionsmechanismen beeinflussen können, ist noch Stand aktueller Forschung.

Wichtige experimentelle Ergebnisse

- Femtosekunden-zeitaufgelöste Untersuchungen zeigen, dass der $C\,^1A_1$-Zustand des Propadienylidens (C_3H_2) nach optischer Anregung bei 250 nm mit einer Ratenkonstante von 70 fs deaktiviert; der heiße Grundzustand wird hierdurch bevölkert. Mit Photofragment-Spektroskopie konnte der darauffolgende H-Verlust in Echtzeit verfolgt werden: Die Ratenkonstante ist hierbei schneller als $1 \times 10^8\,\mathrm{s^{-1}}$ und verläuft statistisch im Einklang mit der RRKM-Theorie.

- Die Phenylcarbene Chlorophenylcarben (CPC) und Trifluoromethylphenylcarben (TFPC) deaktivieren beide in mehreren Schritten nach Anregung bei 265 nm. Das TFPC wurde mit Hilfe von REMPI Spektroskopie untersucht. TPEPICO in Kombination mit Synchrotron-Strahlung ermöglichte es die adiabatischen IPs von CPC und TFPC zu ermitteln: 8.15 eV und 8.47 eV.

- 2-Propyl-Radikale wurden mit Hilfe der Photofragment-Spektroskopie im Bereich zwischen 230 nm und 260 nm untersucht. Hierbei verlieren die Radikale Wasserstoffatome statistisch mit einer Ratenkonstante um $7 \times 10^7\,\mathrm{s^{-1}}$ und 20% der Überschussenergie wird in kinetische Energie des Fragmentes konvertiert.

  1-Propyl-Radikale hingegen verlieren nach optischer Anregung aller Wahrscheinlichkeit nach CH_3.

- Das 2,3-Dimethylbut-2-yl-Radikal ist verwandt mit dem bereits untersuchten t-Butyl-Radikal. Die Radikale unterscheiden sich lediglich durch eine Seitenkette. Dies hat jedoch einen ausgeprägten Einfluss auf die Lebensdauer des angeregten 3p-Zustandes. Die Ratenkonstante wird von 2 ps auf 400 fs heruntergesetzt. Diese Beobachtung ist vermutlich durch einen Symmetriebruch erklärbar.

- Diazirine und halogenierte Kohlenwasserstoffe wurden mit Hilfe von TPEPICO-Spektroskopie charakterisiert. Diese Moleküle kamen als Vorläufer für die Intermediate zum Einsatz. Für die Gewährleistung einer sauberen Intermediat-Darstellung, im Hinblick auf dissoziative Photoionisation, ist dies von besonderer Wichtigkeit.

BIBLIOGRAPHY

1. McNaught, A. D.; Wilkinson, A. *Compendium of Chemical Terminology, The Gold Book*, 2nd ed.; Blackwell Science: New York, 1997. (Cited on page 1.)

2. Franklin, J. L. *Ann. Rev. Phys. Chem.* **1967**, *18*, 261. (Cited on pages 1 and 99.)

3. Baulch, D. L.; Griffiths, J. F.; Richter, R. *Chem. Engineering Science* **1991**, *46*, 2315. (Cited on page 1.)

4. Thaddeus, P.; Gottlieb, C. A.; Mollaaghababa, R.; Vrtilek, J. *J. Chem. Soc. Faraday Trans.* **1993**, *89*, 2125. (Cited on pages 1 and 99.)

5. Flasar, F. M.; et al. *Science* **2005**, *308*, 975.

6. Stahl, F.; Schleyer, P. R.; Schaefer, H.; Kaiser, R. *Planet. Space Sci.* **2002**, *50*, 685.

7. Keller, C. N.; Anicich, V. G.; Cravens, T. E. *Planet. Space Sci.* **1998**, *46*, 1157–74. (Cited on page 1.)

8. Sawamoto, M.; Kamigaito, M. *Trends in Polymer Sci.* **1996**, *4*, 371. (Cited on page 1.)

9. Uemura, T.; Kitagawa, K.; Horike, S.; Kawamura, T.; Kitagawa, S.; Mizunob, M.; Endo, K. *Chem. Comm.* **2005**, *48*, 5968. (Cited on page 1.)

10. Olah, G. A.; Molna, A. *Hydrocarbon Chemistry*; John Wiley & Sons, Inc.: New York, 1995. (Cited on pages 1 and 99.)

11. Bettinger, H. F.; Schreiner, P. R.; Schaefer, H. F. *Carbenes - a testing ground for electronic structure methods*, 1st ed.; Allinger, N. L.; Clark, T.; Gasteiger, J.; Kollman, P. A.; Schaefer, H. F.; Schreiner, P. R., Eds.; John Wiley & Sons: Chichester, 1998. (Cited on pages 2, 67, and 99.)

12. Maier, G.; Reisenauer, H. P.; Rohde, B.; Dehnicke, K. *Chem. Ber.* **1983**, *116*, 732–740. (Cited on page 2.)

13. Taatjes, C. A.; Klippenstein, S. J.; Hansen, N.; Miller, J. A.; Cool, T. A.; Wang, J.; Law, M. E.; Westmoreland, P. R. *Phys. Chem. Chem. Phys.* **2005**, *7*, 806. (Cited on page 2.)

14. Deyerl, H.-J.; Gilbert, T.; Fischer, I.; Chen, P. *J. Chem. Phys.* **1997**, *107*, 3329–3332. (Cited on pages 2 and 120.)

15. Engelking, P. C. *Chem. Rev.* **1991**, *91*, 399–414. (Cited on page 2.)

16. Wolfrum, J. *Faraday Discuss.* **2002**, *119*, 1. (Cited on page 2.)

17. Costa, M.; Vaglieco, B. M.; Corcione, F. E. *Exp. Fluids* **2005**, *39*, 514. (Cited on page 2.)

18. Kohn, D. W.; Clauberg, H.; Chen, P. *Rev. Sci. Instrum.* **1992**, *63*, 4003–4005. (Cited on pages 2, 17, and 100.)

19. Levy, D. H. *Annu. Rev. Phys. Chem.* **1980**, *31*, 197. (Cited on page 2.)

20. Wootten, A.; Bozyan, E. P.; Garrett, D. B.; Loren, R. B.; Snell, R. L. *Astrophys. J.* **1980**, *239*, 844–854. (Cited on page 2.)

21. Warnatz, J. *Combustion Chemsitry*, 1st ed.; Springer: New York, 1984. (Cited on page 2.)

22. Hammond, G. S.; Caldwell, R. A.; King, J. M.; Kristinsson, H.; Whitten, D. G. *Photochem. Photobiol.* **1968**, *7*, 695–703. (Cited on page 2.)

23. Murray, A. J.; Hammond, P. *Phys. Rev. Lett.* **1999**, *82*, 4799–4802. (Cited on page 2.)

24. Ibragimova, L. B. *J. Eng. Phys. Thermophys.* **1981**, *40*, 250–253. (Cited on page 2.)

25. Chen, P.; Colson, S. D.; Chupka, W. A.; Berson, J. A. *J. Phys. Chem.* **1986**, *90*, 2319. (Cited on page 3.)

26. Schlag, E. W. *Berichte der Bunsen-Gesellschaft* **1994**, *98*, 1389.

27. Fischer, I. *Chimia* **2000**, *54*, 96–102. (Cited on page 109.)

28. Beeby, A. *An Introduction to Laser Spectroscopy*, 2nd ed.; Kluwer Academic: New York, 2002. (Cited on page 3.)

29. Hashimoto, M.; Hatanaka, Y. *Eur. J. Org. Chem.* **2008**, *2008*, 2513–2523. (Cited on pages 3, 53, and 63.)

30. Noller, B.; Maksimenka, R.; Fischer, I.; Armone, M.; Engels, B.; Alcaraz, C.; Poisson, L.; Mestdagh, J.-M. *J. Phys. Chem. A* **2007**, *111*, 1771. (Cited on pages 3, 41, 48, 52, 107, 119, 120, 124, 125, and 149.)

31. Ashfold, M. N. R.; Howe, J. D. *Ann. Rev. Phys. Chem.* **1994**, *45*, 57–82. (Cited on page 5.)

32. Ledingham, K. W. D.; Deas, R. M.; Marshall, A.; McCanny, T.; Singhal, R. P.; Kilic, H. S.; Kosmidis, C.; Langley, A. J.; Shaikh, W. *Rapid Commun. Mass Spectrom.* **1995**, *9*, 1522. (Cited on page 5.)

33. Zacharias, H.; Rottke, H.; Danon, J.; Welge, K.-H. *Opt. Commun.* **1981**, *37*, 15. (Cited on page 6.)

34. Michael, J. V.; Weston, R. E. *J. Chem. Phys.* **1966**, *45*, 3632. (Cited on page 6.)

35. Demtröder, W. *Laserspektroskopie*, 5th ed.; Springer Verlag: Berlin, 2007. (Cited on pages 7 and 114.)

36. Park, J.; Bersohn, R.; Oref, I. *J. Chem. Phys.* **1990**, *93*, 5700. (Cited on pages 7 and 42.)

37. Garcia, G. A.; Nahon, L.; Powis, I. *Rev. Sci. Instrum.* **2004**, *75*, 4989. (Cited on pages 8, 10, 11, and 22.)

38. Whitaker, B. *Imaging in Molecular Dynamics*; Cambridge University Press: Cambridge, 2003. (Cited on pages 8, 9, 10, 76, 88, and 91.)

39. Seideman, T. *Annu. Rev. Phys. Chem.* **2002**, *53*, 41–65. (Cited on page 8.)

40. Poisson, L. *Analyse pour TOF et Imaging*, *V. 2.2*, LabVIEW. (Cited on pages 10 and 22.)

41. Greene, C. H.; Zare, R. N. *Ann. Rev. Phys. Chem.* **1982**, *33*, 119. (Cited on pages 10 and 11.)

42. Zare, R. N. *Chem. Phys. Lett.* **1989**, *156*, 1. (Cited on page 10.)

43. Carley, R. E.; Heesel, E.; Fielding, H. H. *Chem. Soc. Rev.* **2005**, *34*, 949. (Cited on page 11.)

44. Zewail, A. H.; et al. *Femtochemistry*; De Schryver, F. C.; De Feyter, S.; Schweitzer, G., Eds.; Wiley-VCH: Weinheim, 2001. (Cited on pages 11 and 12.)

45. Doany, F. E.; Hochstrasser, R. M.; Greene, B. I.; Millard, R. R. *Chem. Phys. Lett.* **1985**, *118*, 1. (Cited on page 11.)

46. Dantus, M.; Rosker, M. J.; Zewail, A. H. *J. Chem. Phys.* **1987**, *87*, 2395. (Cited on pages 11, 12, and 13.)

47. Cheng, P. Y.; Zhong, D.; Zewail, A. H. *J. Chem. Phys* **1995**, *103*, 5153. (Cited on page 12.)

48. Diau, E. W.-G.; De Feyter, S.; Zewail, A. H. *J. Chem. Phys.* **1999**, *110*, 9785–9788. (Cited on page 12.)

49. Smith, D. D.; Rice, S. A.; Struve, W. *Faraday Discuss. Chem. Soc.* **1983**, *75*, 173–182. (Cited on page 13.)

50. Stolow, A. *Annu. Rev. Phys. Chem.* **2003**, *54*, 89–119. (Cited on pages 13, 14, 75, 85, 107, and 119.)

51. Blanchet, V.; Zgierski, M. Z.; Seideman, T.; Stolow, A. *Nature* **1999**, *401*, 52–4. (Cited on page 14.)

52. Palm, H.; Merkt, F. *Appl. Phys. Lett.* **1998**, *73*, 157–159. (Cited on page 14.)

53. Schüßler, T.; Deyerl, H.-J.; Dümmler, S.; Fischer, I.; Alcaraz, C.; Elhanine, M. *J. Chem. Phys.* **2003**, *118*, 9077. (Cited on pages 14 and 68.)

54. Ohno, K.; Okamura, K.; Yamakado, H.; Hoshino, S.; Takami, T.; Yamauchi, M. *J. Phys. Chem.* **1995**, *99*, 14247. (Cited on page 15.)

55. Reiser, G.; Habenicht, W.; Müller-Dethlefs, K.; Schlag, E. W. *Chem. Phys. Lett.* **1988**, *152*, 119. (Cited on page 15.)

56. Ng, C.-Y. *Photoionization and Photodetachment*; World Scientific: Singapore, 2000; Vol. 10 A, B. (Cited on pages 15 and 16.)

57. Céolin, D.; Chaplier, G.; Lemonnier, M.; Garcia, G. A.; Miron, C.; Nahon, L.; Simon, M.; Leclercq, N.; Morin, P. *Rev. Sci. Instrum.* **2005**, *76*, 043302. (Cited on pages 16 and 23.)

58. Proch, D.; Trickl, T. *Rev. Sci. Instrum.* **1989**, *60*, 713. (Cited on page 17.)

59. Zierhut, M.; Dissertation; Universität Würzburg; 2005. (Cited on page 17.)

60. Friderichsen, A. V.; Radziszewski, J. G.; Nimlos, M. R.; Winter, P. R.; Dayton, D. C.; David, D. E.; Ellison, G. B. *J. Am. Chem. Soc.* **2001**, *123*, 1977. (Cited on page 17.)

61. Cotter, R. J. *Time-of-Flight Mass Spectrometry*, 1st ed.; ACS: New York, 1943. (Cited on pages 19 and 20.)

62. Gebhardt, C. R.; Rakitzis, T. P.; Samartzis, P. C.; Ladopoulos, V.; Kitsopoulos, T. N. *Rev. Sci. Instrum.* **2001**, *72*, 3848–3853. (Cited on page 22.)

63. Poisson, L.; Raffael, K. D.; Soep, B.; Mestdagh, J.-M.; Buntinx, G. *J. Am. Chem. Soc.* **2006**, *128*, 3169–3178. (Cited on page 22.)

64. Richard-Viard, M.; Delboulbe, A.; Vervloet, M. *Chem. Phys.* **1996**, *209*, 159–167. (Cited on page 23.)

65. Mercier, B.; Compin, M.; Prevost, C.; Bellec, G.; Thissen, R.; Dutuit, O.; Nahon, L. *J. Vac. Sci. Tech. A* **2000**, *18*, 2533. (Cited on page 23.)

66. Baer, T. *Int. J. Mass Spectrom.* **2000**, *200*, 443–457. (Cited on page 23.)

67. Young, D. *Computational Chemistry: A Practical Guide for Applying Techniques to Real World Problems*, 1st ed.; John Wiley & Sons: New York, 2001. (Cited on page 25.)

68. Helgaker, T.; Gauss, J.; Jørgensen, P.; Olsen, J. *J. Chem. Phys.* **1997**, *106*, 6430–6440. (Cited on pages 26 and 27.)

69. Andersson, M. P.; Uvdal, P. *J. Phys. Chem.* **2005**, *109*, 2937. (Cited on page 27.)

70. Lau, K. C.; Ng, C.-Y. *J. Chem. Phys.* **2005**, *122*, 224310. (Cited on pages 27, 67, and 74.)

71. Check, C. E.; Gilbert, T. M. *J. Org. Chem.* **2005**, *70*, 9828. (Cited on page 27.)

72. Zhao, Y.; Truhlar, D. G. *J. Chem. Theory Comput.* **2008**, *4*, 1849–1868. (Cited on page 27.)

73. Zhao, Y.; Truhlar, D. G. *Acc. Chem. Res.* **2008**, *41*, 157–167. (Cited on page 27.)

74. Boese, A. D.; Martin, J. M. L. *J. Chem. Phys.* **2004**, *121*, 3405. (Cited on pages 27, 48, 88, and 101.)

75. Zheng, W.-R.; Fu, Y.; Guo, Q.-X. *J. Chem. Theory Comput.* **2008**, *4*, 1324–1331. (Cited on page 27.)

76. Mebel, A. M.; Jackson, W. M.; Chang, A. H. H.; Lin, S. H. *J. Am. Chem. Soc.* **1998**, *120*, 5751. (Cited on pages 27, 99, 109, and 116.)

77. Peng, C. Y.; Ayala, P. Y.; Schlegel, H. B.; Frisch, M. J. *J. Comput. Chem.* **1996**, *17*, 49–56. (Cited on pages 28, 88, and 89.)

78. Levchenko, S. V.; Krylov, A. I. *J. Chem. Phys.* **2001**, *115*, 7485–7494. (Cited on page 28.)

79. Cassam-Chenaï, P.; Chandler, G. S. *Int. J. Quantum Chem.* **1993**, *46*, 593–607. (Cited on page 28.)

80. Runge, E.; Gross, E. K. U. *Phys. Rev. Lett.* **1984**, *52*, 997. (Cited on page 29.)

81. Wiberg, K. B.; Stratmann, R. E.; Frisch, M. J. *Chem. Phys. Lett.* **1998**, *297*, 60–64. (Cited on page 29.)

82. Sobolewski, A. L.; Domcke, W. *Phys. Chem. Chem. Phys.* **1999**, *1*, 3065–3072. (Cited on pages 29 and 155.)

83. Hehre, W. J.; Radom, L.; Schleyer, P. R.; Pople, J. A. *Ab initio molecular orbital theory*, 1st ed.; Wiley: New York, 1986. (Cited on page 29.)

84. Woon, D. E.; Dunning, T. H. *J. Chem. Phys.* **1993**, *98*, 1358. (Cited on page 29.)

85. Ditchfield, R.; Hehre, W. J.; Pople, J. A. *J. Chem. Phys.* **1971**, *54*, 724. (Cited on page 29.)

86. Wiberg, K. B. *J. Comput. Chem.* **2004**, *25*, 1342. (Cited on page 30.)

87. Boese, A. D.; Martin, J. M. L.; Handy, N. C. *J. Chem. Phys.* **2003**, *119*, 3005. (Cited on page 30.)

88. Marcus, R. A. *J. Chem. Phys.* **1952**, *20*, 359. (Cited on page 30.)

89. Holbrook, K. A.; Pilling, M. J.; Robertson, S. H. *Unimolecular Reactions*, 1st ed.; John Wiley & Sons: New York, 1996. (Cited on pages 30 and 31.)

90. Marcus, R. A.; Rice, O. K. *J. Phys. Colloide Chem.* **1951**, *55*, 894. (Cited on page 30.)

91. Wiedner, G. M.; Marcus, R. A. *J. Chem. Phys.* **1962**, *37*, 1835. (Cited on page 30.)

92. Forst, W. *Unimolecular Reactions*; Cambridge University Press: Cambridge, 2003. (Cited on page 31.)

93. Stöcker, H. *Taschenbuch mathematischer Formeln und moderner Verfahren*, 4th ed.; Verlag Harri Deutsch: Frankfurt am Main, 1999. (Cited on page 33.)

94. Pai, S.-C. *J. Chromatogr. A* **2004**, *1028*, 89–103. (Cited on page 33.)

95. Pedersen, S.; Zewail, A. H. *Mol. Phys.* **1996**, *89*, 1455–1502. (Cited on pages 33, 34, 35, 37, 83, and 104.)

96. Press, W. H.; Flannery, B. P.; Teukolsky, S. A.; Vetterling, W. T. *Numerical Recipes in C: The Art of Scientific Computing*, 2nd ed.; Cambridge University Press: Cambridge, 1992. (Cited on pages 33 and 34.)

97. Murphy, T. J.; Chrien, R. E.; Klare, K. A. *Rev. Sci. Instrum.* **1997**, *68*, 610. (Cited on page 36.)

98. Murphy, T. J.; Jimerson, J. L.; Berggren, R. R.; Faulkner, J. R.; Oertel, J. *Rev. Sci. Instrum.* **2001**, *72*, 850. (Cited on page 36.)

99. Gloaguen, E.; Mestdagh, J.-M.; Poisson, L.; Lepetit, F.; Visticot, J.-P.; Soep, B.; Coroiu, M.; Eppink, A.; Parker, D. *J. Am. Chem. Soc.* **2005**, *127*, 16529–16534. (Cited on page 37.)

100. Zierhut, M.; Roth, W.; Fischer, I. *J. Phys. Chem. A* **2004**, *108*, 8125–8130. (Cited on pages 39, 115, and 117.)

101. Bach, A.; Hostettler, J. M.; Chen, P. *J. Chem. Phys.* **2006**, *125*, 024304. (Cited on page 39.)

102. D'Anna, A.; Violi, A.; D'Alessio, A. D. *Combust. Flame* **2000**, *121*, 418–429. (Cited on page 39.)

103. Miller, J. A.; Kee, R. J.; Westbrook, C. K. *Annu. Rev. Phys. Chem.* **1990**, *41*, 345–387. (Cited on page 39.)

104. Brum, J. L.; Desmukh, S.; Koplitz, B. *J. Chem. Phys.* **1990**, *93*, 7504. (Cited on pages 39 and 50.)

105. Deyerl, H.; Fischer, I.; Chen, P. *J. Chem. Phys.* **1999**, *110*, 1450. (Cited on pages 39 and 42.)

106. Deyerl, H.-J.; Fischer, I.; Chen, P. *J. Chem. Phys.* **1999**, *111*, 3441. (Cited on pages 39, 42, 51, 117, and 118.)

107. Gilbert, T.; Grebner, T. L.; Fischer, I.; Chen, P. *J. Chem. Phys.* **1999**, *110*, 5485–5488. (Cited on pages 39, 51, and 117.)

108. Zierhut, M.; Roth, W.; Dümmler, S.; Fischer, I. *Chem. Phys.* **2004**, *305*, 123–133. (Cited on pages 39 and 51.)

109. Seakins, P. W.; Robertson, S. H.; Pilling, M. J.; Slagle, I. R.; Gmurczyk, G. W.; Bencsura, A.; Gutman, D.; Tsang, W. *J. Phys. Chem.* **1993**, *97*, 4450. (Cited on page 39.)

110. Wendt, H. R.; Hunziker, H. E. *J. Chem. Phys.* **1984**, *81*, 717–723. (Cited on pages 39, 40, 41, 49, 119, 120, 124, 153, and 155.)

111. Rosenstock, H. M.; Buff, R.; Ferreira, M. A. A.; Lias, S. G.; Parr, A.; Stockbauer, R. L.; Holmes, J. L. *J. Am. Chem. Soc.* **1982**, *104*, 2337. (Cited on page 40.)

112. Zierhut, M.; Noller, B.; Schultz, T.; Fischer, I. *J. Chem. Phys.* **2005**, *122*, 094302. (Cited on pages 41, 48, 52, 119, and 120.)

113. NIST webbook of chemistry *http://webbook.nist.gov/chemistry/* **2001**. (Cited on pages 41 and 101.)

114. Tsukiyama, K.; Bersohn, R. *J. Chem. Phys.* **1987**, *86*, 745–749. (Cited on page 42.)

115. Mordaunt, D. H.; Osborn, D. L.; Neumark, D. M. *J. Chem. Phys.* **1998**, *108*, 2448. (Cited on pages 42 and 51.)

116. North, S. W.; Marr, A. J.; Furlan, A.; Hall, G. E. *J. Phys. Chem. A* **1997**, *101*, 9224–9232. (Cited on page 42.)

117. Dixon, R. N. *J. Chem. Phys.* **1986**, *85*, 1866.

118. Hall, G. E.; Wu, M. *J. Phys. Chem.* **1993**, *97*, 10911. (Cited on page 42.)

119. Quack, M. *Chem. Phys.* **1980**, *51*, 353. (Cited on page 43.)

120. Troe, J. *J. Chem. Phys.* **1979**, *70*, 5107. (Cited on page 43.)

121. Levenberg, K. *Quart. Appl. Math.* **1944**, *2*, 164. (Cited on page 44.)

122. Marquardt, D. *J. Appl. Math.* **1963**, *11*, 431. (Cited on page 44.)

123. Hammond, G. S. *J. Am. Chem. Soc.* **1955**, *77*, 334–338. (Cited on pages 45, 63, and 148.)

124. Knyazev, V. D. *J. Phys. Chem. A* **1998**, *102*, 3916. (Cited on page 46.)

125. East, A. L. L.; Radom, L. *J. Chem. Phys.* **1997**, *106*, 6655. (Cited on pages 46 and 156.)

126. Karas, A. J.; Gilerbert, R. G. *Chem. Phys. Lett.* **1992**, *193*, 181. (Cited on page 47.)

127. Chen, Y.; Rauk, A.; Tschuikow-Roux, E. *J. Phys. Chem.* **1990**, *94*, 2775. (Cited on page 47.)

128. Gilbert, R. G.; Smith, S. C. *Theory of Unimolecular and Recombination Reactions*, 1st ed.; Blackwell Scientific Publications: New York, 1990. (Cited on pages 47 and 99.)

129. Bach, A.; Hostettler, J. M.; Chen, P. *J. Chem. Phys.* **2005**, *123*, 021101. (Cited on pages 48, 52, and 120.)

130. Chase, M. W. *J. Phys. Chem. Ref. Data Monograph 9* **1998**, *9*, 1. (Cited on page 49.)

131. Tsang, W.; Simoes, J. A. M.; Greenberg, A.; Liebman, J. F. *Blackie Academic and Professional, London* **1996**, *1*, 22. (Cited on page 49.)

132. Calvert, J. G.; Sleppy, W. C. *J. Am. Chem. Soc.* **1959**, *81*, 1544. (Cited on pages 49 and 50.)

133. Kerr, J. A.; Calvert, J. G. *J. Am. Chem. Soc.* **1961**, *83*, 3391. (Cited on page 50.)

134. Zheng, X. *Ind. Eng. Chem. Res.* **2006**, *45*, 530. (Cited on page 50.)

135. Moss, R. A. *Acc. Chem. Res.* **2006**, *39*, 267–272. (Cited on pages 53 and 76.)

136. Robin, M. B.; Brundle, C. R.; Kuebler, N. A.; Ellison, G. B.; Widerg, K. B. *J. Chem. Phys.* **1972**, *57*, 1758. (Cited on pages 53 and 61.)

137. Blush, J. A.; Chen, P. *J. Phys. Chem.* **1992**, *96*, 4138–4140. (Cited on page 54.)

138. Graham, W. H. *J. Am. Chem. Soc.* **1965**, *87*, 4396. (Cited on pages 55, 76, and 130.)

139. Brunner, J.; Senn, H.; Richards, F. M. *J. Biol. Chem.* **1980**, *255*, 3313. (Cited on page 130.)

140. Liu, M. T. H.; Ramakrishnan, K. *J. Org. Chem.* **1977**, *42*, 3450–3452. (Cited on pages 55, 76, and 130.)

141. Asher, R. L.; Appelman, E. H.; Ruscic, B. *J. Chem. Phys.* **1996**, *105*, 9781. (Cited on pages 56, 57, and 59.)

142. Weitzel, K.-M.; Booze, J. A.; Baer, T. *Chem. Phys.* **1991**, *150*, 263–273. (Cited on pages 58, 59, 102, and 103.)

143. Schröder, D.; Suelzle, D.; Dutuit, O.; Baer, T.; Schwarz, H. *J. Am. Chem. Soc.* **1994**, *116*, 6395–6400. (Cited on pages 58 and 102.)

144. Kotz, J. C.; Treichel, P. *Chemistry and Chemical Reactivity*, 7th ed.; Cengage Learning: Belmont, 2008. (Cited on pages 59 and 103.)

145. Frisch, M. J.; Trucks, G. W.; Schlegel, H. B.; et al. *Gaussian 03, Revision C.02*, 2004. (Cited on pages 59, 88, and 149.)

146. Brinker, U. H. In *Advances in Carbene Chemistry*; Brinker, U. H., Ed.; Jai Press Inc.: London, 1998; Vol. 2. (Cited on page 63.)

147. Blencowe, A.; Hayes, W. *Soft Matter* **2005**, *1*, 178–205. (Cited on pages 63, 76, and 92.)

148. Bonness, S.; Kirtman, B.; Huix, M.; Sanchez, A. J.; Luis, J. M. *J. Chem. Phys.* **2006**, *125*, 014311. (Cited on page 70.)

149. Mackie, R. A.; Holland, D. M. P.; Shaw, D. A. *J. Phys. B* **2005**, *38*, 161–171. (Cited on page 71.)

150. Ostrovsky, V. N. *J. Phys. B* **2004**, *37*, 4657–4661. (Cited on page 71.)

151. Wannier, G. H. *Phys. Rev.* **1953**, *90*, 817–825. (Cited on page 71.)

152. Pliego, J.; De Almeida, W.; Celebi, S.; Zhu, Z.; Platz, M. *J. Phys. Chem. A* **1999**, *103*, 7481–7486. (Cited on pages 72, 74, 75, 82, 89, 90, 93, 94, and 96.)

153. Gould, I. R.; Turro, N. J.; Butcher, J.; Doubleday, C.; Hacker, N. P.; Lehr, G. F.; Moss, R. A.; Cox, D. P.; Guo, W.; Munjal, R. C.; Perez, L. A.; Fedorynski, M. *Tetrahedron* **1985**, *41*, 1587–1600. (Cited on pages 74, 75, 92, and 95.)

154. Wasserman, E. *J. Chem. Phys.* **1965**, *42*, 3739. (Cited on pages 74, 75, 89, and 95.)

155. Gillespie, R. J.; Robinson, E. A. *Chem. Soc. Rev.* **2005**, *34*, 396–407. (Cited on page 74.)

156. Sander, W.; Bucher, G.; Wierlacher, S. *Chem. Rev.* **1993**, *93*, 1583–1621. (Cited on pages 75 and 96.)

157. Baron, W. J.; Decamp, M. R. *Tetrahedron Lett.* **1973**, 4225–4228. (Cited on page 75.)

158. Geise, C. M.; Hadad, C. M. *J. Org. Chem.* **2002**, *67*, 2532–2540. (Cited on pages 75 and 92.)

159. Sander, W. W. *Spectrochim. Acta* **1987**, *43A*, 637. (Cited on pages 75, 96, and 97.)

160. Wang, J.; Burdzinski, G.; Kubicki, J.; Platz, M. S.; Moss, R. A.; Fu, X. L.; Piotrowiak, P.; Myahkostupov, M. *J. Am. Chem. Soc.* **2006**, *128*, 16446. (Cited on page 75.)

161. Groß, C.; Noller*, B.; Fischer*, I. *Phys. Chem. Chem. Phys* **2008**, *10*, 5196. (Cited on pages 75 and 121.)

162. Noller, B.; Hemberger, P.; Fischer, I.; Alcaraz, C.; Garcia, G.; Soldi-Lose, H. *Phys. Chem. Chem. Phys.* **2009**, DOI:10.1039/b823269e. (Cited on pages 78, 80, and 92.)

163. Nassal, M. *Liebigs Ann. Chem.* **1983**, 1510–1523. (Cited on page 79.)

164. Syage, J. A.; Al Adel, F.; Zewail, A. H. *Chem. Phys. Lett.* **1983**, *103*, 15–22. (Cited on page 81.)

165. McMahon, R. J.; Chapman, O. L. *J. Am. Chem. Soc.* **1987**, *109*, 683. (Cited on pages 82 and 89.)

166. Lee, S.-H.; Tang, K.-C.; Chen, I.-C.; Schmitt, M.; Shaffer, J. P.; Schultz, T.; Underwood, J. G.; Zgierski, M. Z.; Stolow, A. *J. Phys. Chem. A* **2002**, *106*, 8979–8991. (Cited on pages 82, 119, and 124.)

167. Kuthirummal, N.; Weber, P. M. *Chem. Phys. Lett.* **2003**, *378*, 647–653. (Cited on page 82.)

168. Song, J.-K.; Tsubouchi, M.; Suzuki, T. *J. Chem. Phys.* **2001**, *115*, 8810–8818.

169. Tsubouchi, M.; Suzuki, T. *J. Phys. Chem. A* **2003**, *107*, 10897–10903. (Cited on page 82.)

170. Bettinger, H. F.; Schleyer, P. V.; Schaefer, H. F.; Schreiner, P. R.; Kaiser, R. I.; Lee, Y. T. *J. Chem. Phys.* **2000**, *113*, 4250–4264. (Cited on page 84.)

171. Rosenberg, M. G.; Brinker, U. H. *J. Org. Chem.* **2003**, *68*, 4819–4832. (Cited on pages 88 and 92.)

172. Chung, G.; Lee, D. *Chem. Phys. Lett.* **2001**, *350*, 339–344. (Cited on page 89.)

173. Worthington, S. H.; Cramer, C. J. *J. Phys. Org. Chem.* **1997**, *10*, 755. (Cited on page 89.)

174. Cramer, C. J.; Truhlar, D. G.; Falvey, D. E. *J. Am. Chem. Soc.* **1997**, *119*, 12338–12342. (Cited on page 89.)

175. Garcia, V. M.; Castell, O.; Reguero, M.; Caballol, R. *Mol. Phys.* **1996**, *87*, 1395–1404. (Cited on page 90.)

176. Yamada, H.; Taniguchi, N.; Kawasakia, M. *J. Chem. Phys.* **2002**, *117*, 1130. (Cited on page 92.)

177. McMahon, R. J.; Abelt, C. J.; Chapman, O. L.; Johnson, J. W.; Krei, C. L.; LeRoux, J.-P.; Mooring, A. M.; West, P. R. *J. Am. Chem. Soc.* **1987**, *109*, 2456–2469. (Cited on page 92.)

178. West, P. R.; Chapman, O. L.; LeRoux, J. P. *J. Am. Chem. Soc.* **1982**, *104*, 1779–1782. (Cited on page 92.)

179. Raptis, C. A.; Pratt, S. T. *Phys. Rev. Lett.* **2000**, *84*, 5078. (Cited on page 95.)

180. Tao, C.; Reid, S. A.; Schmidt, T. W.; Kable, S. H. *J. Chem. Phys.* **2007**, *126*, 051105. (Cited on page 96.)

181. Hodges, J. A.; McMahon, R. J.; Sattelmeyer, K. W.; Stanton, J. F. *Astrophys. J.* **2000**, *544*, 838–842. (Cited on page 99.)

182. McCarthy, M. C.; Thaddeus, P. *Astrophys. J.* **2002**, *569*, L55.

183. Thaddeus, P.; Gottlieb, C. A.; Mollaaghababa, R.; Vrtilek, J. *J. Chem. Soc., Faraday Trans.* **1993**, *89*, 2125. (Cited on page 99.)

184. Stanton, J. F.; DePinto, J. T.; Seburg, R. A.; Hodges, J. A.; McMahon, R. J. *J. Am. Chem. Soc.* **1997**, *119*, 429–430. (Cited on pages 99, 106, and 117.)

185. Gottlieb, C. A.; Killian, T. C.; Thaddeus, P.; Botschwina, P.; Flügge, J.; Oswald, M. *J. Chem. Phys.* **1993**, *98*, 4478–4485. (Cited on page 99.)

186. Birza, P.; Chirokolava, A.; Araki, M.; Kolek, P.; Maier, J. P. *J. Mol. Spectrosc.* **2005**, *229*, 276–282. (Cited on page 99.)

187. Achkasova, E.; Araki, M.; Denisov, A.; Maier, J. P. *J. Mol. Spectrosc.* **2006**, *237*, 70–75. (Cited on page 99.)

188. Seburg, R. A.; Patterson, E. V.; Stanton, J. F.; McMahon, R. J. *J. Am. Chem. Soc.* **1997**, *119*, 5847. (Cited on pages 99, 106, and 117.)

189. Clauberg, H.; Minsek, D. W.; Chen, P. *J. Am. Chem. Soc.* **1992**, *114*, 99–107. (Cited on pages 99, 106, 110, 112, and 113.)

190. Opinion *Nature* **1997**, *387*, 831. (Cited on page 100.)

191. McGrath, M. P.; Radom, L. *J. Chem. Phys.* **1991**, *94*, 511. (Cited on page 101.)

192. Glukhovtsev, M. N.; Pross, A.; McGrath, M. P.; Radom, L. *J. Chem. Phys.* **1995**, *103*, 1878. (Cited on page 101.)

193. Stoll, H.; Metz, B.; Dolg, M. *J. Comput. Chem.* **2002**, *23*, 767. (Cited on page 101.)

194. Martin, J. M. L.; Sundermann, A. *J. Chem. Phys.* **2001**, *114*, 3408. (Cited on page 101.)

195. Mulliken, R. S. *Phys. Rev.* **1935**, *47*, 413. (Cited on page 105.)

196. Fischer, I. *Chem. Soc. Rev.* **2003**, *32*, 59–69. (Cited on page 109.)

197. Ochsenfeld, C.; Kaiser, R. I.; Lee, Y. T.; Suits, A. G.; Head-Gordon, M. *J. Chem. Phys.* **1997**, *106*, 4141. (Cited on page 109.)

198. Sheehan, S. M.; Parsons, B. F.; Zhou, J.; Garand, E.; Yen, T. A.; Moore, D. T.; Neumark, D. M. *J. Chem. Phys.* **2008**, *128*, 034301. (Cited on page 109.)

199. Edlen, B. *Phys. Scr.* **1982**, *26*, 71. (Cited on page 109.)

200. Casavecchia, P.; Balucani, N.; Cartechini, L.; Capozza, G.; Bergeat, A.; Volpi, G. G. *Faraday Discuss.* **2001**, *119*, 27. (Cited on page 109.)

201. Clary, D.; Buonomo, E.; Sims, I.; Smith, I.; Geppert, W.; Naulin, C.; Costes, M.; Cartechini, L.; Casavecchia, P. *J. Phys. Chem. A* **2002**, *106*, 5541. (Cited on page 109.)

202. Schüßler, T.; Roth, W.; Gerber, T.; Fischer, I.; Alcaraz, C. *Phys. Chem. Chem. Phys.* **2005**, *7*, 819. (Cited on page 110.)

203. Kenney, J. W.; Simons, J.; Purvis, G. D.; Bartlett, R. J. *J. Am. Chem. Soc.* **1978**, *100*, 6930. (Cited on page 113.)

204. Rubio, M.; Stalring, J.; Bernhardsson, A.; Lindh, R.; Roos, B. O. *Theor. Chem. Acc.* **2000**, *105*, 15. (Cited on page 113.)

205. Schmiedl, R.; Dugan, H.; Meier, W.; Welge, K.-H. *Z. Phys. A.* **1982**, *304*, 137–142. (Cited on page 114.)

206. Ogilvie, J. F. *Trans. Faraday Soc.* **1971**, *67*, 2205. (Cited on page 114.)

207. Gasser, M.; Bach, A.; Chen, P. *Phys. Chem. Chem. Phys.* **2008**, *10*, 1133–1138. (Cited on pages 115 and 120.)

208. Noller, B.; Fischer, I. *J. Chem. Phys.* **2007**, *126*. (Cited on page 117.)

209. Fischer, I.; Chen, P. *J. Phys. Chem A* **2002**, *106*, 4291. (Cited on page 117.)

210. Fahr, A.; Hassanzadeh, P.; Laszlo, B.; Huie, R. E. *Chem. Phys.* **1997**, *215*, 59. (Cited on pages 117 and 118.)

211. Goncher, S. J.; Moore, D. T.; Sveum, N. E.; Neumark, D. M. *J. Chem. Phys.* **2008**, *128*, 114303. (Cited on page 117.)

212. Eisfeld, W. *Phys. Chem. Chem. Phys.* **2005**, *7*, 3924–3932. (Cited on page 118.)

213. Eisfeld, W. *J. Phys. Chem. A* **2006**, *110*, 3903–3910. (Cited on page 118.)

214. Blanchet, V.; Stolow, A. *J. Chem. Phys.* **1998**, *108*, 4371–4374. (Cited on page 119.)

215. Geßner, O.; Chrysostom, E. T. H.; Lee, A. M. D.; Wardlaw, D. M.; Ho, M. L.; Lee, S. J.; Cheng, B. M.; Zgierski, M. Z.; Chen, I.-C.; Shaffer, J. P.; Hayden, C. C.; Stolow, A. *Faraday Discuss.* **2004**, *127*, 193–212. (Cited on page 119.)

216. Zewail, A. H. *J. Phys. Chem.* **1996**, *100*, 12701–12724. (Cited on page 119.)

217. Stone, H.; Shechter, H. *J. Org. Chem.* **1950**, *15*, 491–495. (Cited on pages 120 and 131.)

218. Kadi, M.; Davidsson, J.; Tarnovsky, A. N.; Rasmusson, M.; Åkesson, E. *Chem. Phys. Lett.* **2001**, *350*, 93 – 98. (Cited on page 121.)

219. Waits, L. D.; Horwitz, R. J.; Daniel, R. G.; Guest, J. A.; Appling, J. R. *J. Chem. Phys.* **1992**, *97*, 7263–7269. (Cited on page 121.)

220. Hatch, L. F.; Kidwell, L. E. *J. Am. Chem. Soc.* **1954**, *76*, 289. (Cited on page 127.)

221. Hatch, L. F.; Mangold, D. J. *J. Am. Chem. Soc.* **1955**, *77*, 176. (Cited on page 127.)

222. Finkelstein, H. *Ber.* **1910**, *43*, 1528. (Cited on page 127.)

223. Breslow, R.; Ryan, G.; Groves, J. T. *J. Am. Chem. Soc.* **1970**, *92*, 988. (Cited on page 128.)

224. Abendroth, H. J. *Angew. Chem.* **1961**, *73*, 67. (Cited on page 128.)

225. Abendroth, H. J.; Henrich, G. *Angew. Chem.* **1959**, *71*, 283. (Cited on page 128.)

226. Schmitz, E.; Ohme, R. *Org. Synth. Coll.* **1973**, *5*, 897. (Cited on page 129.)

227. Overberger, C. G.; Anselme, J.-P. *J. Org. Chem.* **1964**, *29*, 1188–1190. (Cited on page 130.)

228. Ohme, R.; Preuschhof, H.; Heyne, H.-U. *Org. Synth. Coll.* **1988**, *6*, 78. (Cited on page 132.)

229. Head, J. D. *Int. J. Quantum Chem.* **2003**, *95*, 580. (Cited on page 135.)

230. Hase, W. L.; Bunker, D. L. *QCPE* **1975**, *11*, 291. (Cited on page 136.)

231. Wurz, P.; Gubler, L. *Rev. Sci. Instrum.* **1996**, *67*, 1790–1793. (Cited on pages 143 and 144.)

232. Müller-Dethlefs, K.; Sander, M.; Schlag, E. *Chem. Phys. Lett.* **1984**, *112*, 291. (Cited on pages 143 and 146.)

233. Olah, G. A.; Prakash, G. K. S. *Carbocation Chemistry*, 1st ed.; Wiley-Interscience: New York, 2004. (Cited on page 143.)

234. Schletti, R.; Wurz, P.; Scherer, S.; Siegmund, O. H. *Rev. Sci. Instrum.* **2001**, *72*, 1634–1639. (Cited on page 143.)

235. Wurz, P.; Gubler, L. *Rev. Sci. Instrum.* **1994**, *65*, 871–876. (Cited on page 143.)

236. Galanti, M.; Gott, R.; Renaud, J. F. *Rev. Sci. Instrum.* **1971**, *42*, 1818. (Cited on page 144.)

237. Wiza, J. *Nucl. Instrum. Meth.* **1979**, *162*, 587. (Cited on page 144.)

238. Zinke, O.; Brunswig, H. *Lehrbuch der Hochfrequenztechnik*, 4th ed.; Springer-Verlag: Berlin, 1990. (Cited on page 145.)

239. Cockett, M. C. R. *Chem. Soc. Rev.* **2005**, *34*, 935 – 948. (Cited on page 146.)

240. Worley, S. D. *Chem. Rev.* **1971**, *71*, 295–314. (Cited on page 146.)

241. Merkt, F. *Annu. Rev. Phys. Chem.* **1997**, *48*, 675–709. (Cited on page 146.)

242. Held, A.; Baranov, L. Y.; Selzle, H. L.; Schlag, E. W. *J. Chem. Phys.* **1997**, *106*, 6848–62. (Cited on page 146.)

243. Gentry, W. R.; Giese, C. F. *Rev. Sci. Instum.* **1975**, *46*, 104. (Cited on page 148.)

244. Noller, B.; Master's thesis; University of Würzburg; 2006. (Cited on page 149.)

245. Mebel, A. M.; Morokuma, K.; Lin, M. C. *J. Chem. Phys.* **1995**, *103*, 3440–3449. (Cited on page 150.)

246. Richards, C. A.; Kim, S. J.; Yamaguchi, Y.; Schäfer, H. F. *J. Am. Chem. Soc.* **1995**, *117*, 10104. (Cited on pages 151 and 158.)

247. Matzinger, S.; Fülscher, M. *J. Phys. Chem.* **1995**, *99*, 10747–10751. (Cited on pages 151 and 158.)

248. Atkins, P.; Friedman, R. *Molecular Quantum Mechanics*, 4th ed.; Oxford University Press: New York, 2005. (Cited on pages 151 and 152.)

249. Carmichael, I. *J. Phys. Chem.* **1985**, *89*, 4727. (Cited on page 152.)

250. Roos, B.; Taylor, P.; Siegbahn, P. E. M. *J. Chem. Phys.* **1980**, *48*, 157. (Cited on page 152.)

251. Karlström, G.; Lindh, R.; Malmqvist, P.-.; Roos, B. O.; Ryde, U.; Veryazov, V.; Widmark, P.-O.; Cossi, M.; Schimmelpfennig, B.; Neogrady, P.; Seijo, L. *Comput. Mater. Sci.* **2003**, *28*, 222. (Cited on page 152.)

252. Andersson, K.; Malmqvist, P.-A.; Roos, B. O.; Sadlej, A. J.; Wolinski, K. *J. Phys. Chem.* **1990**, *94*, 5483. (Cited on page 152.)

253. Lengsfield III, B. H.; Siegbahn, P. E. M.; Liu, B. *J. Chem. Phys.* **1984**, *81*, 710. (Cited on pages 152, 153, and 156.)

254. Poirier, R.; Kari, R.; Csizmadia, I. G. *Handbook of Gaussian Basis Sets*, 1st ed.; Elsevier: New York, 1985. (Cited on page 152.)

255. Pacansky, J.; Koch, W.; Miller, M. D. *J. Am. Chem. Soc.* **1991**, *113*, 317. (Cited on page 156.)

256. Demel, O.; Pittner, J.; Carsky, P.; Hubac, I. *J. Phys. Chem. A* **2004**, *108*, 3125–3128. (Cited on page 158.)

PUBLICATIONS

Full list of publications:

1. M. Zierhut, B. Noller, T. Schultz, I. Fischer* **Excited-state decay of hydrocarbon radicals, investigated by femtosecond time-resolved photoionization: Ethyl, propargyl, and benzyl**. *J. Chem. Phys.* (2005), *122*, 094302.

2. S. Amthor, B. Noller, C. Lambert* **UV/Vis/NIR spectral properties of triarylamines and their corresponding radical cations**. *Chem. Phys.* (2005), *316*, 141.

3. B. Noller, R. Maksimenka, I. Fischer*, M. Armone, B. Engels, C. Alcaraz, L. Poisson*, J.-M. Mestdagh **Femtosecond dynamics of the *tert*-butyl radical**. *J. Phys. Chem. A* (2007), *111*, 1771.

4. B. Noller, I. Fischer* **Photodissociation dynamics of the 2-propyl radical**. *J. Chem. Phys.* (2007), *126*, 144302.

5. C. Groß, B. Noller*, I. Fischer* **On the photodissociation of propadienylidene, l-C_3H_2**. *Phys. Chem. Chem. Phys.* (2008), *10*, 5196.

6. B. Noller, L. Poisson, R. Maksimenka, I. Fischer*, J.-M. Mestdagh* **Femtosecond dynamics of isolated phenylcarbenes**. *J. Am. Chem. Soc.* (2008), *130*, 14908.

7. B. Noller, L. Poisson, R. Maksimenka, G. Oliver, I. Fischer*, J.-M. Mestdagh* **Ultrafast dynamics of isolated phenylcarbenes, followed by femtosecond time-resolved velocity map imaging**. *J. Phys. Chem. A* (2009), *113*, 3041.

8. B. Noller, P. Hemberger, I. Fischer*, C. Alcaraz*, G. A. Garcia*, H. Soldi-Lose **The photoionization of two phenylcarbenes and their diazirine precursors investigated using synchrotron radiation**. *Phys. Chem. Chem. Phys.* (2009), *DOI:10.1039/b823269e*.

9. B. Noller, M. Margraf, C. Schröter, T. Schultz, I. Fischer* **Excited-state lifetime of propadienylidene, l-C_3H_2**. *Phys. Chem. Chem. Phys.* (2009), *DOI:10.1039/b901765h*.

ACKNOWLEDGMENTS

At first I want to thank my two *supervisors Prof. Dr. I. Fischer and Prof. Dr. J.-M. Mestdagh* for giving me the opportunity to perform my PhD in two countries on the basis of a *"cotutelle"* in scientifically very interesting areas. It is so much fun to have supervisors who support their students in all aspects and take their time to pass on the many years of experience and expertise. Thanks to them it was possible for me to gain a lot of scientific knowledge on laser spectroscopy, synthesis, programming, quantum chemical calculations and building scientific equipment and they helped me to acquire international experience by giving me the possibility to do part of my thesis in France. I know this was also acquainted with lots of work from both sides. Thank you so much.

Many thanks to my *family and Alexandra*; without you I would probably at some point have completely forgotten that there is a lot more than just science. I have to admit there were some frustrating moments and I would have not passed this test without you. You are the family that made it possible for me get the education I wanted and even (hopefully) get a doctor degree at the end. This I all owe to you. Alex, even though we spent my years at the university so far apart, you always supported and encouraged me. This would have never worked out with any other girlfriend than you, thanks.

Dr. L. Poisson, you are one of the persons I very much look up to. Already during my first stay at Saclay as a diploma student I was very impressed by all your scientific knowledge. You helped me a lot on performing the femtosecond experiments of the phenylcarbenes and showed me everything I needed to know about femtosecond time-resolved experiments using velocity map imaging. It was a great joy for me to work so successfully with you. Dear *Patrick H.*, thanks for being without doubt the best diploma student I ever worked with (and later on a great friend as a PhD student). It was a great time working so efficiently together with you at the synchrotron in France (Soleil). Without you this work would not have proceeded so fast and you made a large contribution to our publication. I also very much enjoyed going to the fitness center and reading BMS magazines with you. *Michael S.*, you helped to simplify and improve almost all aspects of data acquisition in our group and helped me many times with your impressive knowledge on computers. Together you and I started in the gas phase laboratory without hardly any knowledge on laser spectroscopy and no other PhD students with years of experience to ask. Everything was harder for us than for the new generation, but we got things going. Thanks for the great time. *Markus M.*, we spent our entire studies together starting the first semester. Thank you for being such a great friend and colleague. No matter what they did to us (e. g., two semesters of OC right after another), we always passed the tests in the first try and they never got us down. *Dr. S. Gräfe*, it was a great time always going out to play tennis with you and thank you so much for the personal advice you gave me. *Dr. W. Roth*, thank you for the many hints and tips you gave us all after coming back to the

This thesis is my own original work. Only cited references have been used.

Würzburg/Paris, March 16, 2009

Dipl.-Chem. Bastian M. Noller